AD-A078 615 NATIONAL AERONAUTICS AND SPACE ADMINISTRATION HAMPTO--ETC F/G 20/4
EFFECTS OF RELAXED STATIC LONGITUDINAL STABILITY ON A SINGLE-ST--ETC(U)
DEC 79 D C FREEMAN, A W WILHITE

UNCLASSIFIED NASA-L-13243 NASA-TP-1594 NL

1 OF 2
ADA 078615

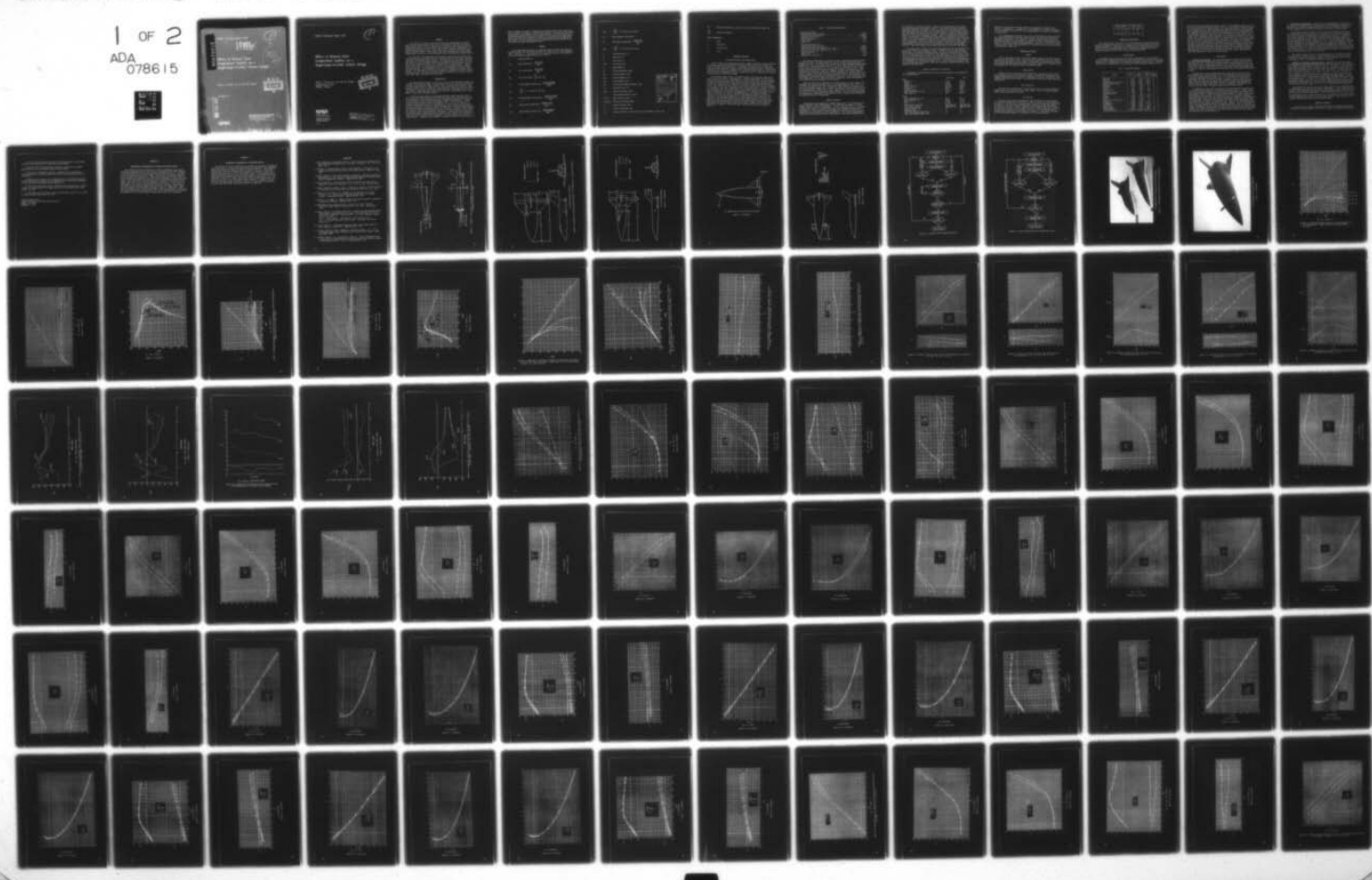

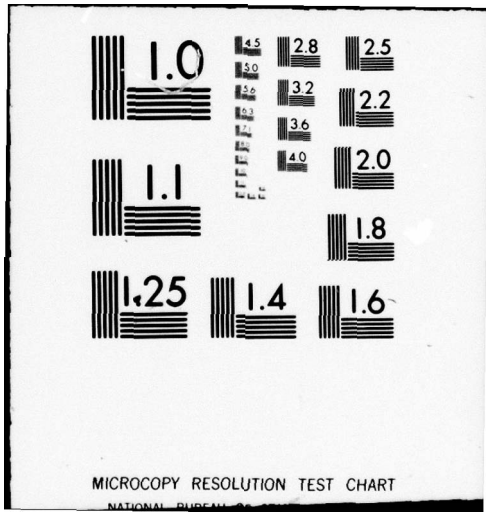
1.0
1.1
1.25
1.4
1.6
1.8
2.0
2.2
2.5
2.8
3.2
3.6
4.0
4.5
5.0
5.6
MICROCOPY RESOLUTION TEST CHART

NASA Technical Paper 1594

Effects of Relaxed Static Longitudinal Stability on a Single-Stage-To-Orbit Vehicle Design

Delma C. Freeman, Jr., and Alan W. Wilhite

DECEMBER 1979

NASA

NASA Technical Paper 1594

Effects of Relaxed Static Longitudinal Stability on a Single-Stage-To-Orbit Vehicle Design

Delma C. Freeman, Jr., and Alan W. Wilhite
Langley Research Center
Hampton, Virginia

NASA
National Aeronautics
and Space Administration

Scientific and Technical Information Branch

1979

SUMMARY

The effects of relaxing longitudinal stability requirements on single-stage-to-orbit space vehicles were studied by comparing the mass and performance characteristics of two vehicles, one required to have positive levels of longitudinal stability and the other with relaxed stability requirements in a computer-aided design process. Both vehicles were required to meet the same mission characteristics. Wind-tunnel tests were conducted over a Mach number range from 0.3 to 4.63 to verify estimated vehicle aerodynamic characteristics.

The results of these analyses and tests have shown that the vehicle with relaxed stability requirements has an estimated gross lift-off mass 10 percent less than the baseline vehicle design. The analyses have also shown that both configurations have acceptable hypersonic aerodynamic characteristics and that the use of a deployable canard on the vehicle with relaxed stability requirements could result in a significant reduction in the landing speed. Because of the large ratio of body-planform area to wing-planform area of the control configured design, the aerodynamic center was very dependent upon Mach number. However, the configuration did exhibit acceptable trimmed lift coefficients and lift-drag ratios. The model was directionally unstable over the entire supersonic Mach number and angle-of-attack range.

INTRODUCTION

The Space Shuttle Program is currently in the final development stages and hardware is being fabricated. Current studies within the National Aeronautics and Space Administration (NASA) indicate that a follow-on Earth orbital transportation system could be required in the 1995 time frame, provided that such a system offers clear and significant cost/performance advantages over the existing system. Based upon these projections, there is a continuing effort within NASA to study these advanced systems.

As part of these studies, the Langley Research Center has been investigating new technology areas that can favorably impact the cost/performance of future systems. One technology area that has been addressed is the relaxation of conventional vehicle static longitudinal stability requirements. Using existing vehicle design analysis techniques (refs. 1 to 3), the effects of relaxing longitudinal stability requirements on single-stage-to-orbit space vehicles (vertical take-off, horizontal landing) were studied by comparing the mass and performance characteristics of two vehicles. One vehicle was designed for positive levels of longitudinal stability (baseline vehicle) and the other was designed with relaxed stability requirements (control-configured vehicle). Significant weight savings have been realized in both fighter and transport aircraft by control configuring these designs (relaxing conventional stability requirements). Through various schemes, the control system in these vehicles is

used to augment the vehicle longitudinal and lateral-directional stability. This study was an attempt to identify any benefits to be derived from control configuring a single-stage-to-orbit vehicle system. Both the baseline and control-configured vehicles were designed for the same mission requirements. Wind-tunnel tests were conducted to verify estimated vehicle aerodynamics. The results of these analyses and tests showing the relative merits of the two vehicle designs are presented herein.

SYMBOLS

The longitudinal analyses are referred to both the body and stability system of axes, and the lateral analyses are referred to the body system of axes. (See fig. 1.) The origins of the axes were located to correspond to the center-of-gravity positions shown in figure 2.

b reference span, m

C_D drag coefficient, $\dfrac{\text{Drag force}}{q_\infty S}$

C_L lift coefficient, $\dfrac{\text{Lift force}}{q_\infty S}$

C_{L_α} lift-curve slope, $\dfrac{\Delta C_L}{\Delta \alpha}$, per deg

C_l rolling-moment coefficient, $\dfrac{\text{Rolling moment}}{q_\infty S b}$

C_{l_β} $= \dfrac{\Delta C_l}{\Delta \beta}$, $\beta = 0^\circ$ and 5°, per deg

C_m pitching-moment coefficient, $\dfrac{\text{Pitching moment}}{q_\infty S \bar{c}}$

C_N normal-force coefficient, $\dfrac{\text{Normal force}}{q_\infty S}$

C_n yawing-moment coefficient, $\dfrac{\text{Yawing moment}}{q_\infty S b}$

C_{n_β} $= \frac{\Delta C_n}{\Delta \beta}$, $\beta = 0^\circ$ and 5°, per deg

C_p base pressure coefficient

C_Y side-force coefficient, $\frac{\text{Side force}}{q_\infty S}$

C_{Y_β} $= \frac{\Delta C_Y}{\Delta \beta}$, $\beta = 0^\circ$ and 5°, per deg

$\bar{c}$ reference chord, m

D drag force, N

L lift force, N

L/D lift-drag ratio

ℓ body length, m

M free-stream Mach number

M_X rolling moment, m-N

M_Y pitching moment, m-N

M_Z yawing moment, m-N

q_∞ free-stream dynamic pressure, N/m^2

S reference area, m^2

T/W thrust-to-weight ratio

V free-stream velocity, m/sec

X,Y,Z body reference axes

X_s, Y_s, Z_s stability reference axes

α angle of attack, deg

β angle of sideslip, deg

δ_e elevon deflection, positive when trailing edge is down, deg

δ_F body flap deflection, positive when trailing edge is down, deg

$\frac{x_{cp}}{\ell}$ center of pressure

Model components:

B body

F body flap

V vertical tail

W wing

METHOD OF ANALYSIS

Design Description and Requirements

In this study, two single-stage-to-orbit (SSTO) concepts have been designed as vertical take-off and horizontal landing systems using liquid oxygen and liquid hydrogen rocket propulsion. The design requirements for the SSTO vehicles were based primarily on space shuttle mission specifications. Although the advanced vehicle might be designed for a different mission than the shuttle, the shuttle design requirements provide a convenient means for comparing the performance potential of advanced systems.

An advanced vehicle such as the SSTO concept could possibly become operational during the 1990's. Consequently, a 15-year advancement in both structural and propulsion technology beyond the space shuttle level has been assumed. A 25-percent mass reduction from current structures technology was projected in reference 4 basically due to advanced structural concepts and advanced materials. This 25-percent mass reduction from shuttle technology has been assumed for the wing, body, tail, propellant tanks, and landing gear. No mass reduction was assumed for the other subsystems or the thermal protection system. In the area of propulsion, the engine characteristics were based on space shuttle main-engine technology that has been extrapolated for a two-position nozzle. As shown in reference 5, a mix of fixed and two-position nozzles provided an increase in vehicle performance with an associated decrease in vehicle size. Therefore, the propulsion system for the two vehicles was divided into two parts with some of the engines having fixed nozzles (system I) and the other engines having two positions to provide variable expansion ratio (system II). The control-configured vehicle (CCV) had 6 rocket engines and the baseline vehicle had 7 engines. The rocket engine characteristics are presented in table I.

TABLE I.- ROCKET ENGINE CHARACTERISTICS

System I (fixed nozzle):	
Vacuum specific impulse I_{sp}, sec	440.5
Vacuum sea-level thrust per engine, N	3 388 924
Sea-level thrust per engine, N	3 024 640
Fuel density, kg/m^3	70.48
Oxidizer density, kg/m^3	1137.42
Mixture ratio	7.0
Expansion ratio	40.0
System II (two-position nozzle):	
Vacuum specific impulse I_{sp}, sec	466.5
Vacuum sea-level thrust per engine, N	3 588 952
Sea-level thrust per engine (Expansion ratio = 200), N	1 660 019
Sea-level thrust per engine (Expansion ratio = 40), N	3 203 164
Fuel density, kg/m^3	70.48
Oxidizer density, kg/m^3	1137.42
Mixture ratio	7.0
Expansion ratio (two-position)	40/200

The baseline SSTO vehicle was sized to meet a space shuttle mission which delivered to orbit a 29 500-kg payload in an 18.3-m cylindrical bay with a diameter of 4.6 m. The vehicle was launched vertically from NASA Kennedy Space Center with a thrust-to-weight ratio of 1.3 and an ideal velocity at burnout of 8700 m/sec and entered a 92.6- by 185.2-km orbit inclined at 28.5°. The ascent trajectory performance was determined by using the trajectory program discussed in reference 6. With this computer program, the vehicle mass at orbital injection was maximized for various constraints by varying nozzle transition altitude, pitch rate, and angle-of-attack history. The trajectory was constrained by a maximum axial acceleration of 3g (1g = 9.81 m/sec^2) and a maximum normal force of 2.5 times the vehicle landed mass, which corresponds to a 2.5g subsonic pull-up maneuver during reentry.

After the vehicle has completed an orbital mission, it must reenter the atmosphere at hypersonic speeds, have a crossrange capability of 1100 n. mi., and then land horizontally. For the baseline SSTO vehicle, the design criterion at hypersonic speeds was a stable trim angle of attack from 25° to 50°. The landing design criteria were a level flying speed of 170 knots, an angle of attack of 15°, and a statically stable vehicle. The CCV configuration had the same design requirements as the baseline vehicle except static longitudinal stability was not a requirement.

Design Synthesis

The Optimal Design Integration (ODIN) system (ref. 2) was used for the design synthesis of the SSTO vehicles. For the baseline vehicle a design scheme similar to that of references 1, 2, and 5 was used (fig. 3). In these analyses, the vehicle is sized by both ascent performance and aerodynamic requirements. Three nested iteration loops are required to arrive at a configuration which satisfies all the requirements. The internal performance loop starts by generating surface coordinates for the vehicle geometry which

are analyzed for volumes and areas. Masses are then predicted using historical mass estimating relationships (ref. 7). The lift-off thrust-to-weight requirement dictates the number of rocket engines which then establish a base area requirement for enclosure of the rocket nozzles. The mass ratio requirement for orbital velocity scales the vehicle length in order to provide enough volume for the correct propellant loading. After the performance considerations are converged, the aerodynamic requirements are checked in the outer two loops. The wing is scaled and moved to meet landing speed and static stability criteria and then checked for a hypersonic trim angle-of-attack range. Subsonic aerodynamics are predicted by the methods of reference 8, and hypersonic aerodynamics are predicted by using the hypersonic arbitrary body program (ref. 9). The final vehicle point design satisfies all initial requirements.

The scheme used to design the control-configured vehicle was somewhat different than that of the baseline vehicle. Because of the relaxed stability philosophy in the design synthesis process, the CCV configuration was configured to achieve the desired hypersonic trim capability. As can be seen in figure 4, no consideration was given in this design approach to the subsonic characteristics of the vehicle, as had been done with the baseline configuration. The body geometry was perturbed interactively to achieve the desired hypersonic trim capability by increasing fineness ratio. Since increasing fineness ratio also increased body wetted area, there was a trade-off between hypersonic trim capability and body mass.

Geometric Definition of Vehicles

The geometric characteristics of the two configurations are presented in the following table:

	Baseline	CCV
Body:		
Length, m	57.63	66.79
Width, m	16.657	15.925
Height, m	10.006	9.568
Wetted area, m^2	2291.98	2338.6
Volume, m^3	6944.69	6400
Fineness ratio	4.09	4.99
Total planform area, m^2	810.34	815.18
Base area, m^2	156	142.6
Wing:		
Area (theoretical), m^2	836	557.4
Area (exposed), m^2	386.89	217.8
Span, m	45.537	37.18
$\bar{c}$, m	21.701	17.71
Root airfoil sections	NACA 0010-64	NACA 0010-64
Tip airfoil section	NACA 0012-64	NACA 0012-64
Wing incidence, deg	1.5	1.5
Dihedral, deg	7	7
Wing leading-edge sweep, deg	50	50
Wing trailing-edge sweep, deg	0	0

Drawings of the baseline and CCV vehicles are presented in figures 2(a) and 2(b), respectively. A comparison of the planforms of the two configurations is presented in figure 2(c), and a photograph of the models is presented in figure 5(a).

As is subsequently discussed, the result of the design synthesis program was a CCV configuration that was slightly stable subsonically; therefore, a deployable canard with an area equal to 5 percent of the reference area was designed and tested to investigate the effects of subsonic longitudinal instability on the CCV configuration landing speed. A sketch of the canard is presented in figure 2(d), and a photograph of the model with the canard installed is presented in figure 5(b).

APPARATUS AND TESTS

Models

A 0.01-scale model of each of the two designs (baseline and CCV) was constructed for wind-tunnel tests. The models were constructed from the configuration lines generated in the analyses. Both models were constructed with movable elevons and body flap, and a fold-out canard (5 percent of reference area) was designed for the CCV model tests at subsonic speeds.

Wind Tunnels

Subsonic and transonic tests were conducted in the Langley 8-foot transonic pressure tunnel to determine the static, longitudinal, and lateral aerodynamic characteristics of the model. Supersonic tests were conducted in the Langley Unitary Plan wind tunnel. The hypersonic results have been reported in reference 10.

Test Conditions

The tests were conducted over a Mach range from 0.3 to 4.63 at Reynolds numbers from 2 to 5 million based on body length. The test angle-of-attack range varied from about -2° to 32°.

Corrections

The static force data presented have been corrected for sting bending. All drag data presented are total drag in that the base drag has not been subtracted out. For all tests, boundary-layer transition strips were applied to the model in the form of bands of sparsely distributed carborundum grains, 0.16 cm wide, located 1.27 cm streamwise from the leading edge of all lifting surfaces and 3.05 cm aft of the nose. The size of the carborundum grains, determined by using the sizing methods of reference 11 and used in the tests at the various Mach numbers, is presented in the following table:

Mach number	Grain size
0.3 to 1.20	No. 120
2.36 to 4.63	No. 45

RESULTS AND DISCUSSION

The study approach taken was to use the previously discussed analytical methods to design the vehicles and to predict their mass properties and estimated aerodynamics. Subsequently, an extensive wind-tunnel program was conducted and this aerodynamic data base is presented in appendixes A and B. Selected results have been used in the following discussion.

Mass Analysis

Any payoff from the change in the design requirements of the baseline-vehicle static longitudinal stability that could benefit from control-configured design would be demonstrated by a reduction in design vehicle weight. Presented in table II is a comparison of the projected vehicle component masses for the

TABLE II.- VEHICLE MASS COMPARISON

Component	Baseline, kg	CCV (canard-off), kg	Baseline -CCV, kg	Percent reduction
Wing group	14 817	9 856	4 961	33
Tail group	3 317	2 158	1 159	35
Body group	45 288	42 550	2 738	6
Induced environmental protection	27 128	24 062	3 066	11
Landing, docking, recovery	6 513	5 822	691	10
Propulsion	48 249	43 392	4 857	10
Prime power	1 774	1 774	0	0
Electrical	2 311	2 240	71	3
Hydraulic	2 454	2 226	228	9
Control surfaces	2 664	2 501	163	6
Avionics	2 021	2 021	0	0
Environmental control	1 857	1 857	0	0
Personnel provisions	790	790	0	0
Growth	11 147	9 888	1 259	11
Dry mass	170 330	151 137	19 244	11
Personnel	705	705	0	0
Cargo	29 484	29 484	0	0
Reaction control system (RCS)	68	68	0	0
Residuals	9 905	8 904	1 001	10
Landing mass	210 492	190 298	20 246	9
RCS propellant	4 536	4 536	0	0
Entry mass	215 028	194 834	20 246	9
Reserve fluids	2 825	2 539	286	10
Inflight losses	2 825	2 539	286	10
Ascent propellant	1 412 198	1 269 418	142 780	10
Gross lift-off mass	1 632 876	1 469 330	163 597	10

baseline and control-configured vehicle designs. The component masses are not the result of detailed design analyses, but it is believed that they can be used as an indication of the vehicle masses, and comparisons made by using the same basic assumptions would give valid relative masses for the two study vehicles. The comparison shows that the control-configured vehicle has an estimated gross lift-off mass 10 percent less than that of the baseline vehicle design. The largest single component weight reduction is a 33-percent reduction in the wing weight due to the 43-percent reduction in exposed wing area. The 1213-kg reduction in the vertical tail mass noted in the table is a result of reduced vertical tail size not associated with the relaxed static longitudinal stability. The mass of the canard was not considered in the mass analyses, but, based upon the most conservative estimates, the canard mass could not exceed 900 kg, and therefore would not change the conclusion drawn from the canard-off analyses. The results of the mass analyses showed that because of the larger wing the baseline vehicle had a center of gravity at 0.70 body length, approximately 0.01 body length aft of that for the CCV design.

Aerodynamics

Estimated aerodynamics.- The estimated hypersonic stability and performance for the control-configured design presented in figure 6 show that with the combination of a body flap and small positive elevon deflection, the configuration could be trimmed hypersonically over an angle-of-attack range from 10° to 60°. Results presented in figure 7 show that the baseline design vehicle had very much the same hypersonic characteristics as the control-configured design.

A comparison of the estimated hypersonic longitudinal stability with experimental data obtained at Mach 20 in the hypersonic helium tunnel facility at the Langley Research Center (ref. 10) is presented for the control-configured and baseline vehicle designs in figures 8 and 9, respectively. These data show that for the body alone, body wing, and body wing with body flap, there is reasonable agreement between the estimated and experimental results, and the small differences seen in the hypersonic longitudinal stability would not affect the design integration of either vehicle.

A comparison of the subsonic estimates with experimentally measured data for the two vehicle designs is presented in figures 10 and 11. These results show significant differences in the estimated longitudinal stability and the experimental values. The measured data show the model to be more stable than the estimates had indicated. An investigation of the estimation technique shows that the vehicle body contribution to subsonic stability was consistently underestimated. Since the control-configured design integration process was not constrained by subsonic aerodynamics, this error in the estimated subsonic stability does not affect this vehicle design. However, for the baseline vehicle, this error impacts the design integration process. Even so, the experimental aerodynamics indicate that with the center of gravity at 70-percent body length, the vehicle does achieve near-optimal subsonic performance for a stable vehicle, as there is 1-percent or less body-length stability at the landing attitude and trim elevon deflection.

Experimental aerodynamics.- Because of the estimated mass savings of the CCV vehicle, attributed to the relaxed stability, the model was tested subsonically with a small destabilizing canard to further decrease the stability of the configuration and assess its impact on the vehicle landing speed.

The subsonic stability and trim for the control-configured vehicle with and without the canard are presented in figures 12 and 13, and the trimmed lift coefficient and lift-drag ratio are presented in figure 14. Because of the vehicle stability ($0.055\bar{c}$ stable) and the elevon deflection required for trim, a lift decrement of 0.131 was incurred in order to subsonically trim the configuration at landing attitude ($\alpha = 15^{o}$). Since longitudinal stability was not required for the CCV configuration, the destabilizing influence of the canard (considered to be deployable at subsonic speeds) was acceptable. The resulting effects of the canard on trimmed lift coefficient and lift-drag ratio are shown in figure 14. As can be seen, the deployed canard increased the trim lift coefficient by 0.22 over that obtained with the elevons, which reduced the vehicle landing speed from 190 to 162 knots.

The subsonic stability and trim characteristics of the baseline vehicle are presented in figures 15 and 16. These results show that even with the large wing, sized for longitudinal stability and for landing with the center of gravity at 0.70ℓ, the subsonic stability is marginal.

Summary of aerodynamic characteristics.- Specific stability and performance parameters have been extracted from the CCV data base and are presented as a function of Mach number in figures 17 to 19. In figure 17, the lift-curve slope and aerodynamic-center location (x_{cp}/ℓ) are presented as functions of Mach number for angles of attack of 0^{o}, 10^{o}, 20^{o}, and 30^{o}. Figure 17(a) shows that, as expected, maximum C_{L_α} occurs near Mach 1, and C_{L_α} decreases at both subsonic and supersonic conditions. The data of figure 17(b) show that the aerodynamic-center location is very dependent upon Mach number. For the vehicle during entry, the aerodynamic center moves from approximately 0.66 at Mach numbers near 4 ($\alpha = 20^{o}$) to 0.72 at Mach numbers near 1 ($\alpha = 10^{o}$). These aerodynamic-center variations are much larger than those experienced by wing-dominated configurations, as can be seen by a comparison of the variations of static margin with Mach number (ref. 12) for a wing-dominated configuration.

The trimmed lift coefficient and lift-drag ratio of the CCV configuration are presented in figures 18(a) and 18(b), respectively. These results are comparable to the space shuttle and show no major deficiencies in the ability to satisfy shuttle mission requirements. The directional stability C_{n_β} of the CCV configuration is presented in figure 19. The vehicle is statically stable at Mach numbers from 0.3 to 1.2 over an angle-of-attack range from 0^{o} to 10^{o}, which is the expected flight angle-of-attack range.

SUMMARY OF RESULTS

The results of a study to determine the effects of relaxed longitudinal stability on a single-stage-to-orbit vehicle design are summarized as follows:

1. The control-configured vehicle has an estimated gross lift-off mass 10 percent less than that of the baseline vehicle design.

2. Both the control-configured and baseline vehicles can be trimmed hypersonically over an acceptable angle-of-attack range.

3. The use of a deployable canard as a destabilizer on the control-configured vehicle at subsonic speeds can reduce the landing speed from 190 to 162 knots.

4. Because of the large ratio of body-planform to wing-planform area of the control-configured vehicle, the aerodynamic center is much more dependent on Mach number than wing-dominated configurations.

5. The control-configured vehicle showed no major deficiencies in either trimmed lift coefficient or lift-drag ratio over the test Mach number range from 0.3 to 4.63.

6. The model was directionally stable at Mach numbers from 0.3 to 1.2 over an angle-of-attack range from 0° to 10°.

Langley Research Center
National Aeronautics and Space Administration
Hampton, VA 23665
November 21, 1979

APPENDIX A

EXPERIMENTAL AERODYNAMICS OF CONTROL-CONFIGURED VEHICLE

The results of tests to determine the static longitudinal and lateral-directional characteristics of the control-configured vehicle (CCV) configuration are presented in the basic data plots of figures 20 to 27. The effect of configuration buildup on the subsonic longitudinal aerodynamic characteristics is presented in figure 20. These results show that the body alone is quite unstable, but addition of the wing has, as expected, a large stabilizing effect. The longitudinal stability and elevon effectiveness through a Mach number range from 0.3 to 4.63 are presented in figure 21. These results are summarized in the section entitled "Results and Discussion." The effect of the canard on the subsonic longitudinal stability, and elevon effectiveness with the canard on are presented in figures 22 and 23, respectively. Base pressures measured over the test Mach number range are presented in figure 24. The lateral-directional characteristics of the CCV configuration are presented in figures 25 to 27, with effects of canard and vertical tail presented.

APPENDIX B

EXPERIMENTAL AERODYNAMICS OF BASELINE VEHICLE

The results of tests to determine the subsonic and transonic longitudinal characteristics of the baseline configuration are presented in this appendix. These data include the basic data plots of figures 28 to 30. The effect of configuration buildup at subsonic Mach numbers is presented in figure 28. These results show that like the CCV configuration, the body alone is quite unstable and the wing has a large stabilizing effect. The longitudinal stability and elevon effectiveness over a Mach number range from 0.3 to 1.2 are presented in figure 29. These results show that the configuration has near-neutral stability at the lowest Mach numbers; however, at angles of attack above 8^{o}, the model shows a tendency to pitch up. Base pressures measured over the test Mach number range are presented in figure 30.

REFERENCES

1. Henry, Beverly Z.; and Decker, John P.: Future Earth Orbit Transportation Systems/Technology Implications. Astronaut. & Aeronaut., vol. 14, no. 9, Sept. 1976.

2. Phillips, W. Pelham; Decker, John P.; Rau, Timothy R.; and Glatt, C. R.: Computer-Aided Space Shuttle Orbiter Wing Design Study. NASA TN D-7478, 1974.

3. Hepler, Andrew K.; Zeck, Howard; Walker, William H.; and Shafer, Daniel E.: Applicability of the Control Configured Design Approach to Advanced Earth Orbital Transportation Systems. NASA CR-2723, 1978.

4. Brooks, George W.: Developing Structures Technology for the Day After Tomorrow. Astronaut. & Aeronaut., vol. 11, no. 7, July 1973, pp. 56-66.

5. Eldred, Charles H.; Rehder, John J.; and Wilhite, Alan W.: Nozzle Selection for Optimized Single Stage Shuttles, [Preprint] IAF-76-162, Oct. 1976.

6. Brauer, G. L.; Cornick, D. E.; Habeger, A. R.; Petersen, F. M.; and Stevenson, R.: Program To Optimize Simulated Trajectories (POST). Volume 1 - Formulation Manual. NASA CR-132689, 1975.

7. Glatt, C. R.: WAATS - A Computer Program for Weights Analysis of Advanced Transportation Systems. NASA CR-2420, 1974.

8. USAF Stability and Control Datcom. Contracts AF 33(616)-6460 and F33615-75-C-3067, McDonnell Douglas Corp., Oct. 1960. (Revised Apr. 1976.)

9. Gentry, Arvel E.; and Smyth, Douglas N.: Hypersonic Arbitrary-Body Aerodynamic Computer Program (Mark III Version). Rep. DAC 61552 (Air Force Contract Nos. F33615 67 C 1008 and F33615 67 C 1602), McDonnell Douglas Corp., Apr. 1968.
   Vol. I - User's Manual. (Available from DDC as AD 851 811.)
   Vol. II - Program Formulation and Listings. (Available from DDC as AD 851 812.)

10. Bernot, Peter T.: Aerodynamic Characteristics of Two Single-Stage-to-Orbit Vehicles at Mach 20.3. NASA TM X-3550, 1977.

11. Braslow, Albert L.; Hicks, Raymond M.; and Harris, Roy V., Jr.: Use of Grit-Type Boundary-Layer Transition Trips on Wind Tunnel Models. NASA TN D-3579, 1966.

12. Freeman, Delma C., Jr.; and Fournier, Roger H.: Static Aerodynamic Characteristics of a Single-Stage-to-Orbit Vehicle With Low Planform Loading at Mach Numbers From 0.3 to 4.63. NASA TM-74056, 1977.

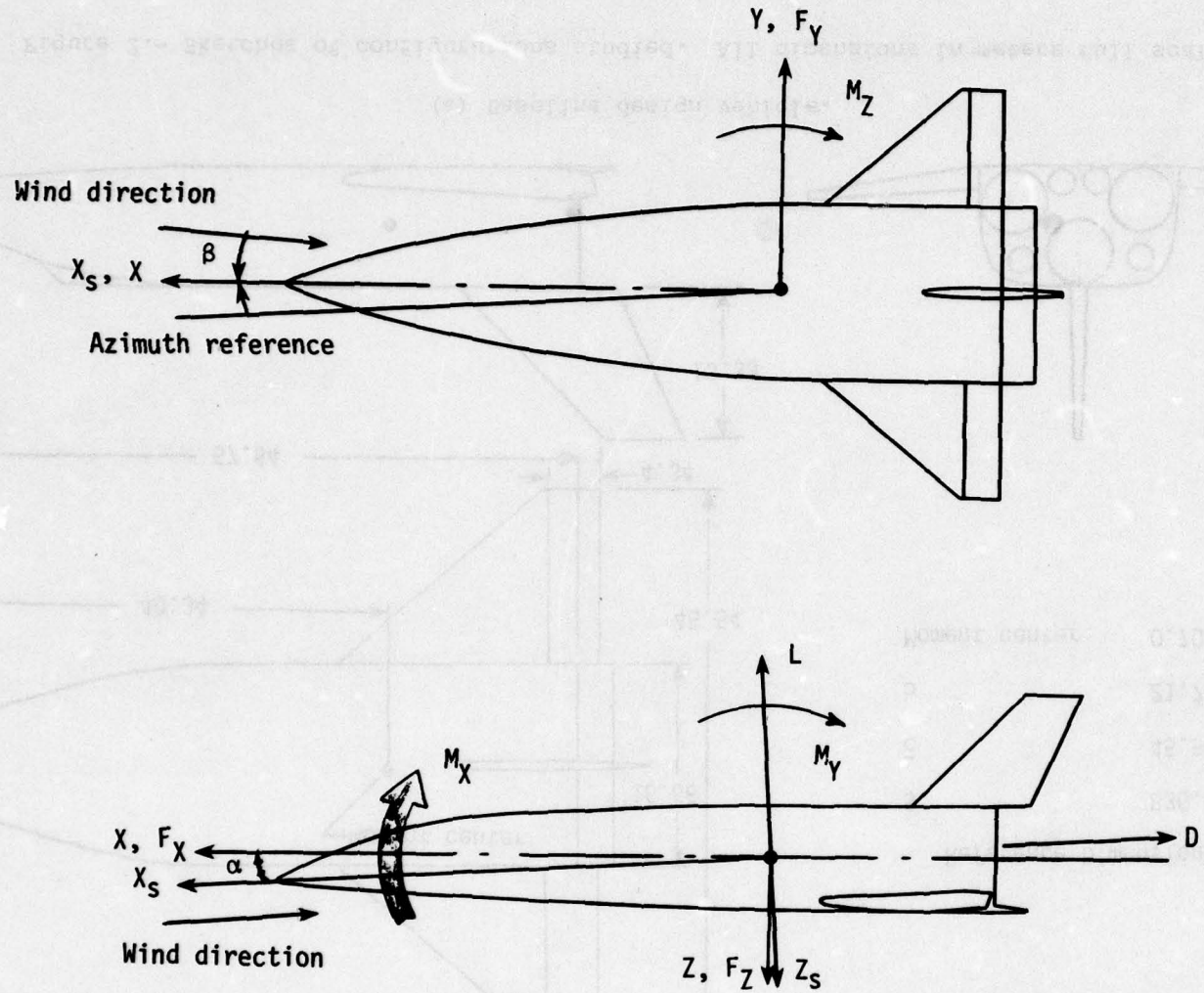

Figure 1.- System of axes used in investigation. Arrows indicate positive direction of moments, forces, and angles.

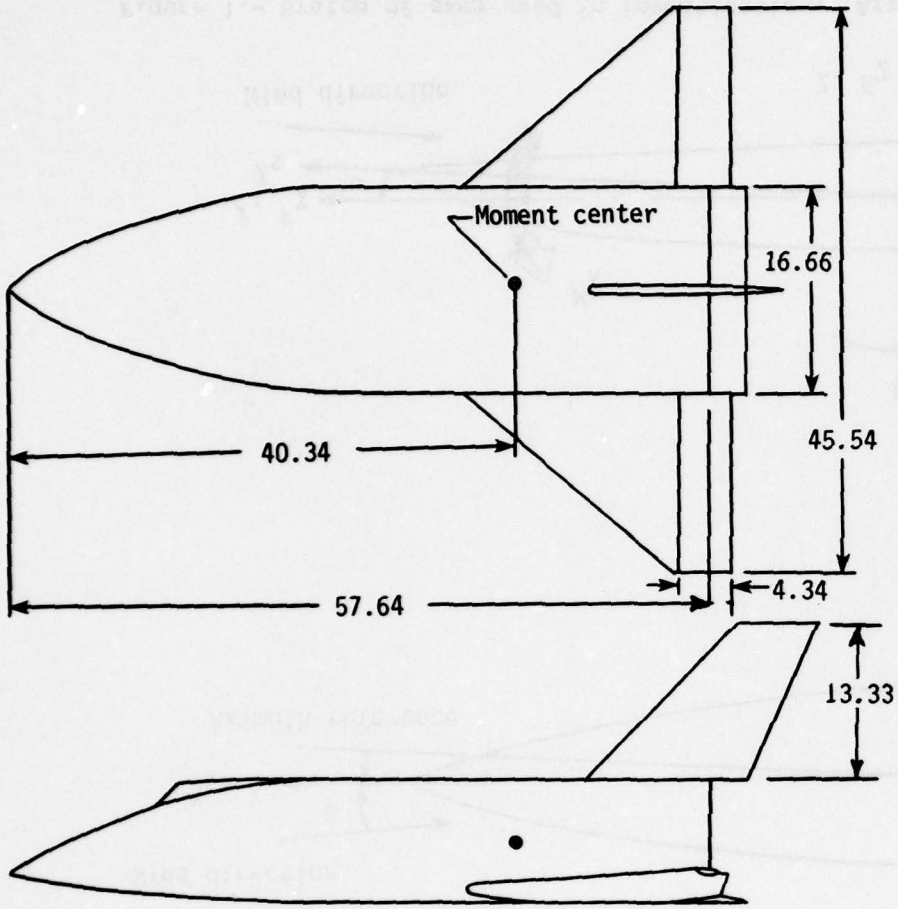

Reference Dimensions

S	836.0 m^2
$\bar{c}$	45.54 m
b	21.70 m
Moment center	0.70 ℓ

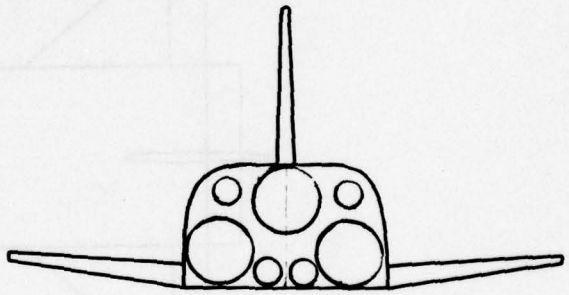

(a) Baseline design vehicle.

Figure 2.- Sketches of configurations studied. All dimensions in meters full scale.

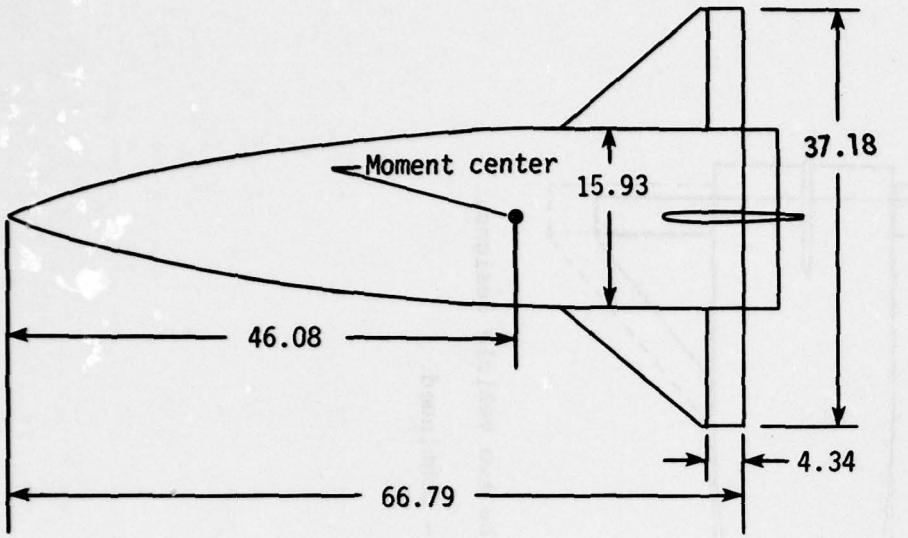

Reference Dimensions

S	557.40 m^2
$\bar{c}$	17.71 m
b	37.18 m
Moment center	0.69ℓ

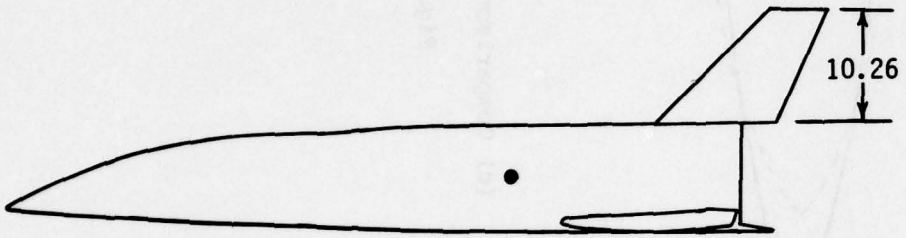

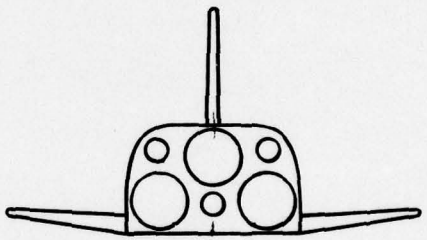

(b) CCV configuration.

Figure 2.- Continued.

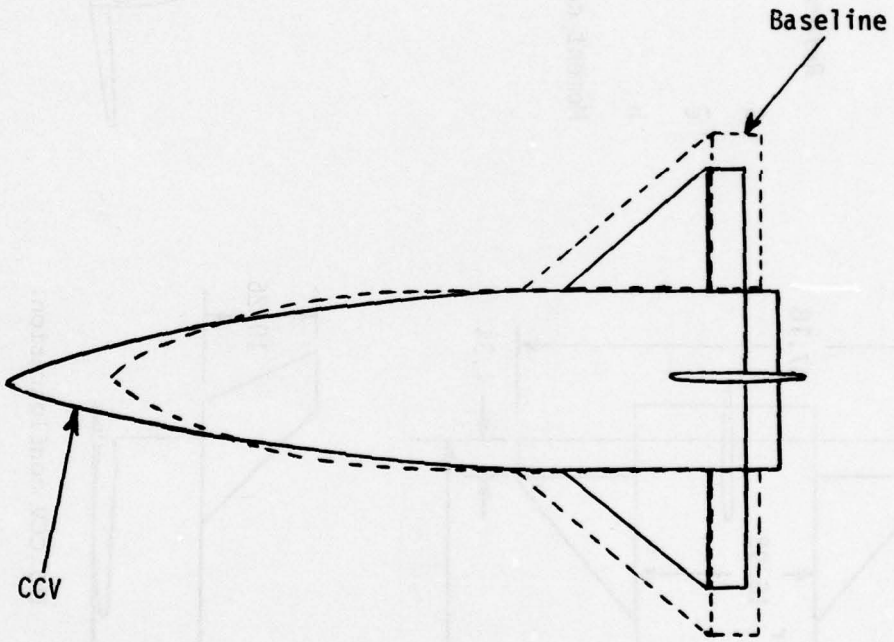

(c) Comparison of the two vehicle designs.

Figure 2.- Continued.

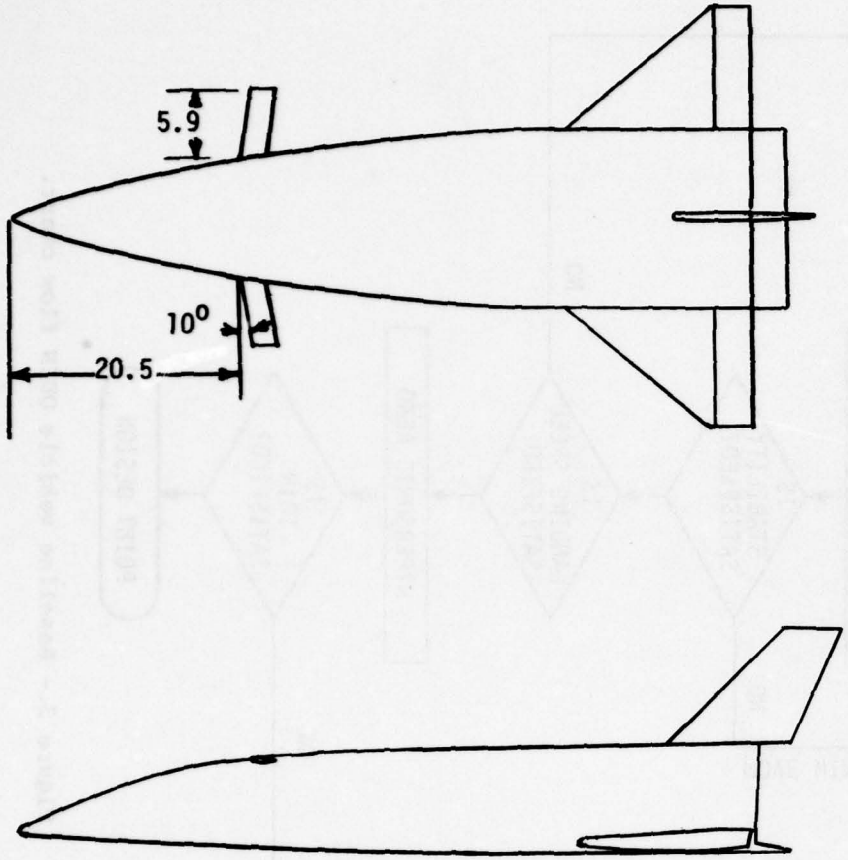

Canard Dimensions

Area	27.87 m^2
Chord	2.36 m^2
Exposed span	11.80 m
Leading-edge sweep	10°
Incidence	-4°
Aspect Ratio	5

(d) Canard details.

Figure 2.- Concluded.

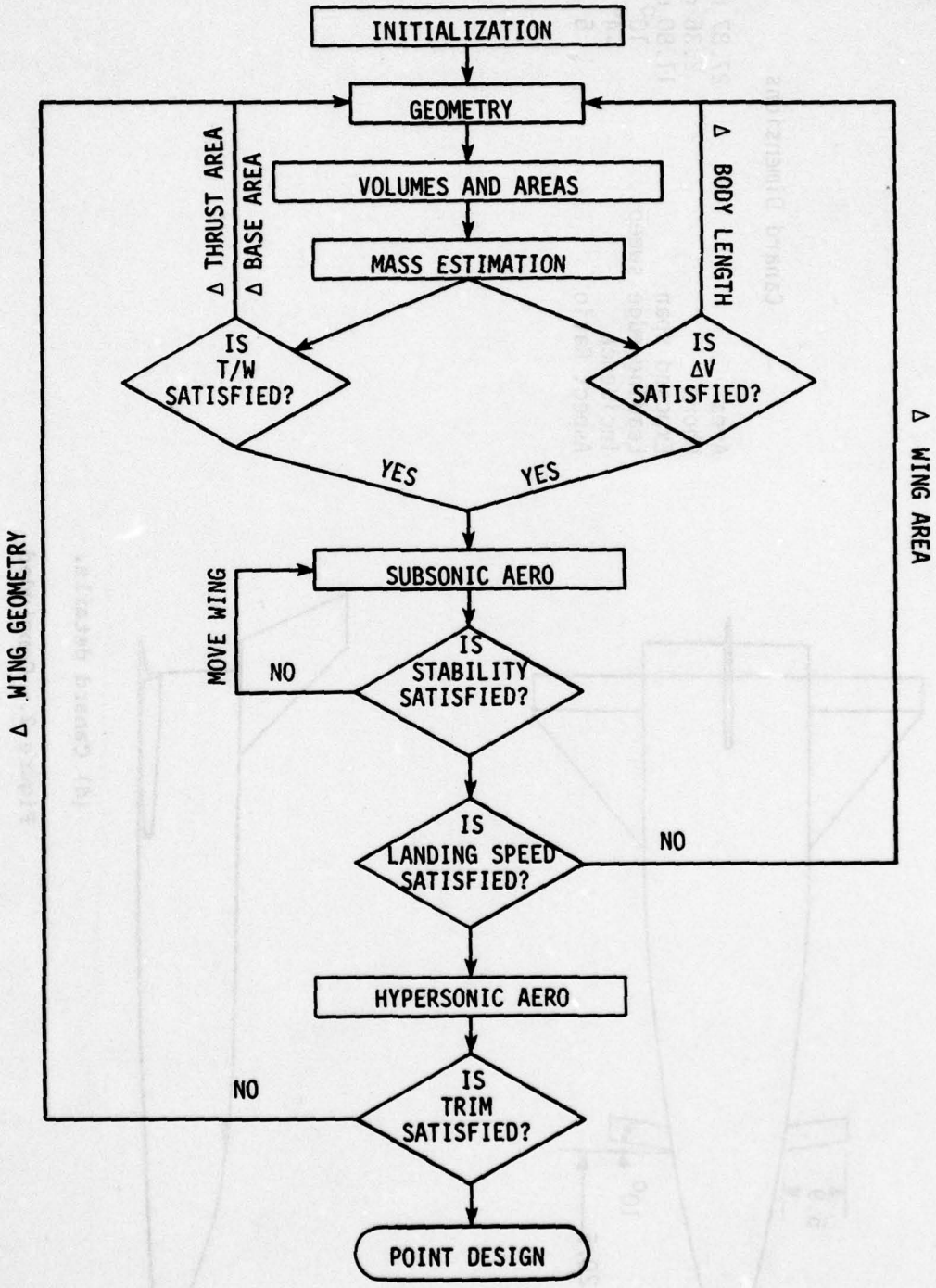

Figure 3.- Baseline vehicle ODIN flow chart.

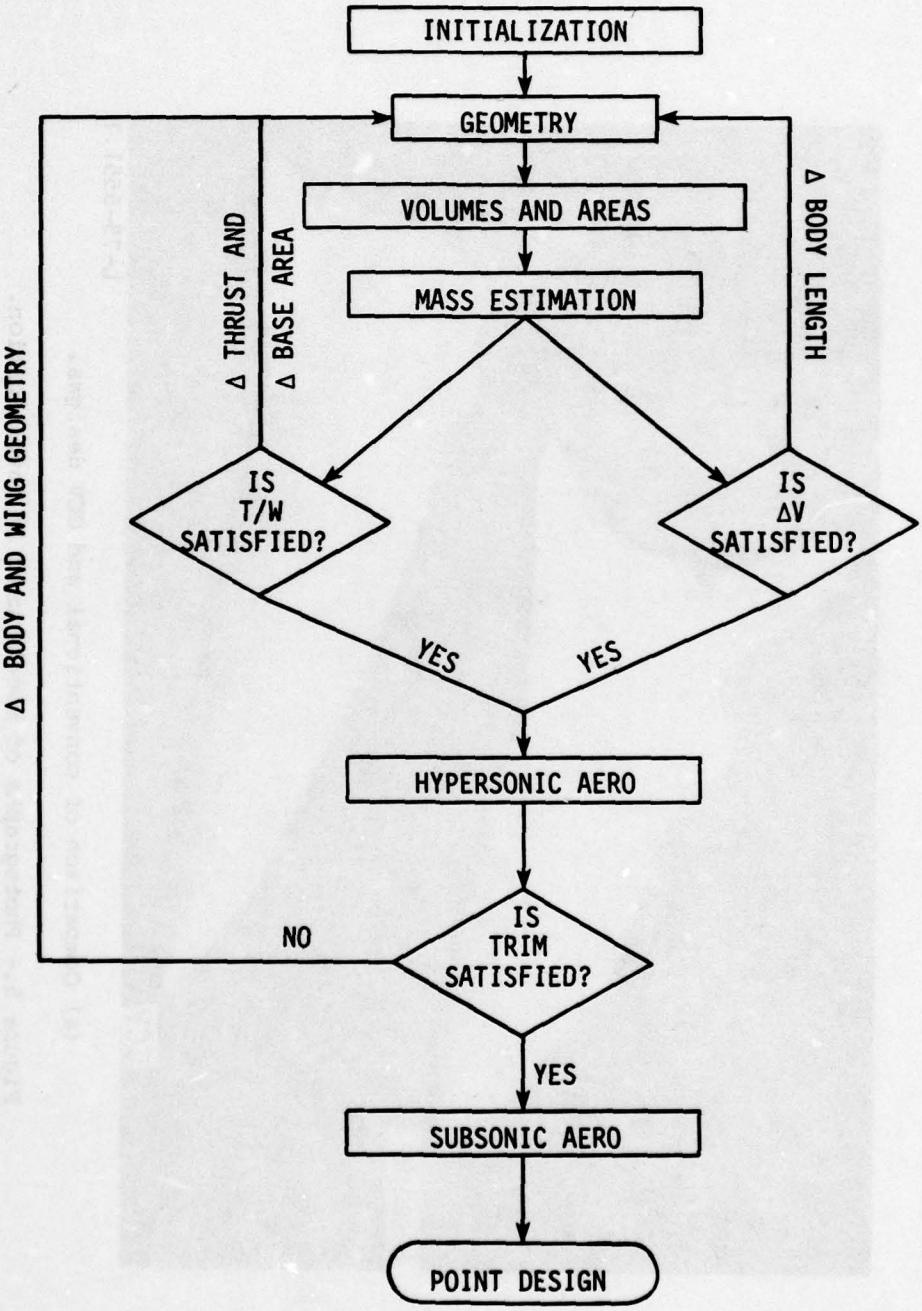

Figure 4.- Control-configured vehicle ODIN flow chart.

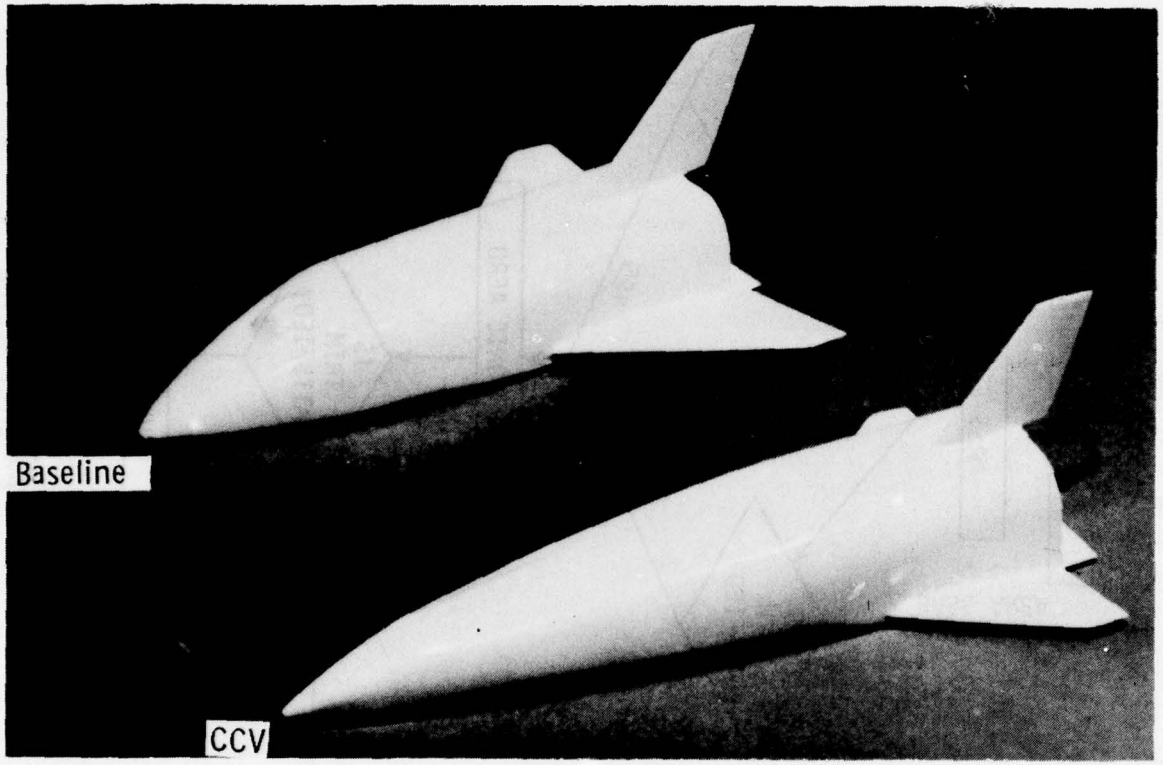

L-75-5551.1

(a) Comparison of conventional and CCV designs.

Figure 5.- Photographs of models used in investigation.

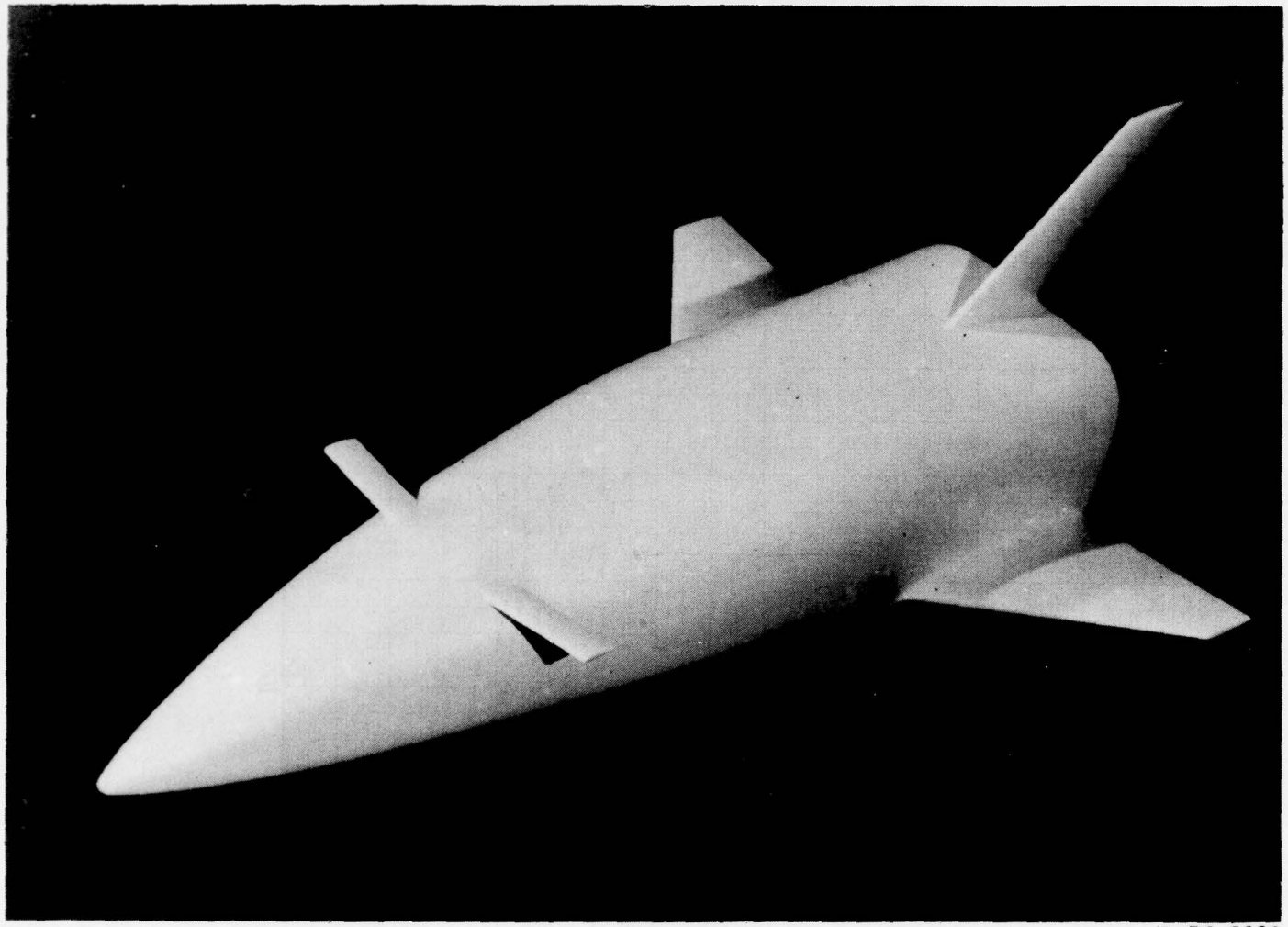

L-76-5089

(b) CCV model with canard deployed.

Figure 5.- Concluded.

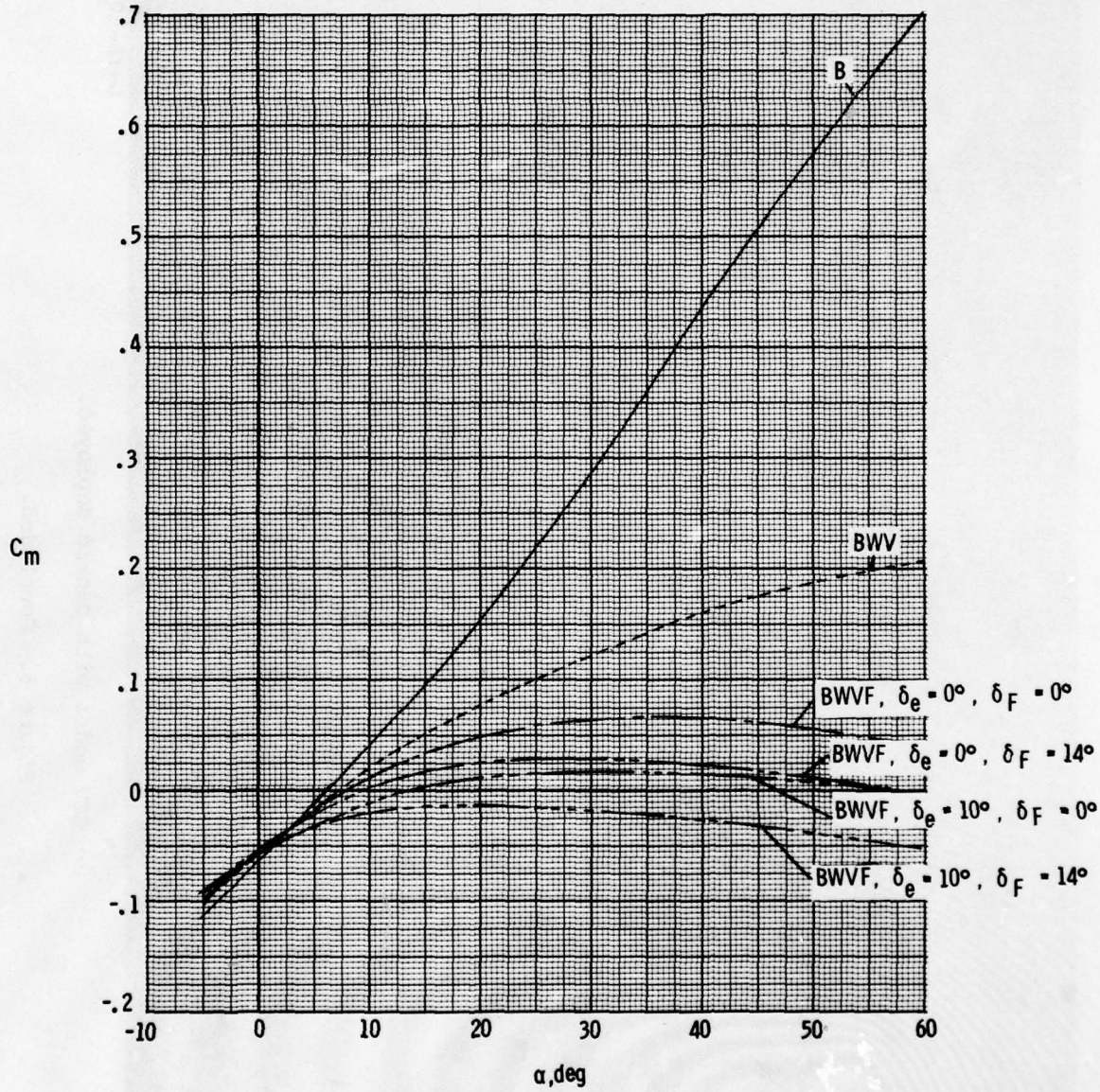

(a) C_m versus α.

Figure 6.- Estimated hypersonic stability and performance of CCV configuration. Moment center at 0.69 body length. M = 20.3.

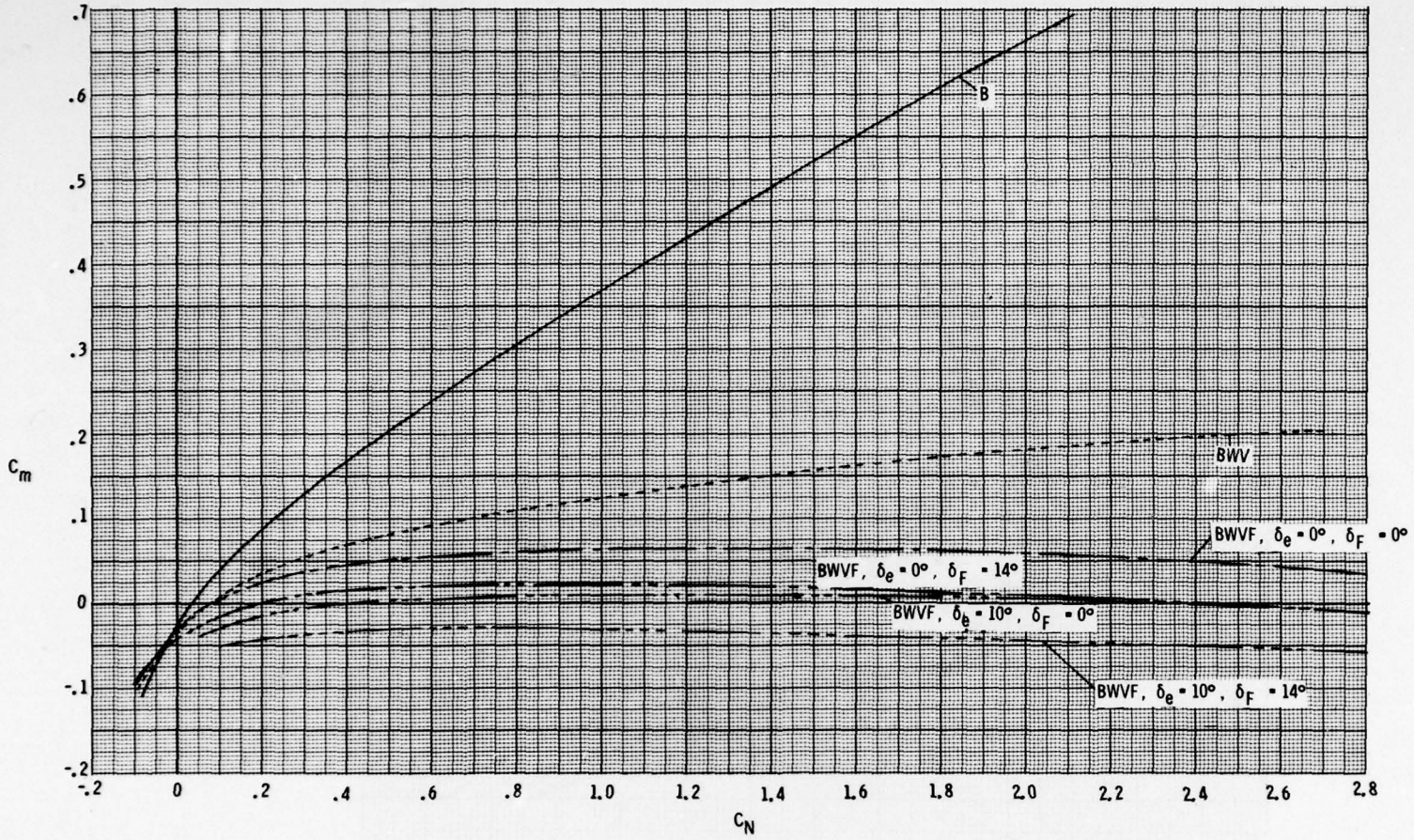

(b) C_m versus C_N.

Figure 6.- Continued.

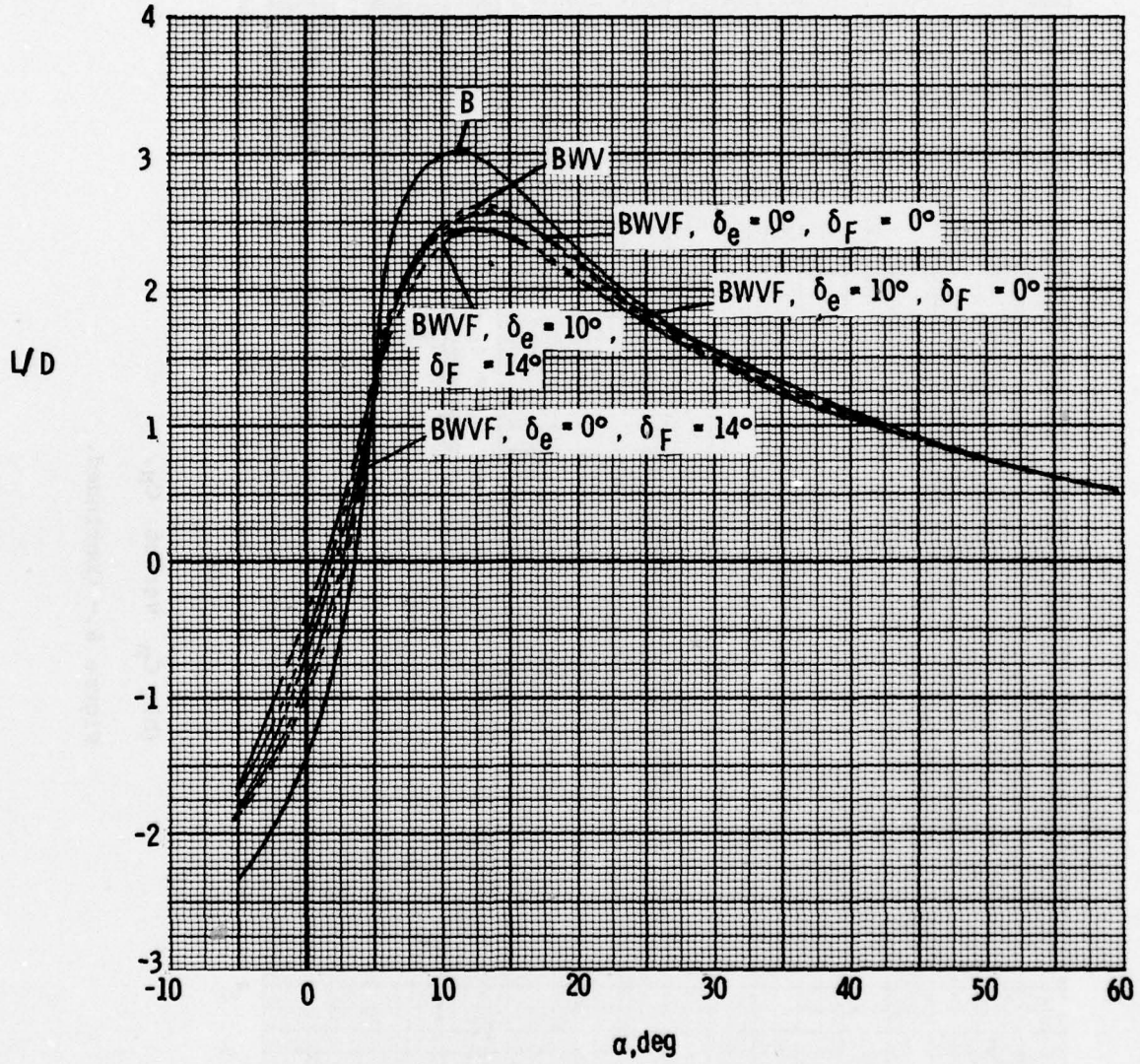

(c) L/D versus α.

Figure 6.- Concluded.

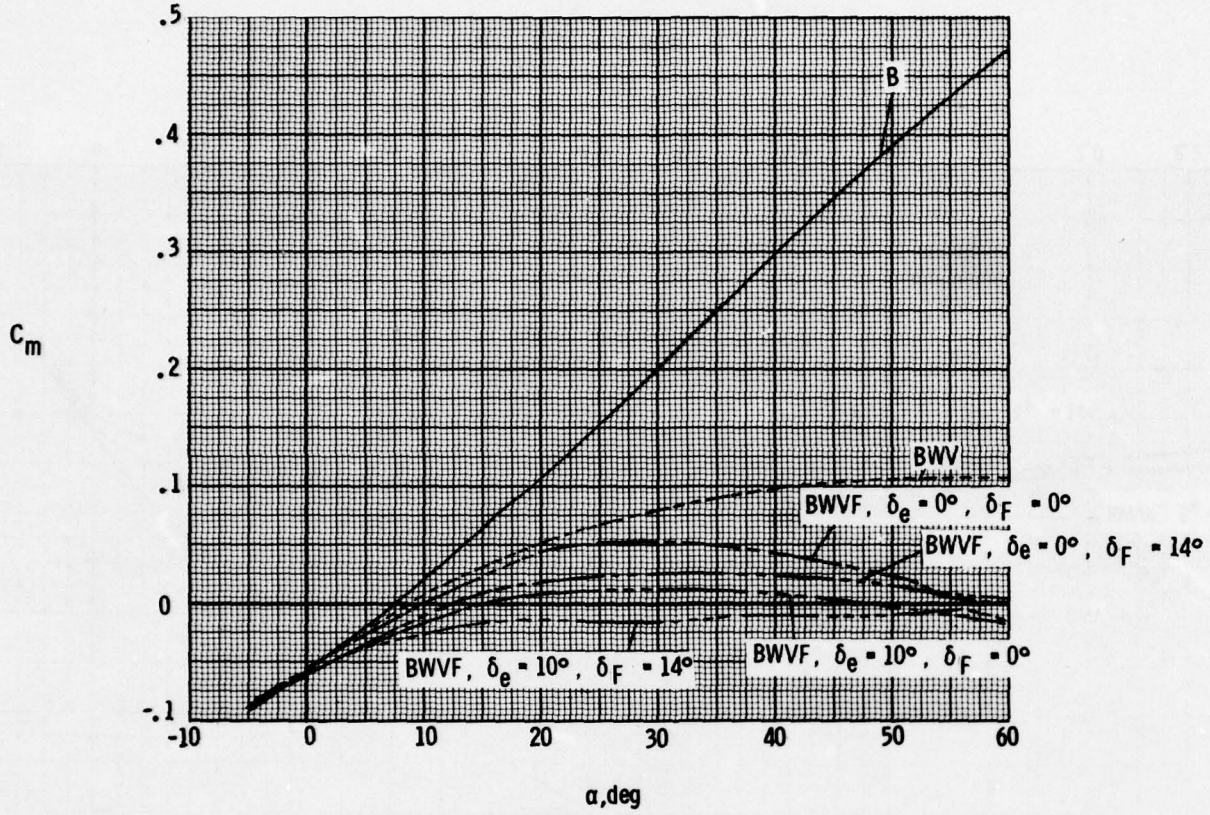

(a) C_m versus α.

Figure 7.- Estimated hypersonic stability and performance of baseline configuration. Moment center at 0.70 body length.

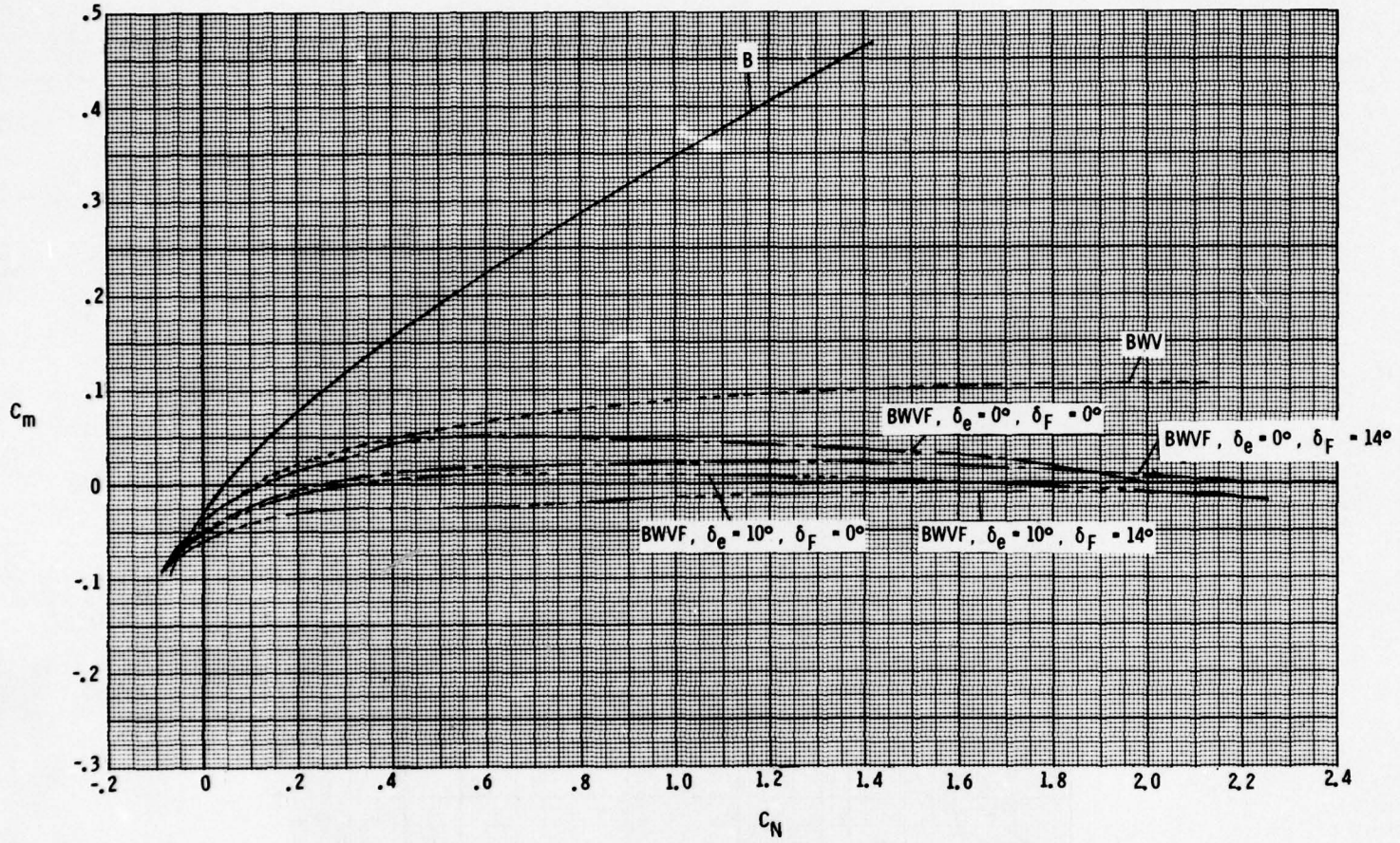

(b) C_m versus C_N.

Figure 7.- Continued.

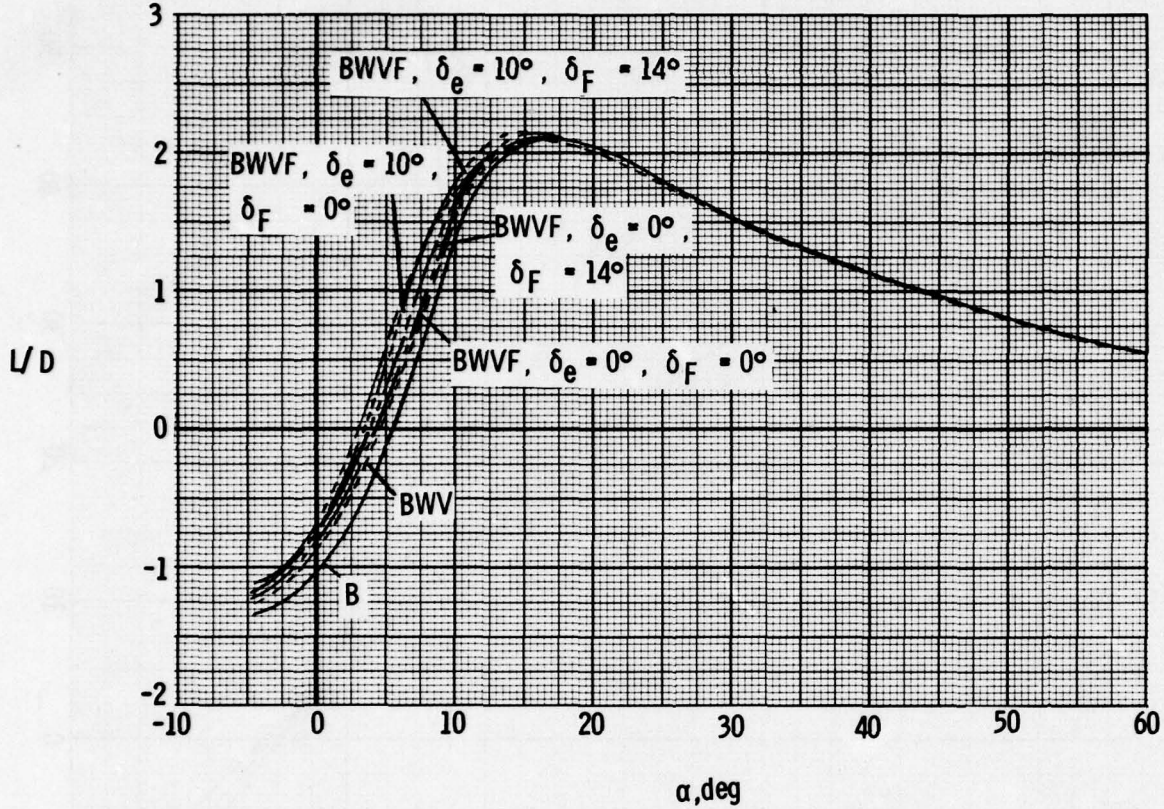

(c) L/D versus α.

Figure 7.- Concluded.

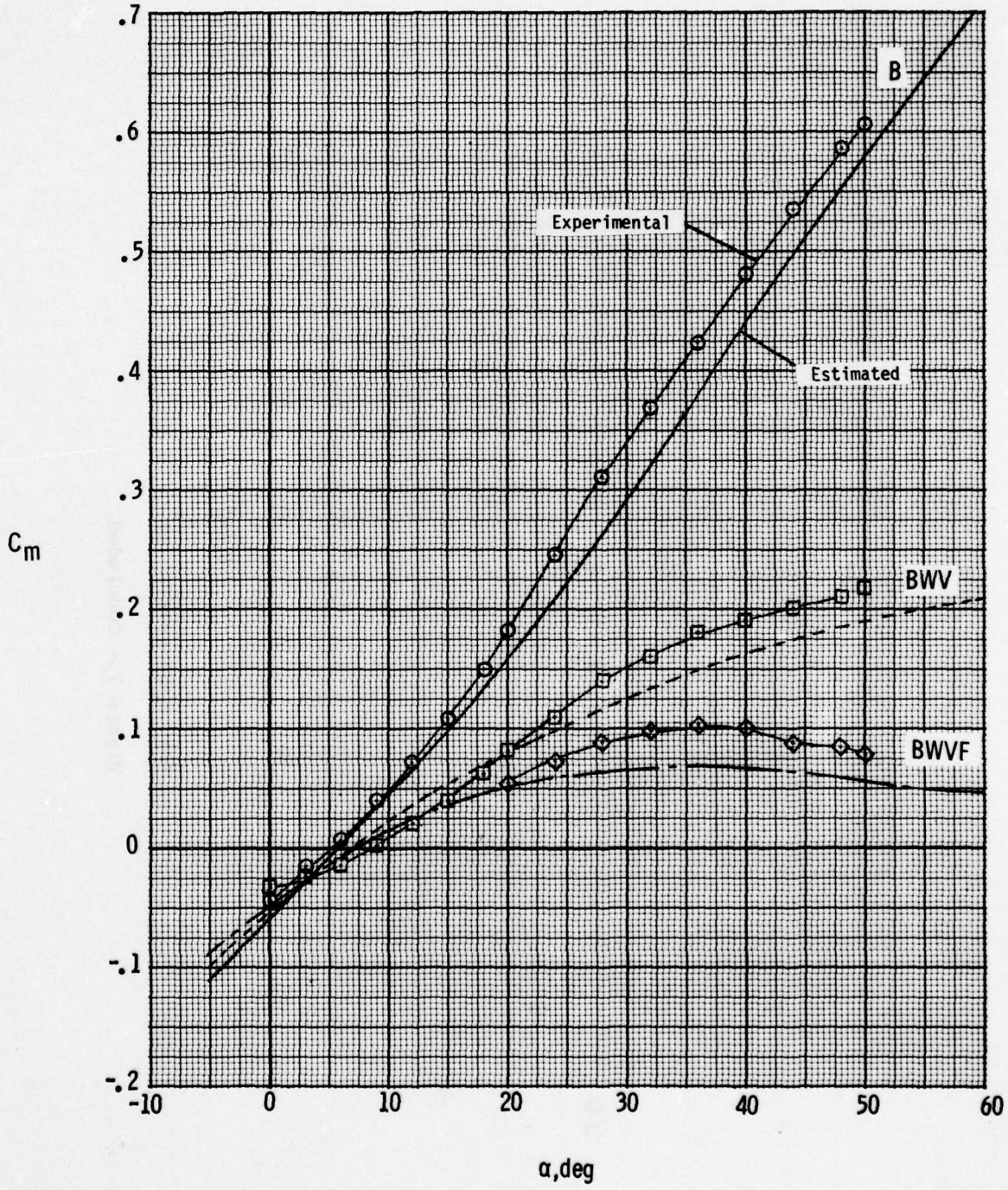

Figure 8.- Comparison of estimated and measured hypersonic longitudinal stability for CCV configuration. Moment center at 0.69 body length. M = 20.3; $\delta_e = 0^o$; $\delta_F = 0^o$.

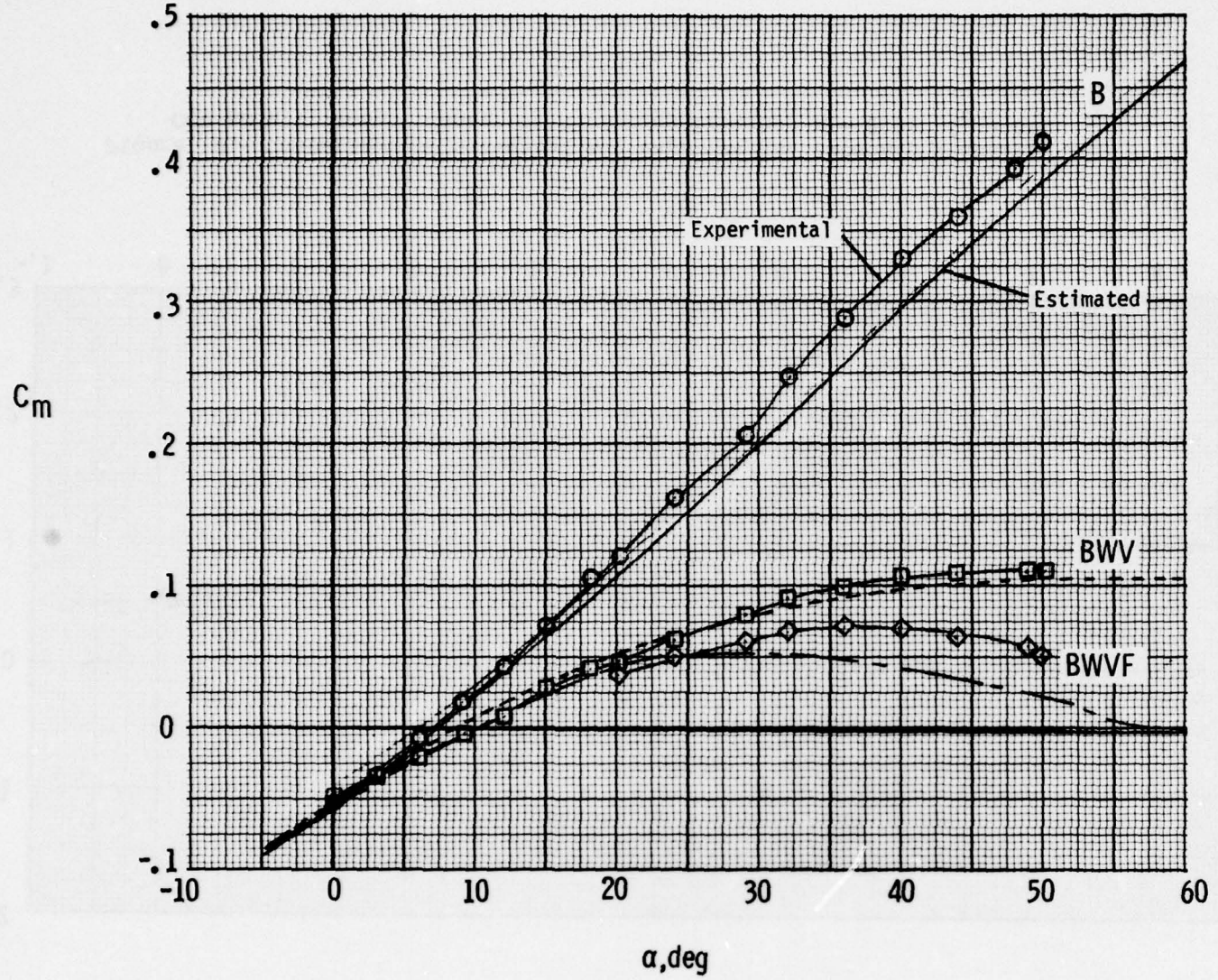

Figure 9.- Comparison of estimated and measured hypersonic longitudinal stability for baseline configuration. Moment center at 0.70 body length. M = 20.3; $\delta_e = 0^o$; $\delta_F = 0^o$.

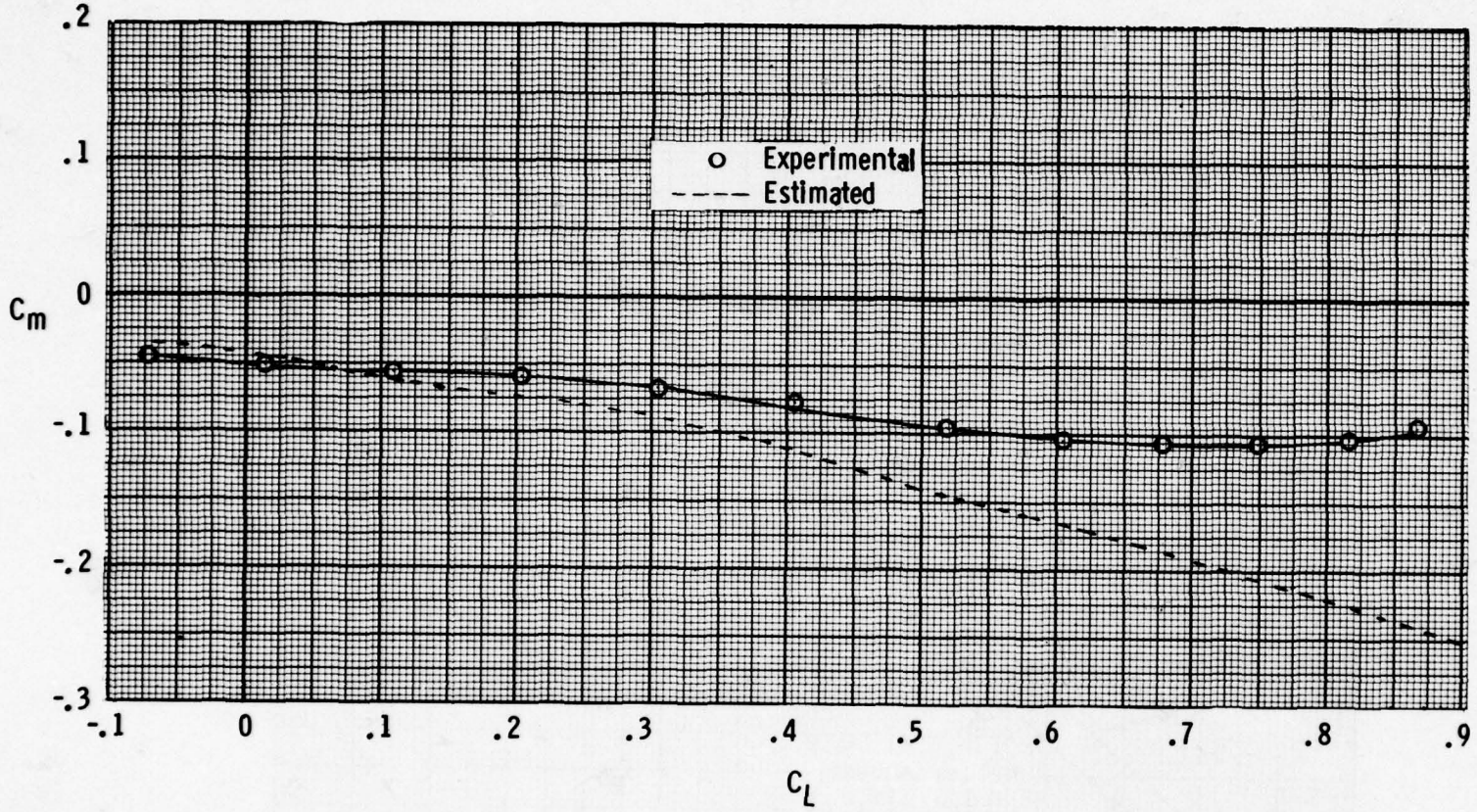

Figure 10.- Comparison of estimated and experimental subsonic stability for CCV model. Moment center at 0.69 body length. M = 0.3; $\delta_e = 0^o$.

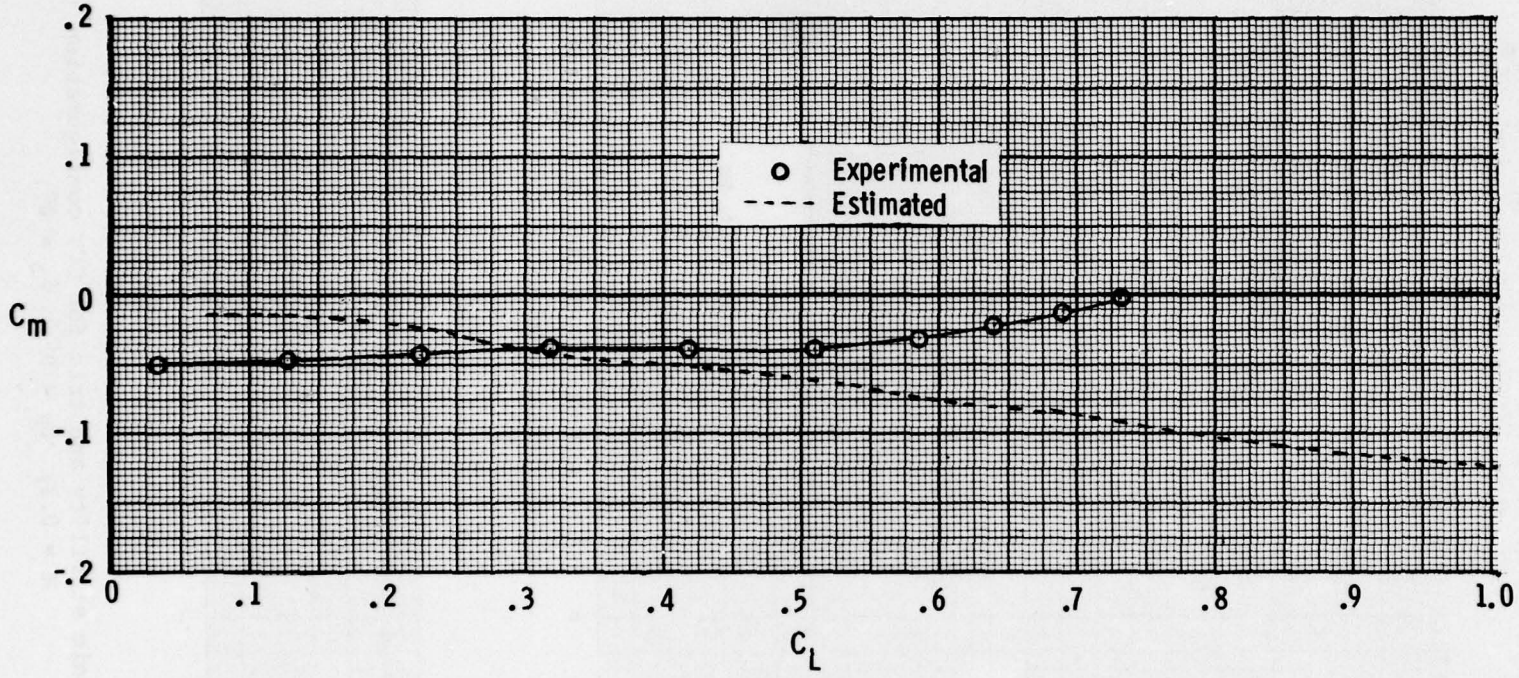

Figure 11.- Comparison of estimated and experimental subsonic stability for baseline configuration. Moment center at 0.70 body length. M = 0.3; $\delta_e = 0^o$.

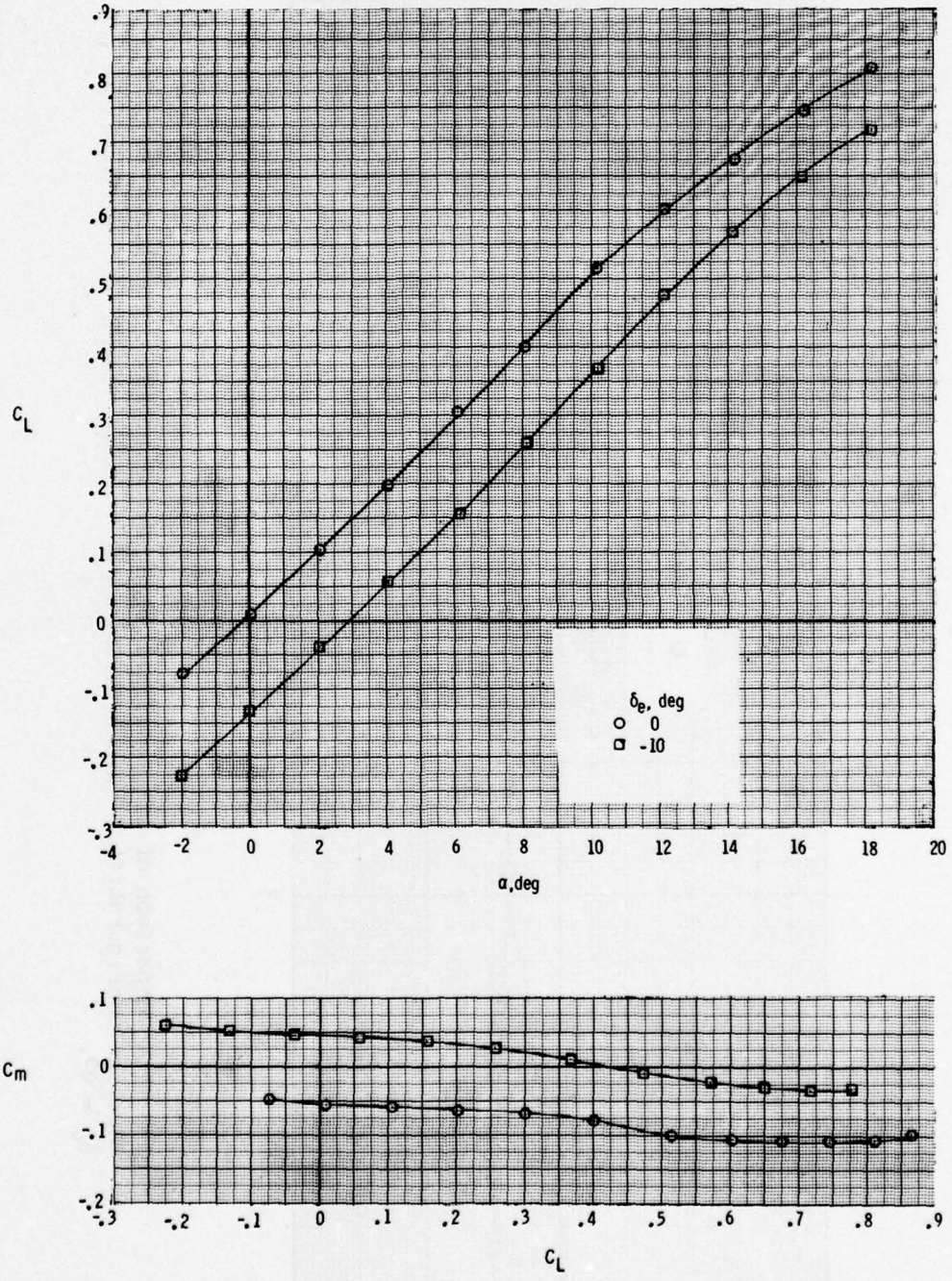

Figure 12.- Subsonic stability and trim for CCV configuration (canard-off). $M = 0.3$; $\delta_F = 0^o$; $\delta_e = 0^o$.

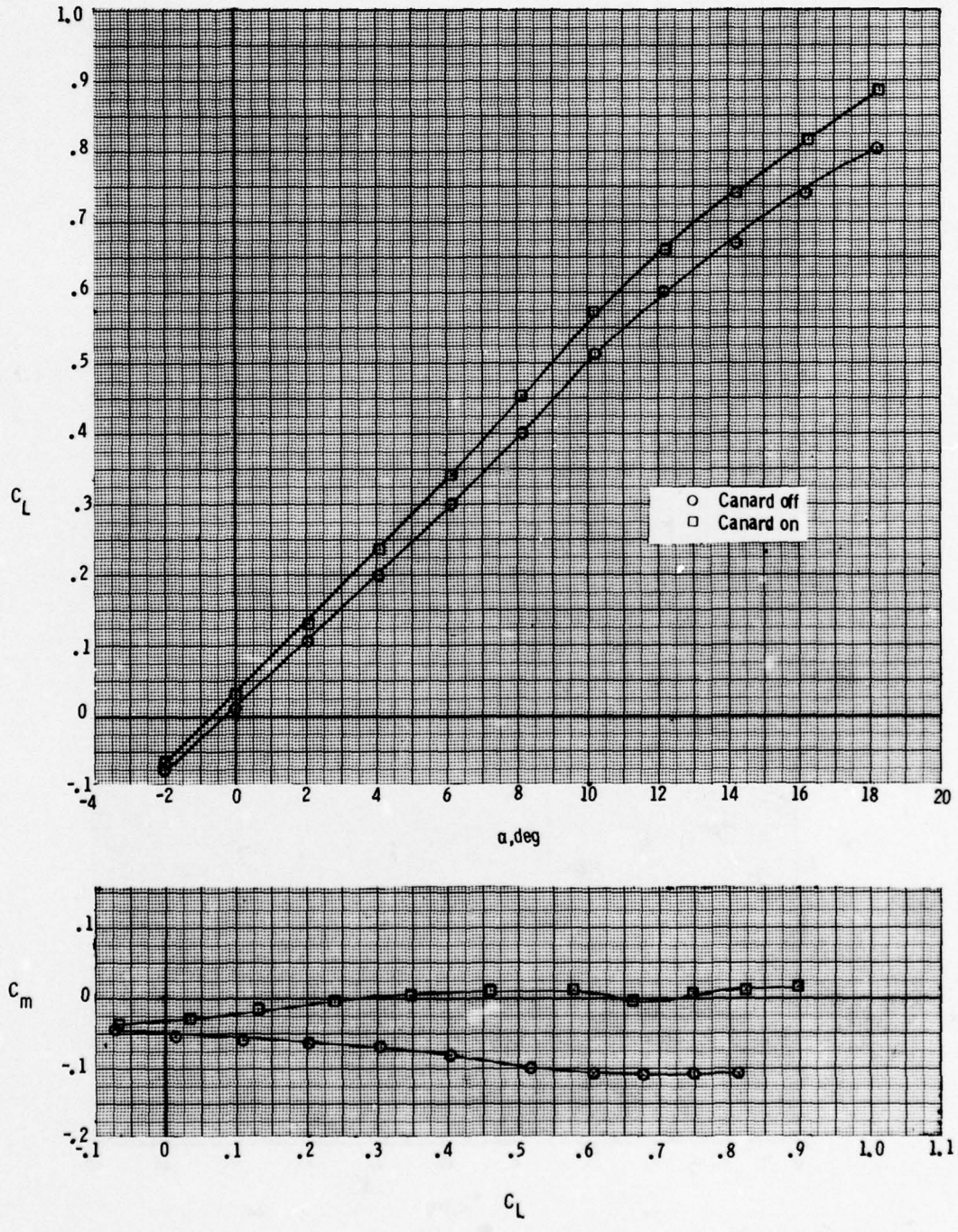

Figure 13.- Effect of canard on subsonic characteristics for CCV configuration. M = 0.3; $\delta_F = 0^o$; $\delta_e = 0^o$.

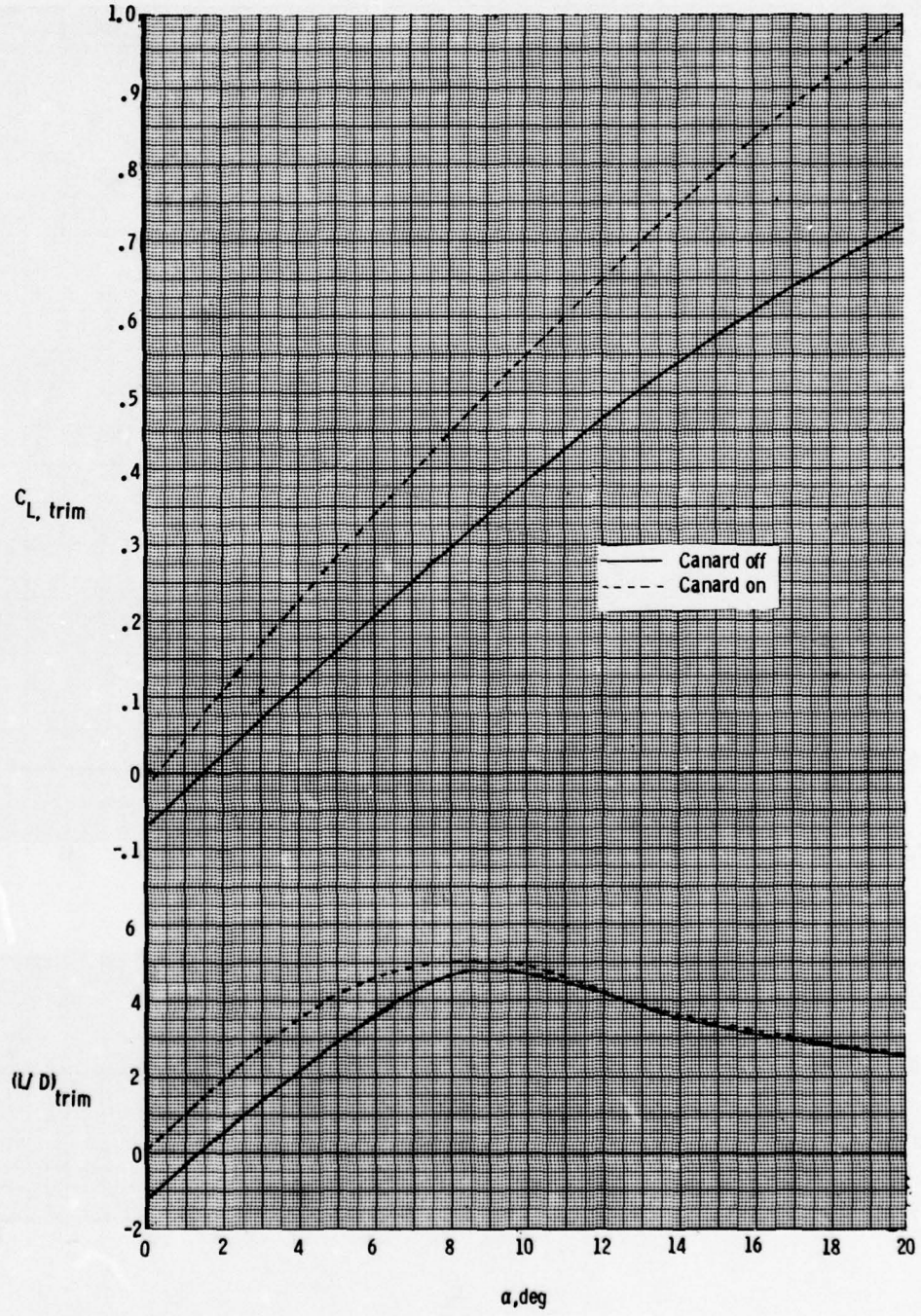

Figure 14.- Subsonic trimmed lift coefficient and lift-drag ratio for CCV configuration. M = 0.3.

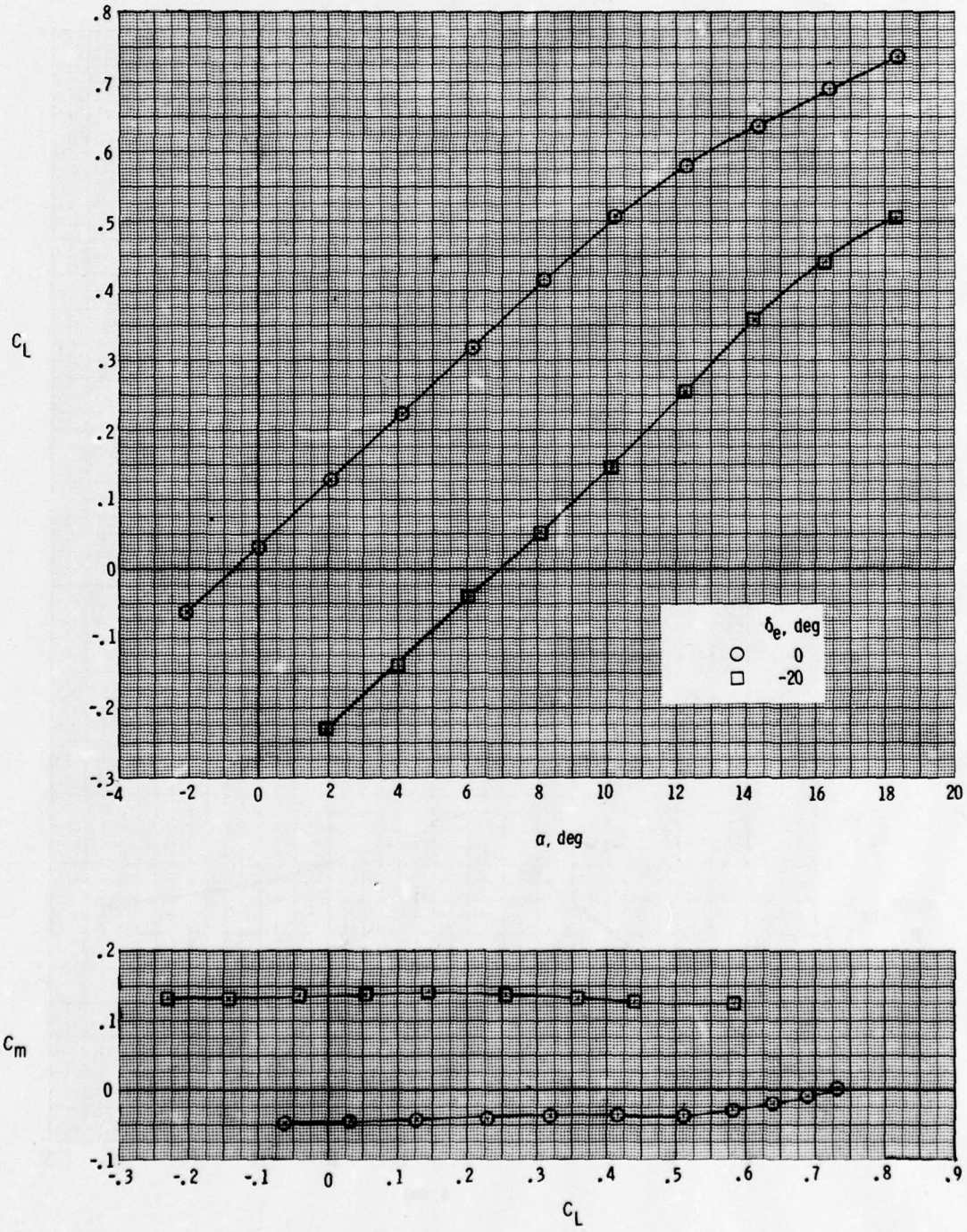

Figure 15.- Subsonic stability and trim characteristics for baseline configuration. M = 0.3; $\delta_F = 0^o$.

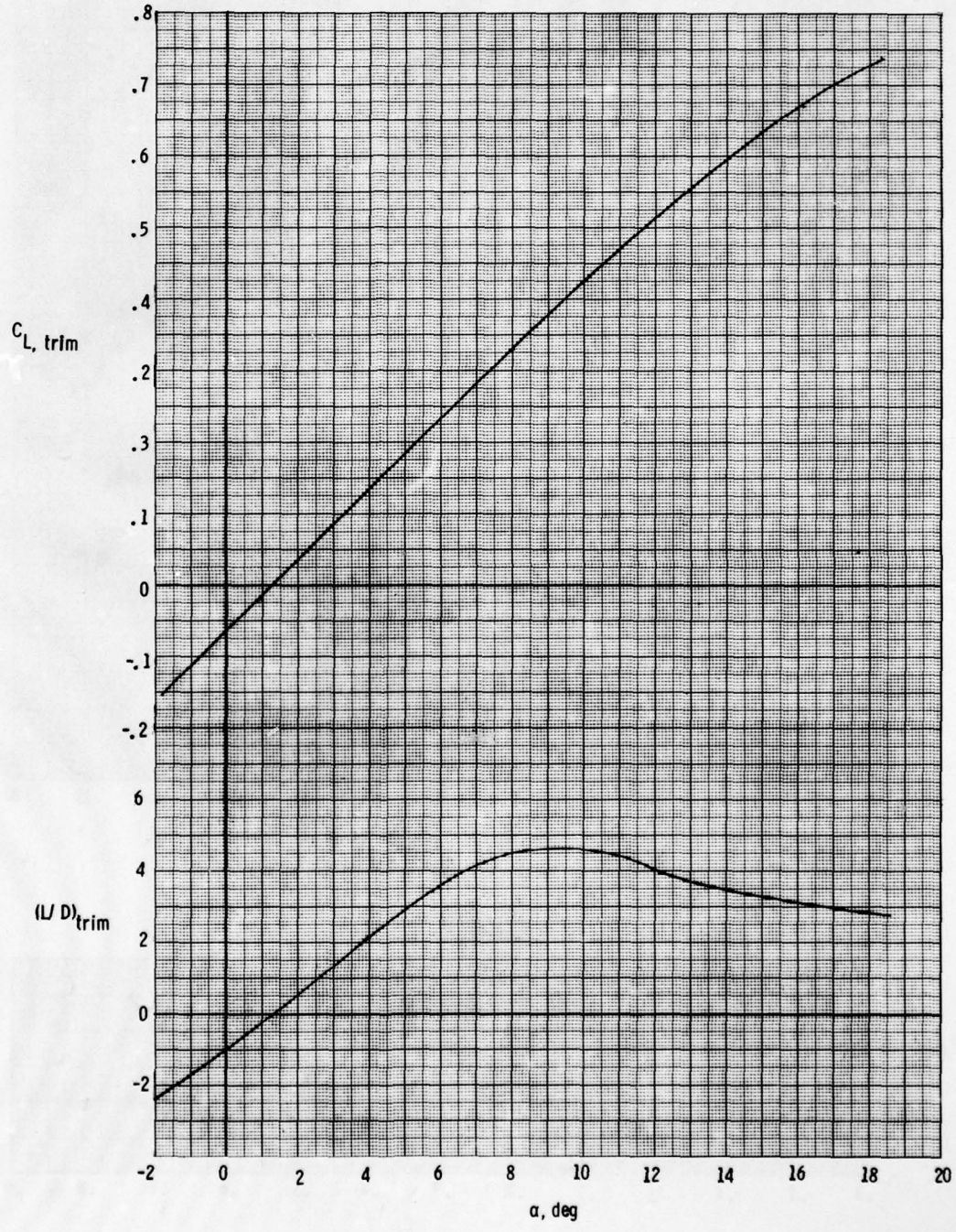

Figure 16.- Subsonic trimmed lift coefficient and lift-drag ratio for baseline configuration. M = 0.3.

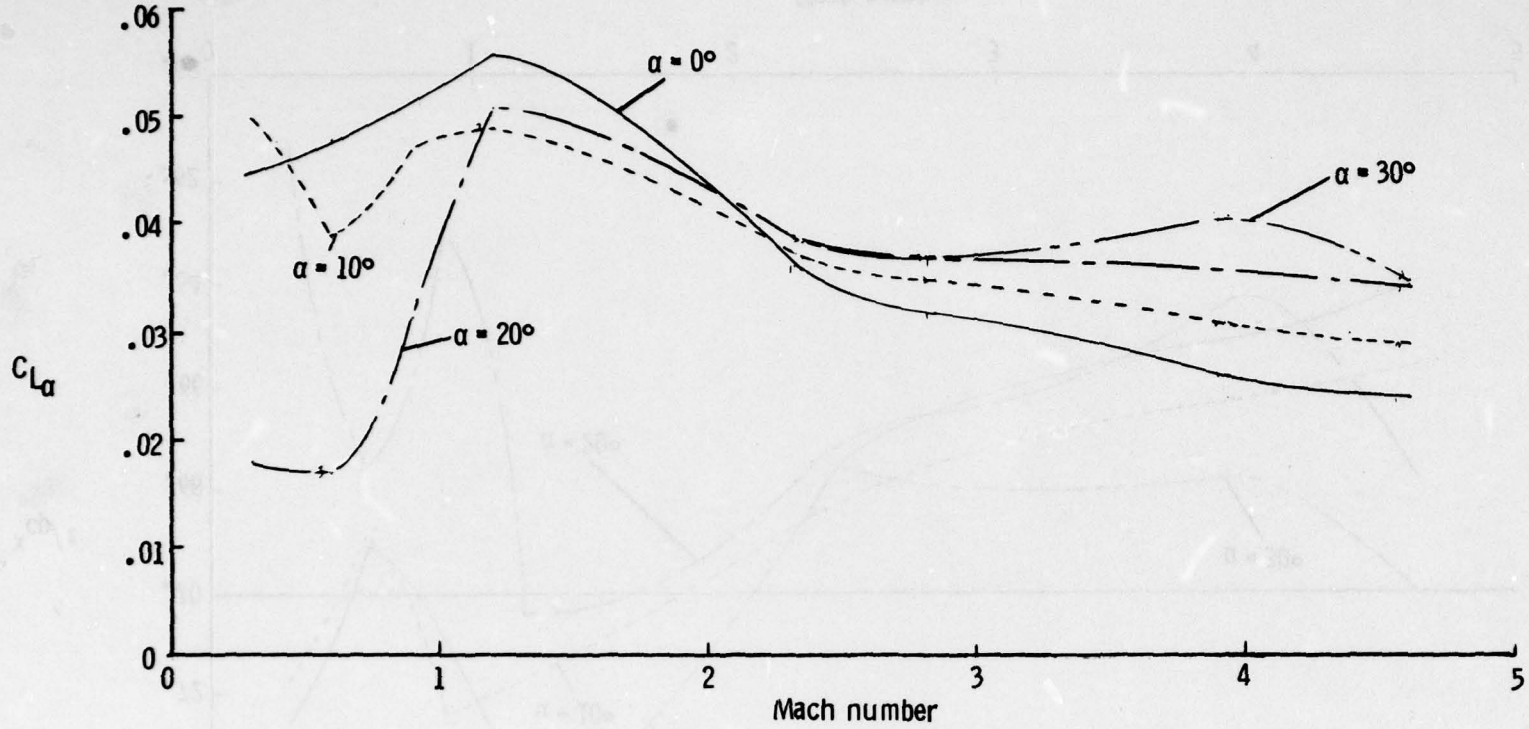

(a) C_{L_α} versus Mach number.

Figure 17.- Lift-curve slope and aerodynamic center location for CCV configuration as a function of Mach number. $\delta_e = 0^o$; $\delta_F = 0^o$.

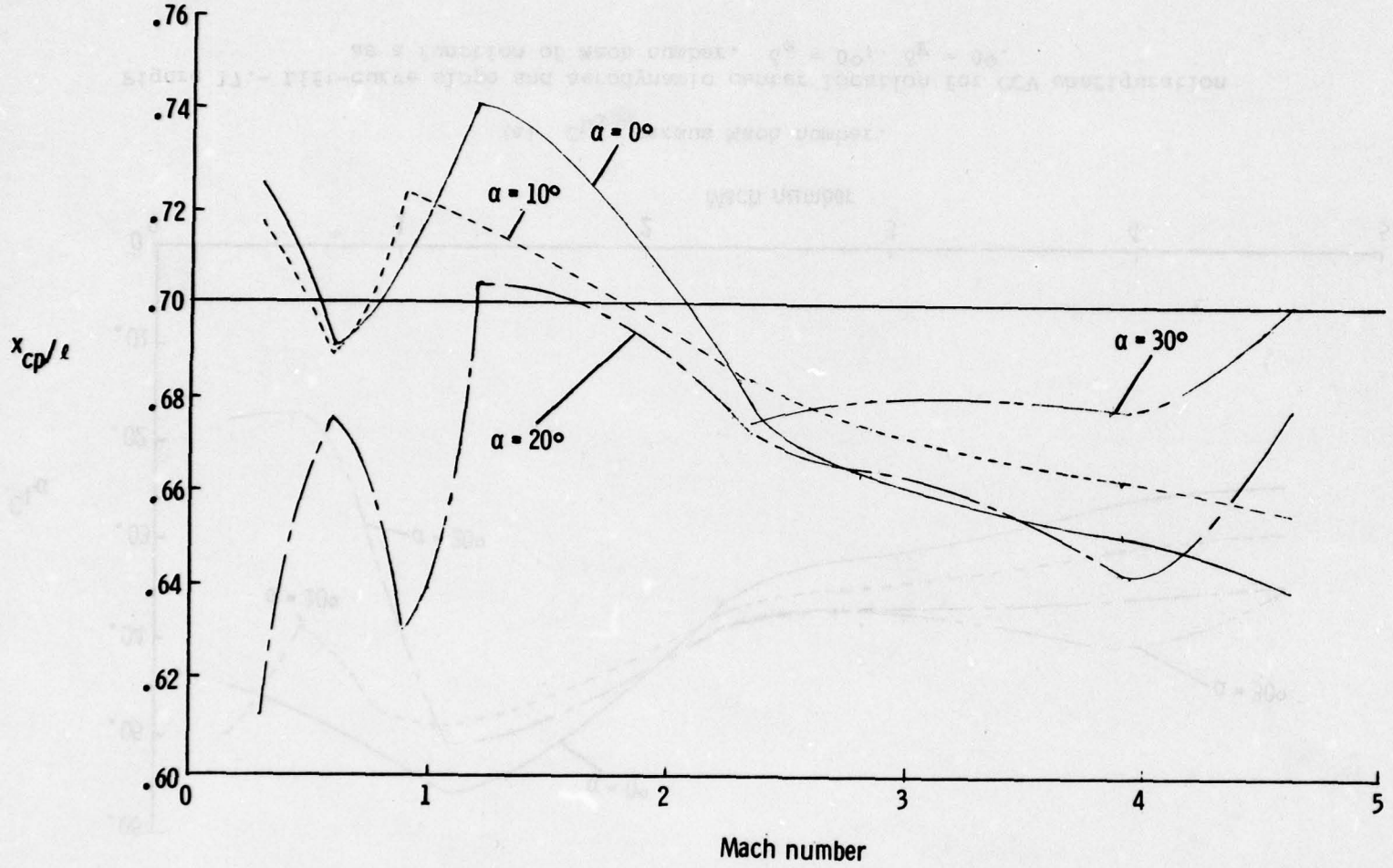

(b) x_{cp}/ℓ versus Mach number.

Figure 17.- Concluded.

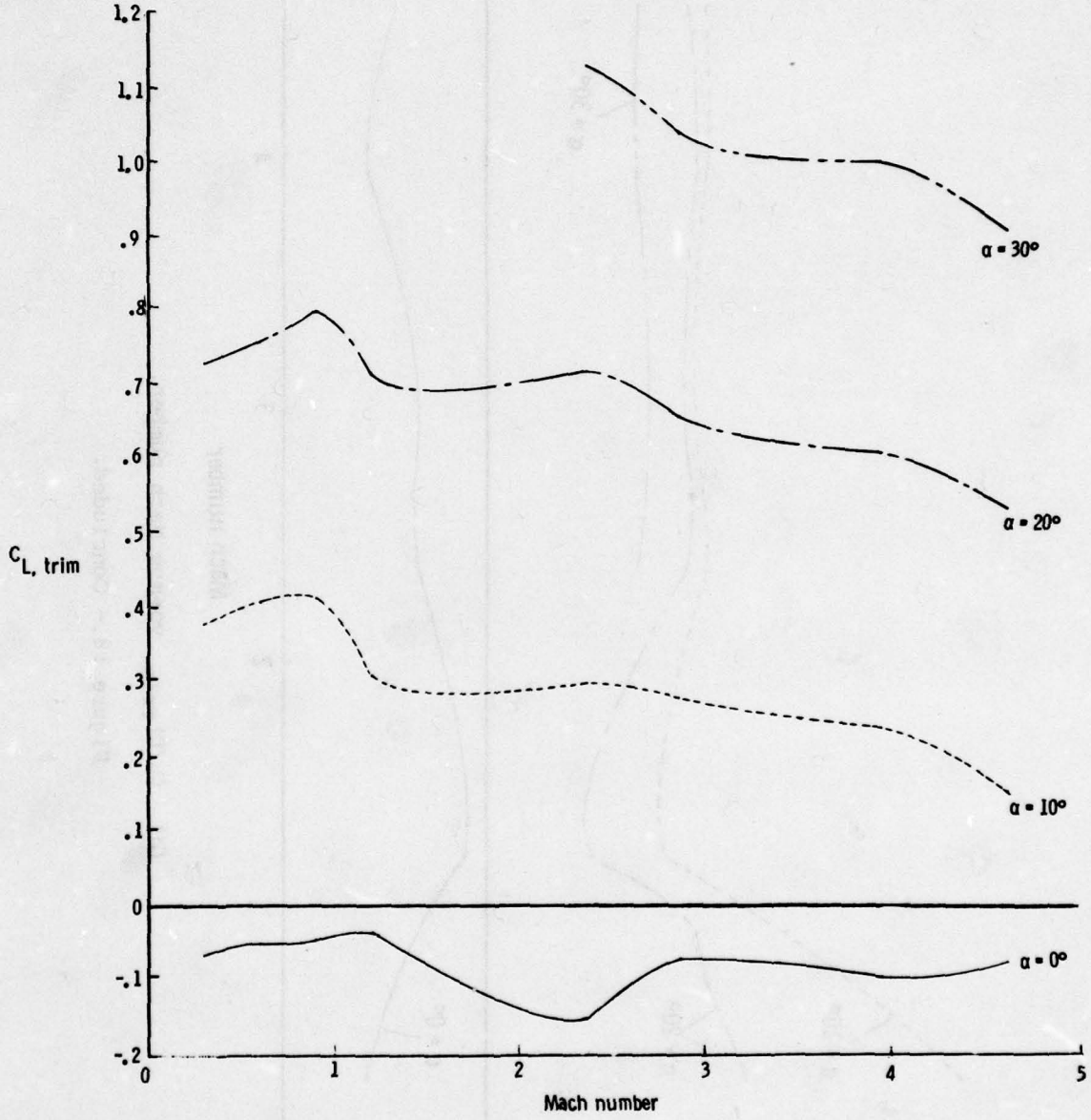

(a) $C_{L,trim}$ versus Mach number.

Figure 18.- Trimmed lift coefficient and lift-drag ratio for CCV configuration as a function of Mach number.

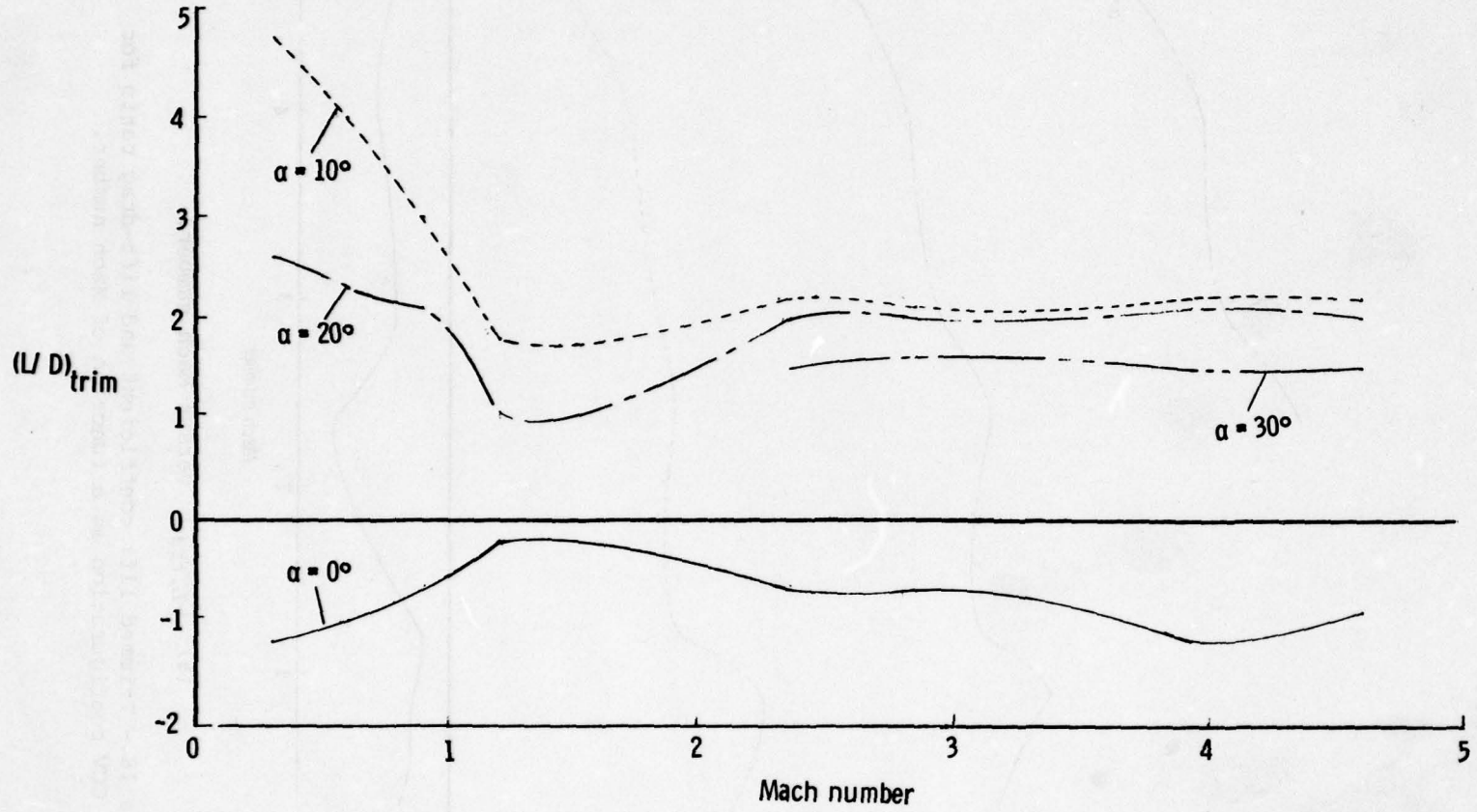

(b) $(L/D)_{trim}$ versus Mach number.

Figure 18.- Concluded.

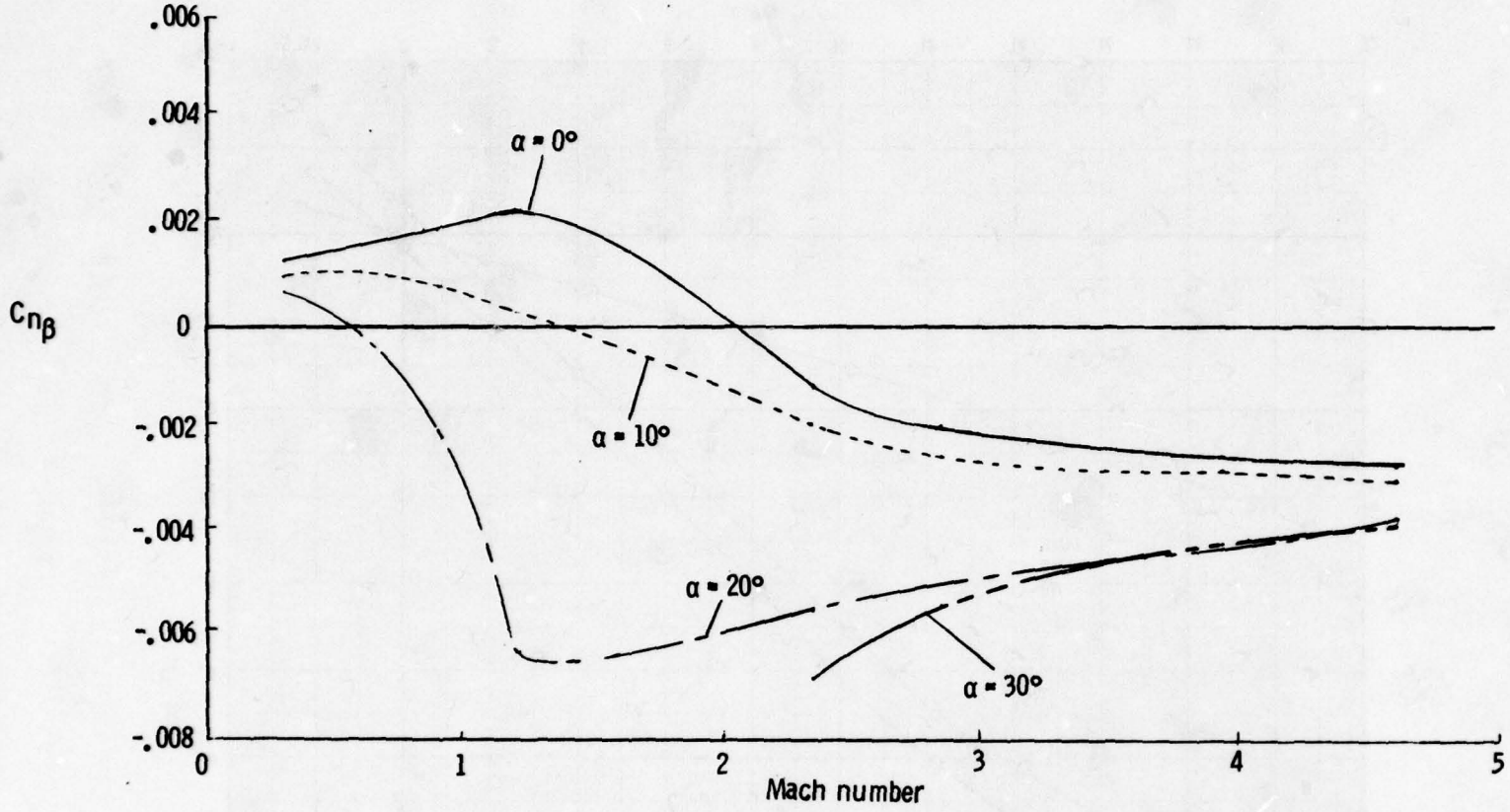

Figure 19.- Directional stability of CCV configuration presented as a function of Mach number. Canard off; $\delta_e = 0°$; $\delta_f = 0°$.

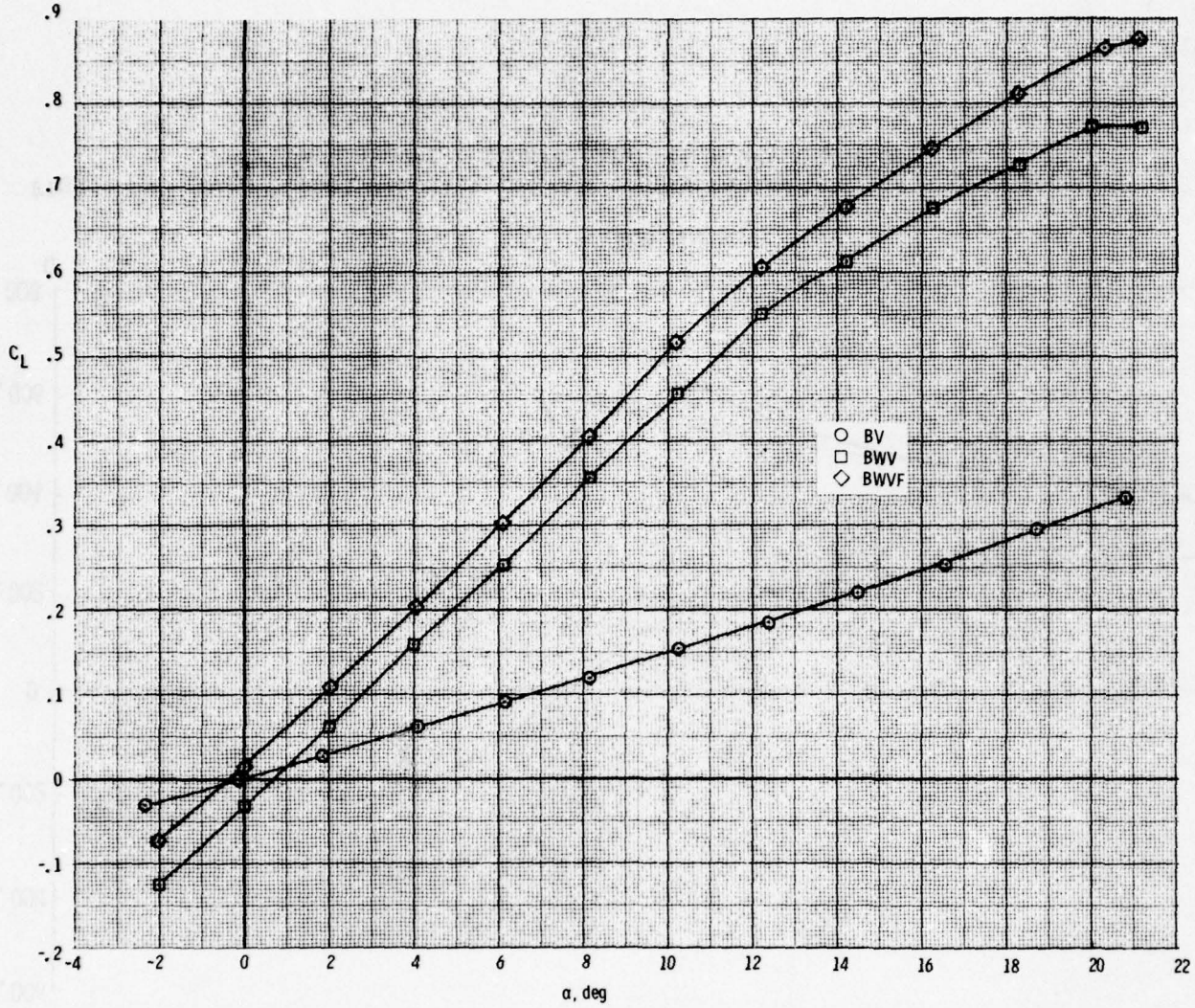

(a) C_L versus α.

Figure 20.- Effect of body buildup on longitudinal characteristics of CCV configuration. M = 0.3; $\delta_e = 0^o$; $\delta_F = 0^o$.

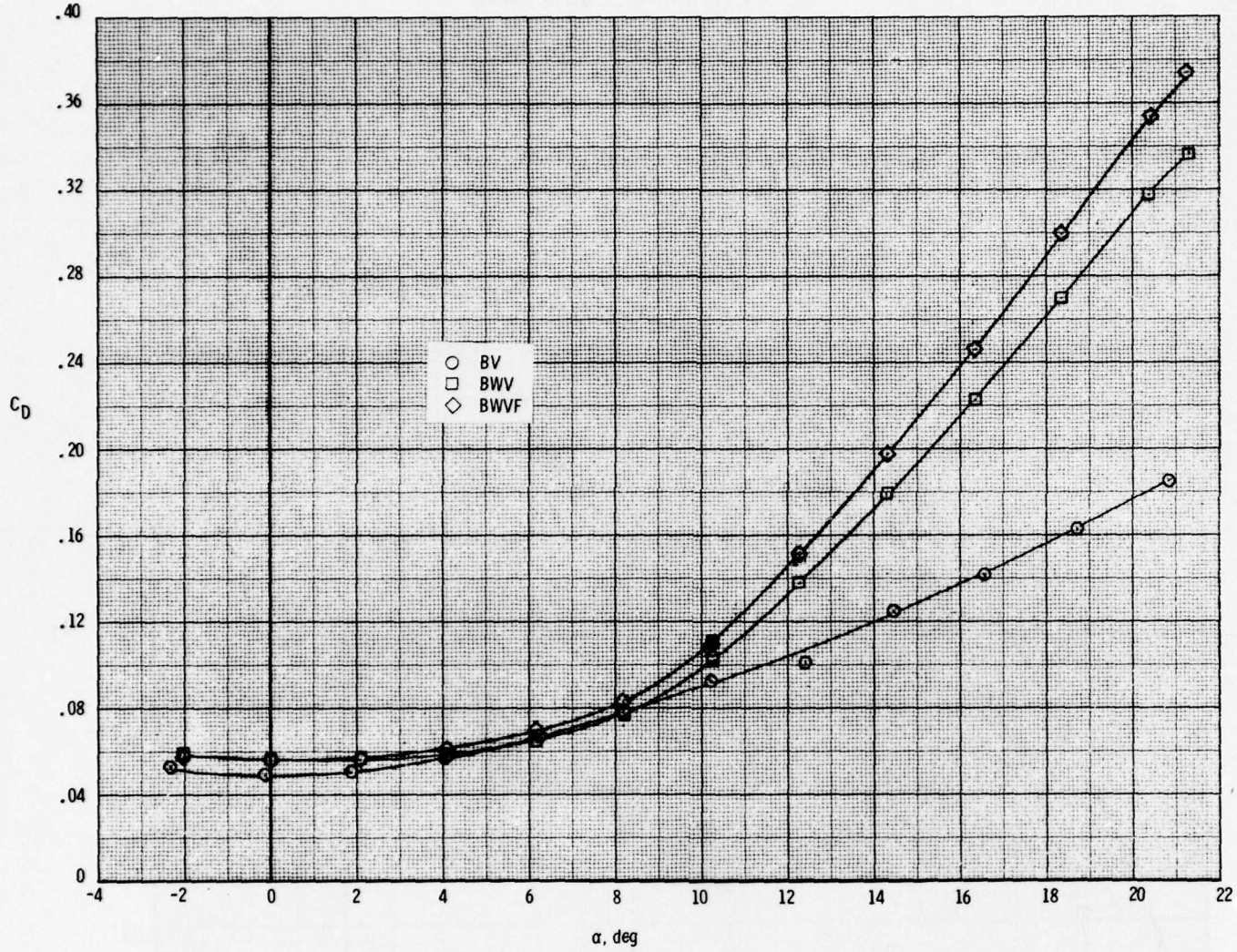

(b) C_D versus α.

Figure 20.- Continued.

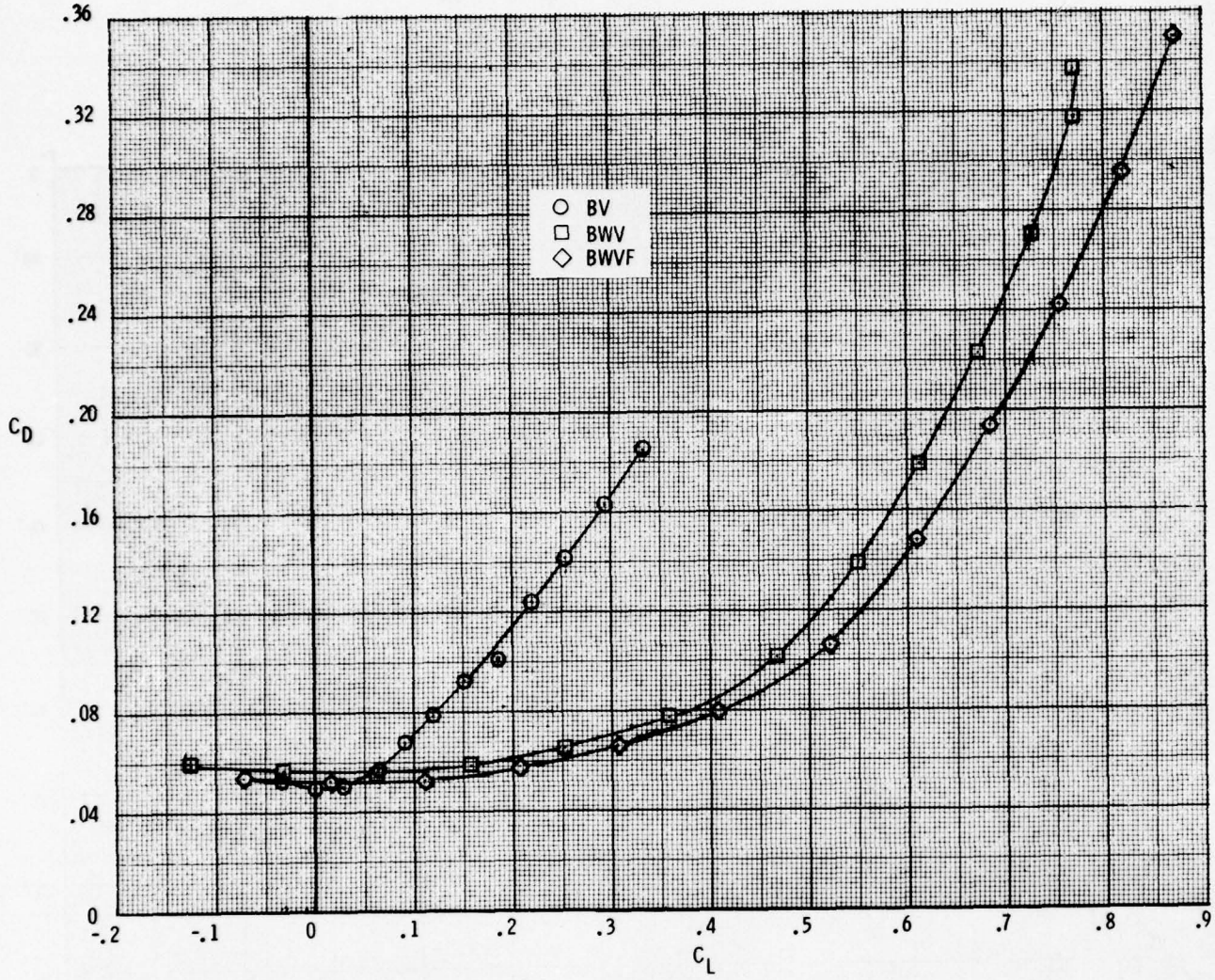

(c) C_D versus C_L.

Figure 20.- Continued.

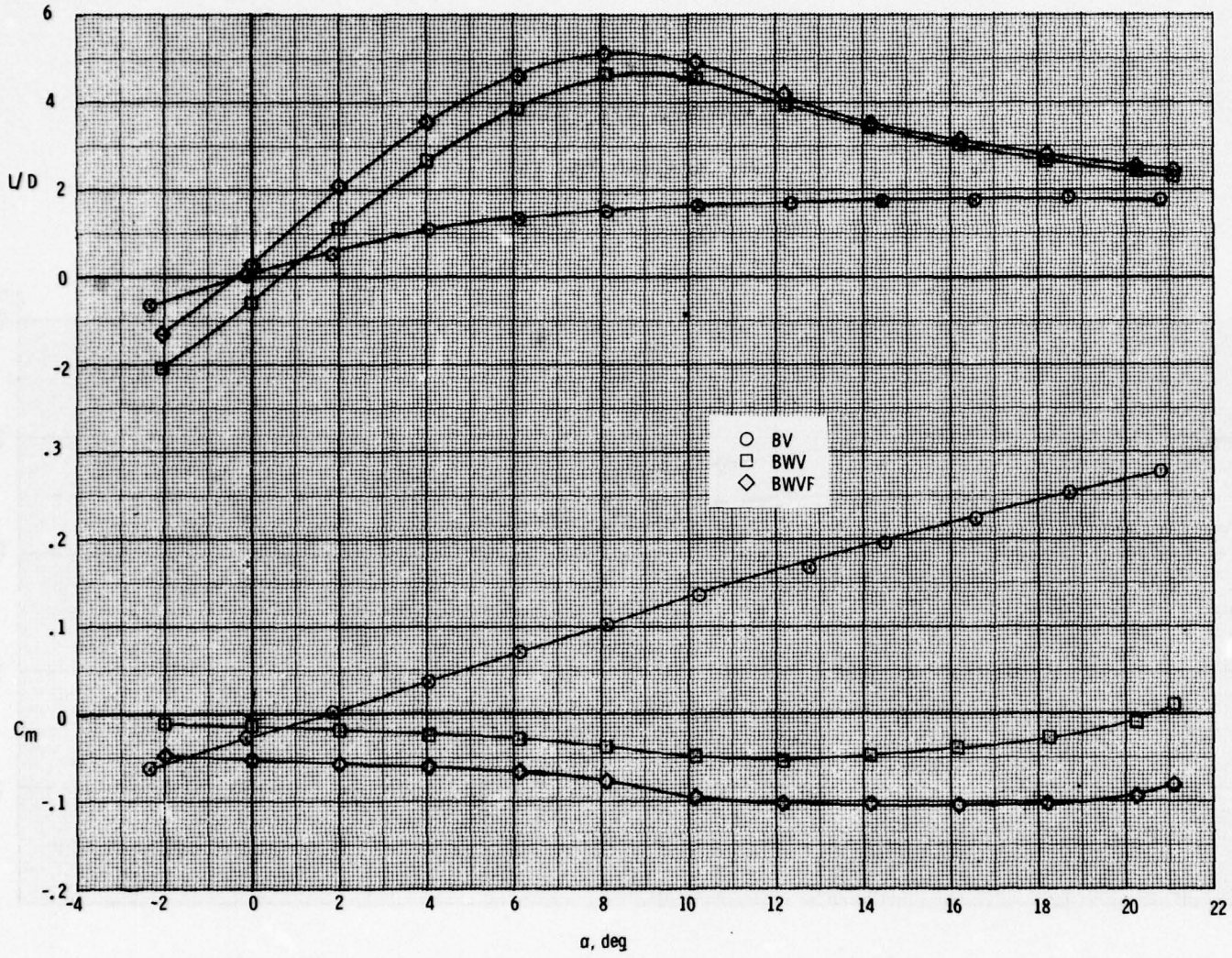

(d) L/D and C_m versus α.

Figure 20.- Continued.

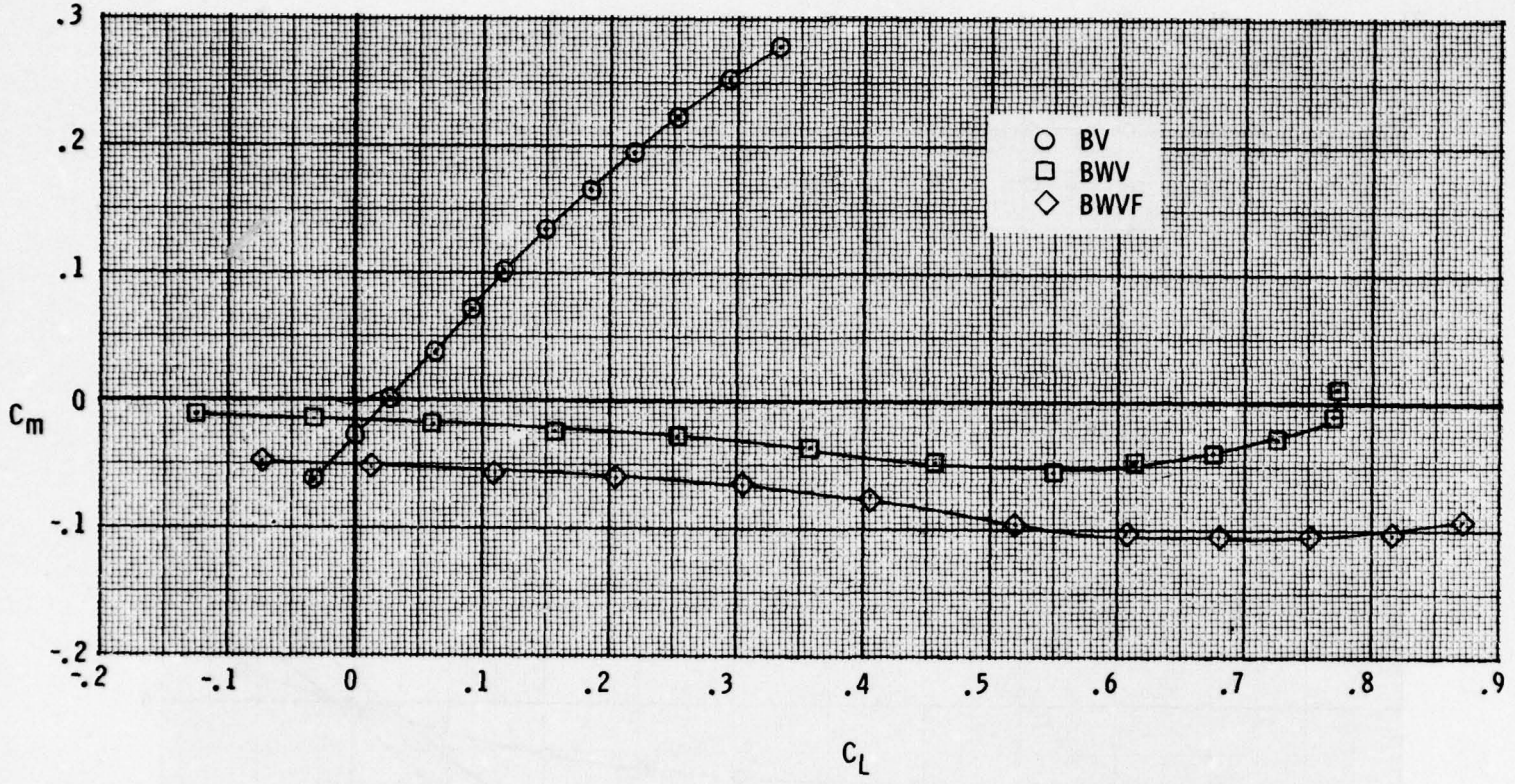

(e) C_m versus C_L.

Figure 20.- Concluded.

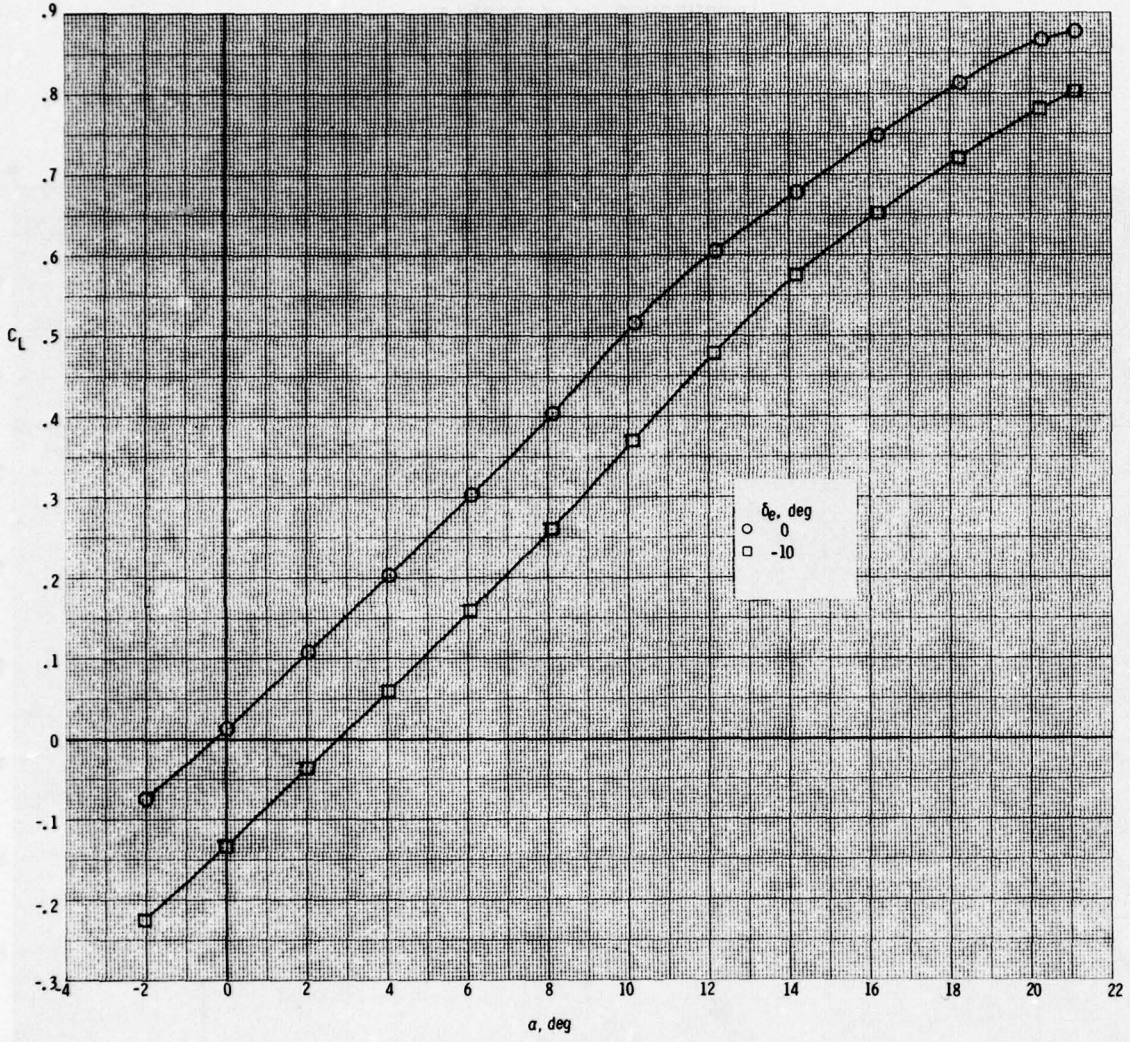

(a) M = 0.3.

Figure 21.- Static longitudinal characteristics of CCV model. Canard off; $\delta_F = 0^o$.

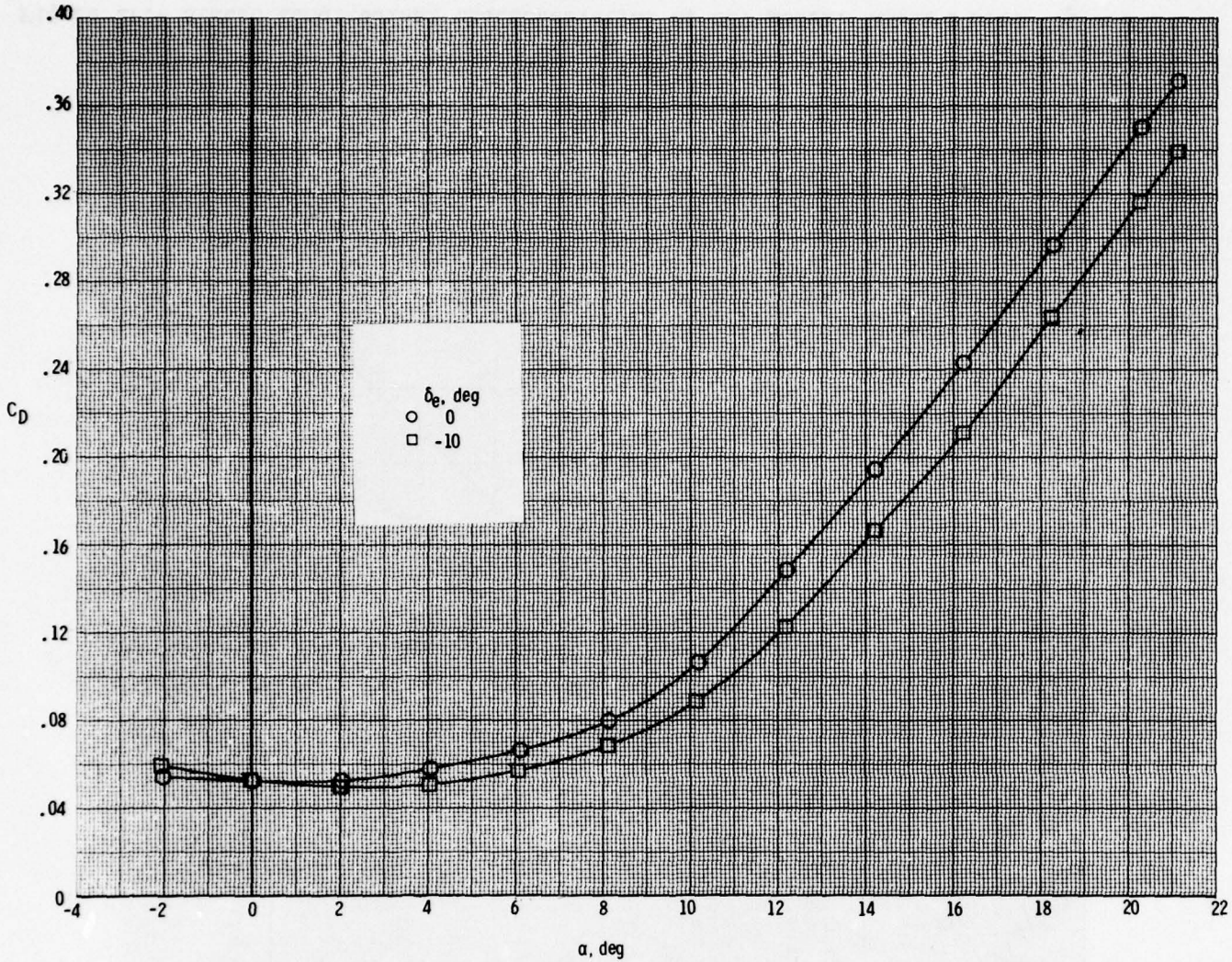

(a) Continued.

Figure 21.- Continued.

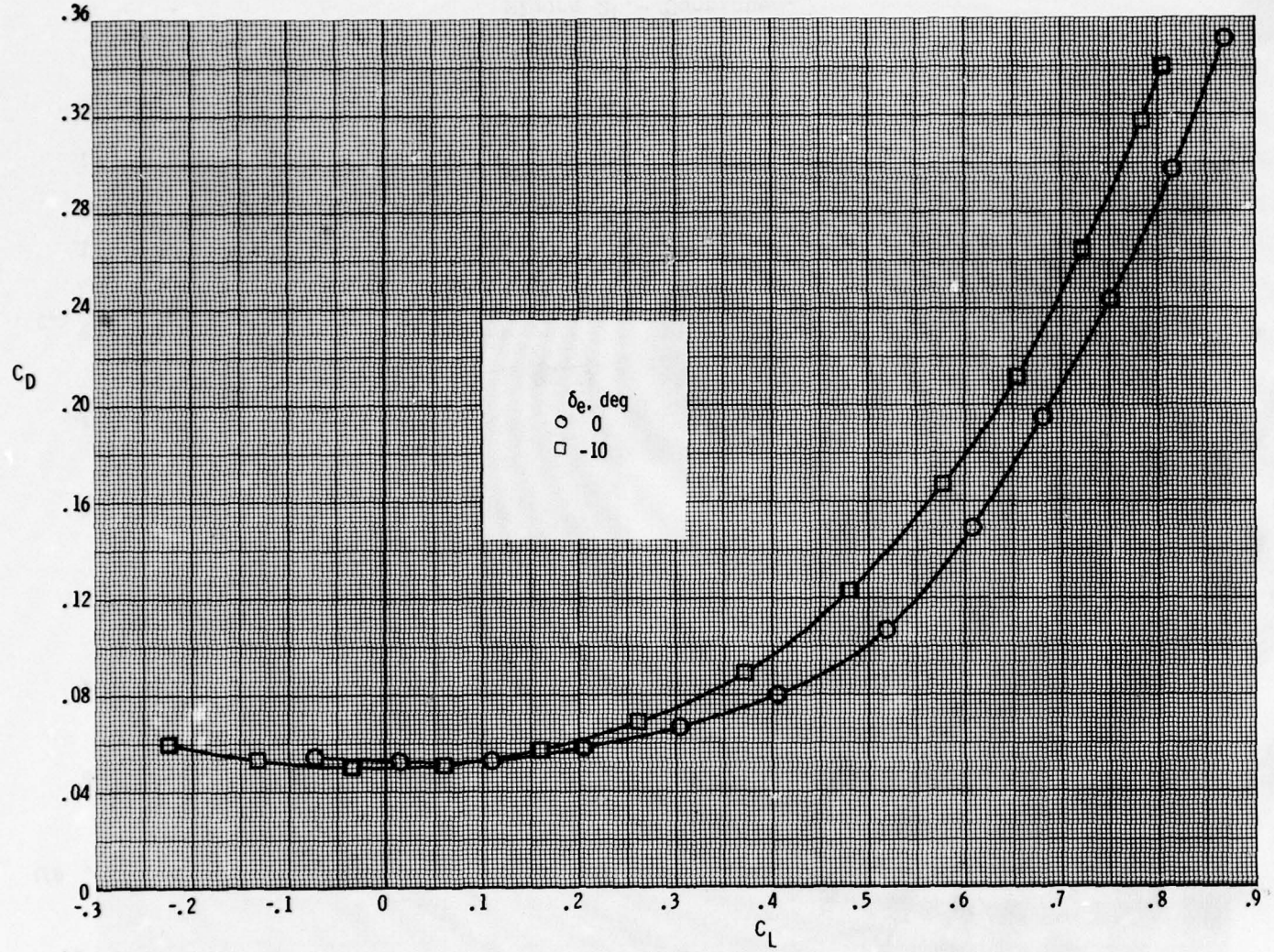

(a) Continued.

Figure 21.- Continued.

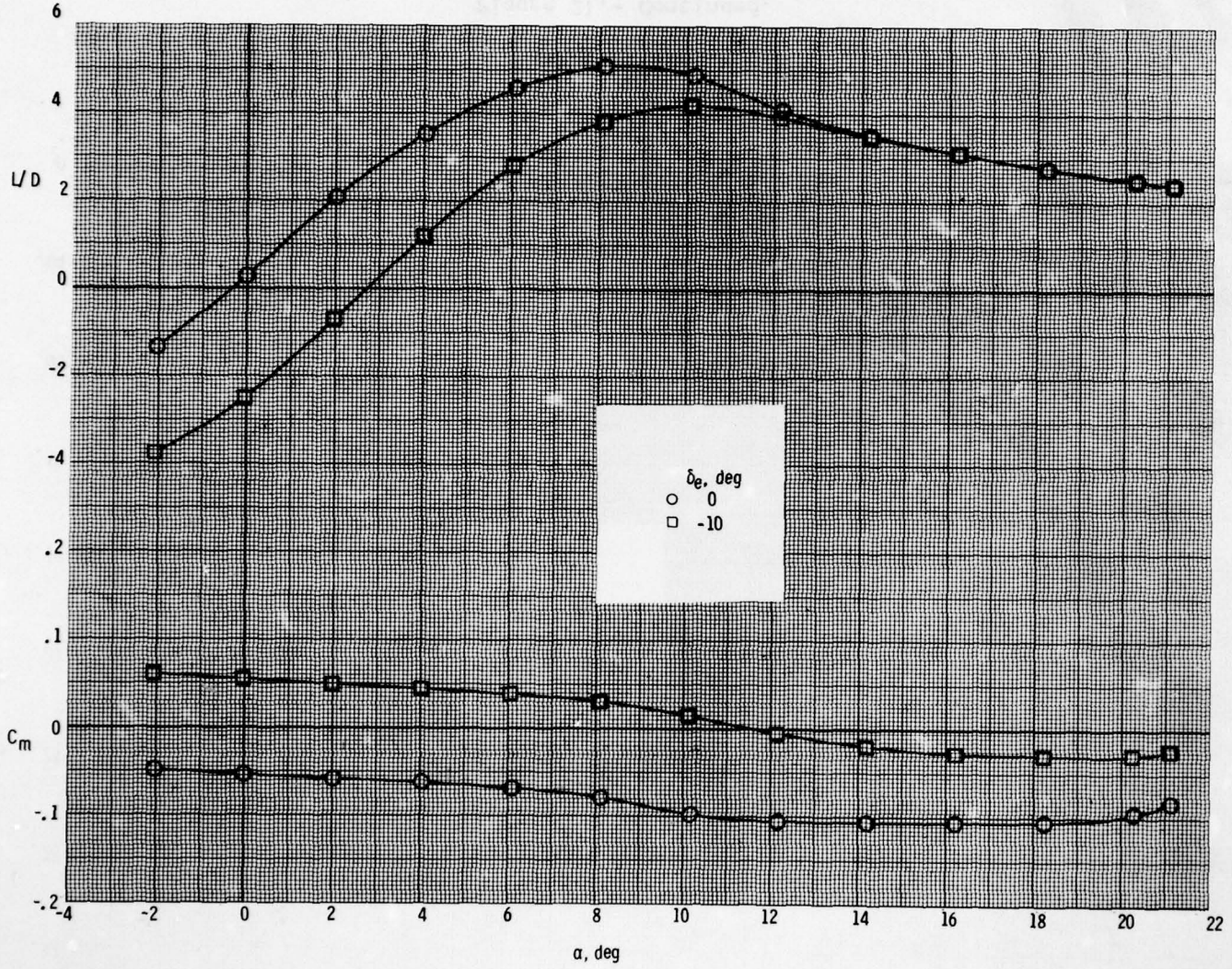

(a) Continued.

Figure 21.- Continued.

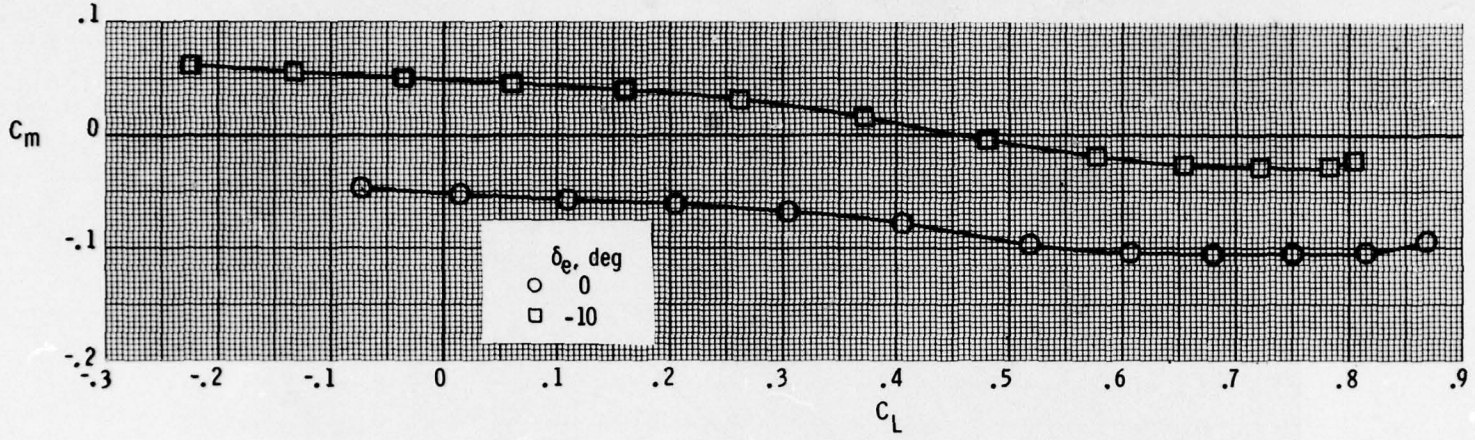

(a) Concluded.

Figure 21.- Continued.

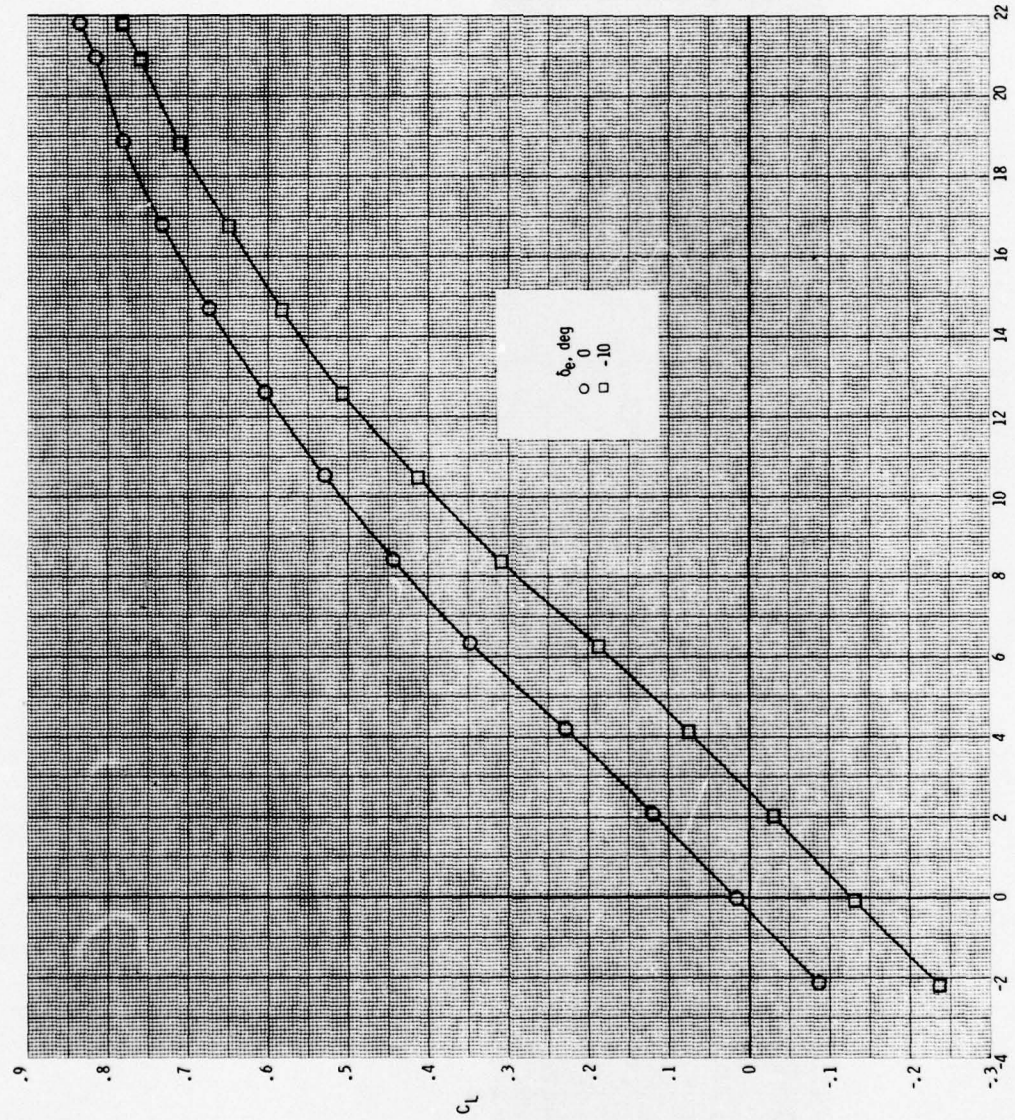

(b) $M = 0.6$.

Figure 21.- Continued.

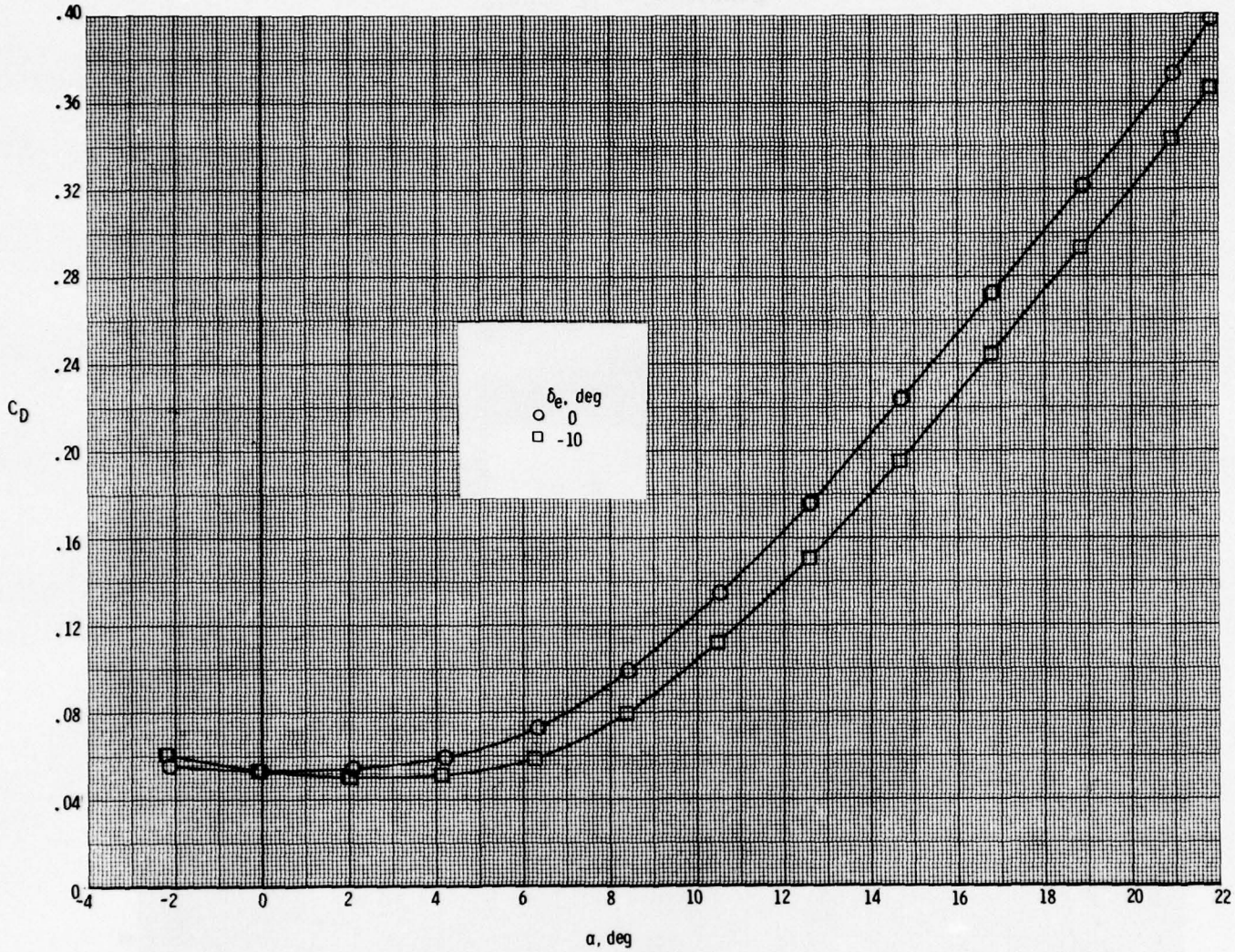

(b) Continued.

Figure 21.- Continued.

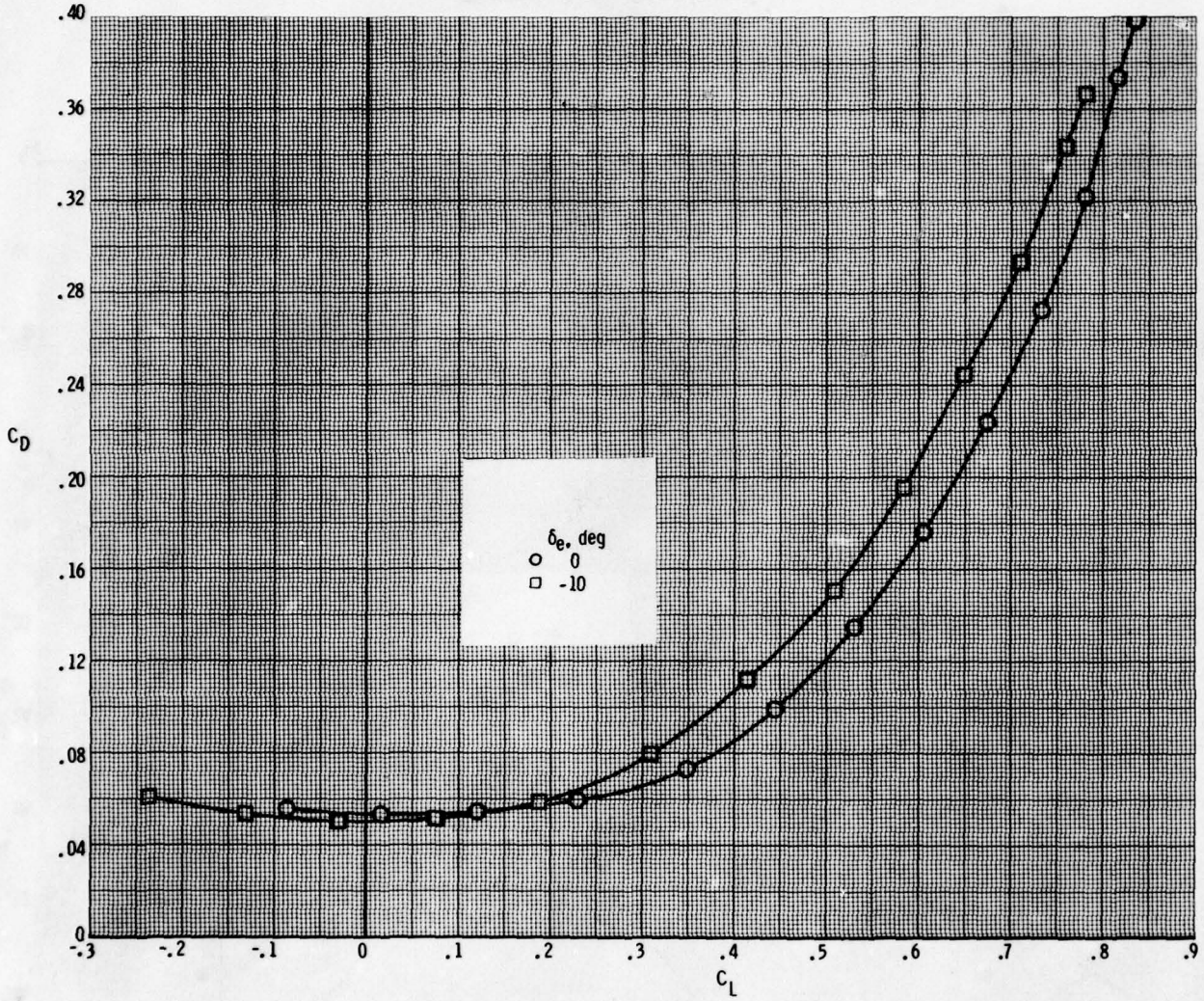

(b) Continued.

Figure 21.- Continued.

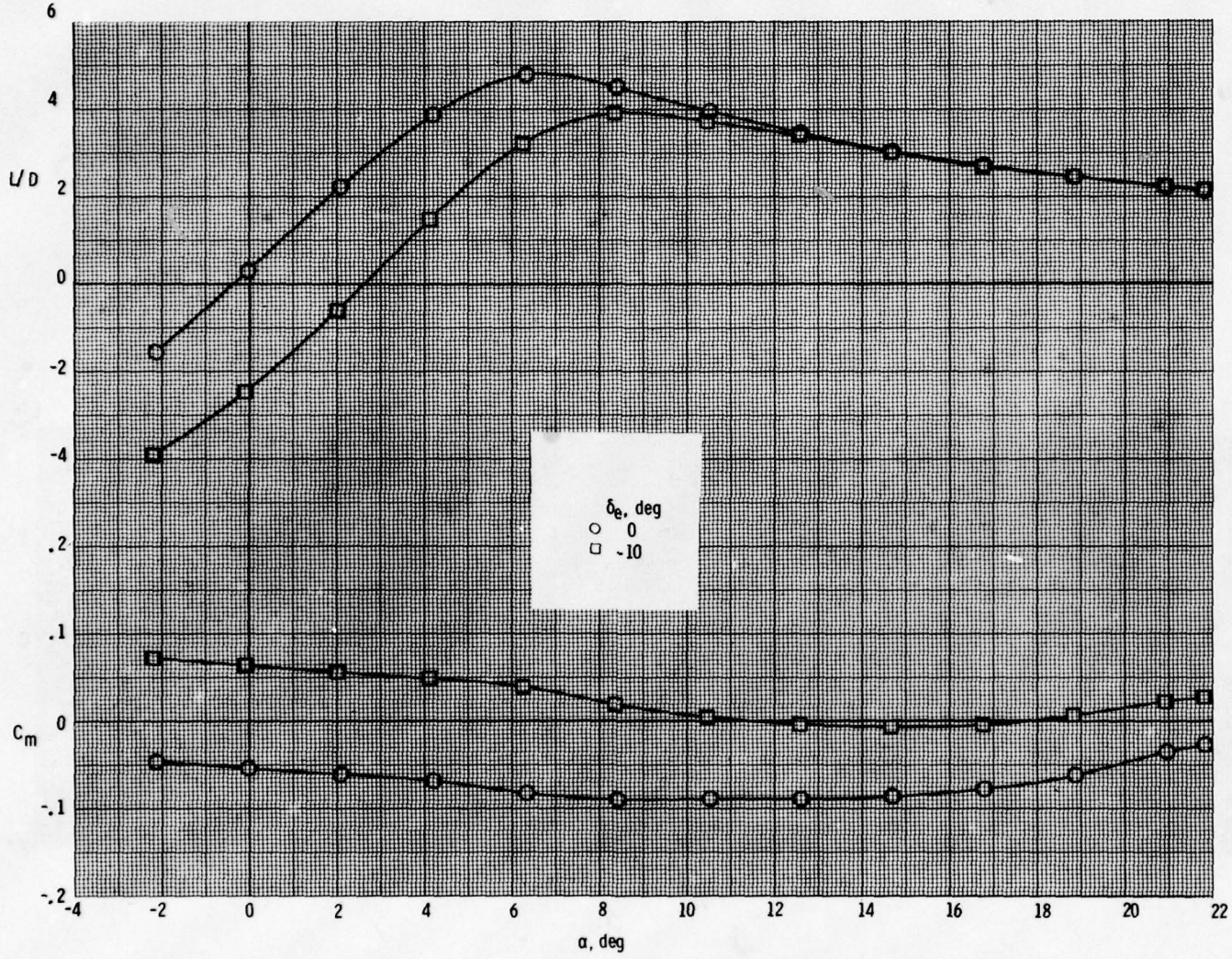

(b) Continued.

Figure 21.- Continued.

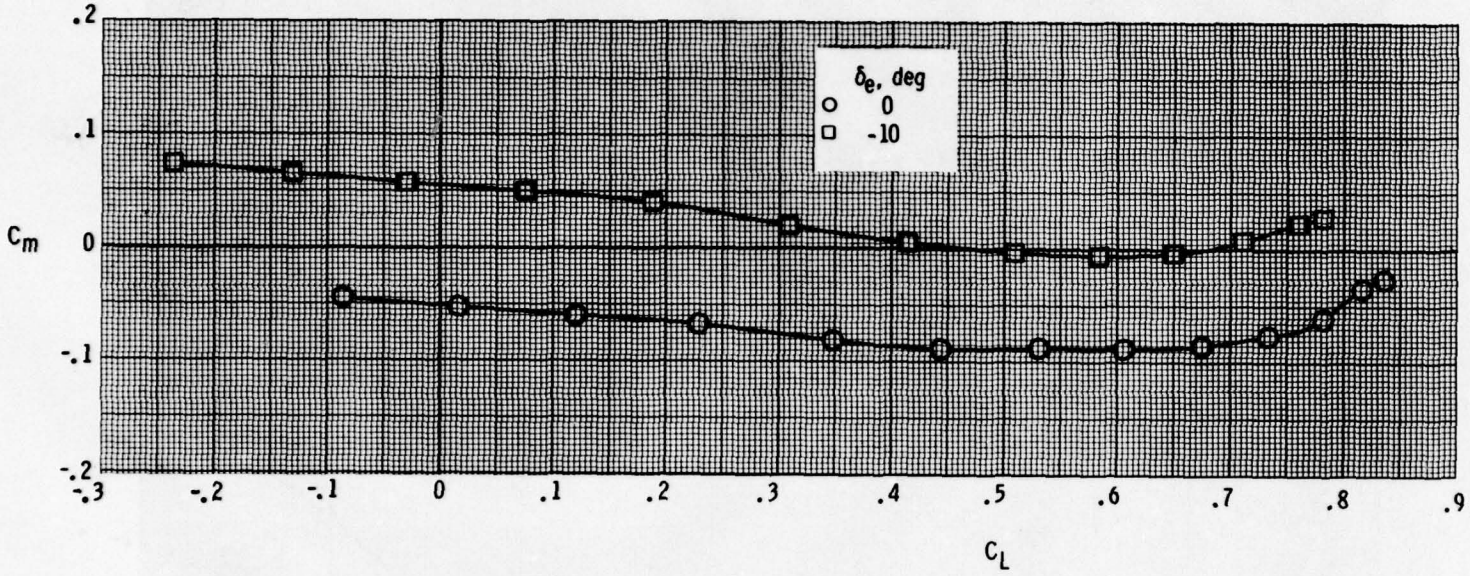

(b) Concluded.

Figure 21.- Continued.

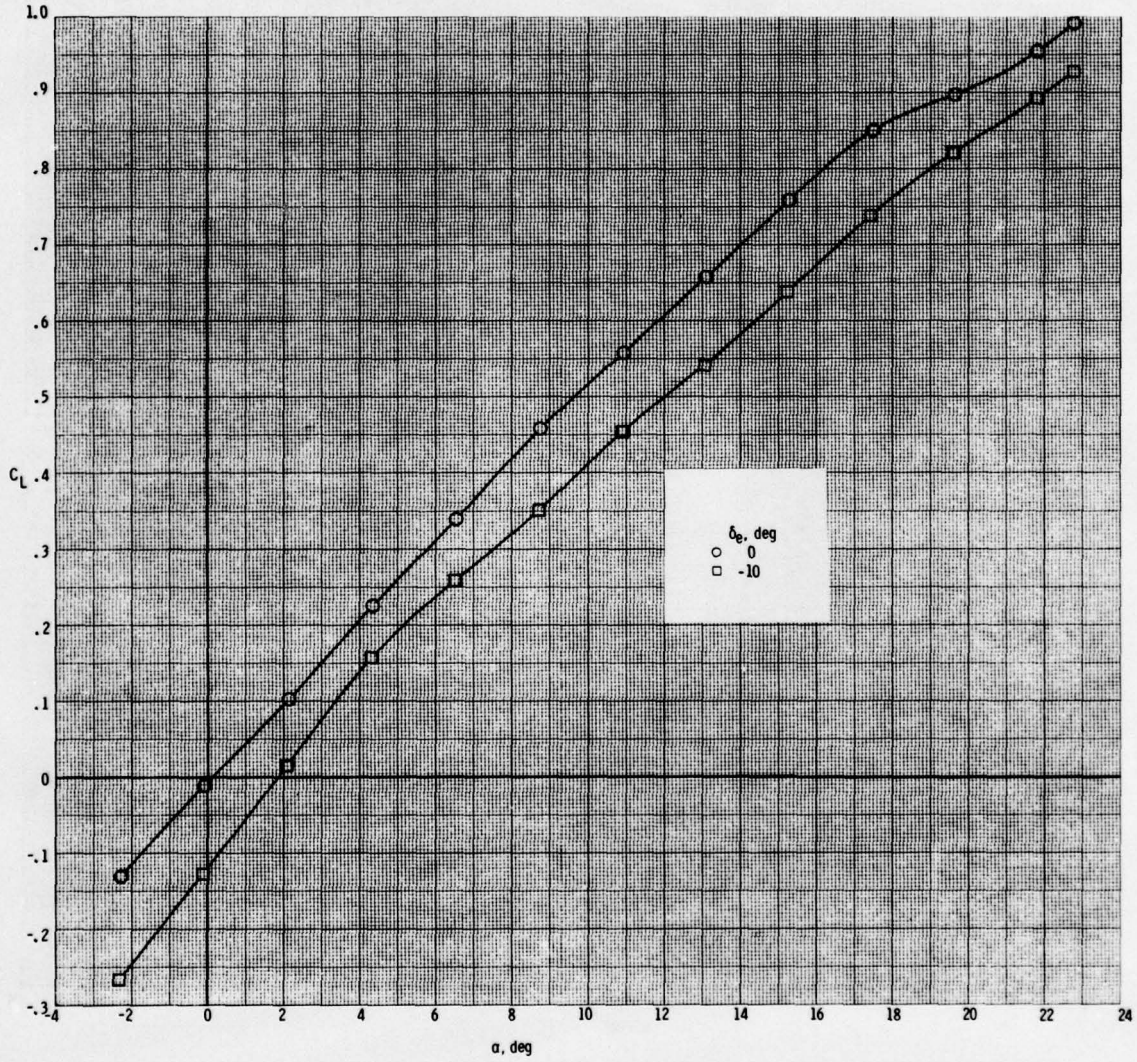

(c) M = 0.9.

Figure 21.- Continued.

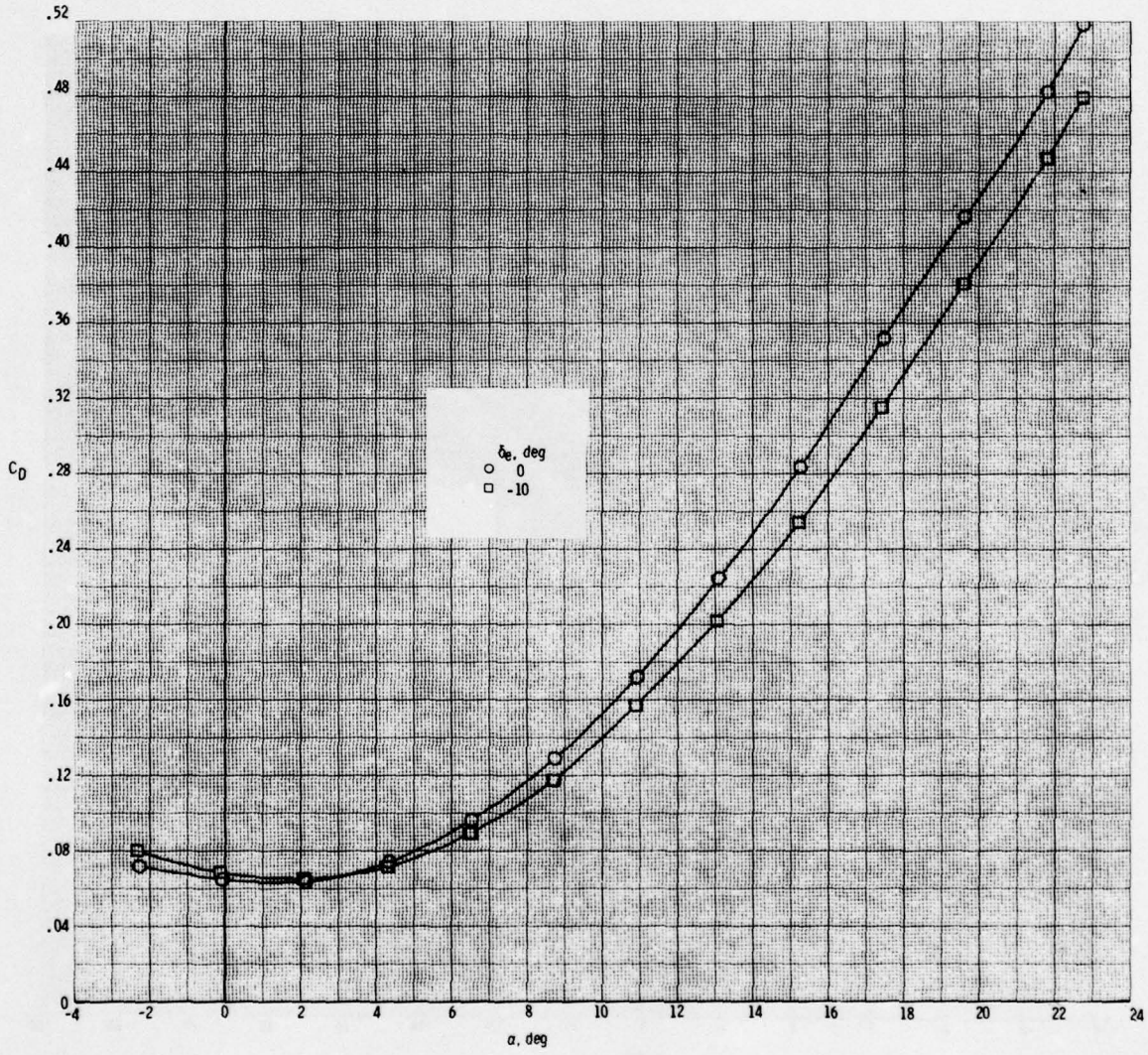

(c) Continued.

Figure 21.- Continued.

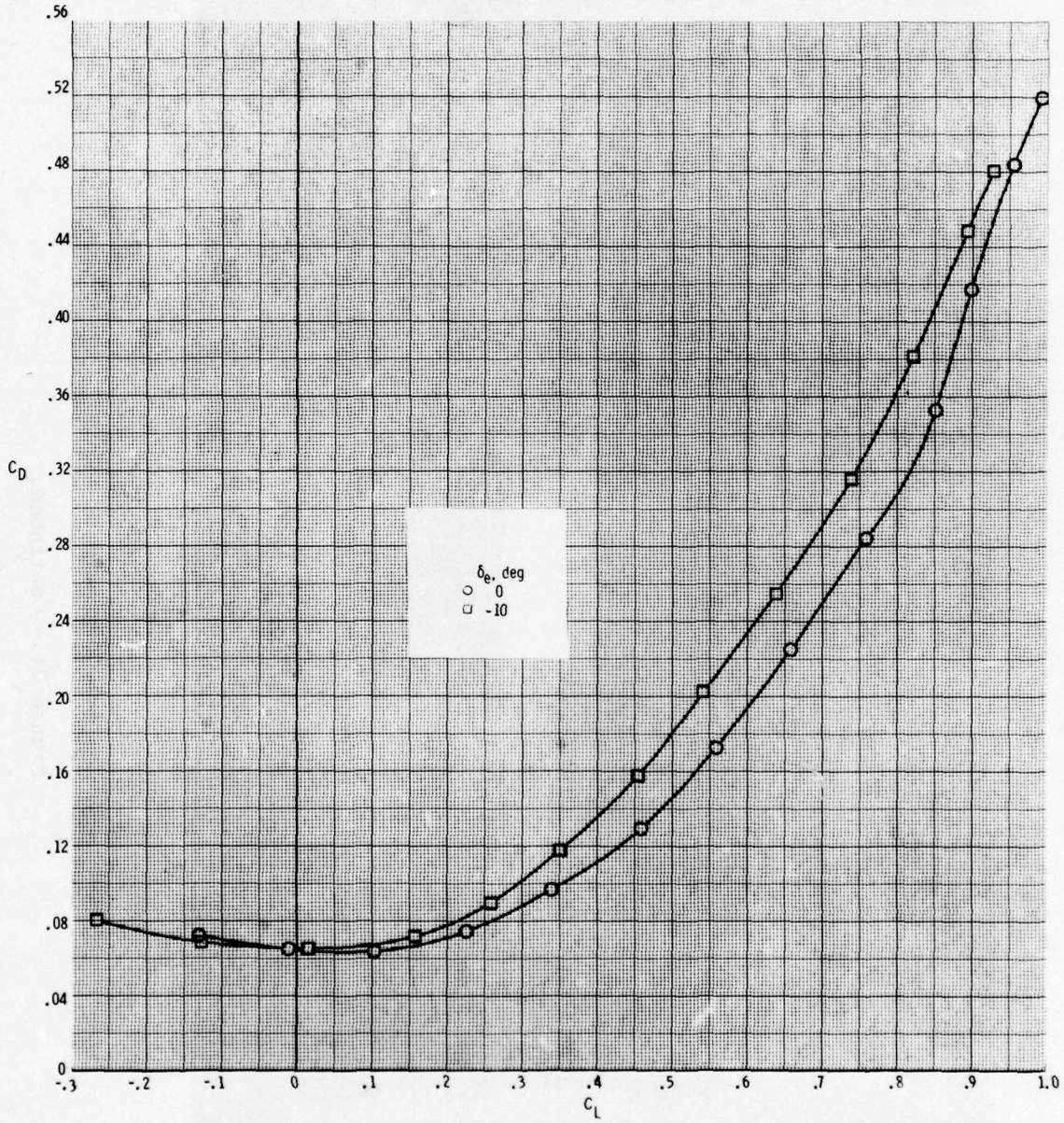

(c) Continued.

Figure 21.- Continued.

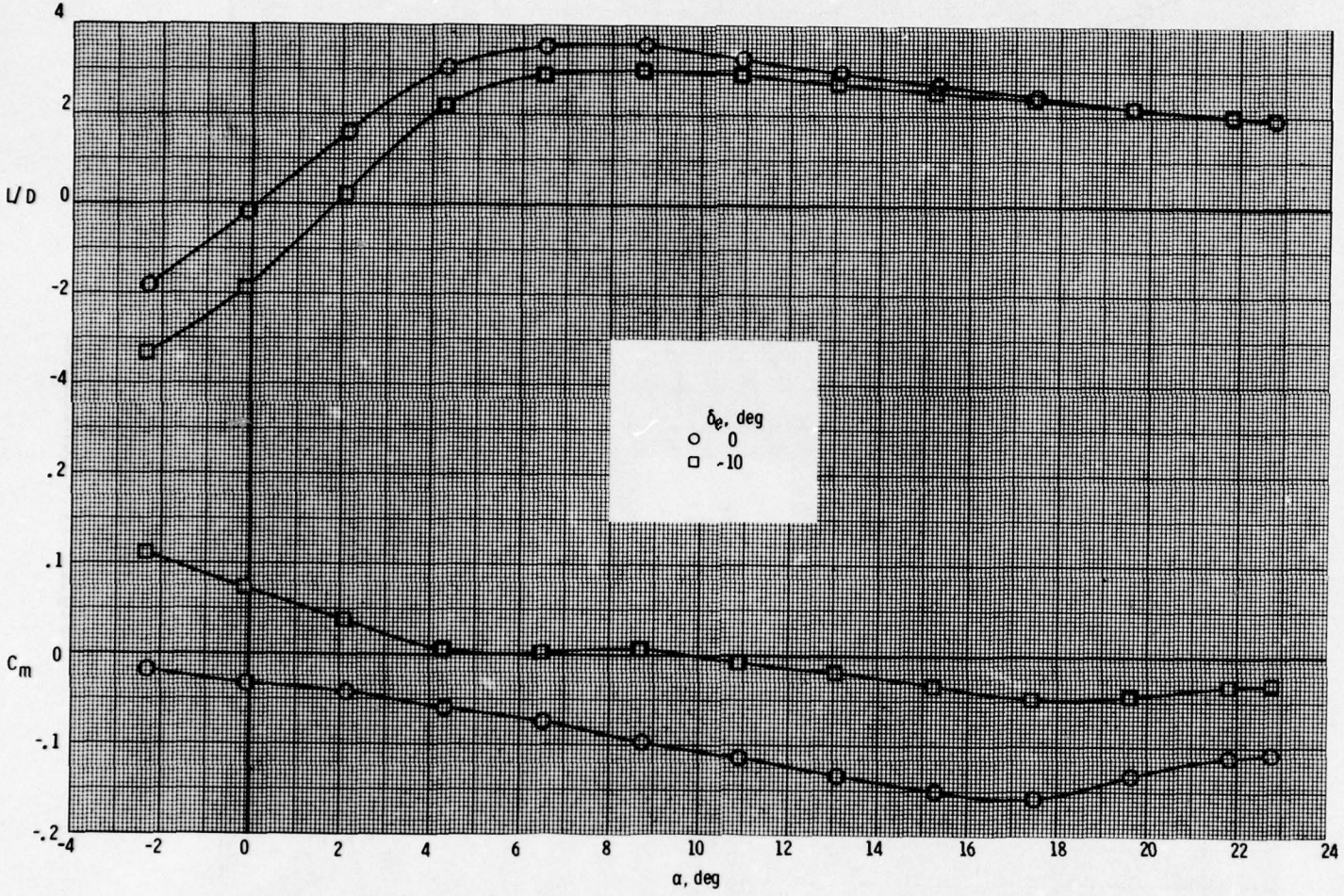

(c) Continued.

Figure 21.- Continued.

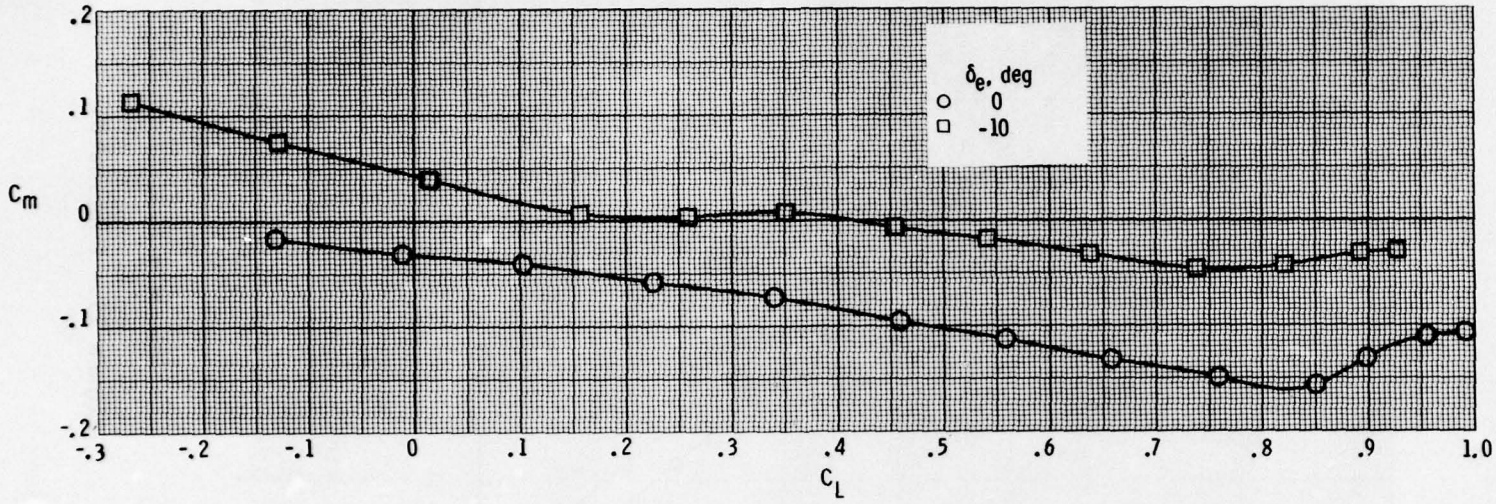

(c) Concluded.

Figure 21.- Continued.

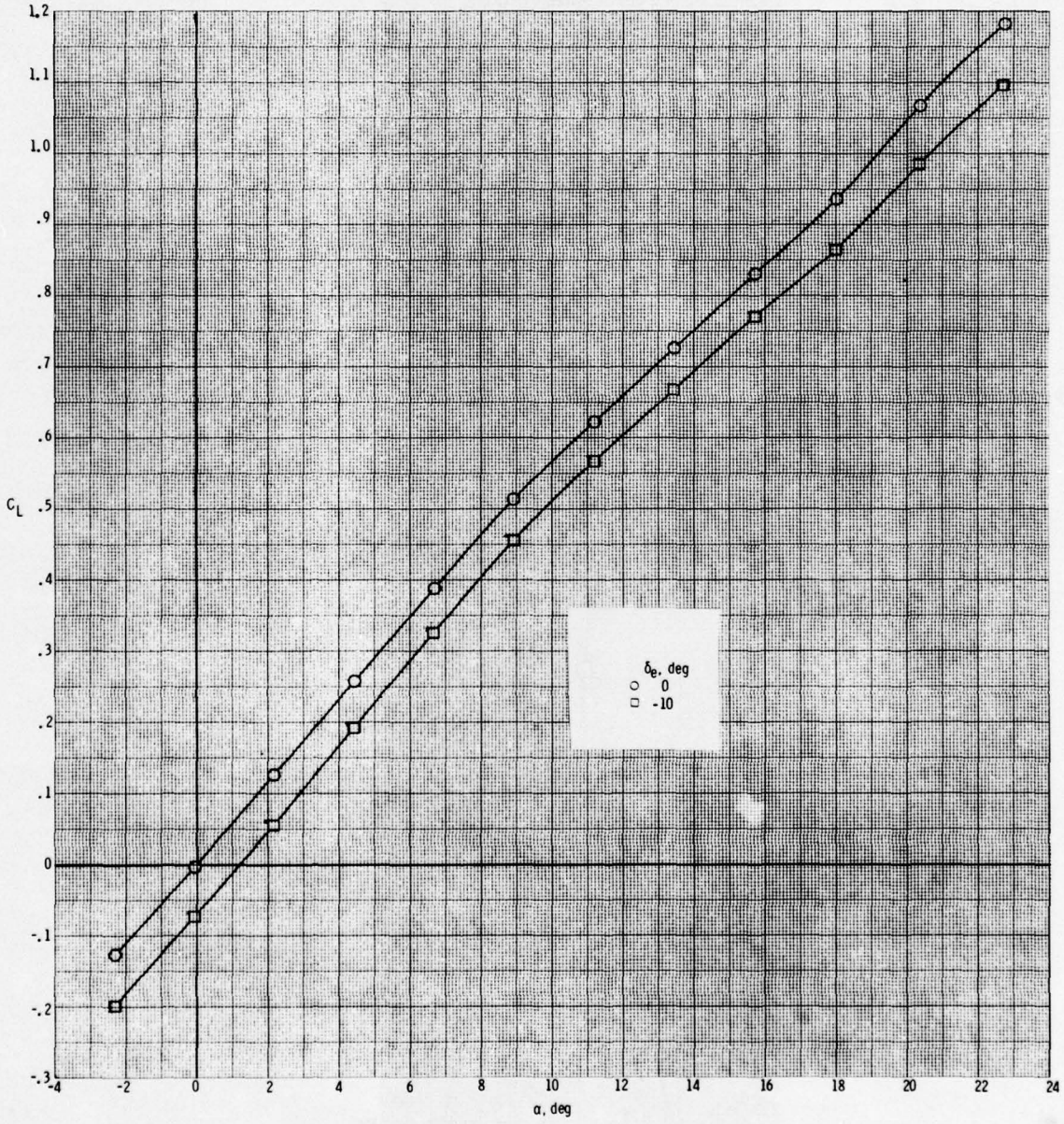

(d) M = 1.2.

Figure 21.- Continued.

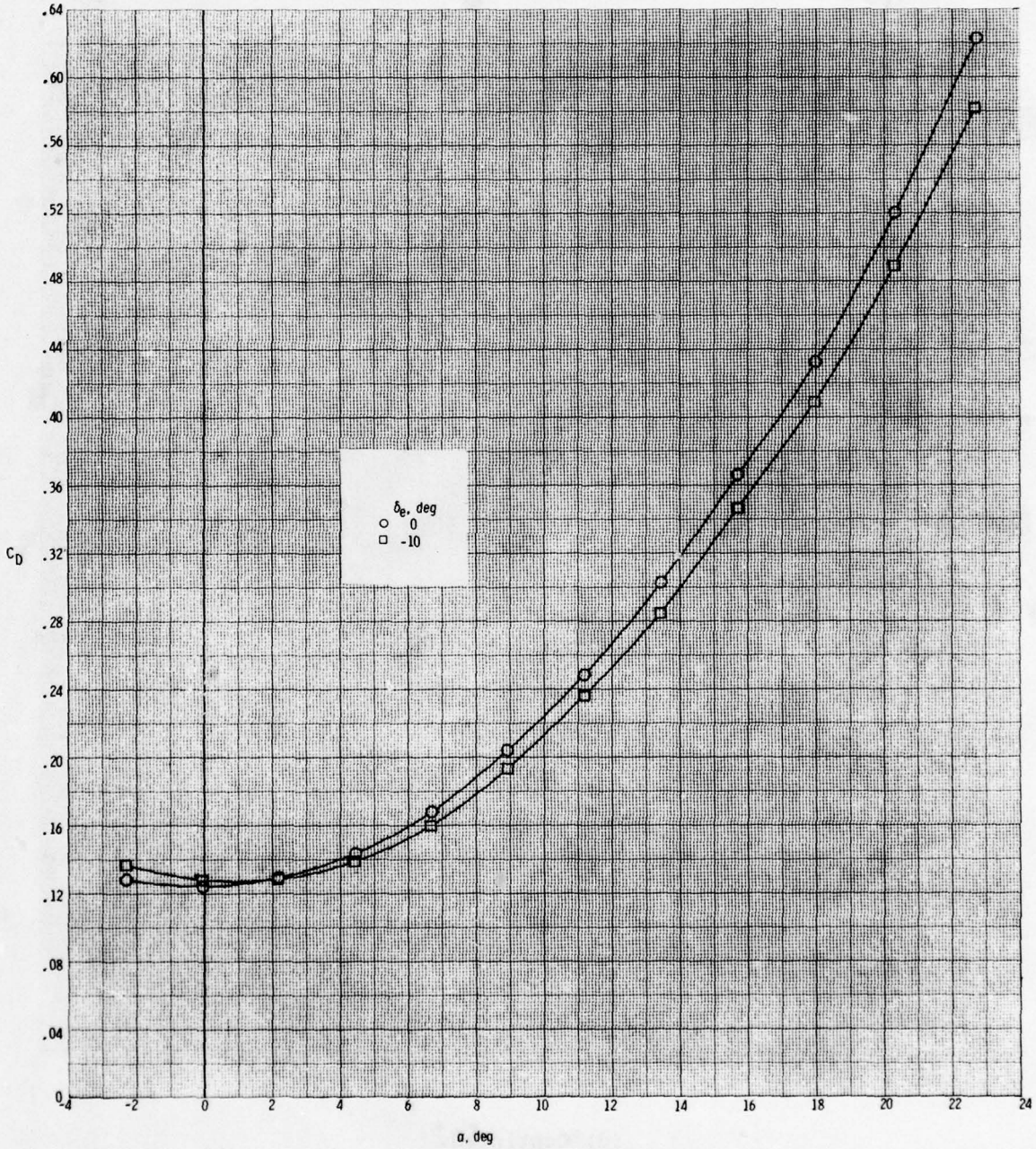

(d) Continued.

Figure 21.- Continued.

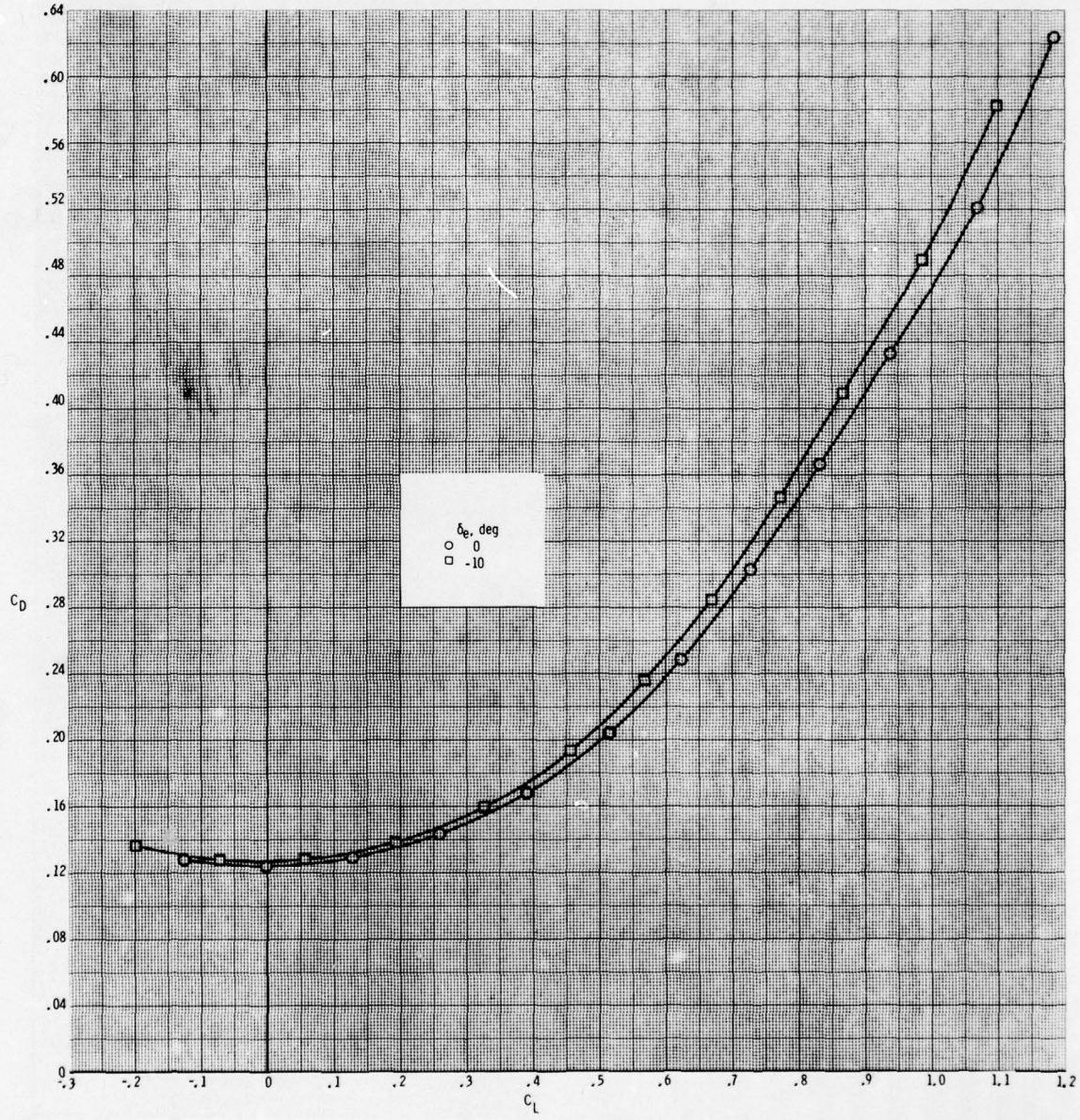

(d) Continued.

Figure 21.- Continued.

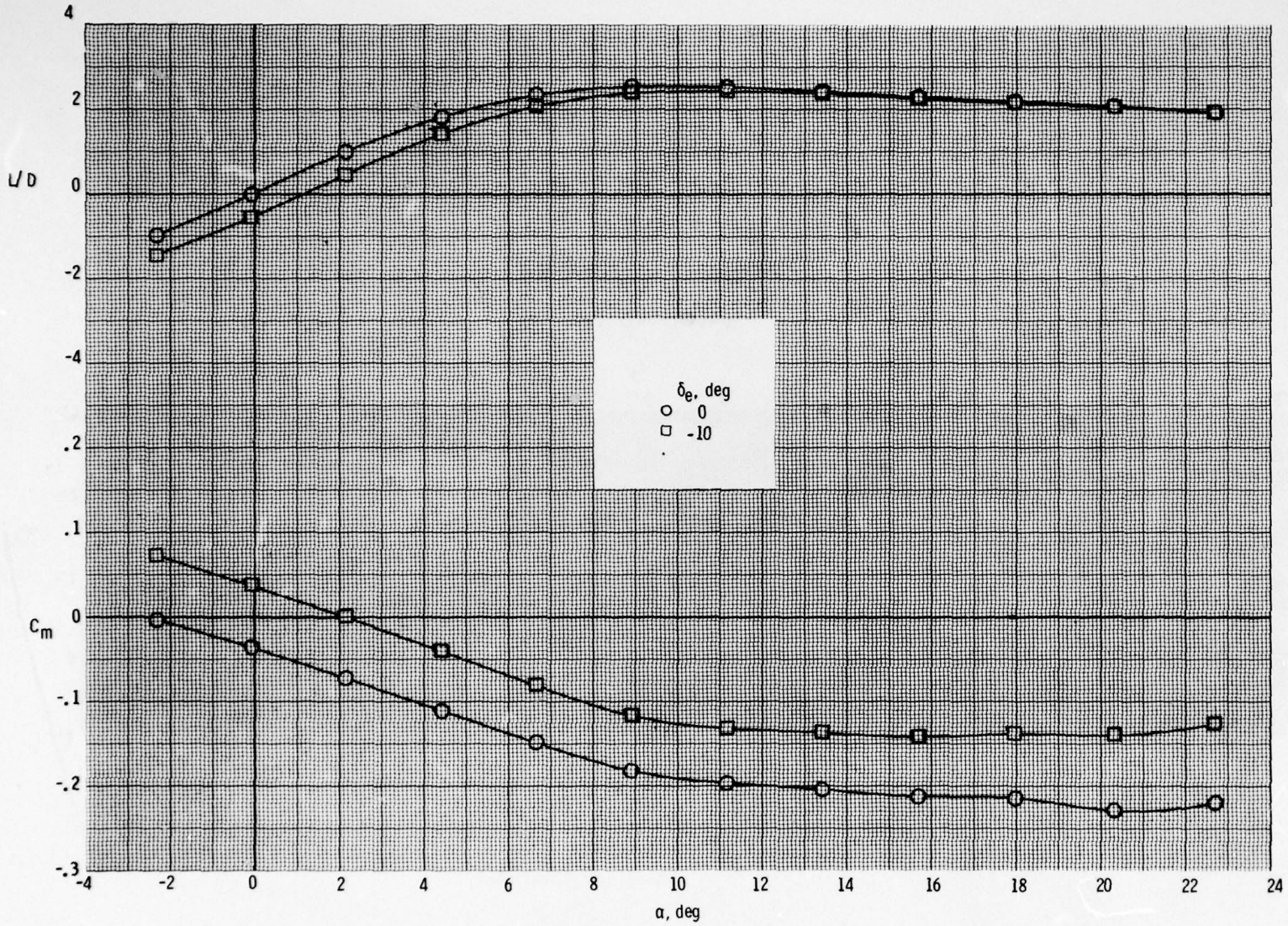

(d) Continued.

Figure 21.- Continued.

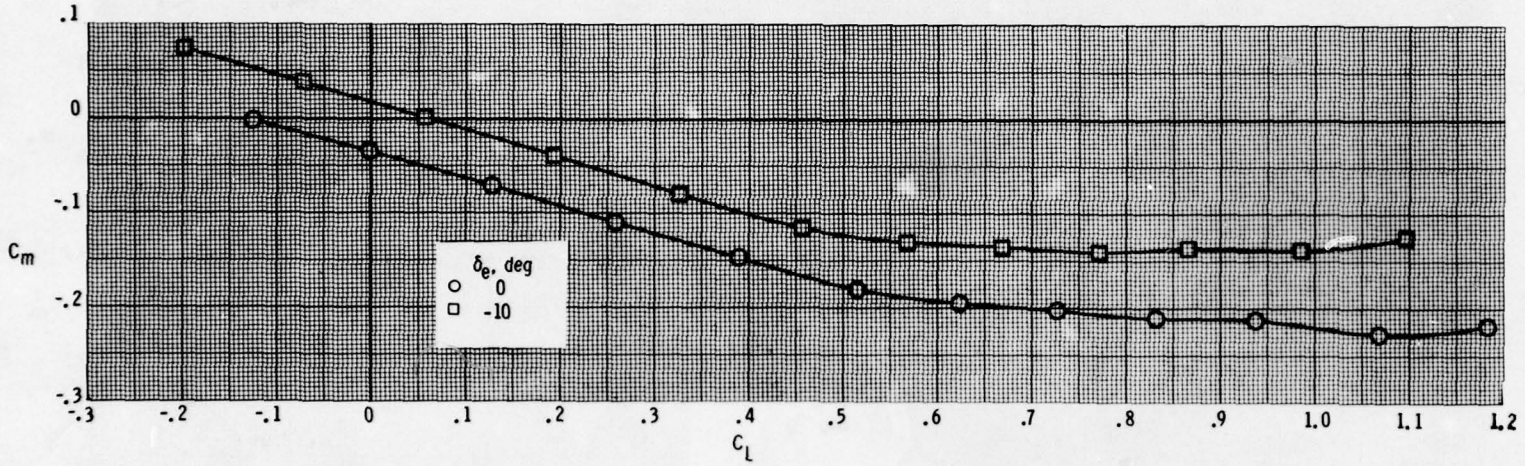

(d) Concluded.

Figure 21.- Continued.

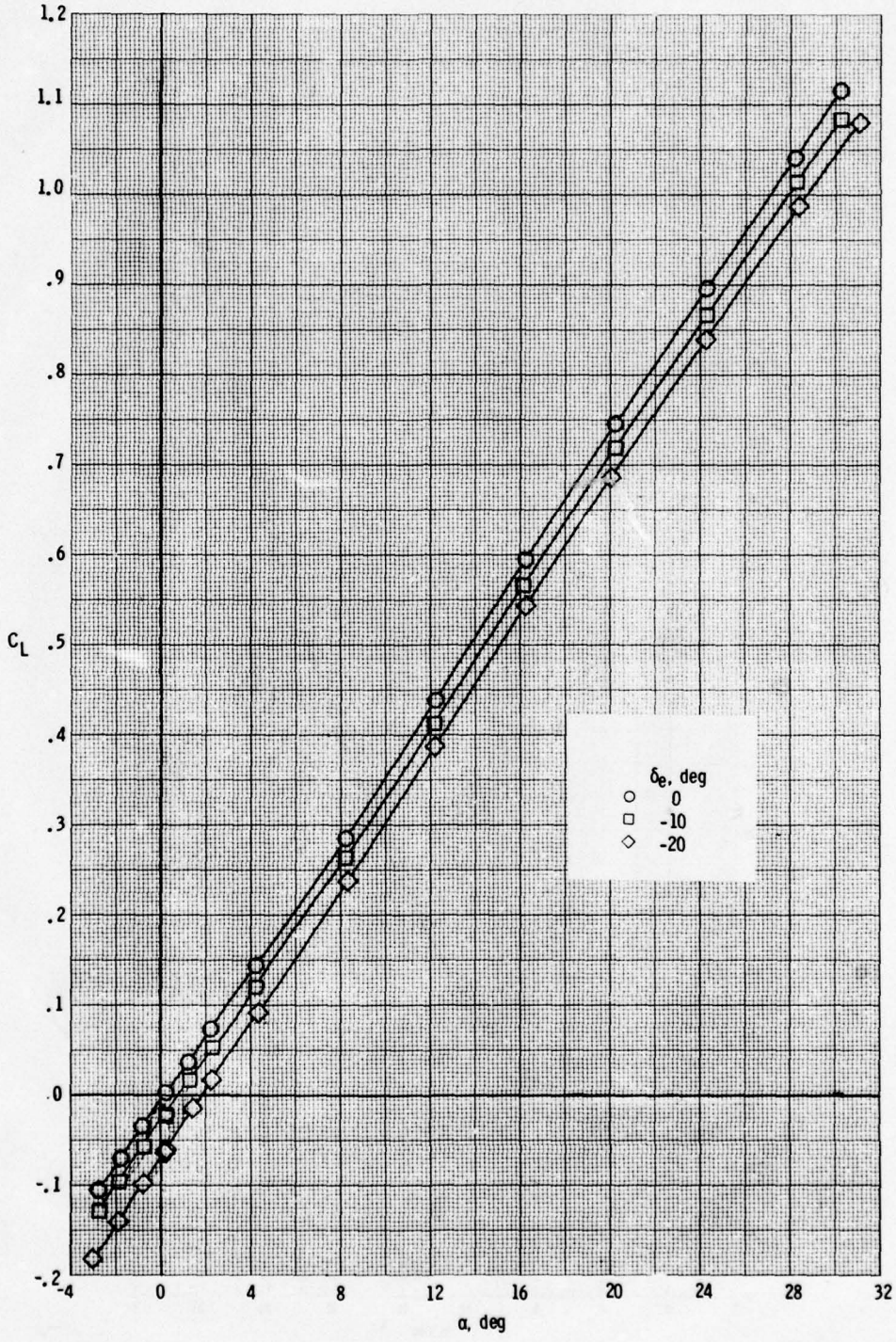

(e) M = 2.36.

Figure 21.- Continued.

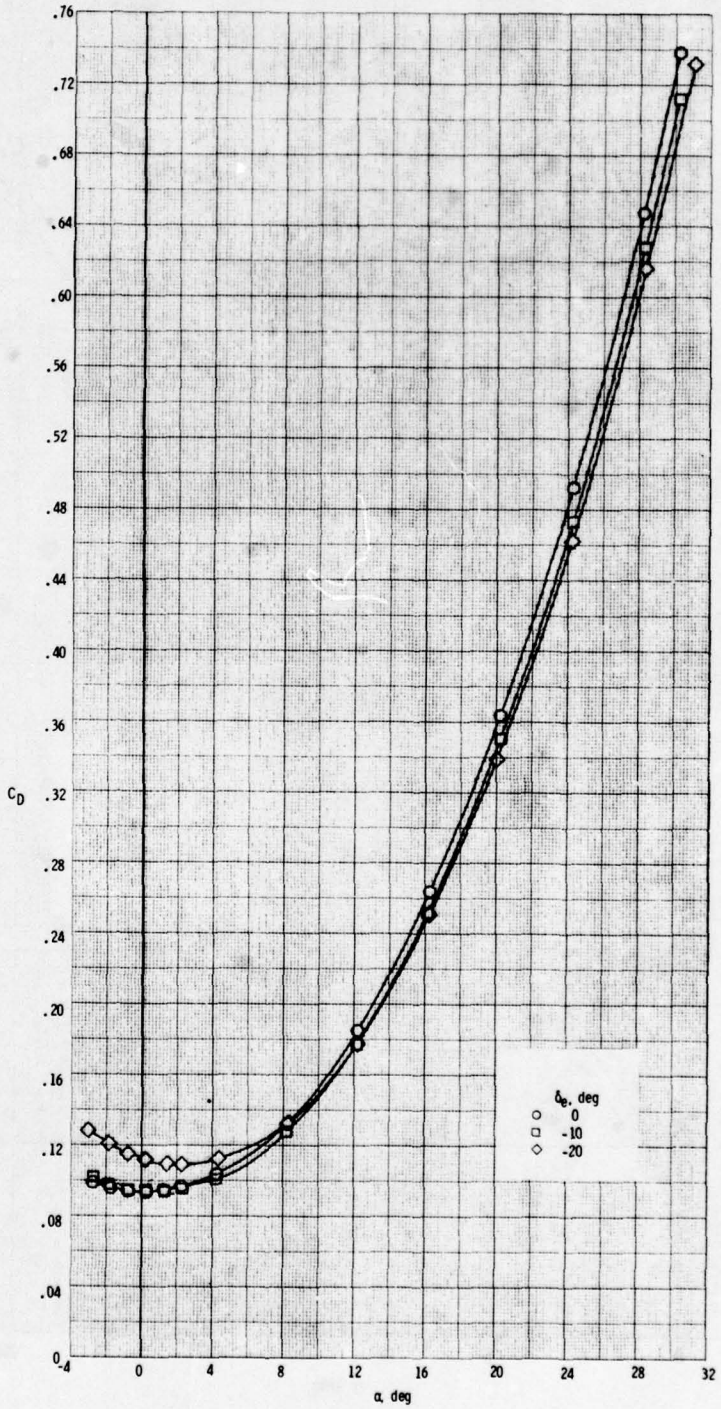

(e) Continued.

Figure 21.- Continued.

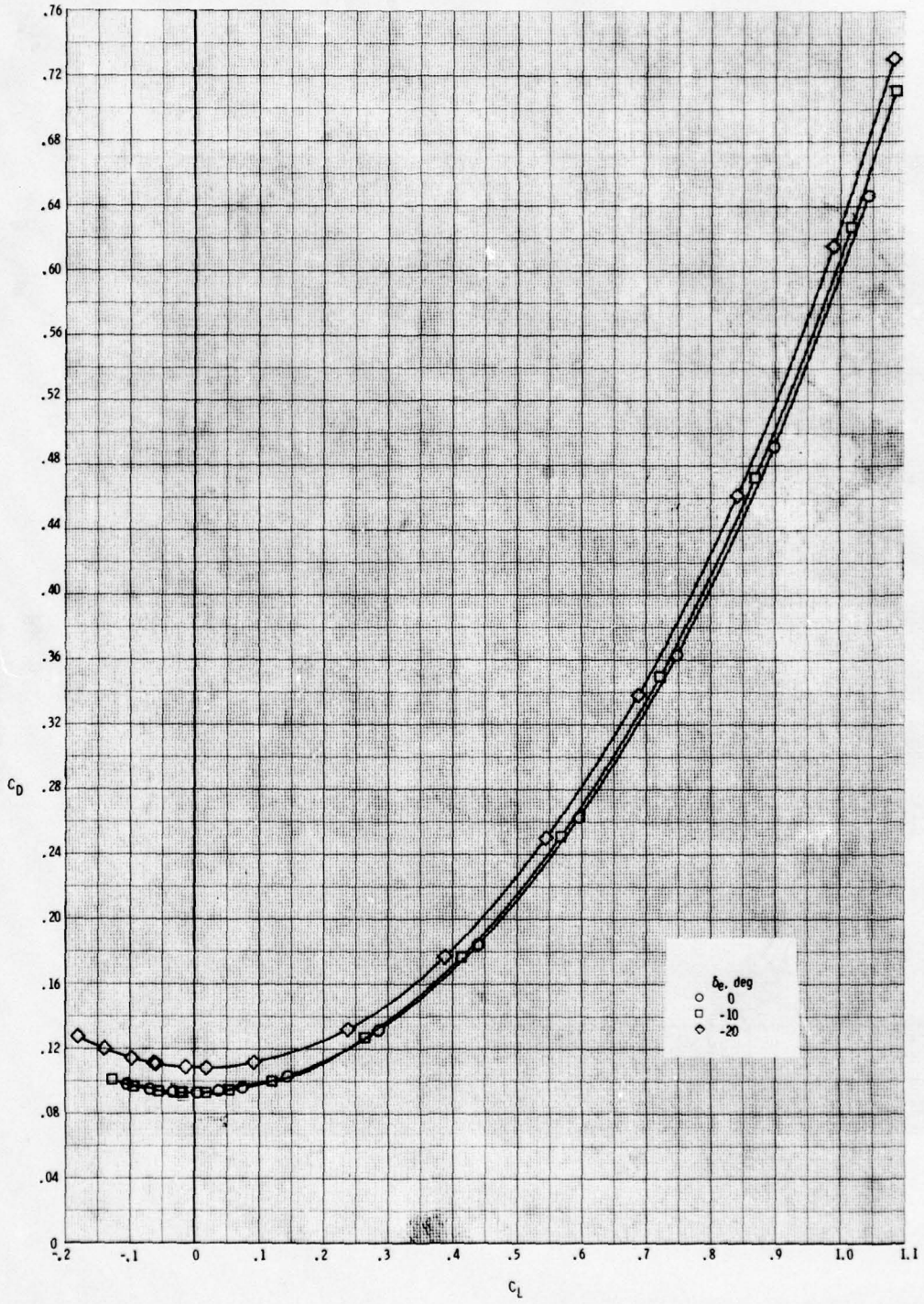

(e) Continued.

Figure 21.- Continued.

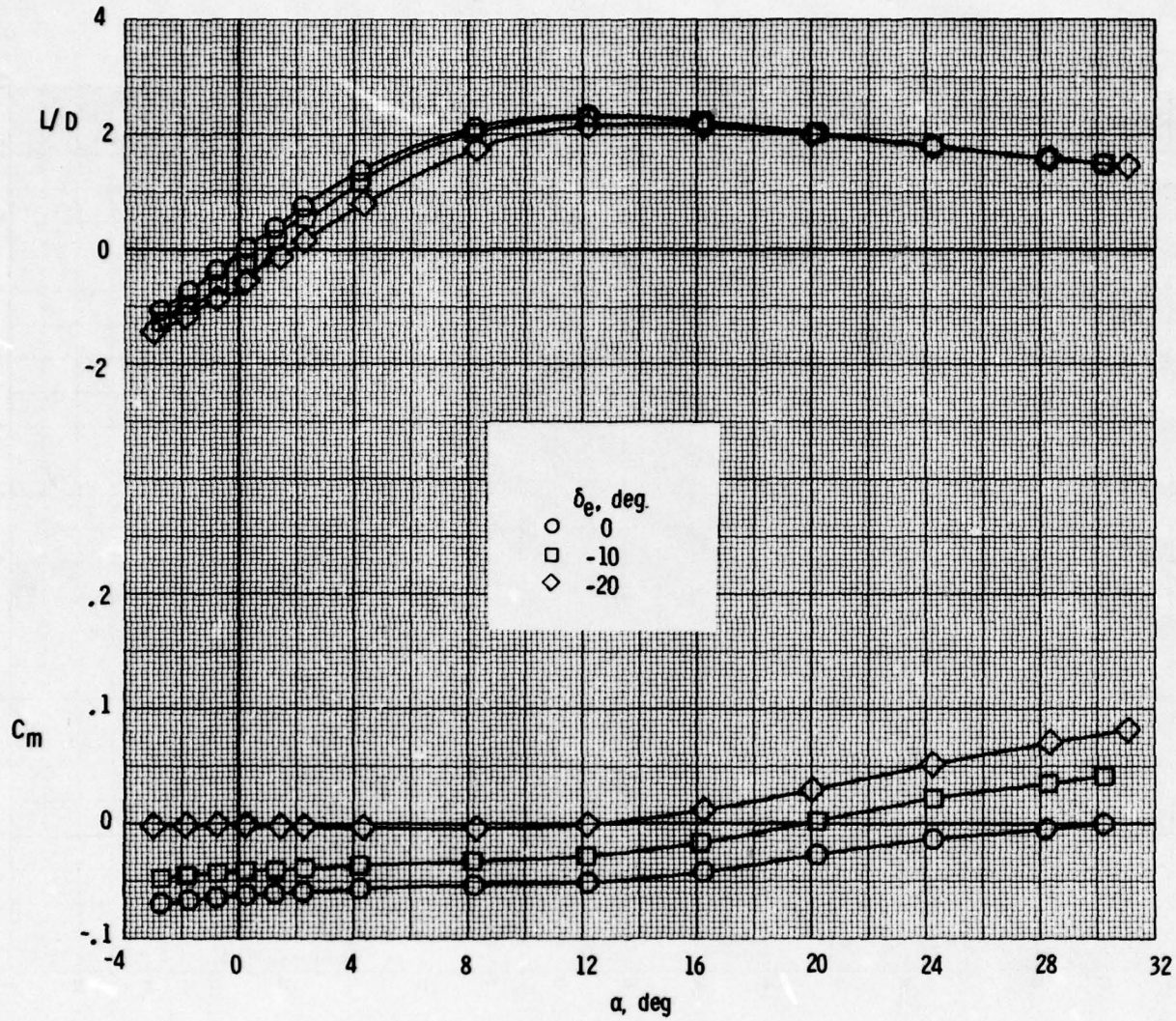

(e) Continued.

Figure 21.- Continued.

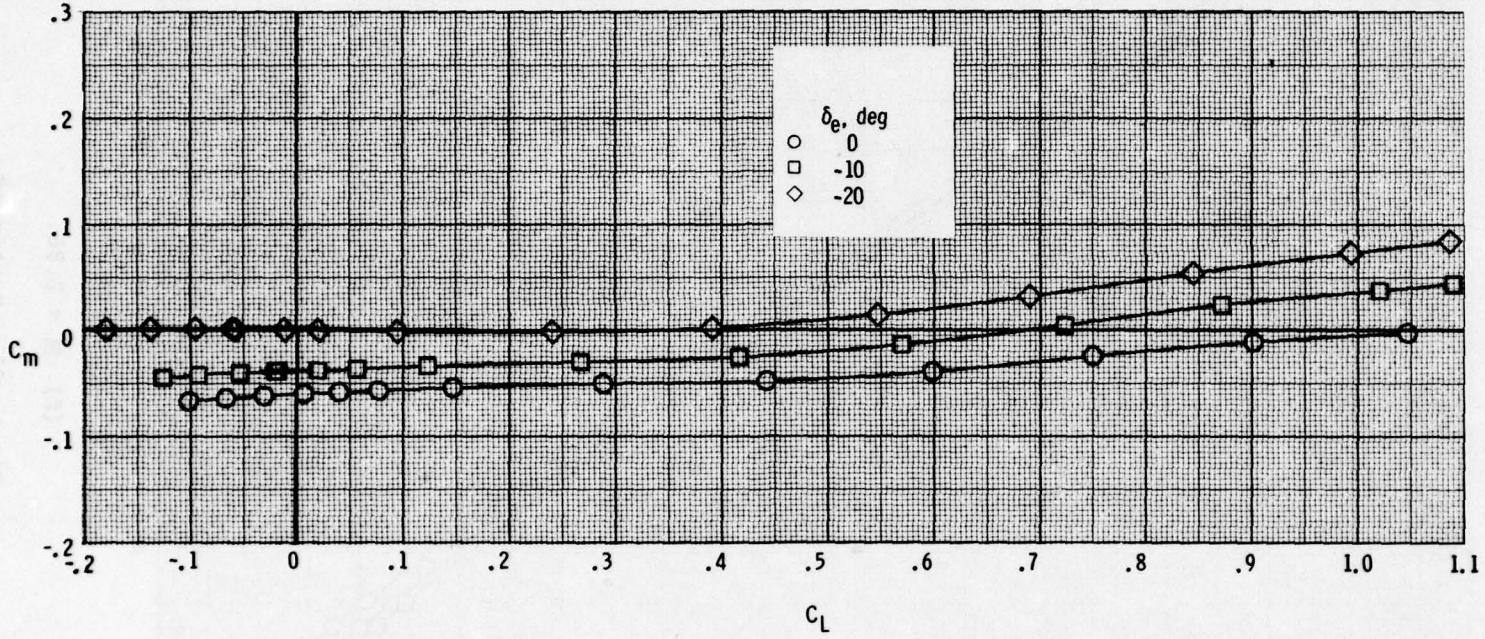

(e) Concluded.

Figure 21.- Continued.

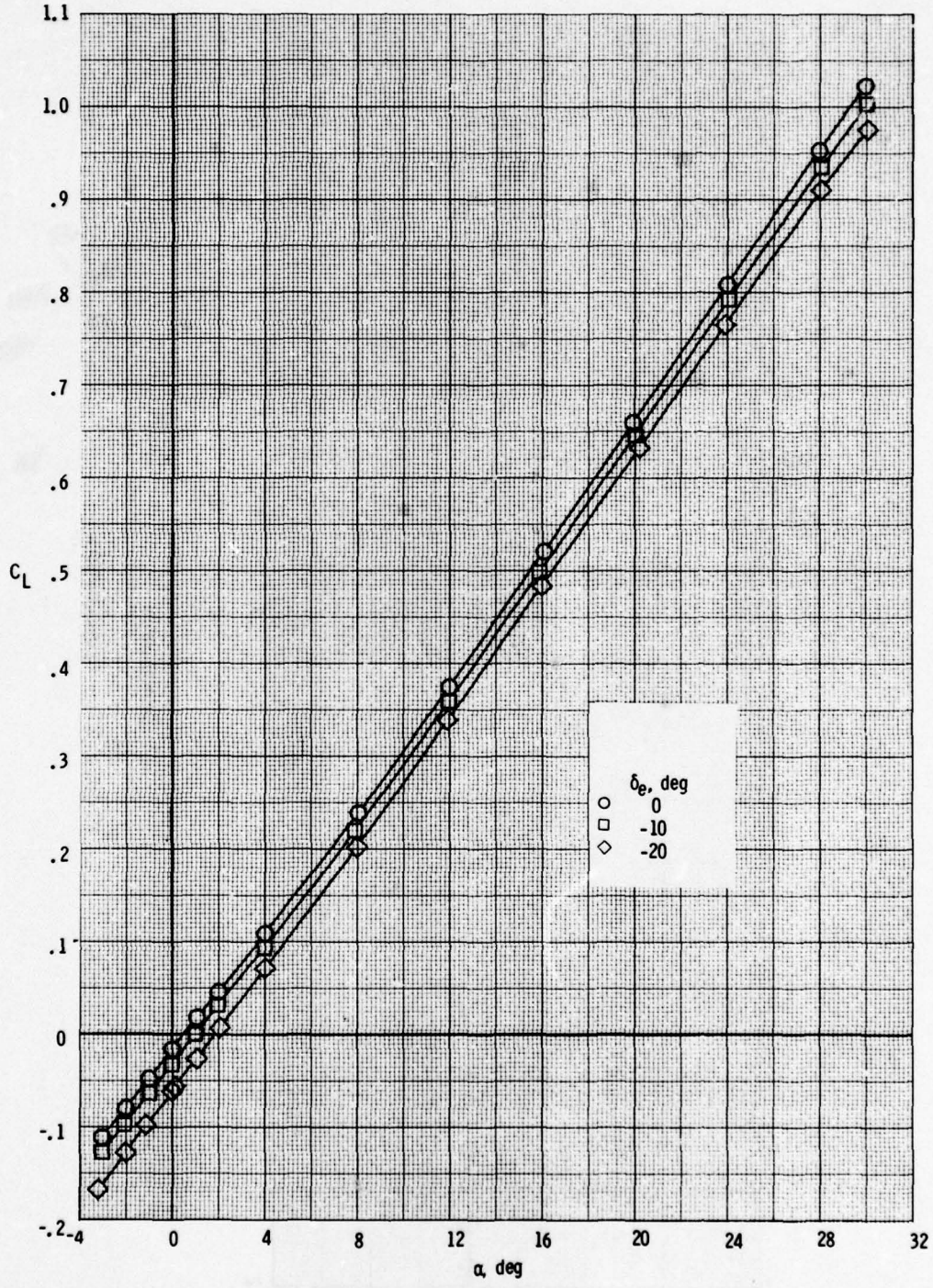

(f) M = 2.86.

Figure 21.- Continued.

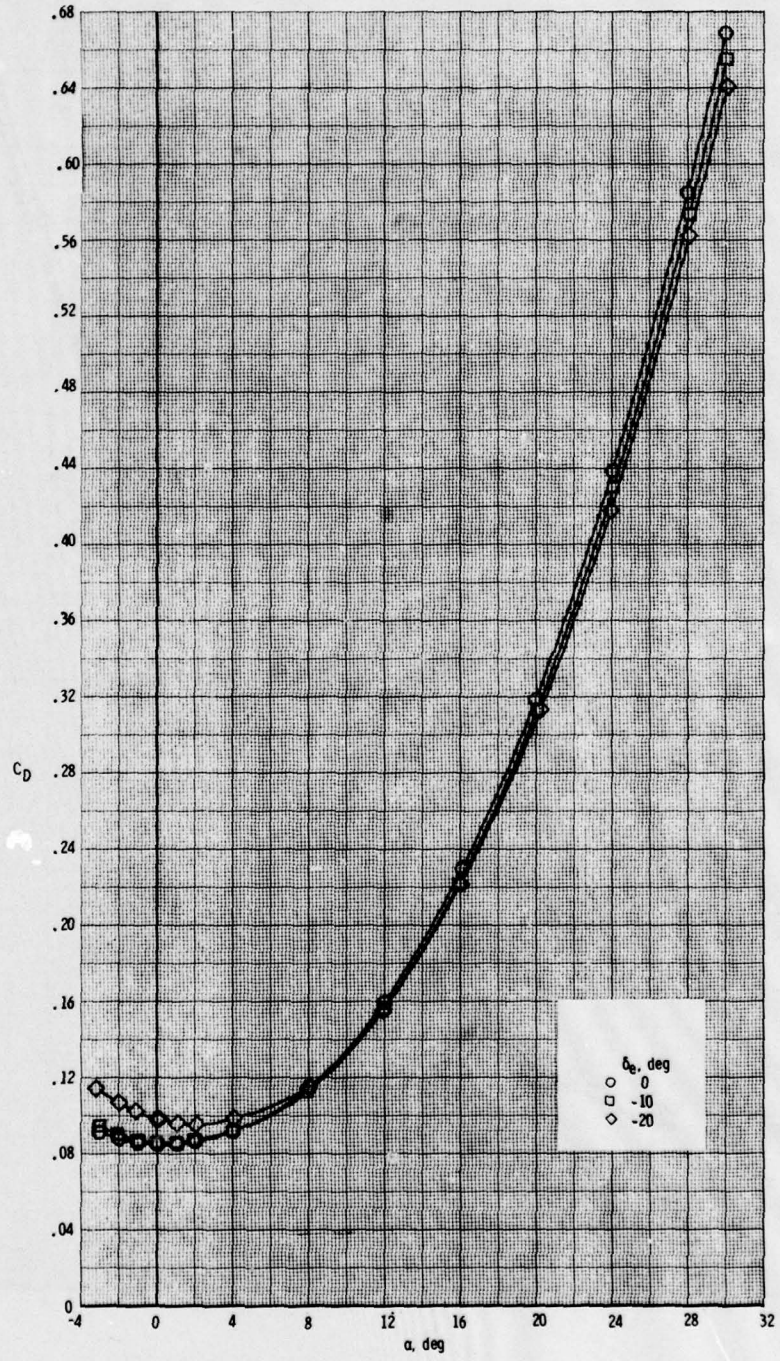

(f) Continued.

Figure 21.- Continued.

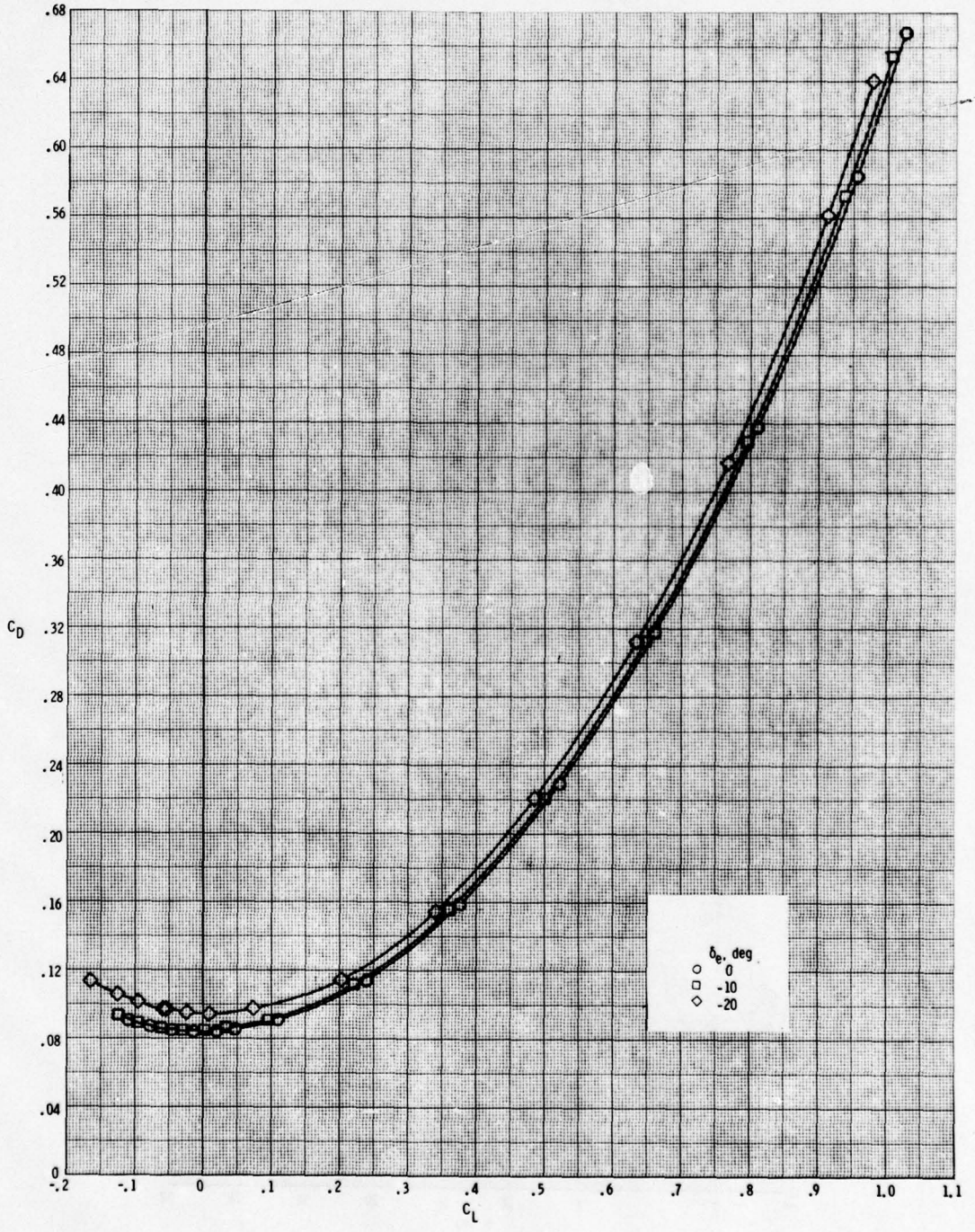

(f) Continued.

Figure 21.- Continued.

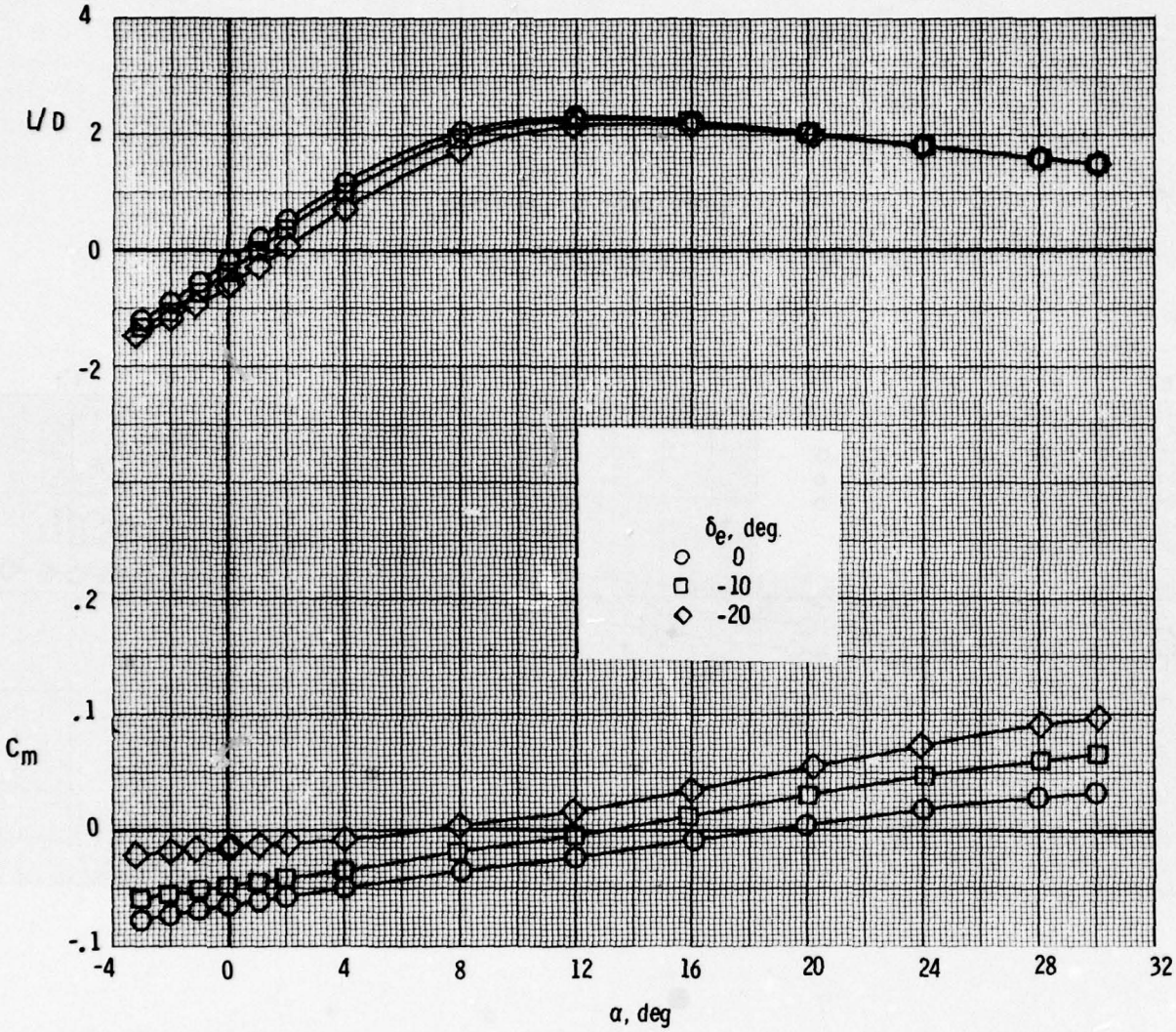

(f) Continued.

Figure 21.- Continued.

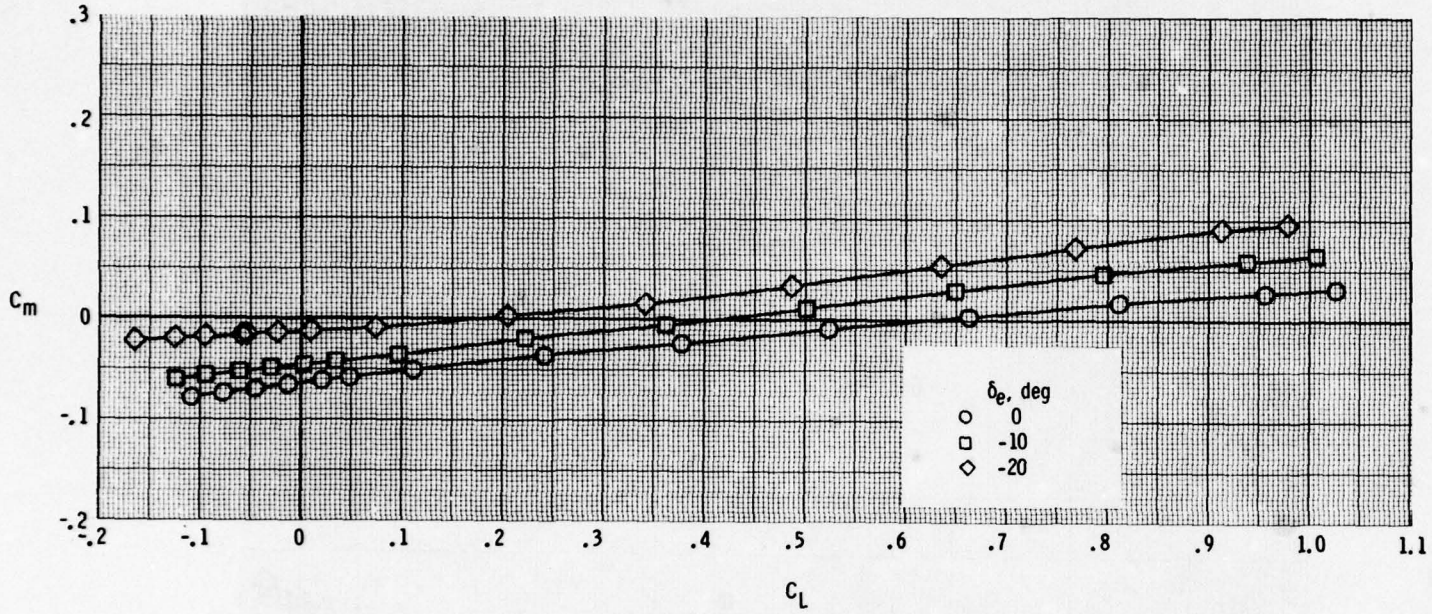

(f) Concluded.

Figure 21.- Continued.

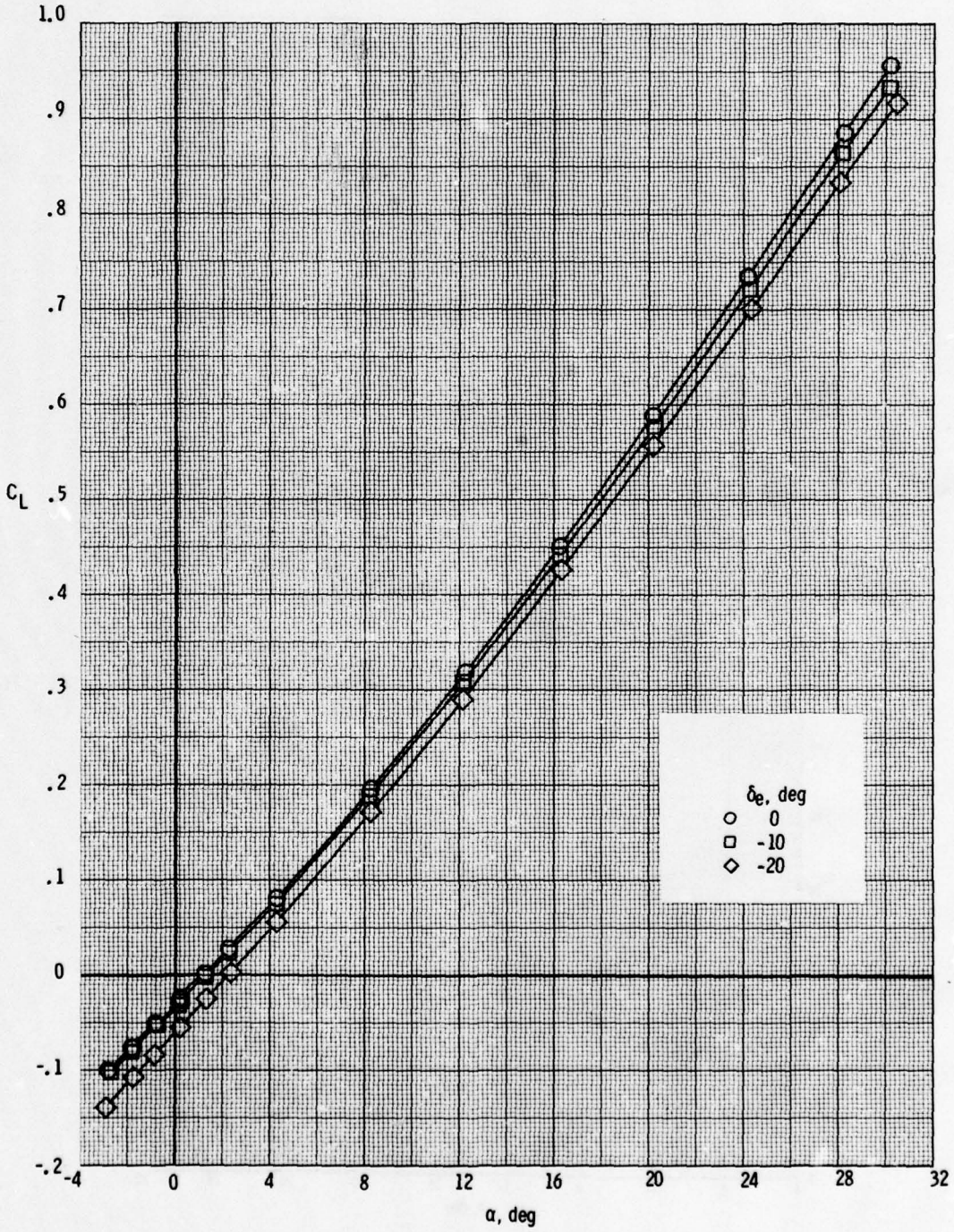

(g) M = 3.95.

Figure 21.- Continued.

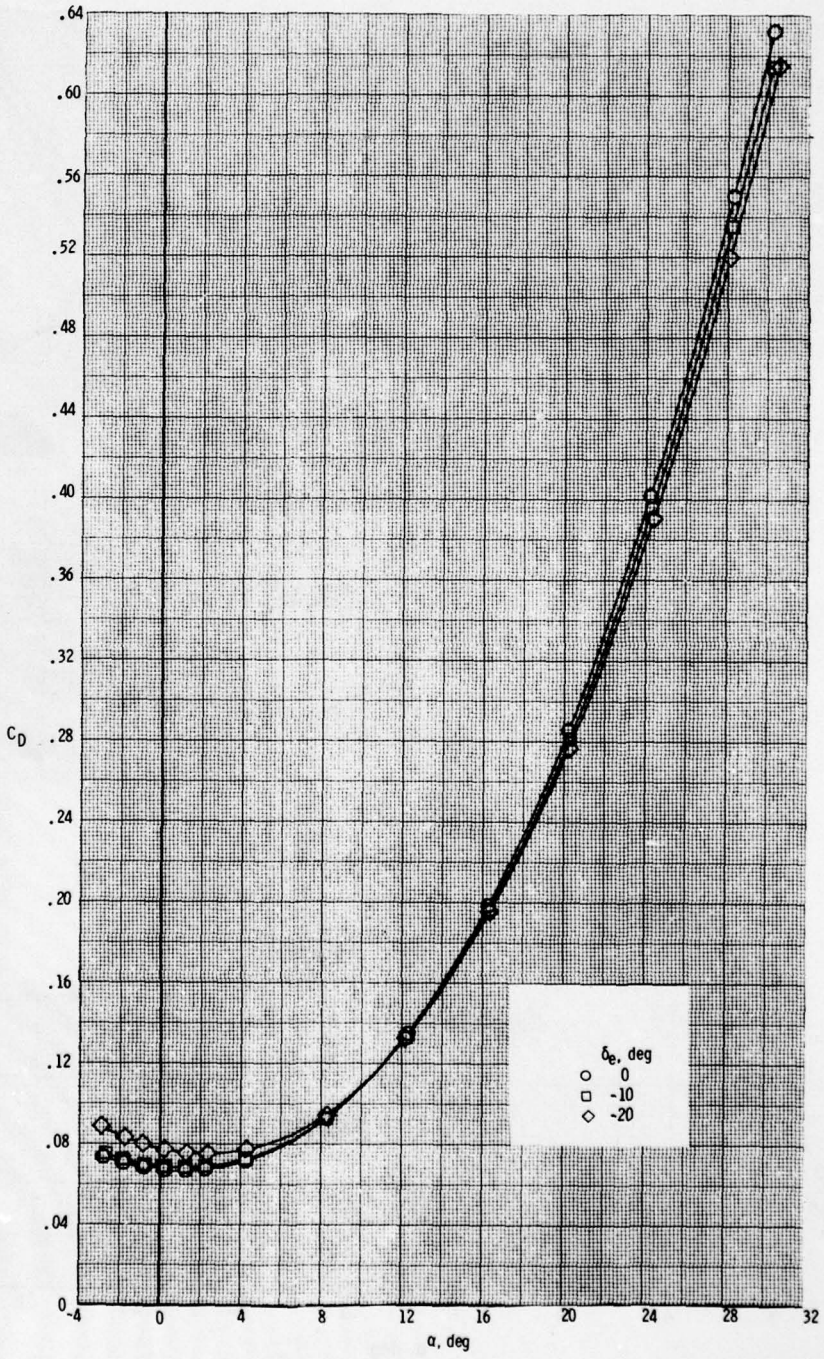

(g) Continued.

Figure 21.- Continued.

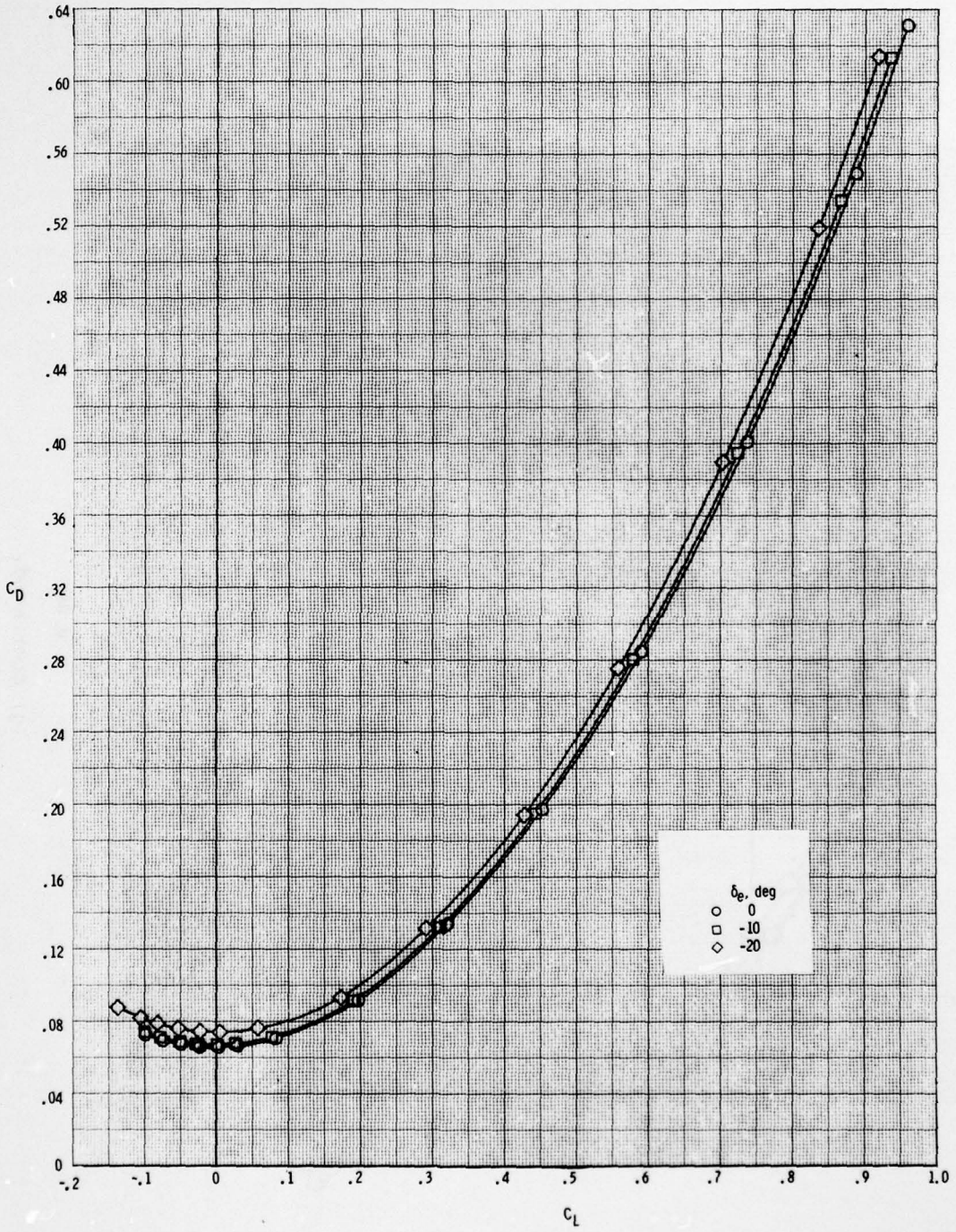

(g) Continued.

Figure 21.- Continued.

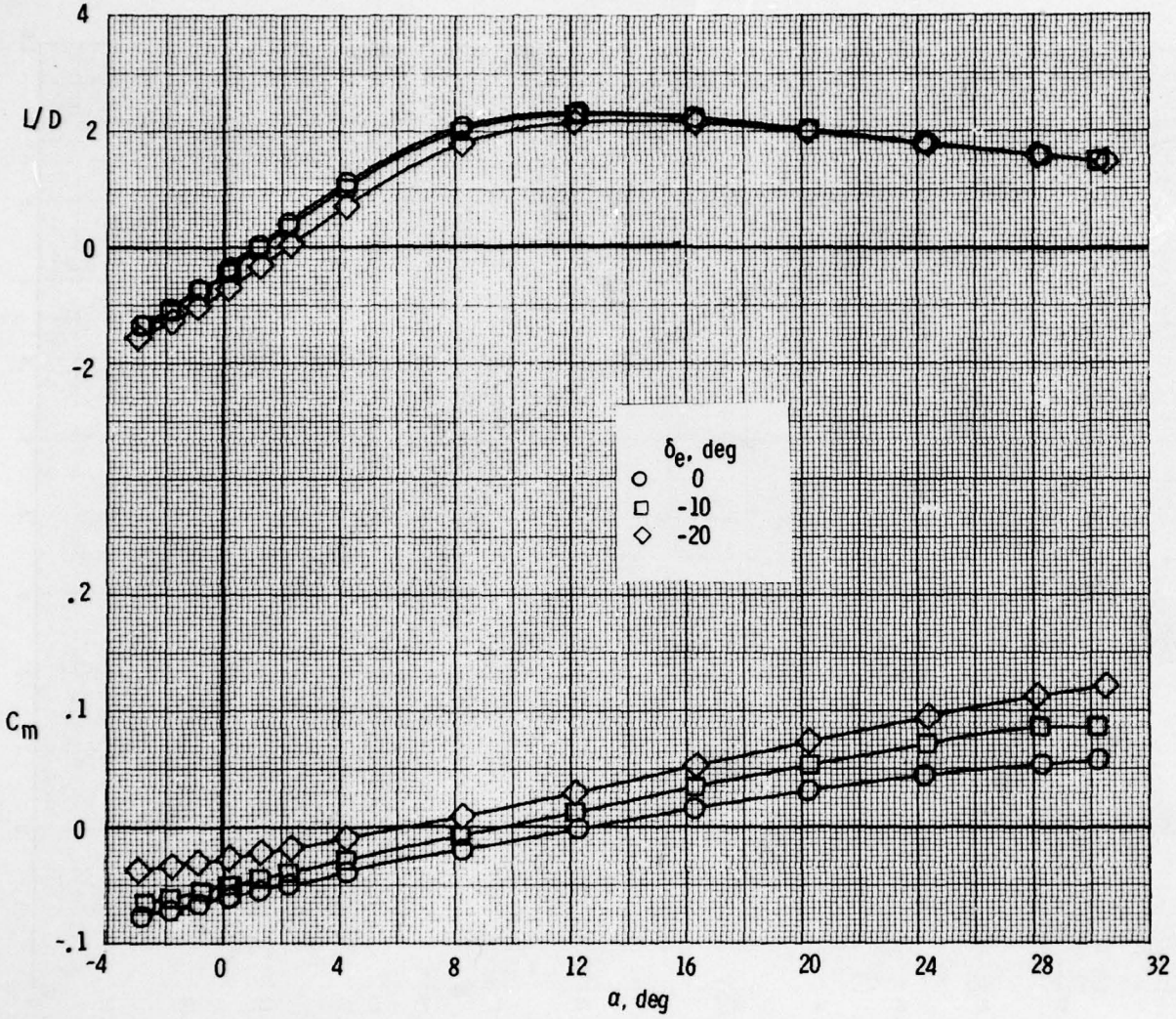

(g) Continued.

Figure 21.- Continued.

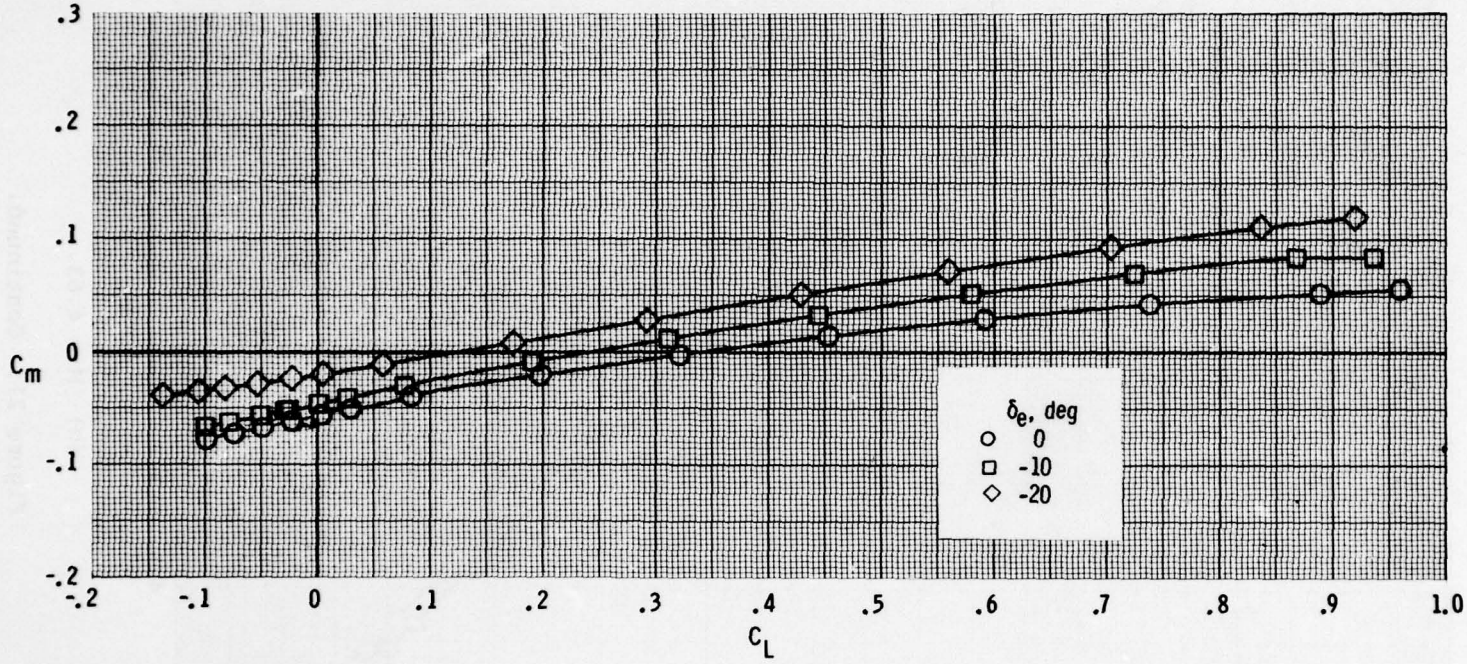

(g) Concluded.

Figure 21.- Continued.

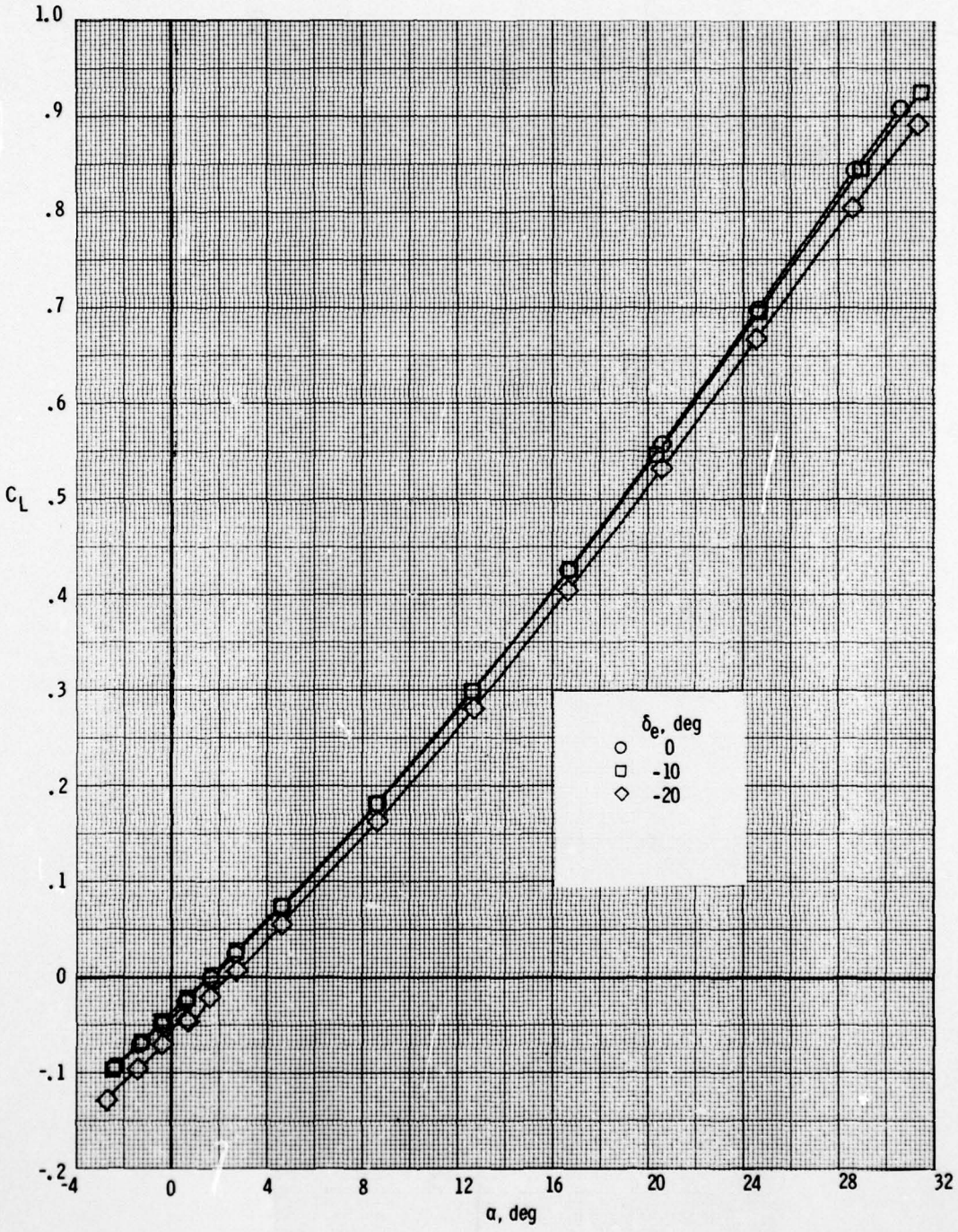

(h) M = 4.63.

Figure 21.- Continued.

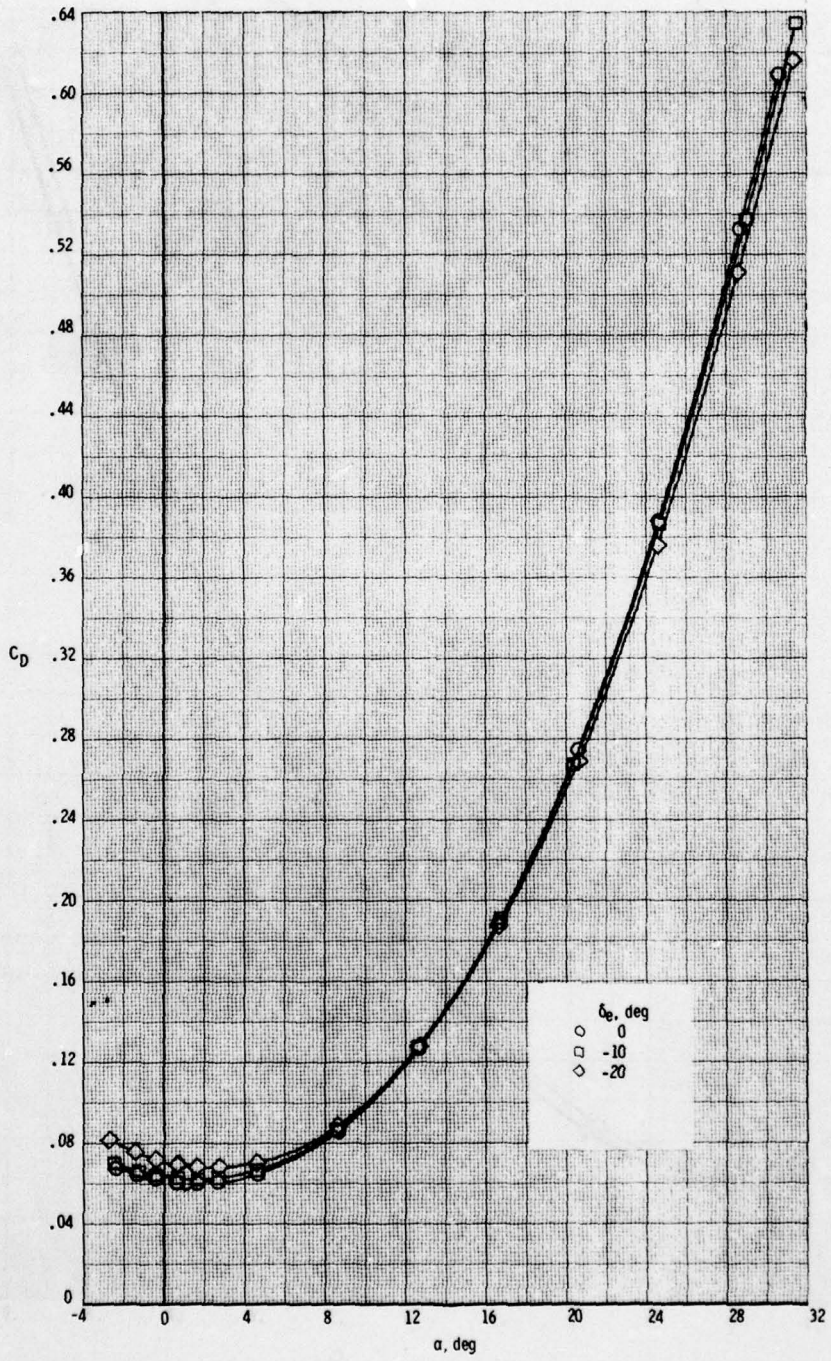

(h) Continued.

Figure 21.- Continued.

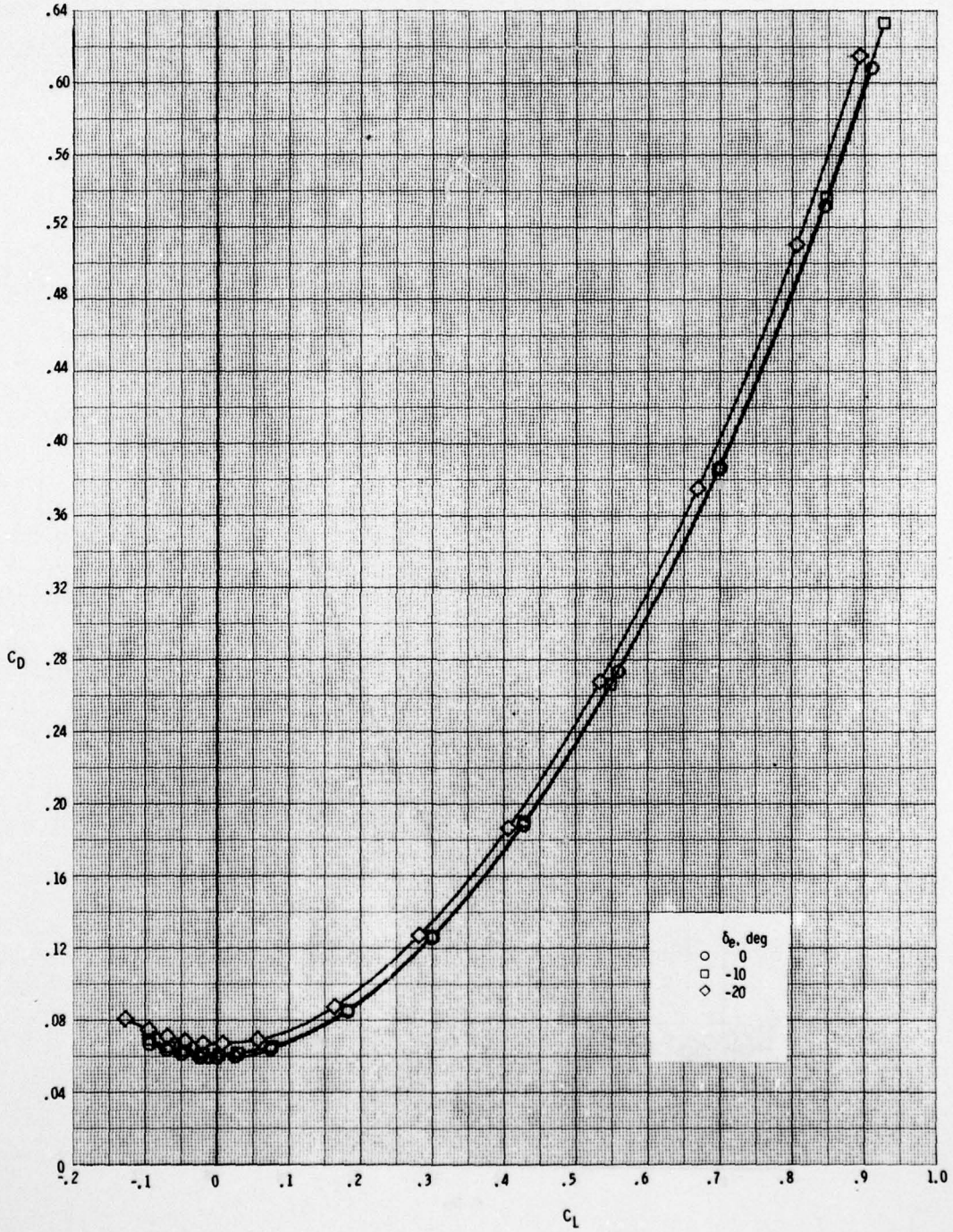

(h) Continued.

Figure 21.- Continued.

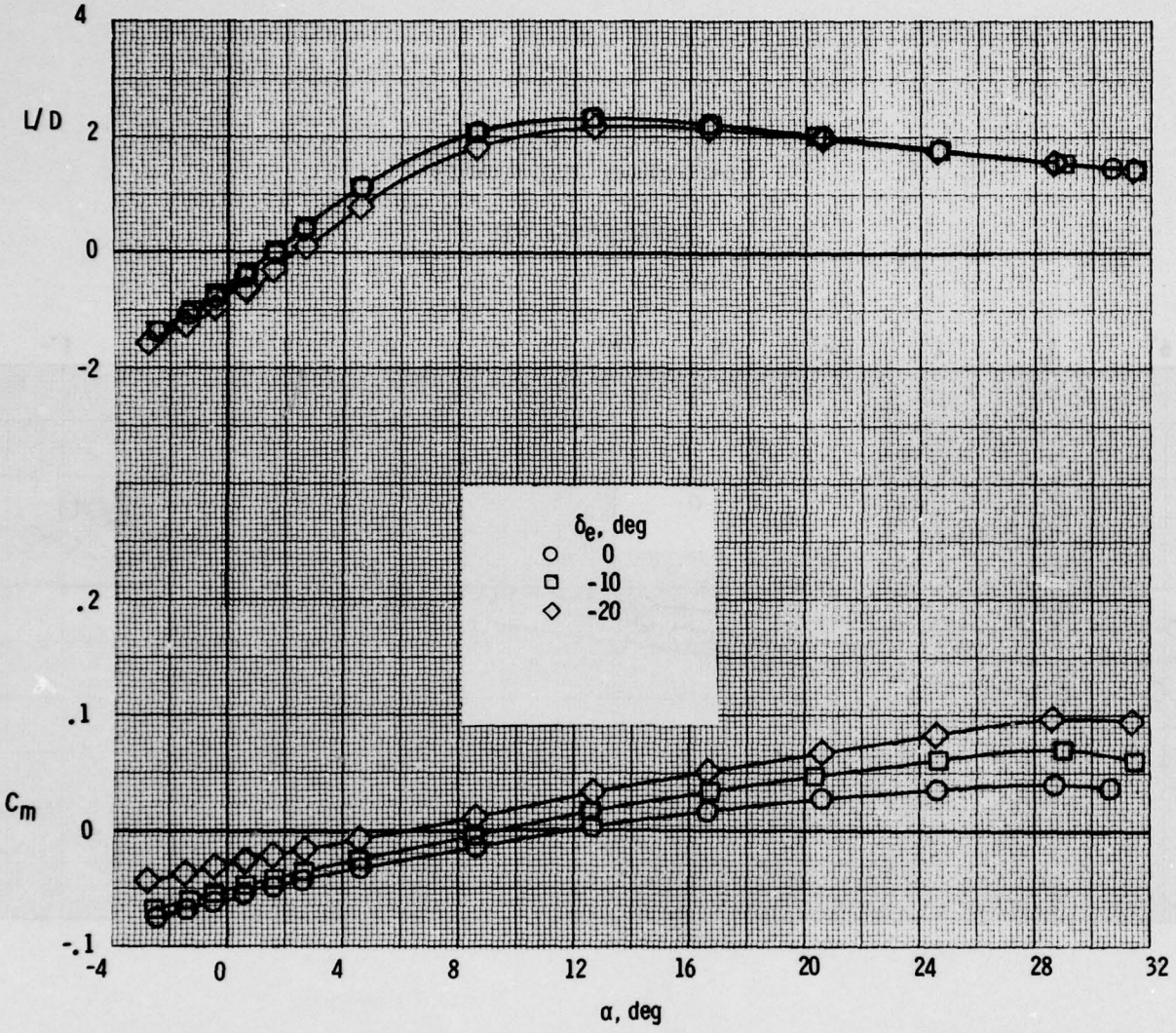

(h) Continued.

Figure 21.- Continued.

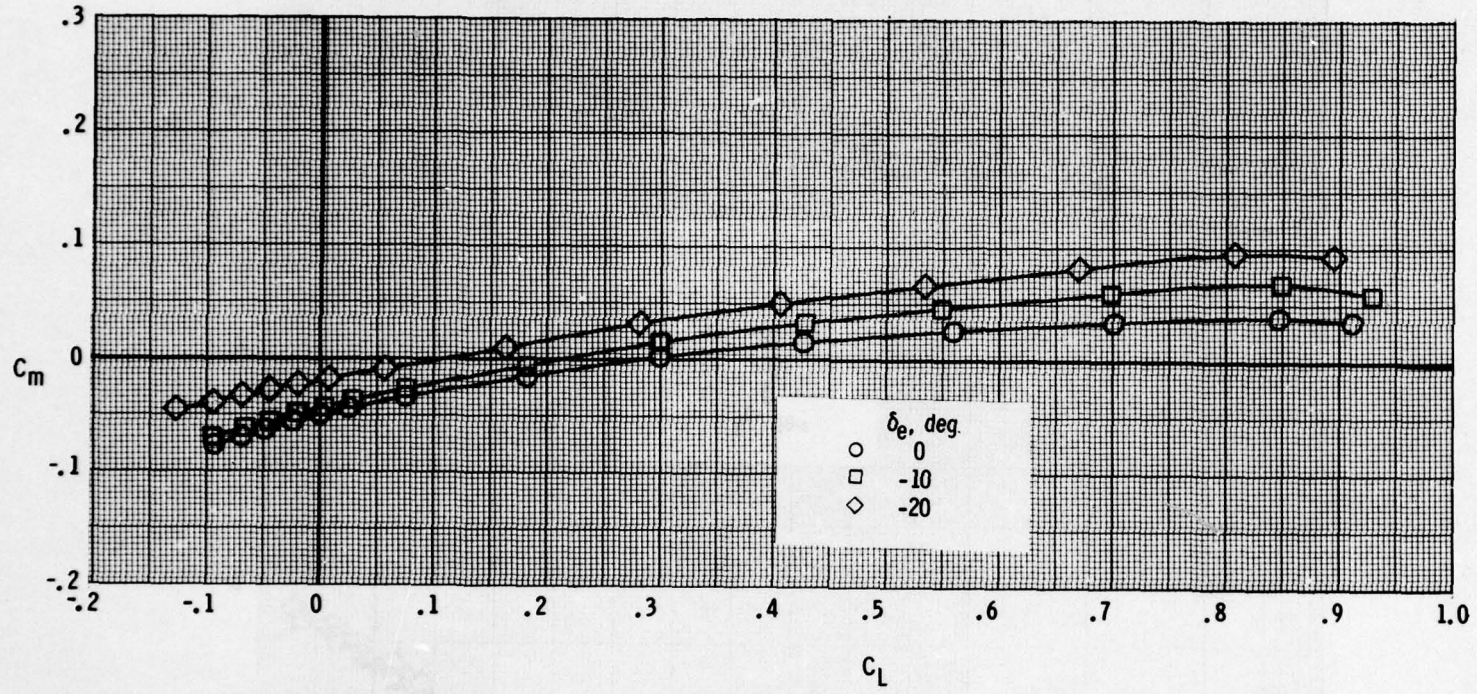

(h) Concluded.

Figure 21.- Concluded.

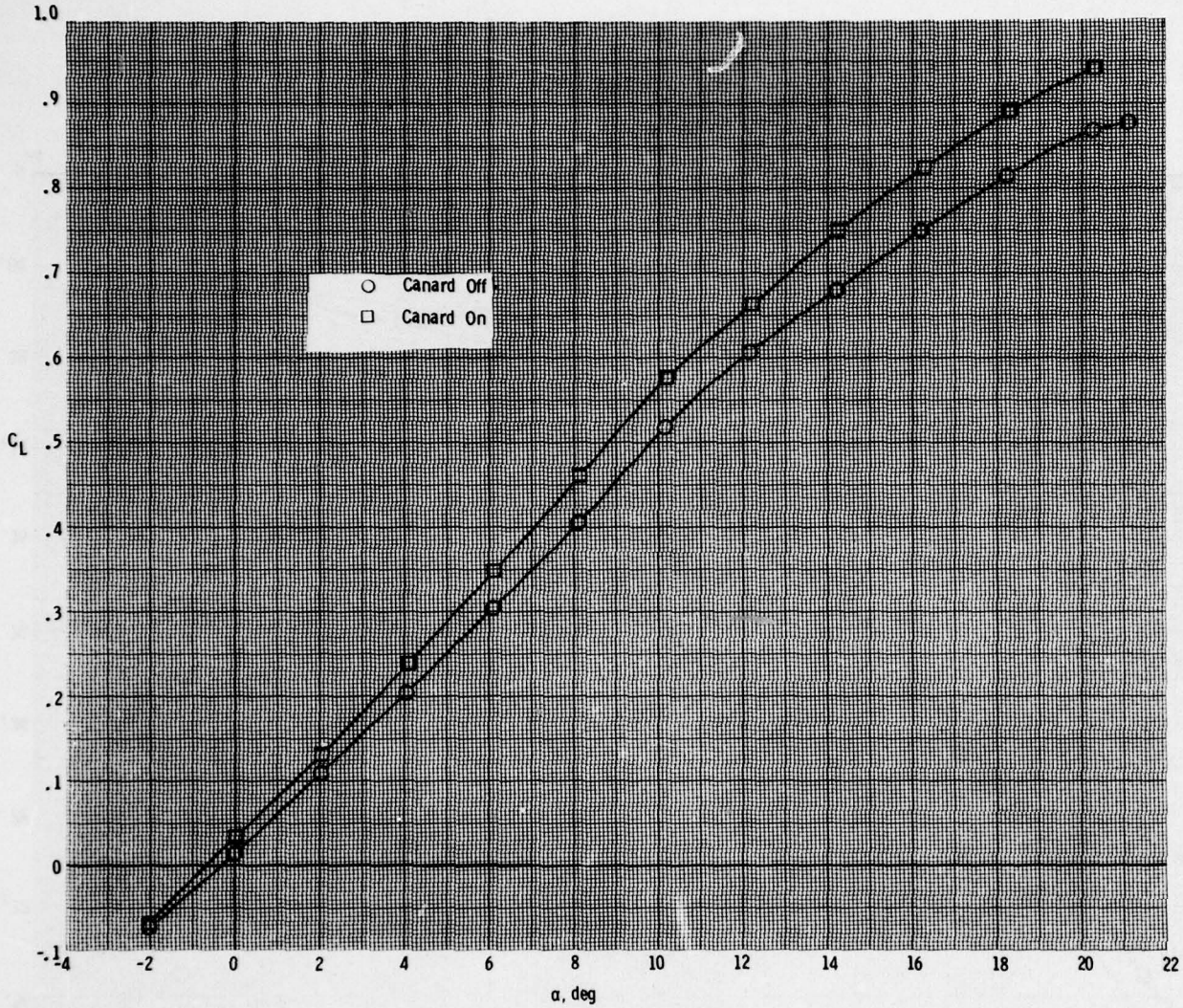

(a) C_L versus α.

Figure 22.- Effect of canard on longitudinal aerodynamic characteristics of CCV model. M = 0.3; $\delta_e = 0^o$; $\delta_F = 0^o$.

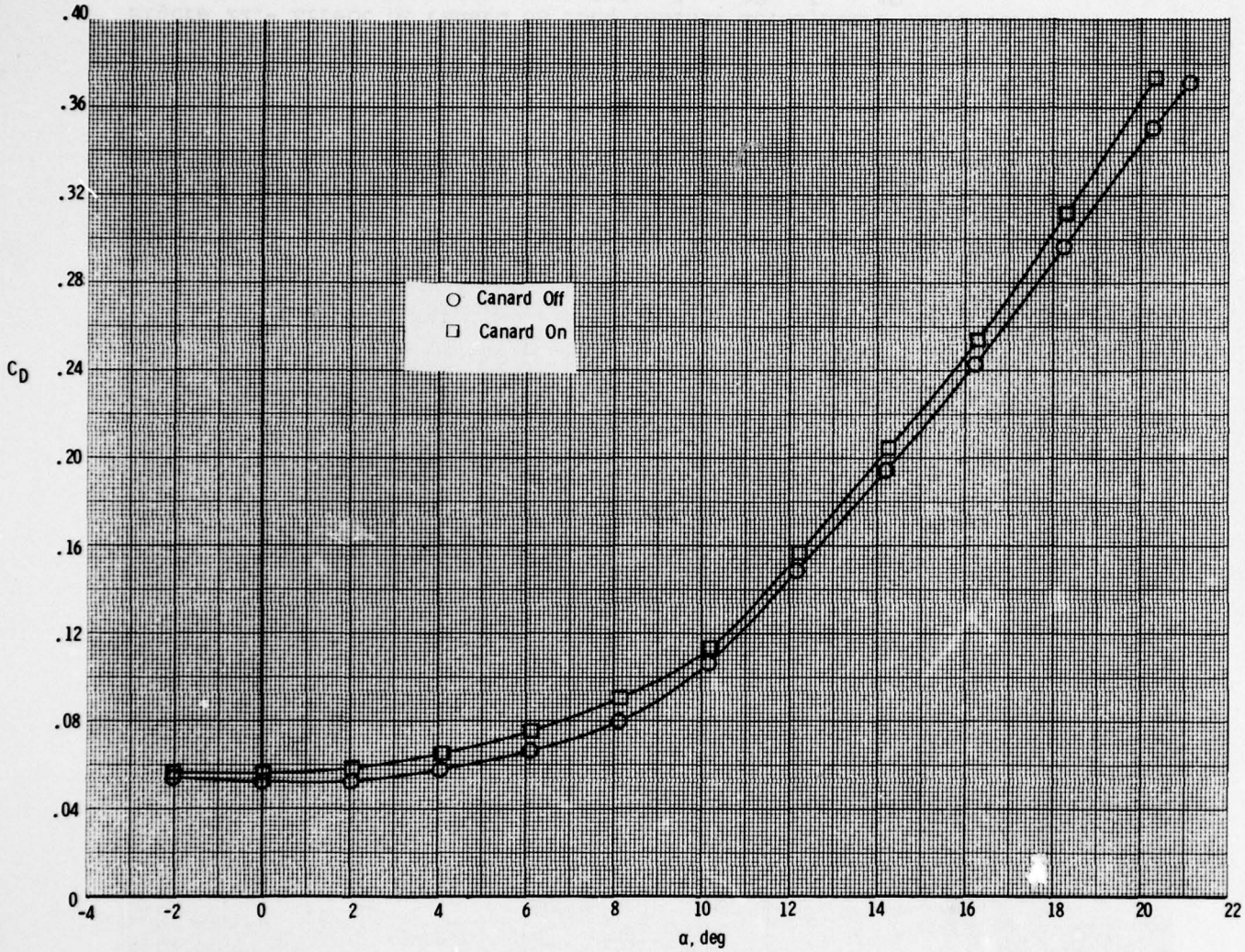

(b) C_D versus α.

Figure 22.- Continued.

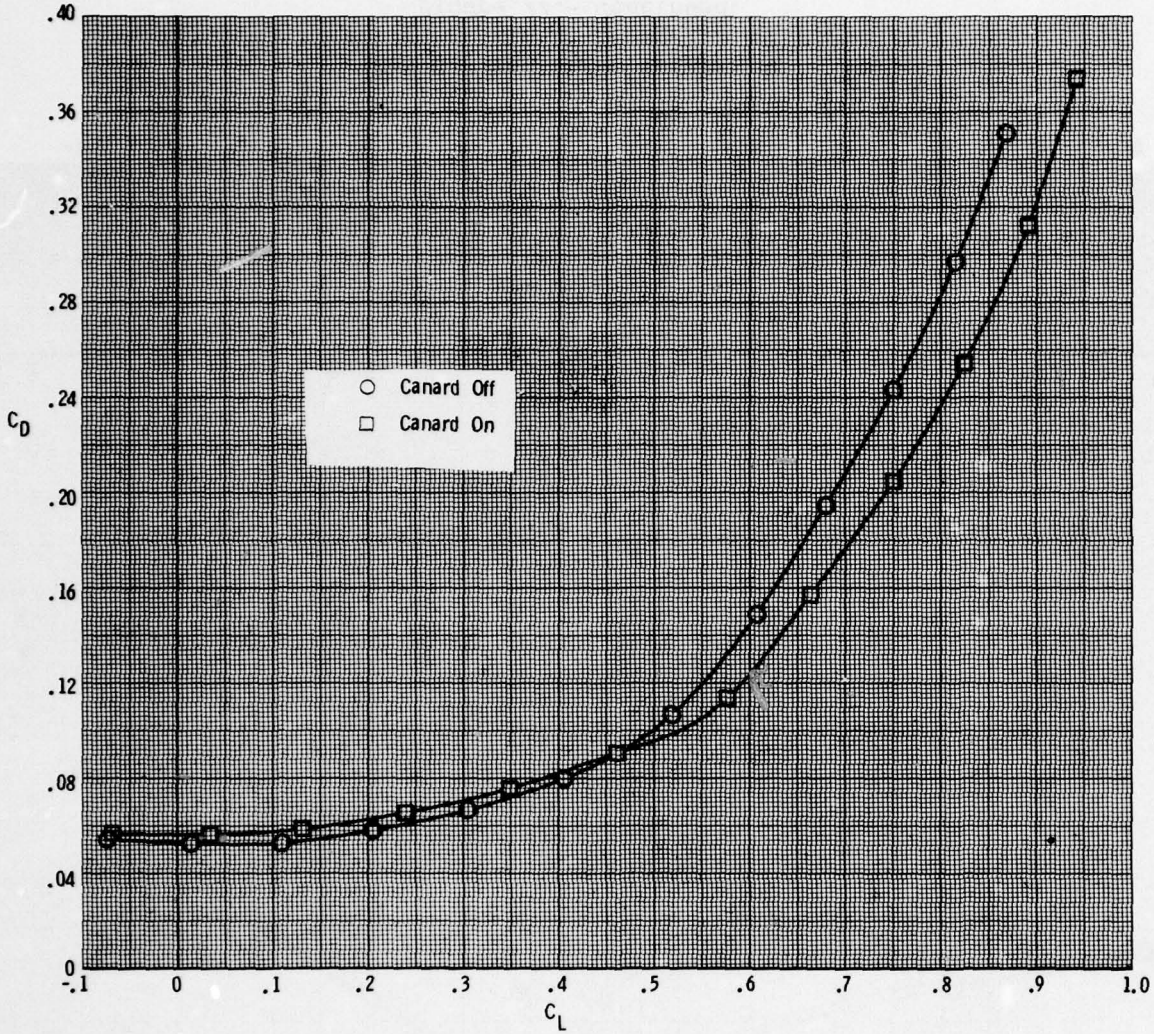

(c) C_D versus C_L.

Figure 22.- Continued.

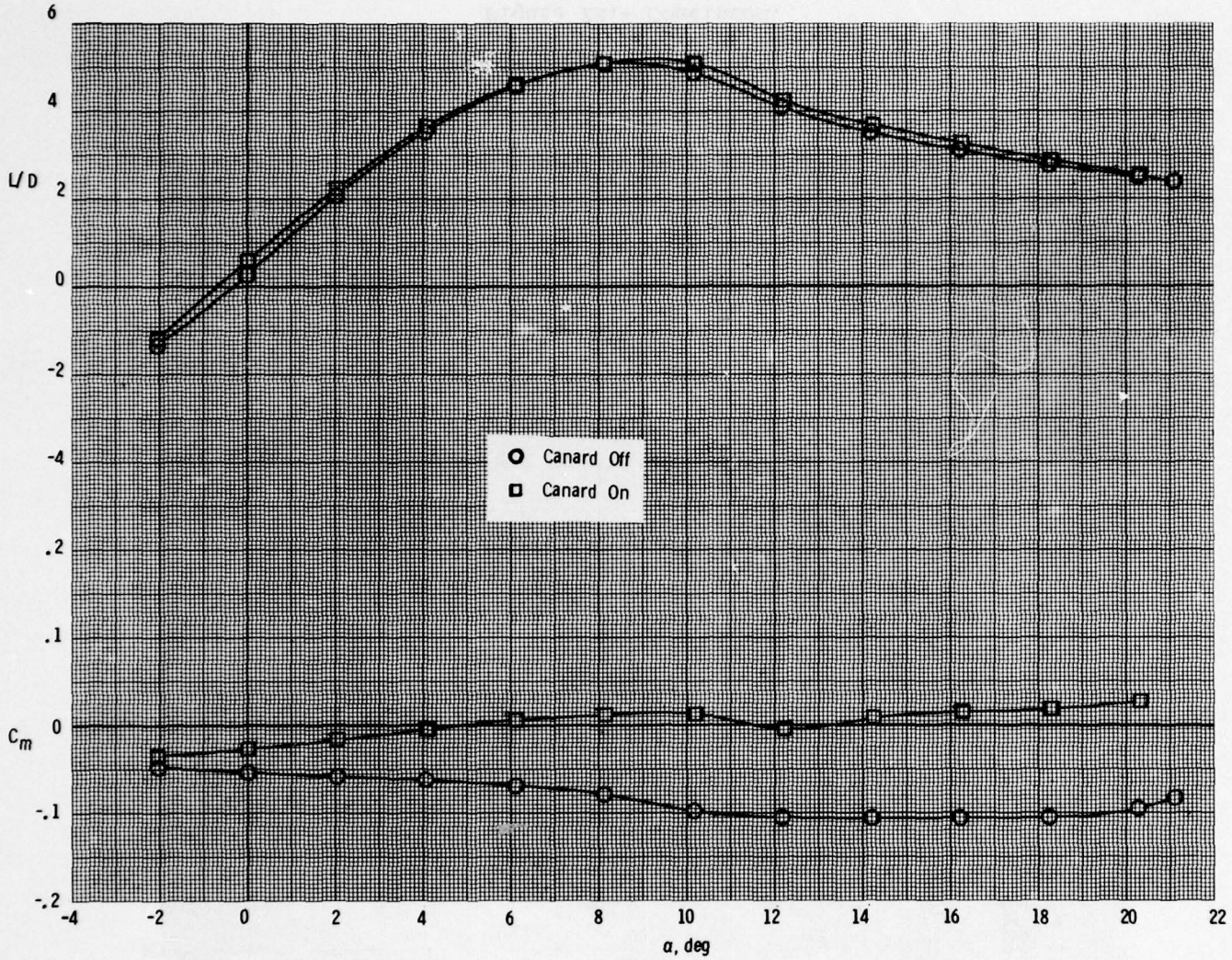

(d) C_m and L/D versus α.

Figure 22.- Continued.

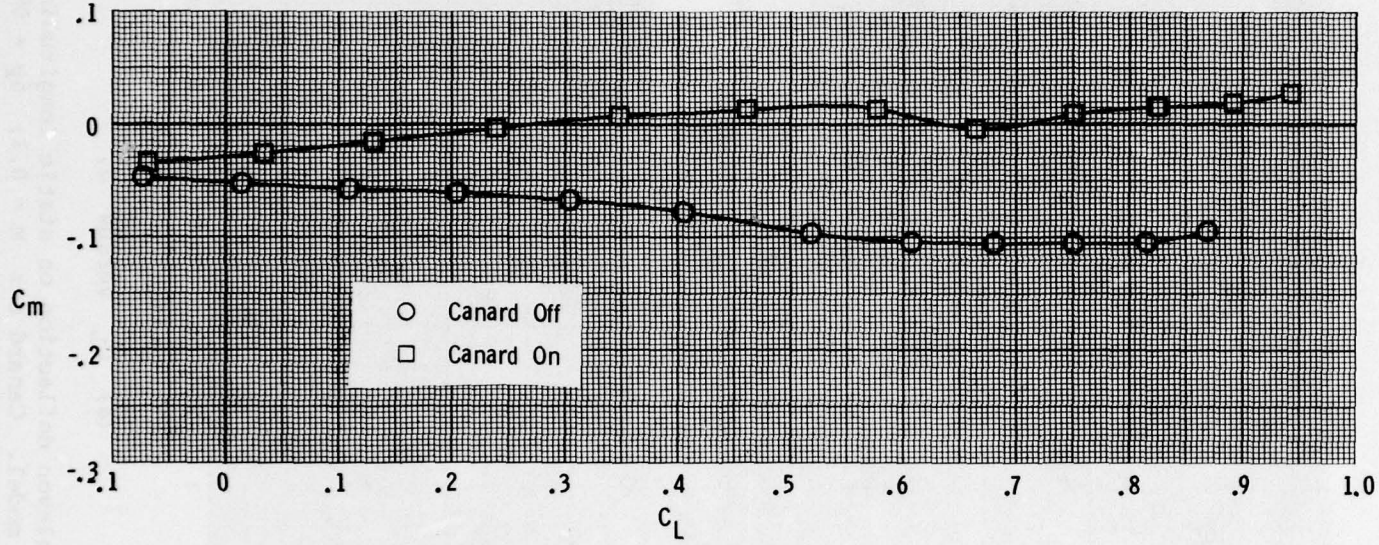

(e) C_m versus C_L.

Figure 22.- Concluded.

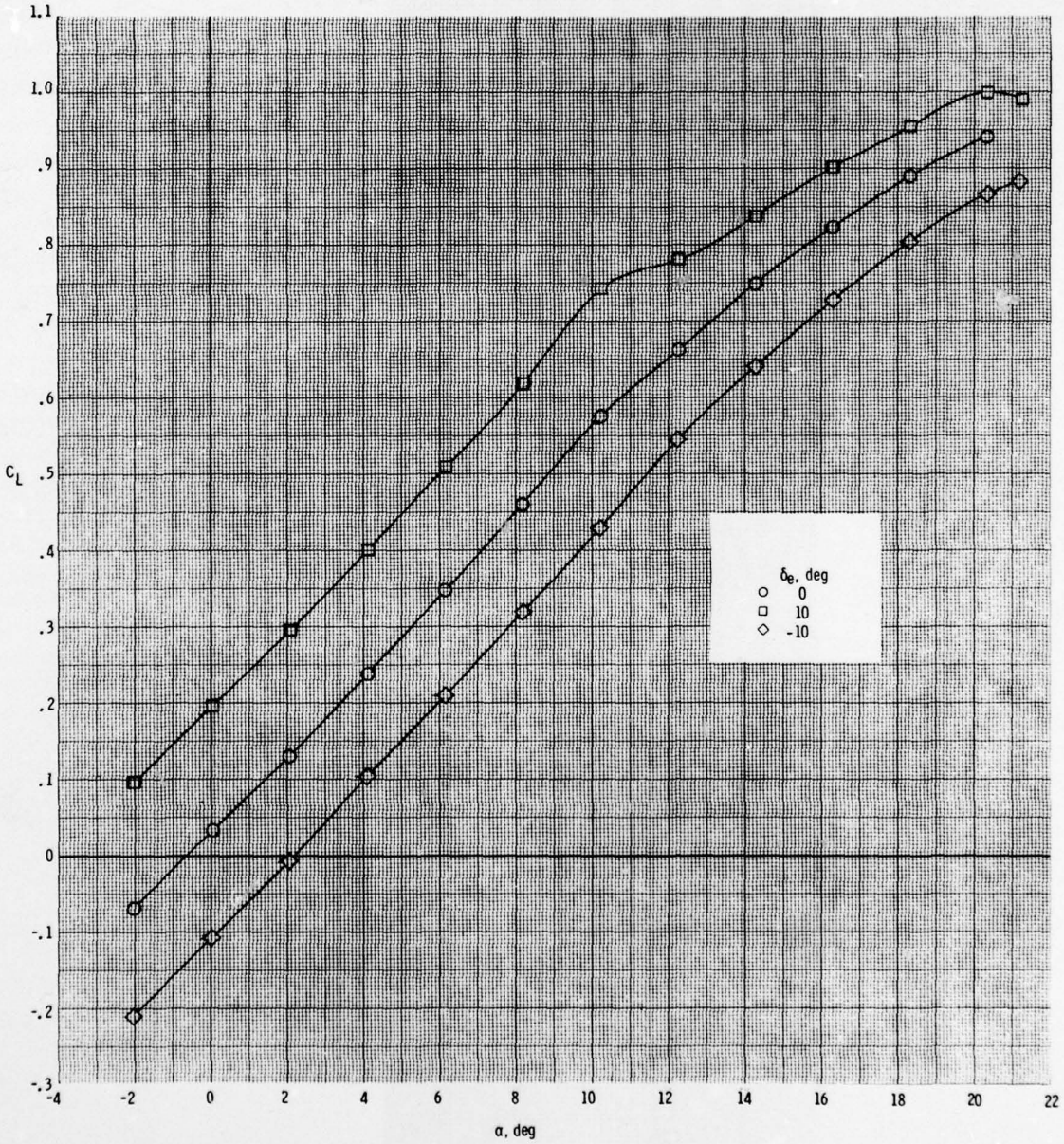

(a) C_L versus α.

Figure 23.- Effect of elevon deflection on static longitudinal characteristics of CCV model. Canard on; M = 0.3; $\delta_F = 0^o$.

AD-A078 615 NATIONAL AERONAUTICS AND SPACE ADMINISTRATION HAMPTO--ETC F/G 20/4
EFFECTS OF RELAXED STATIC LONGITUDINAL STABILITY ON A SINGLE-ST--ETC(U)
DEC 79 D C FREEMAN, A W WILHITE

UNCLASSIFIED NASA-L-13243 NASA-TP-1594 NL

2 OF 2
ADA
078615

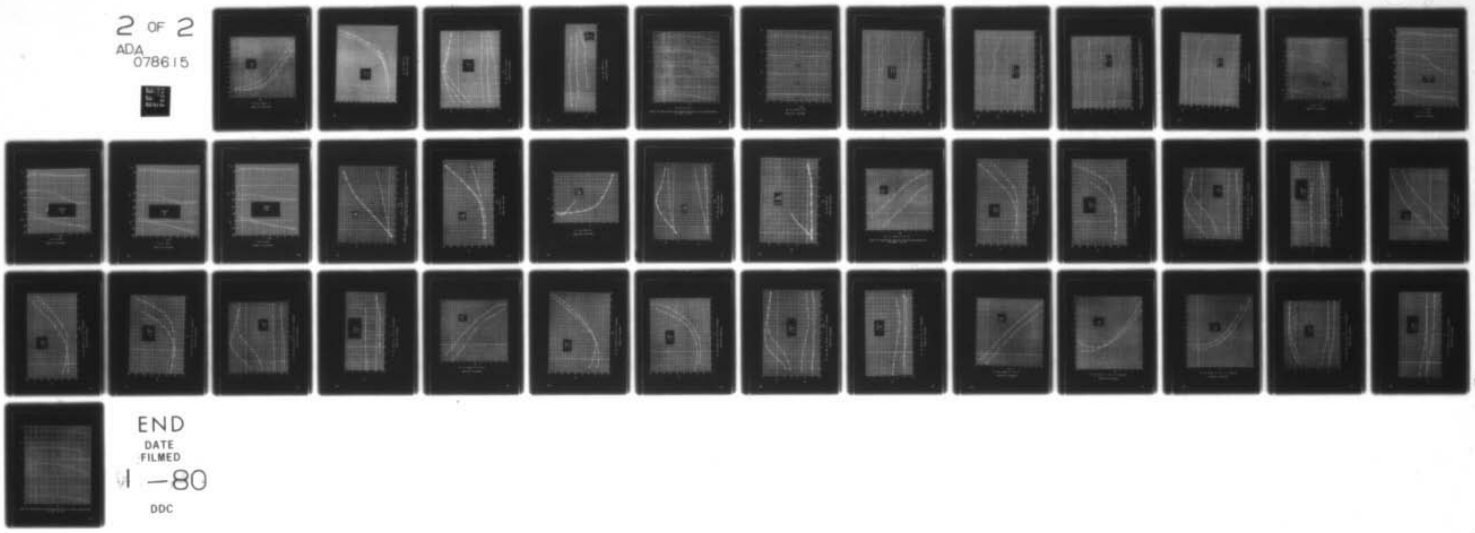

END
DATE
FILMED
1 -80
DDC

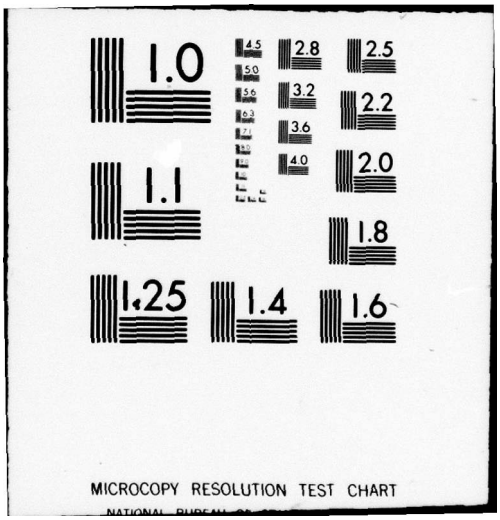
1.0
1.1
1.25
1.4
1.6
1.8
2.0
2.2
2.5
2.8
3.2
3.6
4.0
4.5
5.0
5.6
6.3
MICROCOPY RESOLUTION TEST CHART

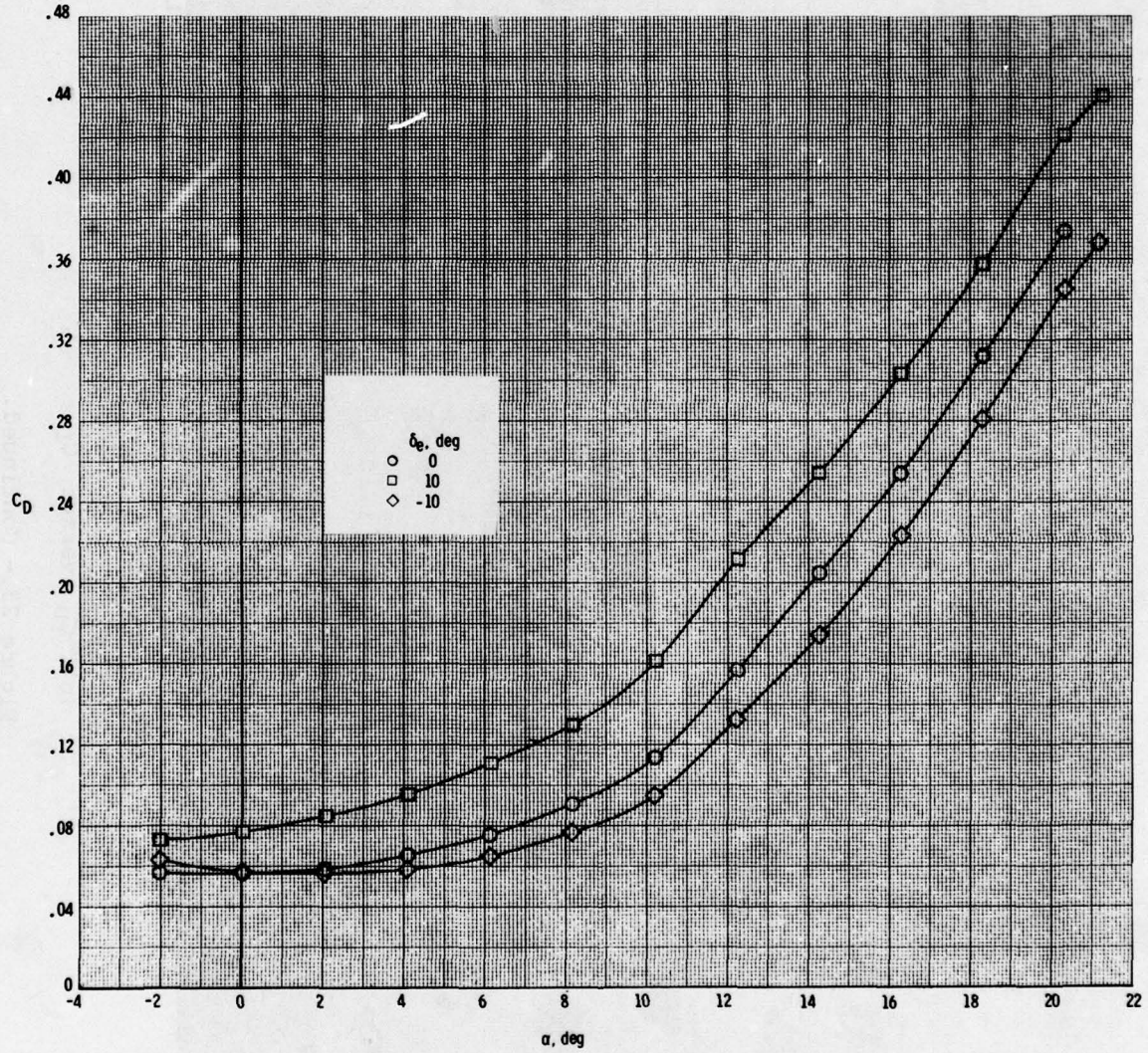

(b) C_D versus α.

Figure 23.- Continued.

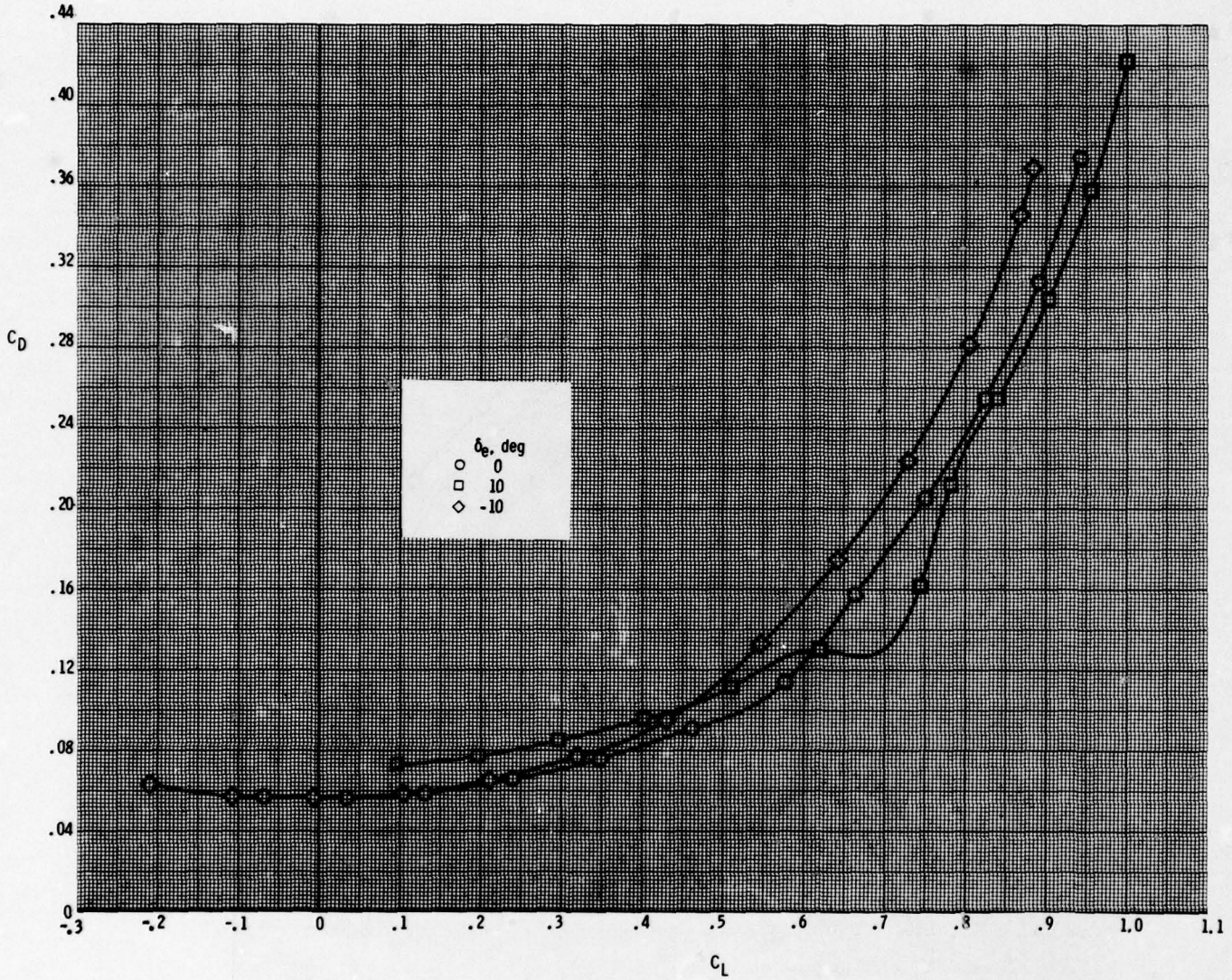

(c) C_D versus C_L.

Figure 23.- Continued.

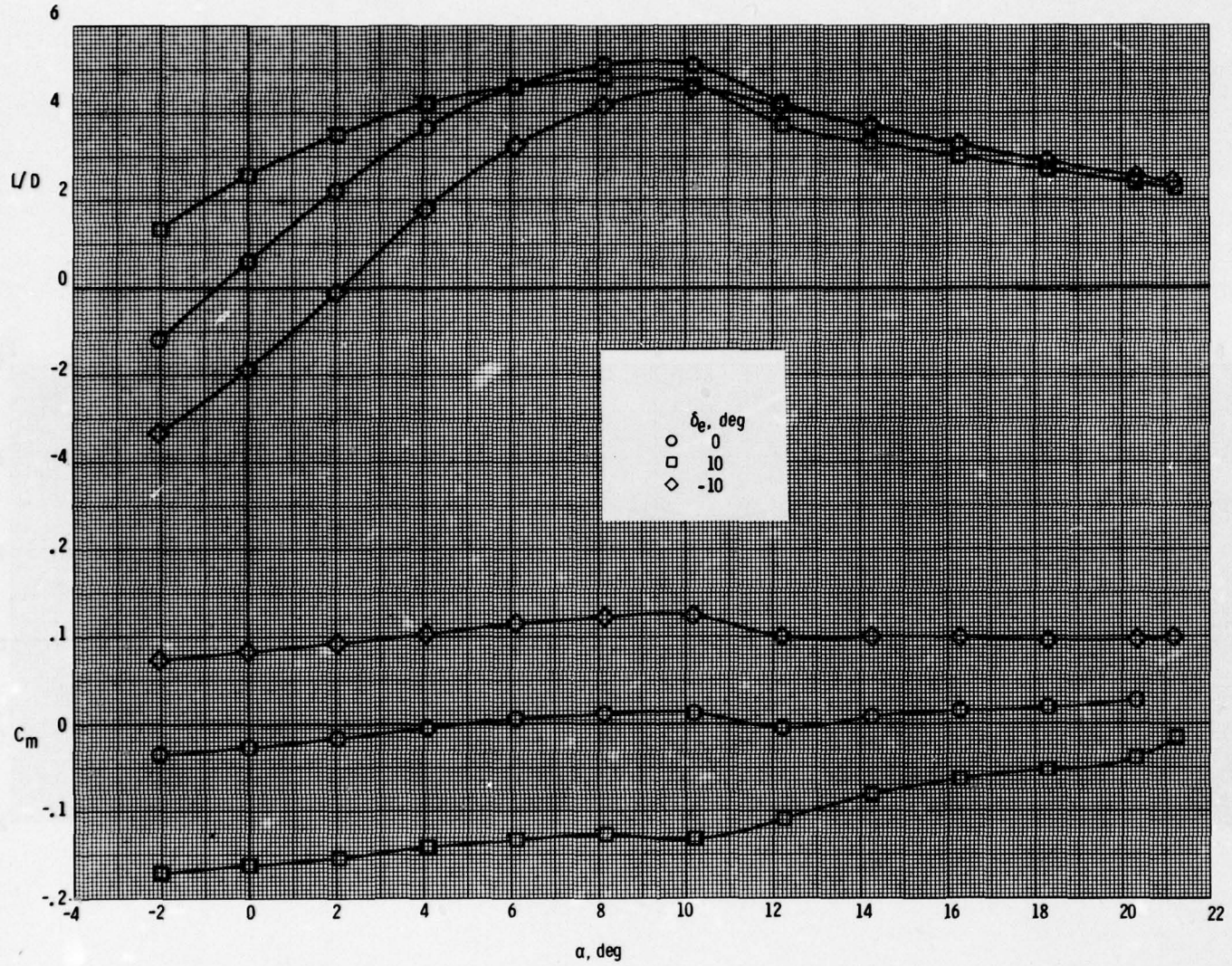

(d) C_m and L/D versus α.

Figure 23.- Continued.

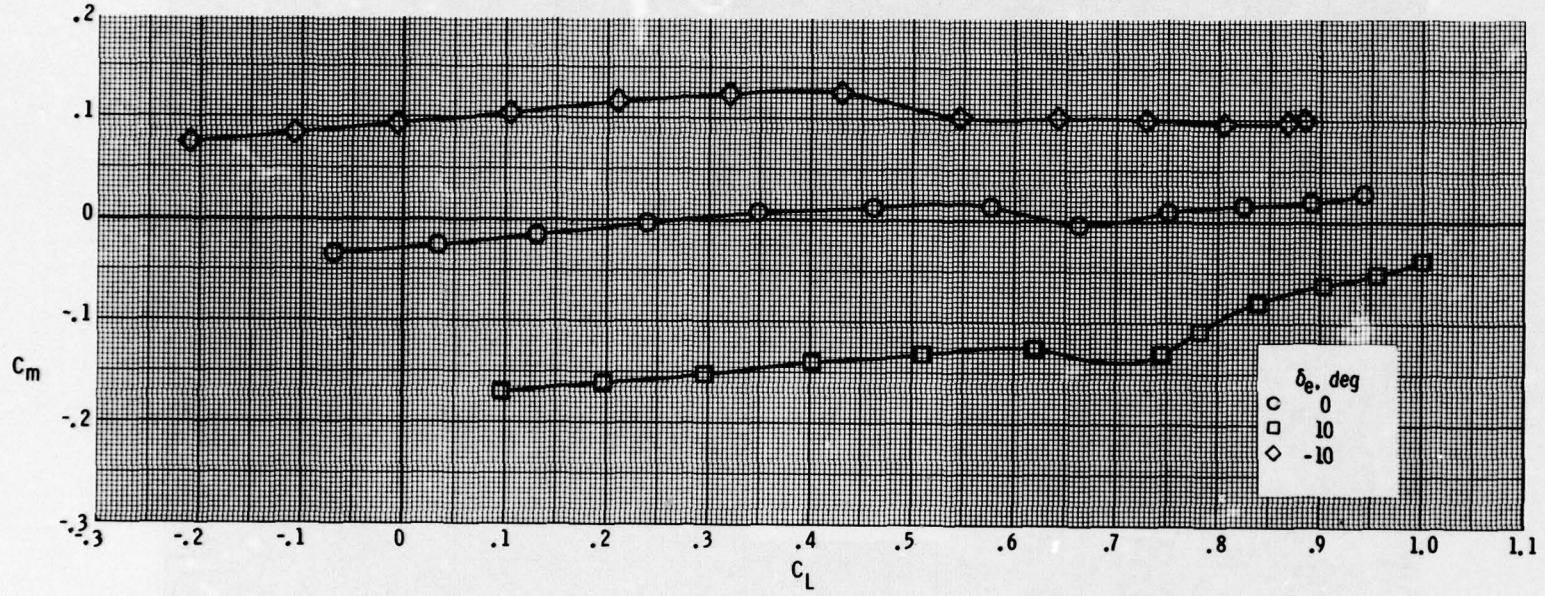

(e) C_m versus C_L.

Figure 23.- Concluded.

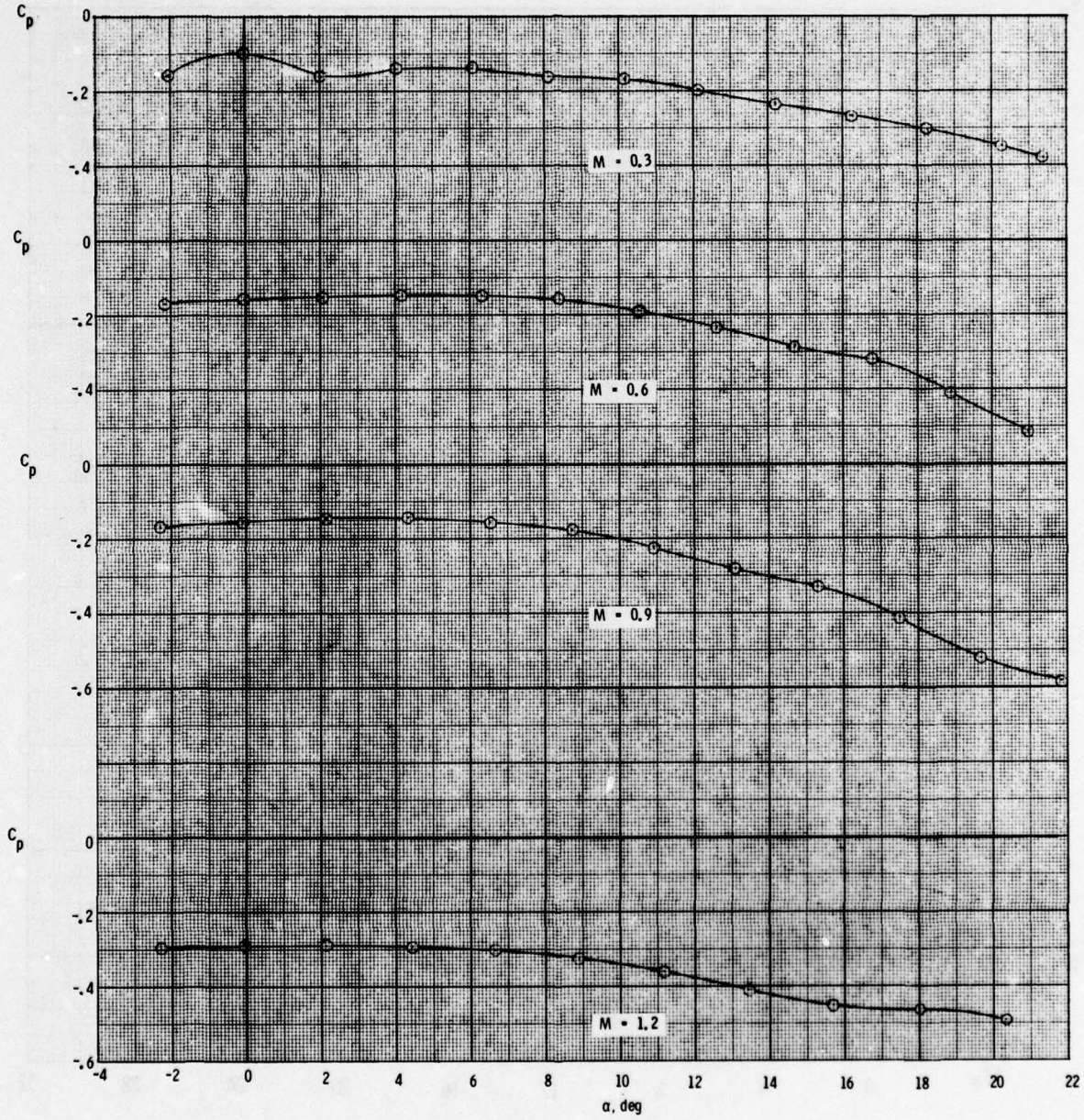

(a) M = 0.3 to 1.2.

Figure 24.- Base pressure data measured during tests of CCV configuration. $\delta_e = 0^o$; $\delta_F = 0^o$.

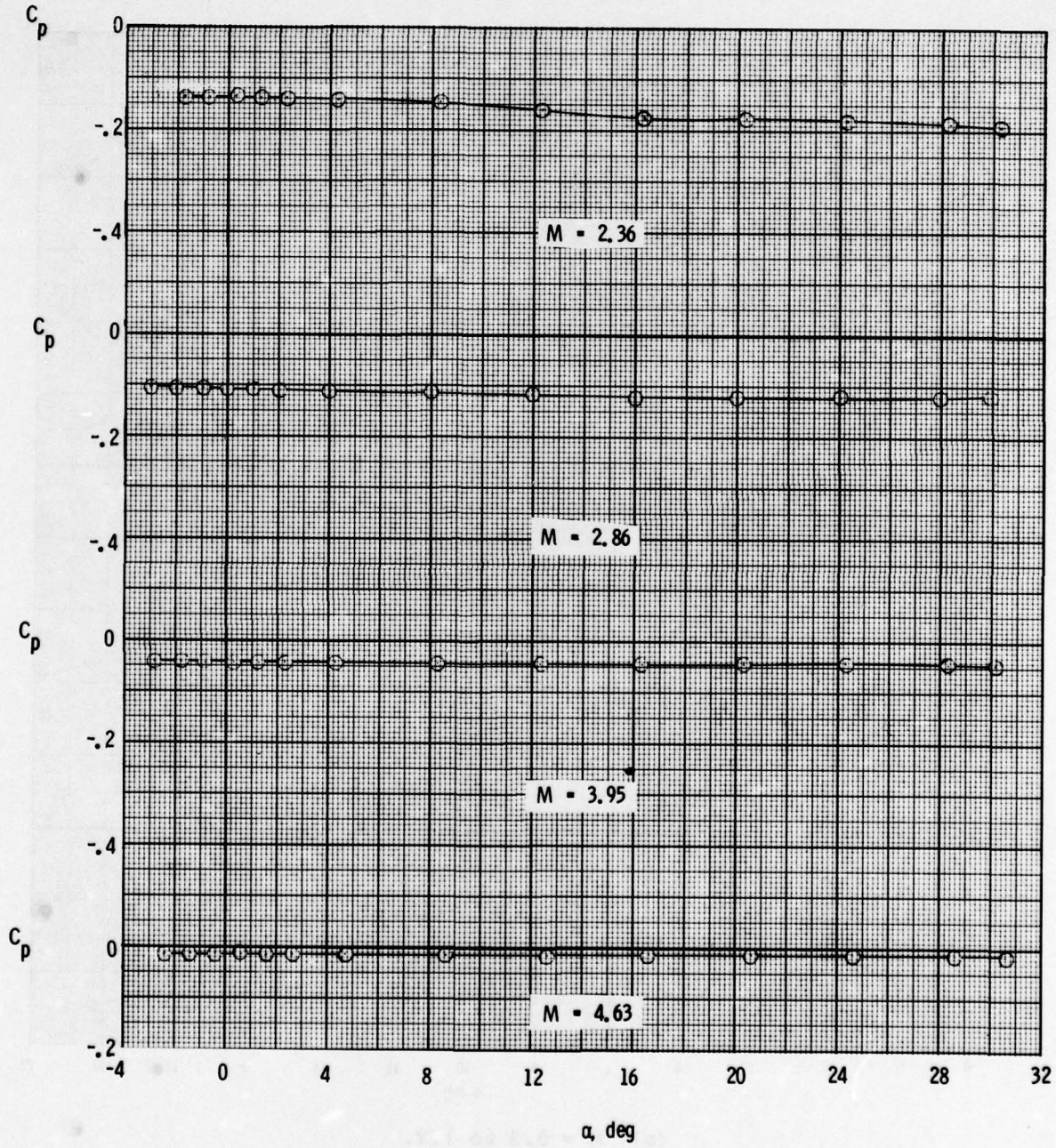

(b) M = 2.36 to 4.63.

Figure 24.- Concluded.

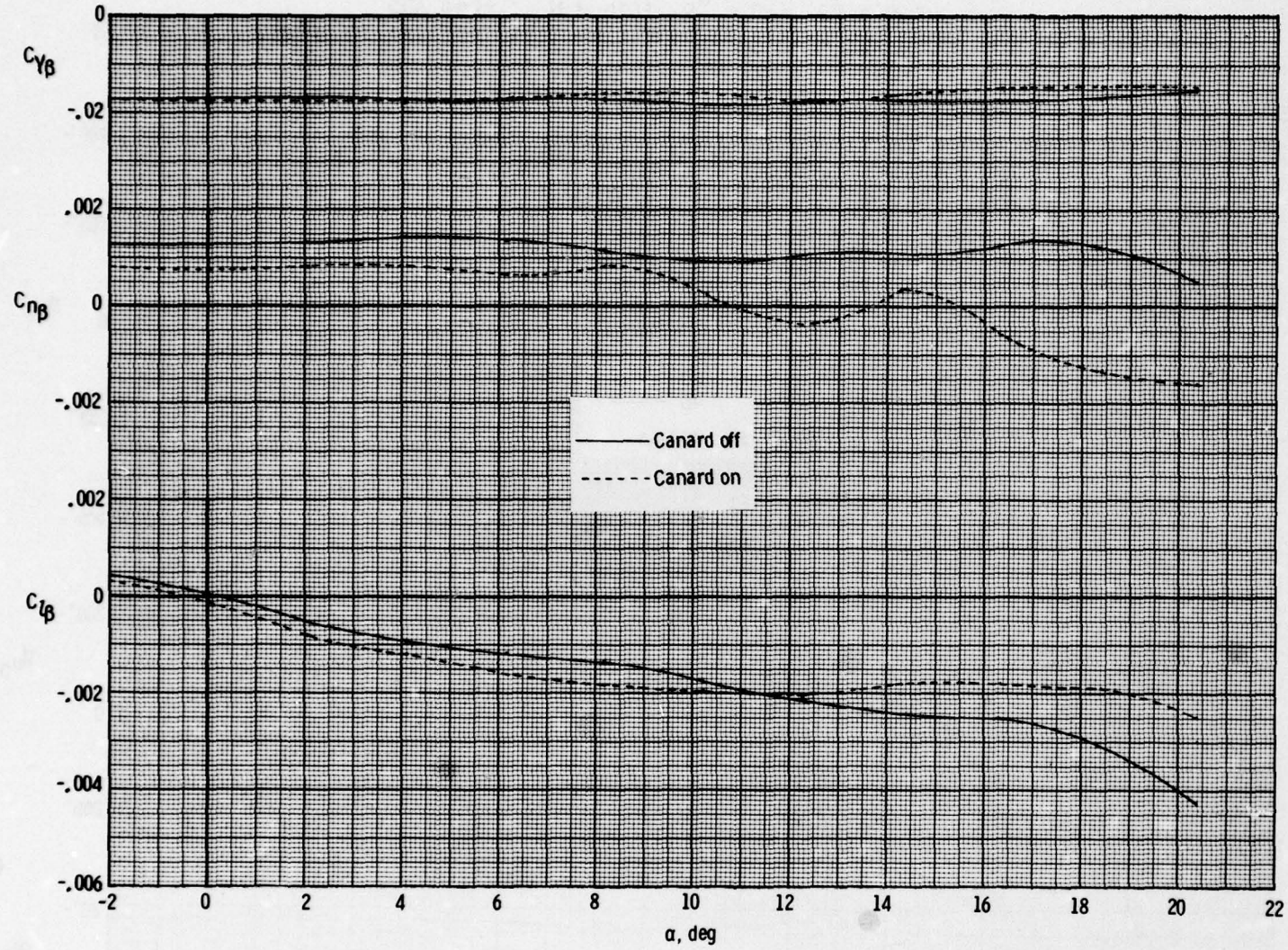

Figure 25.- Effect of canard on static lateral-directional characteristics of CCV model. M = 0.3; $\delta_e = 0^o$; $\delta_F = 0^o$.

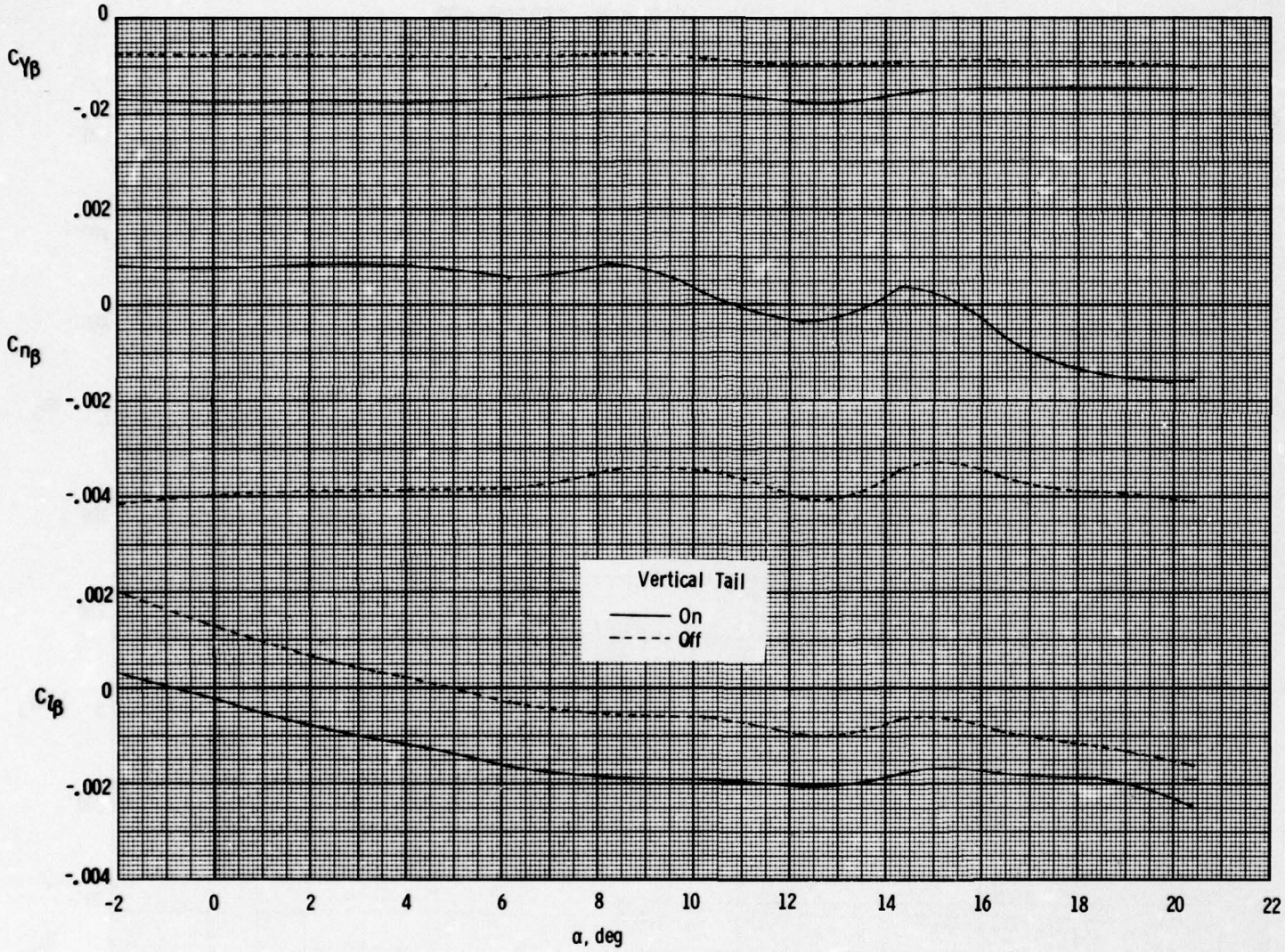

Figure 26.- Effect of vertical tail on static lateral-directional characteristics of CCV model. M = 0.3; $\delta_e = 0^o$; $\delta_F = 0^o$.

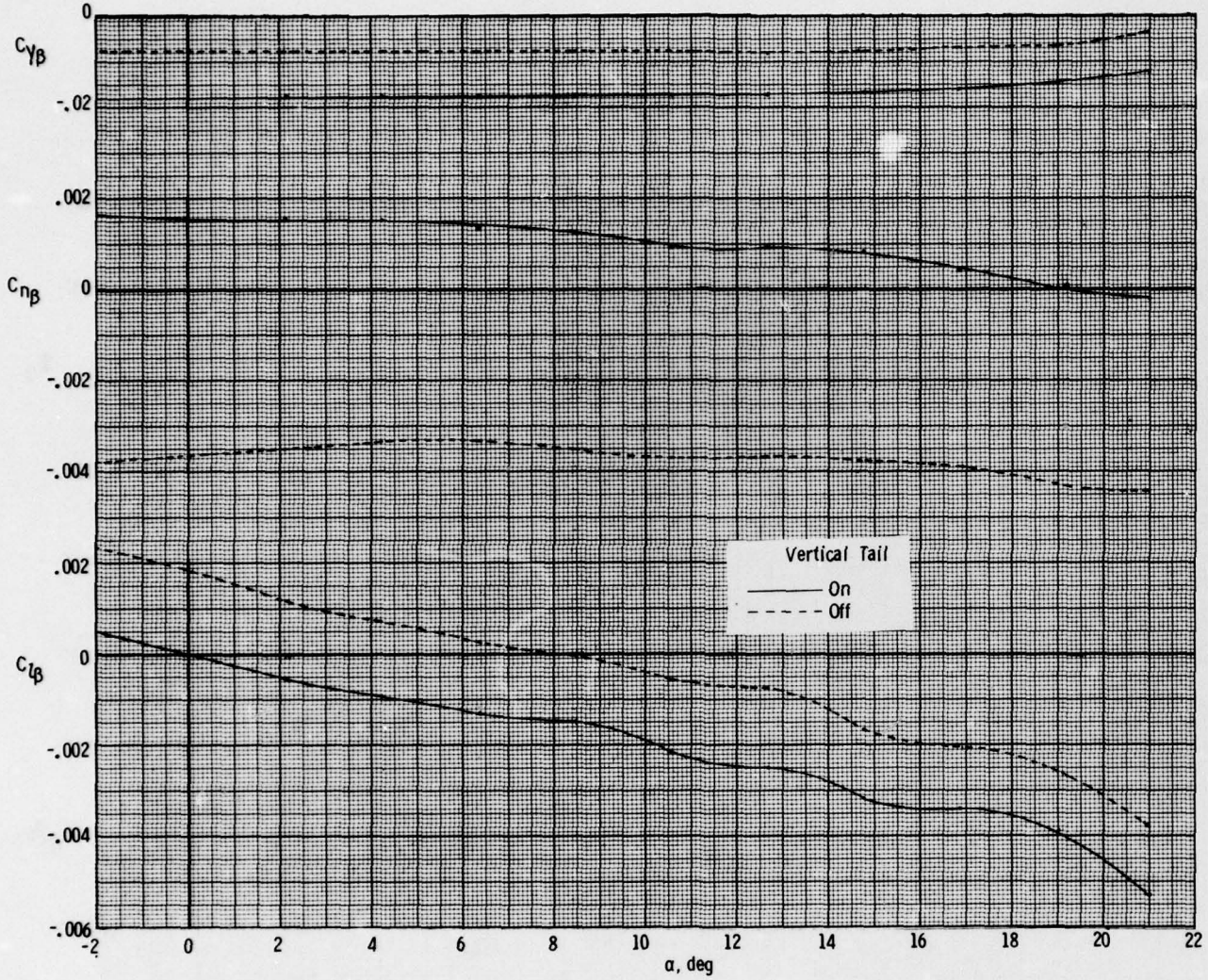

(a) M = 0.6.

Figure 27.- Effect of vertical tail on lateral-directional characteristics of CCV model at various Mach numbers. Canard off; $\delta_e = 0^o$; $\delta_F = 0^o$.

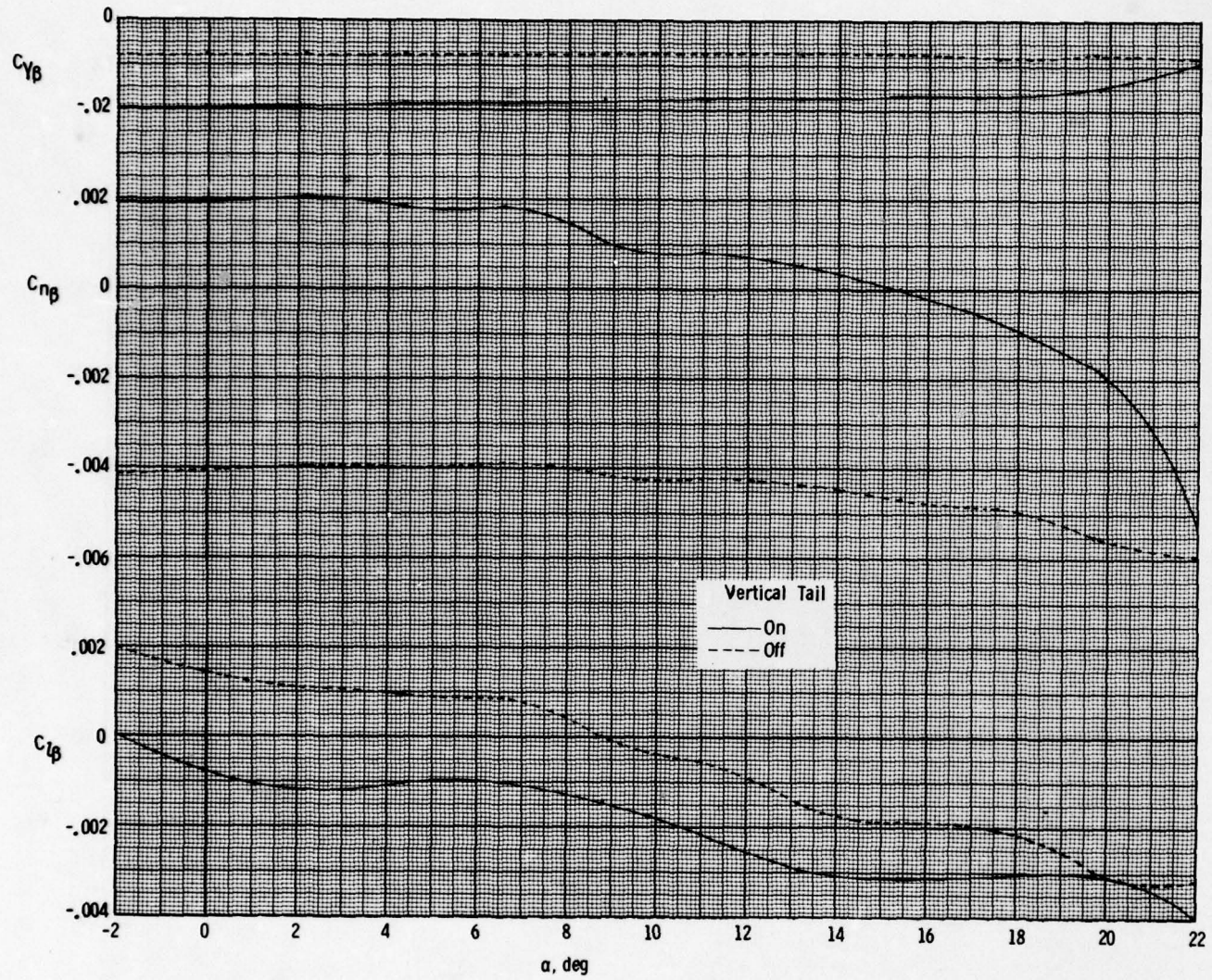

(b) M = 0.9.

Figure 27.- Continued.

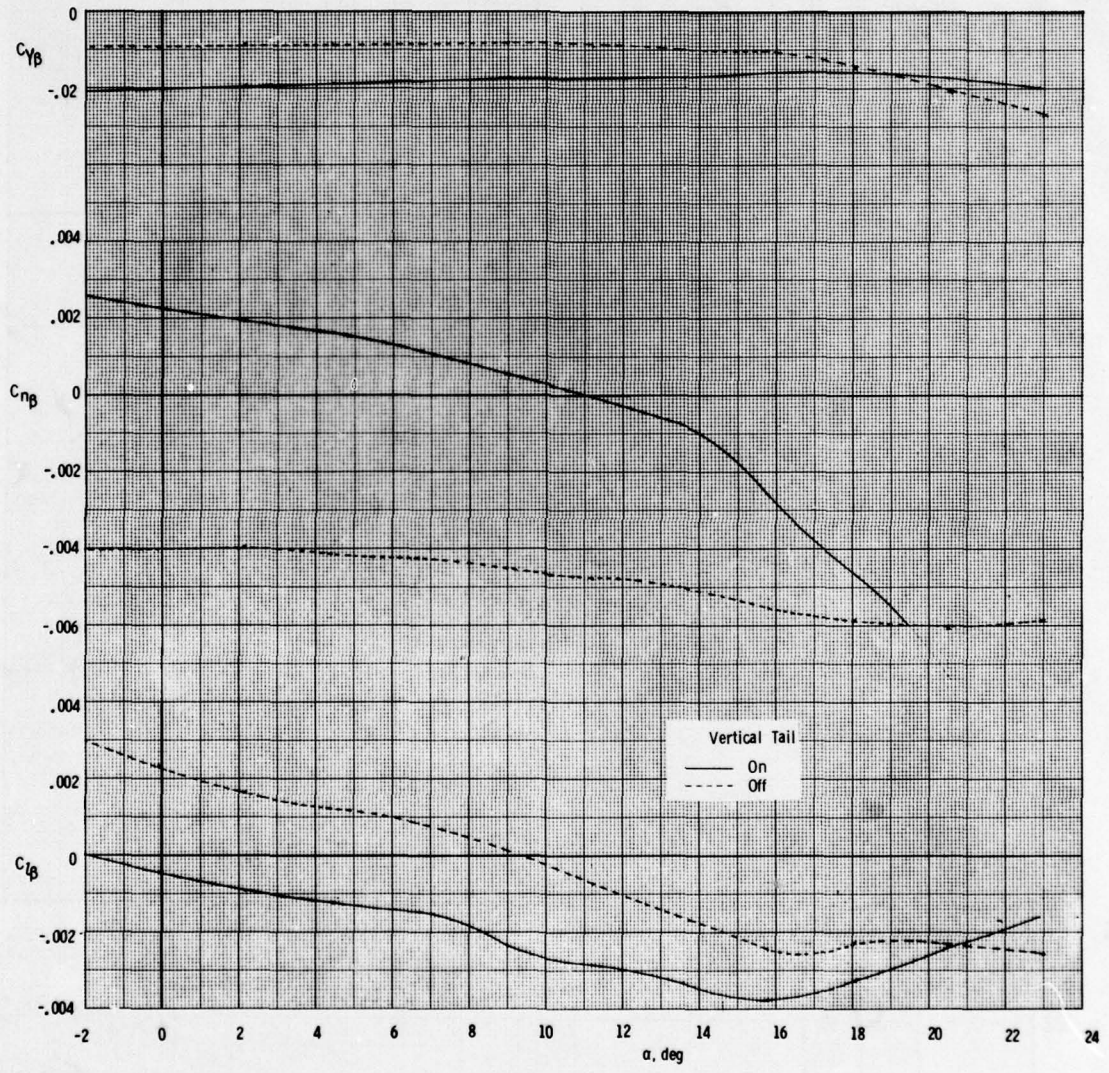

(c) M = 1.2.

Figure 27.- Continued.

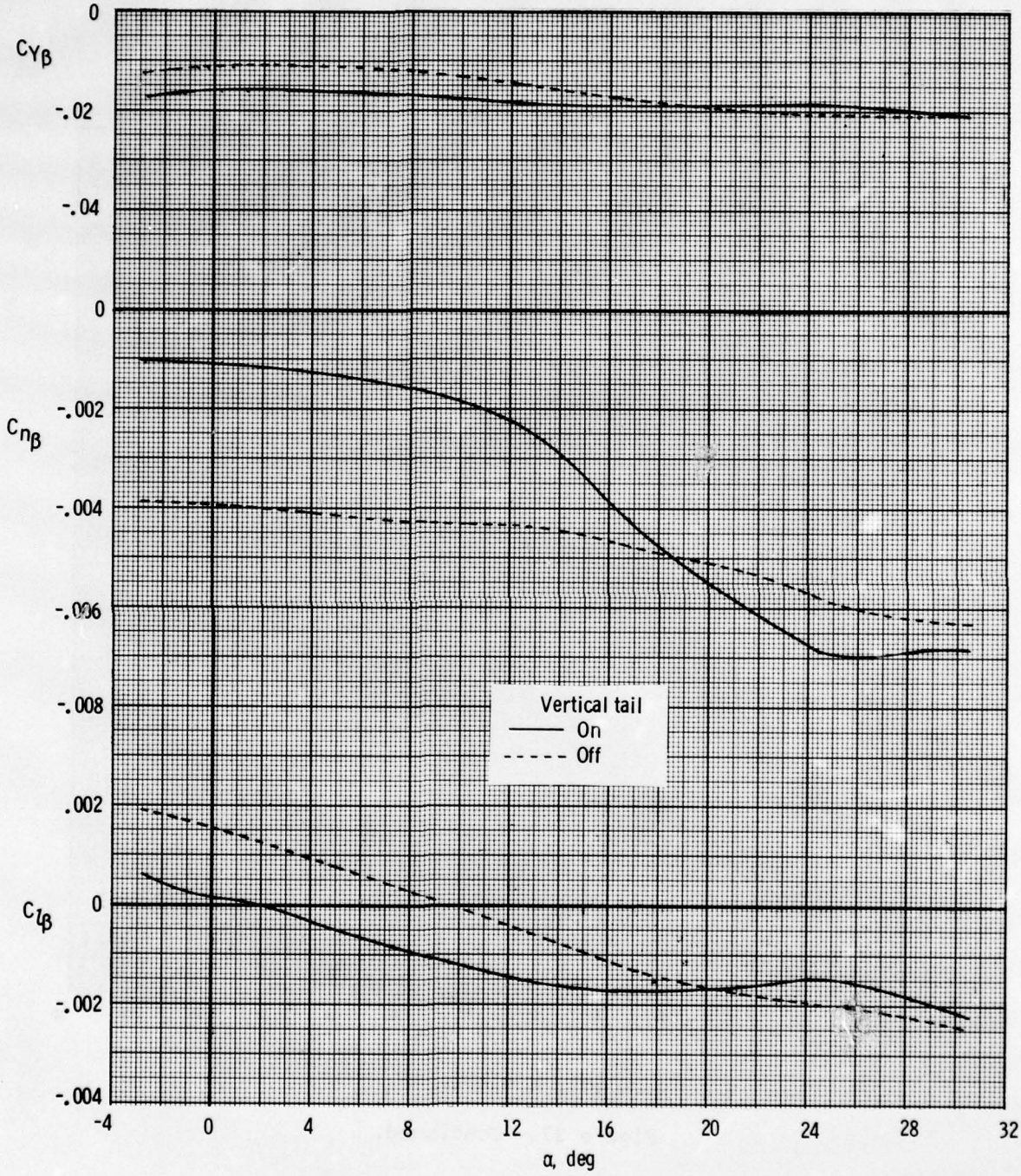

(d) M = 2.36.

Figure 27.- Continued.

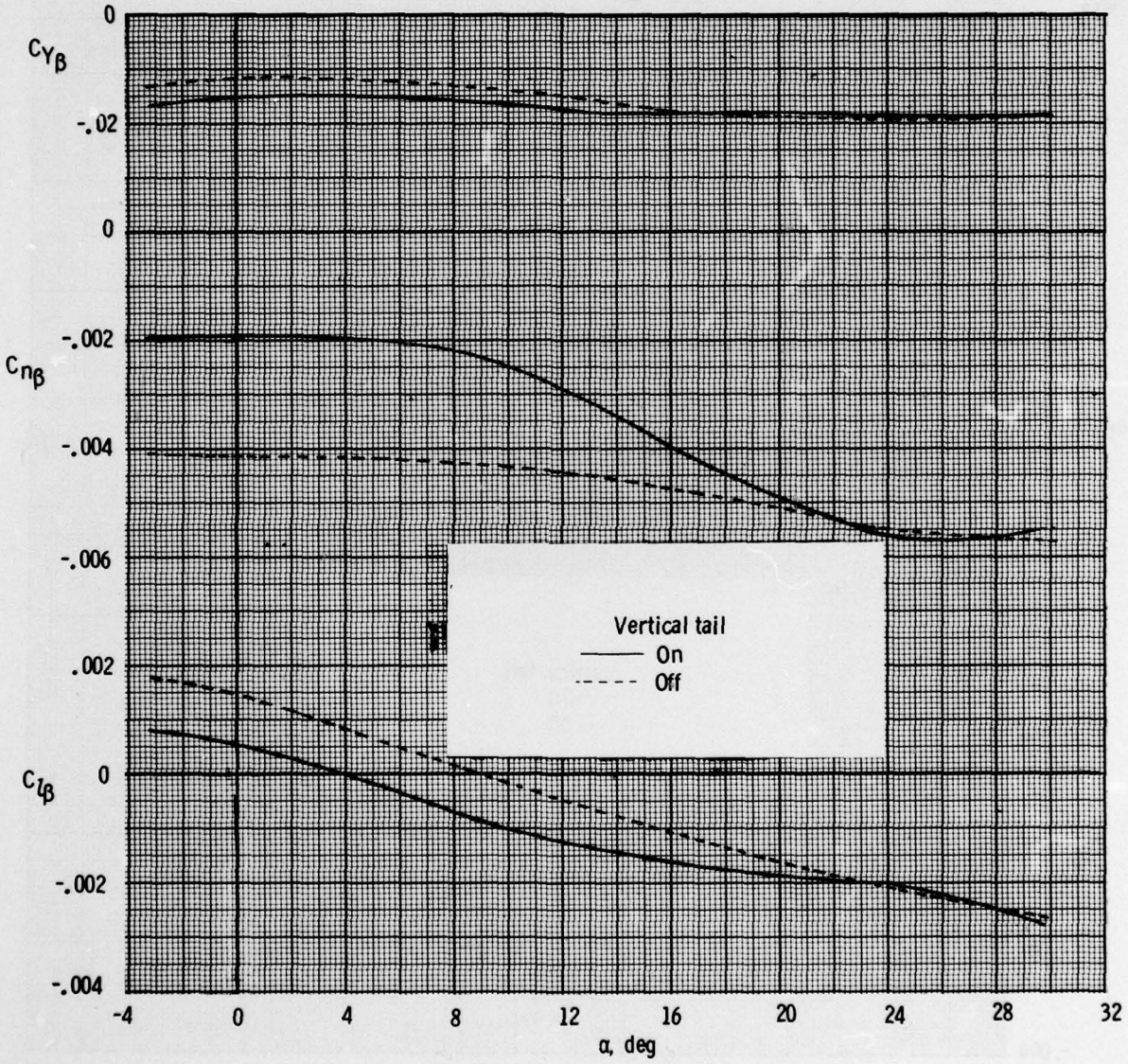

(e) M = 2.86.

Figure 27.- Continued.

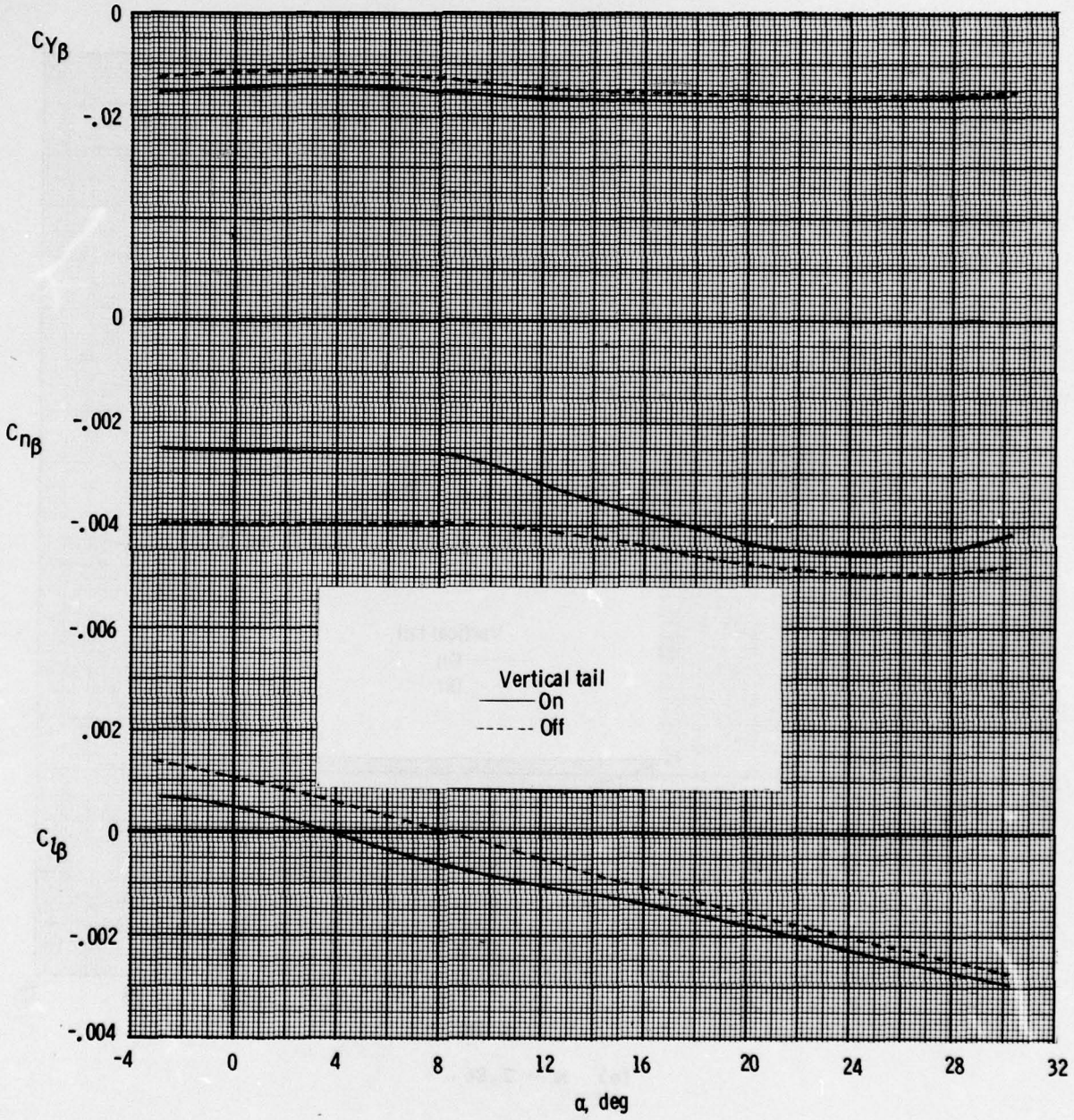

(f) M = 3.95.

Figure 27.- Continued.

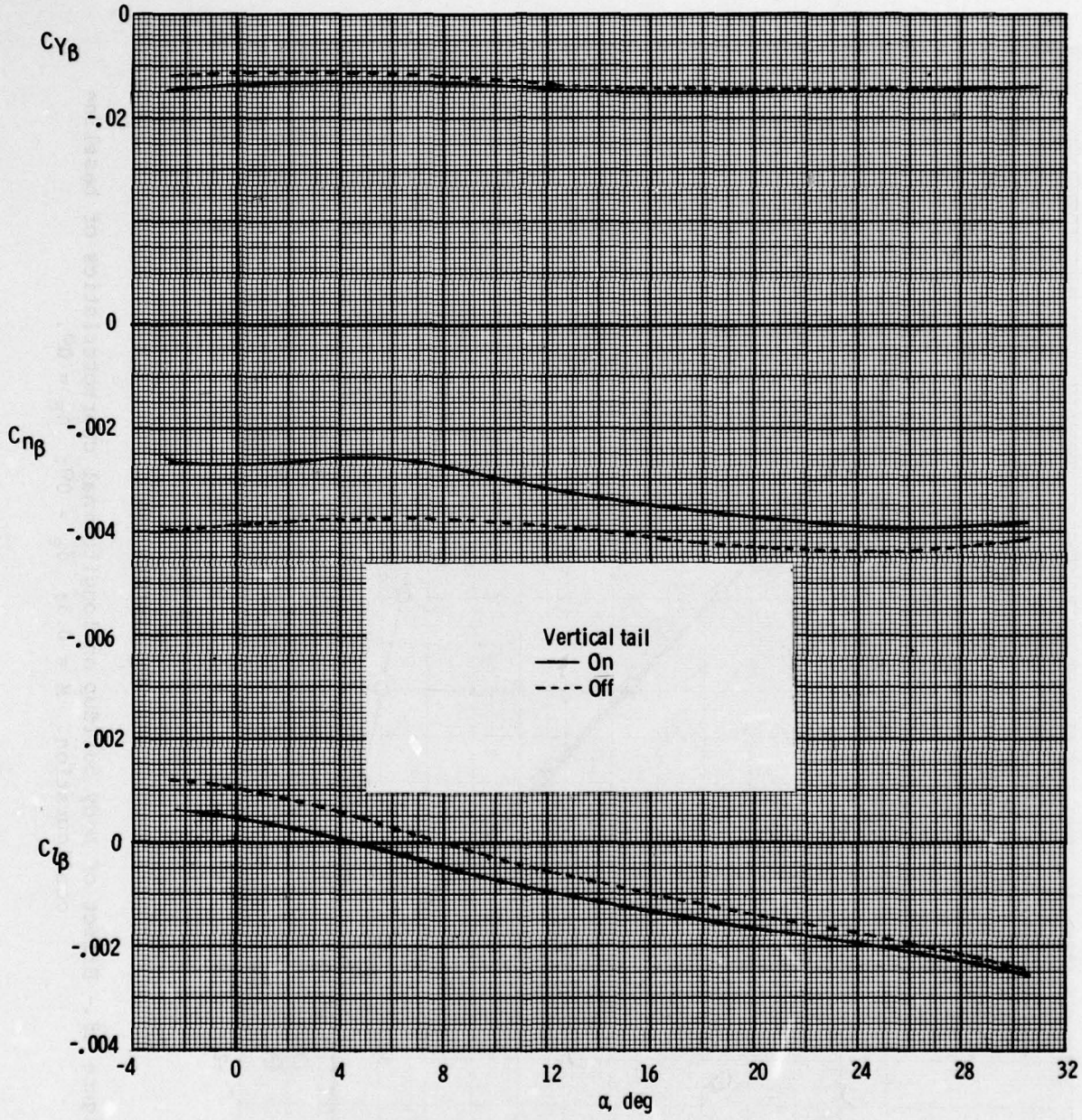

(g) M = 4.63.

Figure 27.- Concluded.

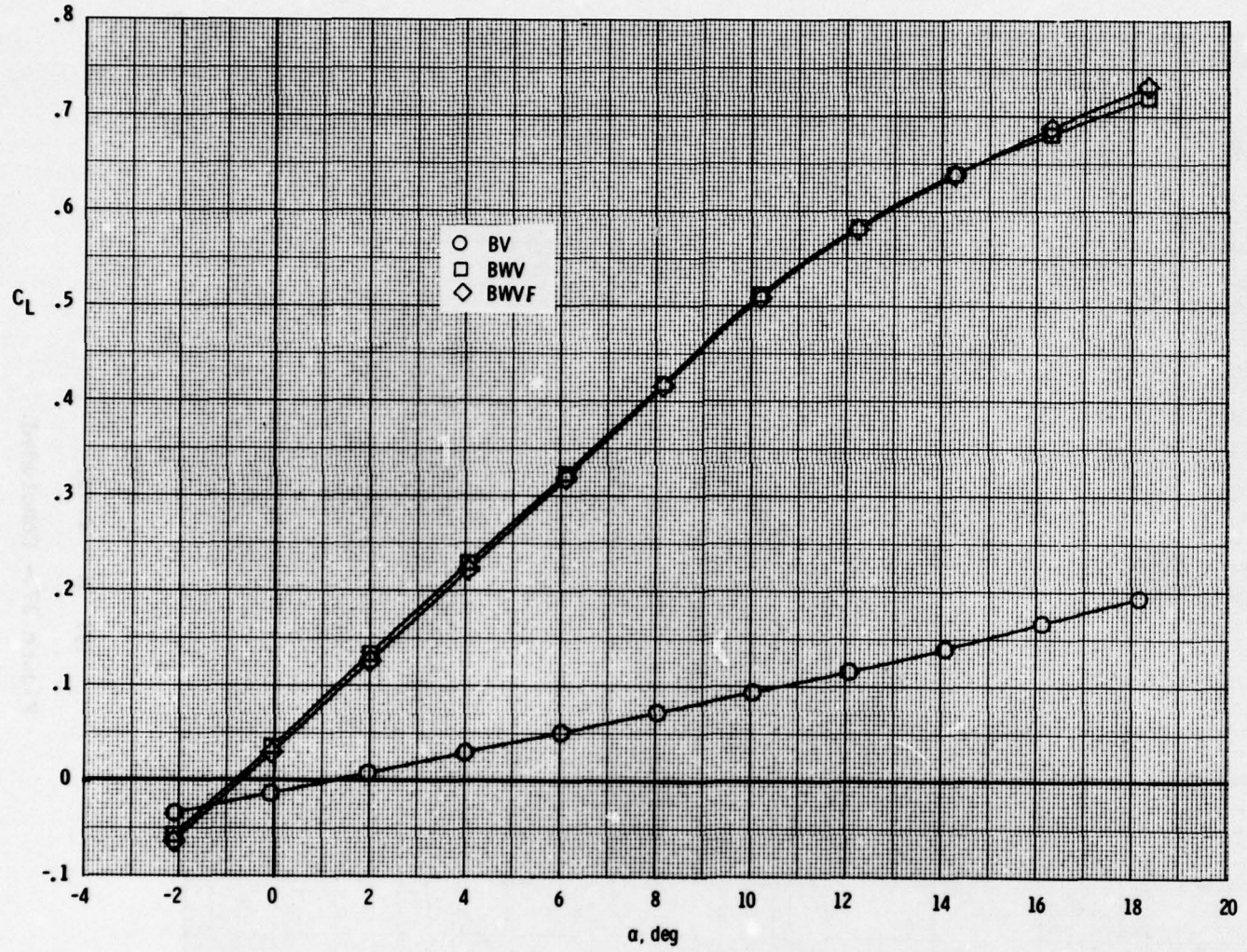

(a) C_L versus α.

Figure 28.- Effect of body buildup on longitudinal characteristics of baseline configuration. M = 0.3; $\delta_e = 0^o$; $\delta_F = 0^o$.

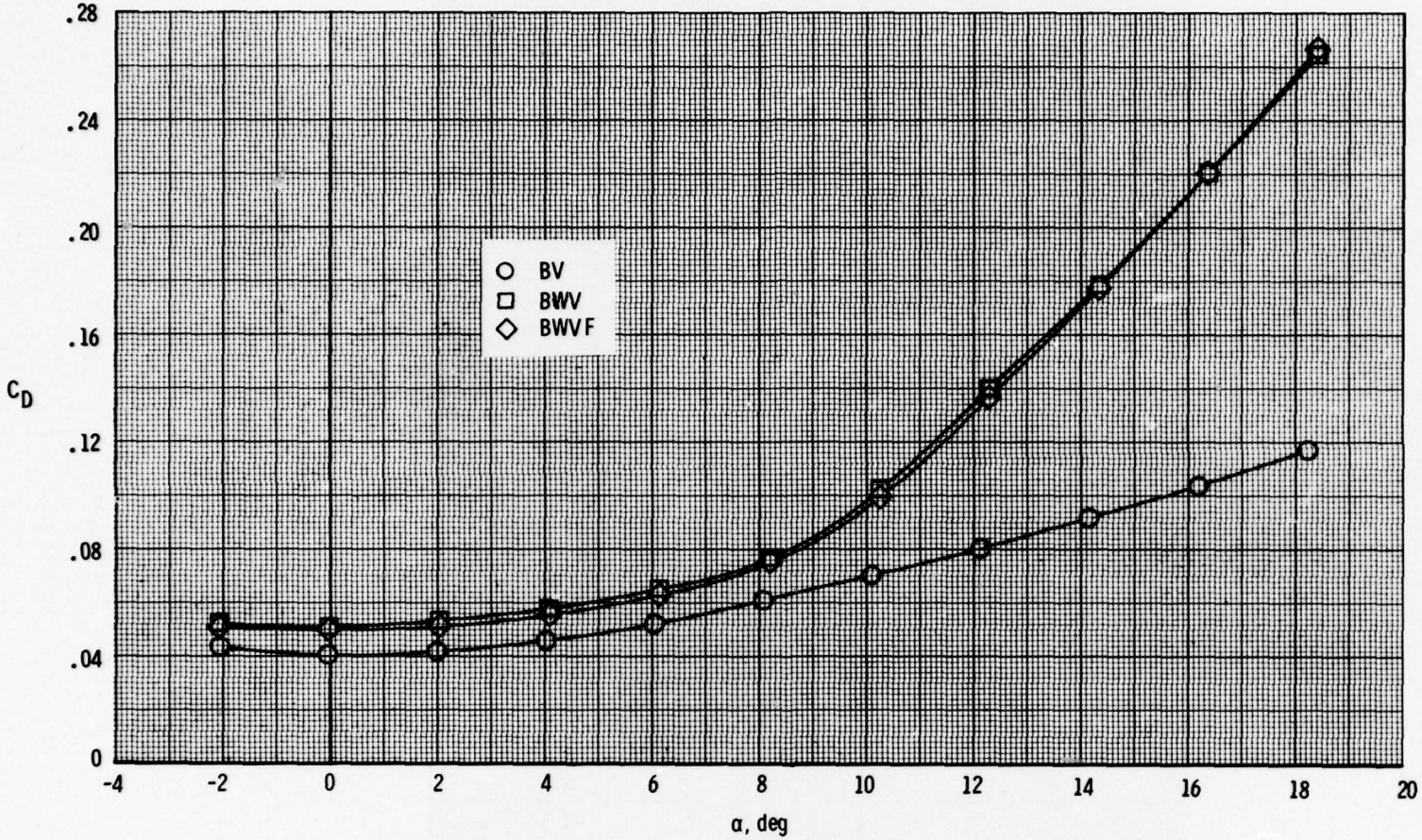

(b) C_D versus α.

Figure 28.- Continued.

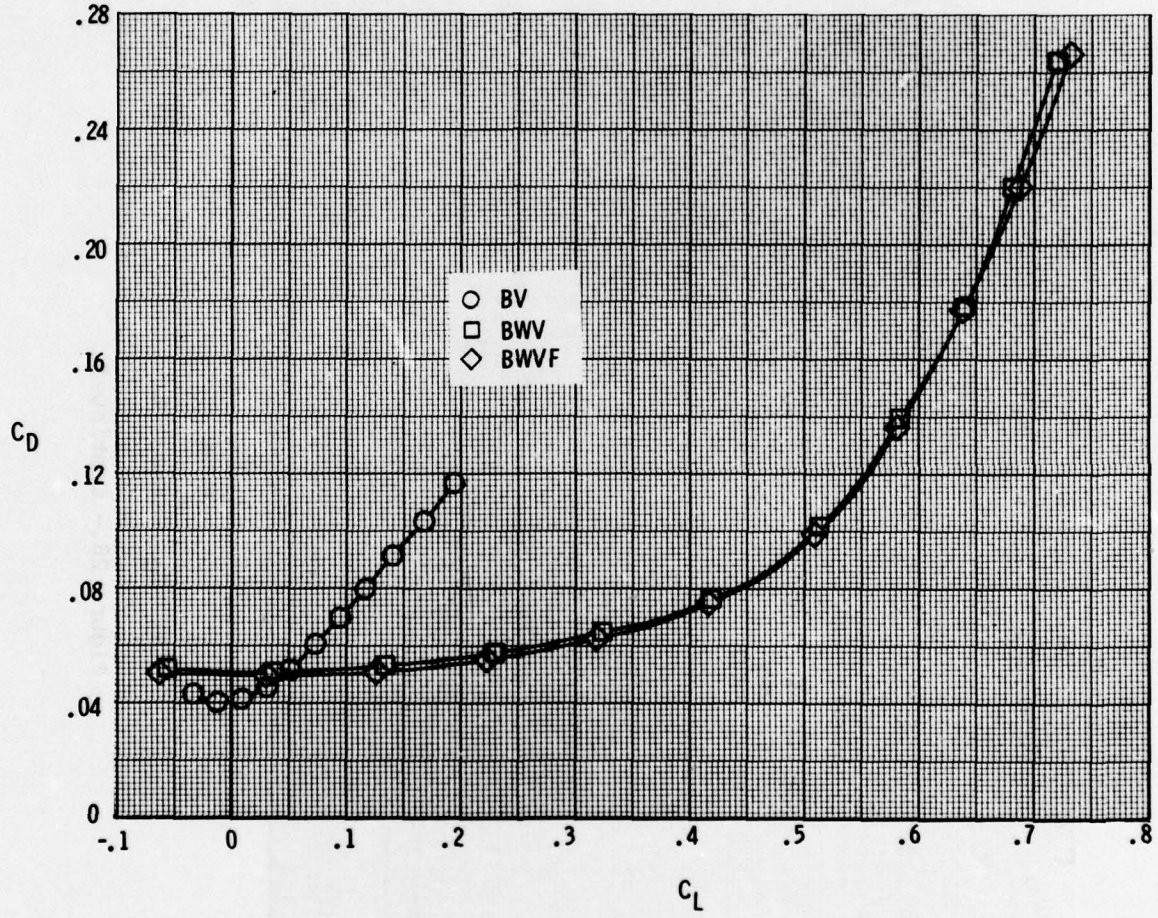

(c) C_D versus C_L.

Figure 28.- Continued.

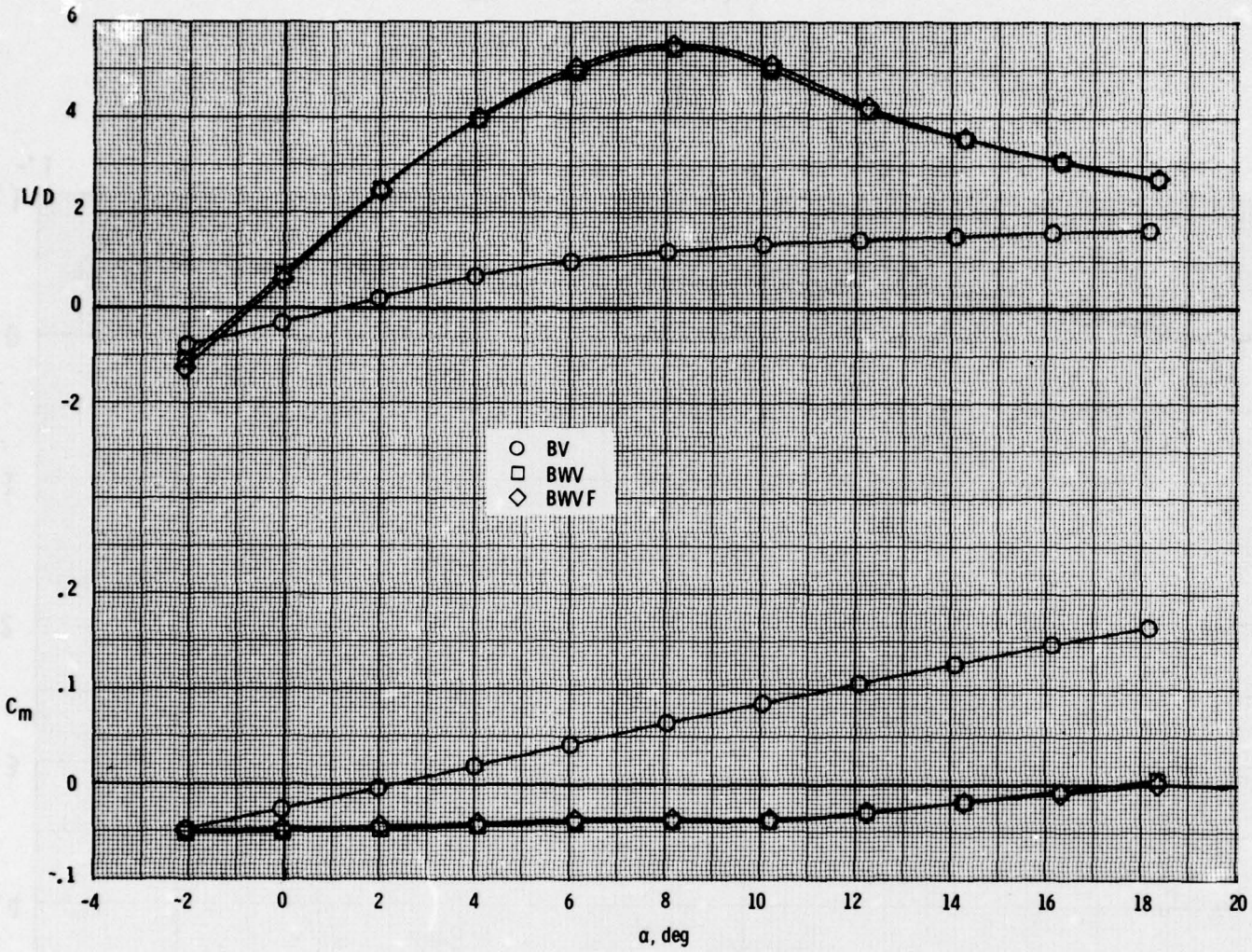

(d) L/D and C_m versus α.

Figure 28.- Continued.

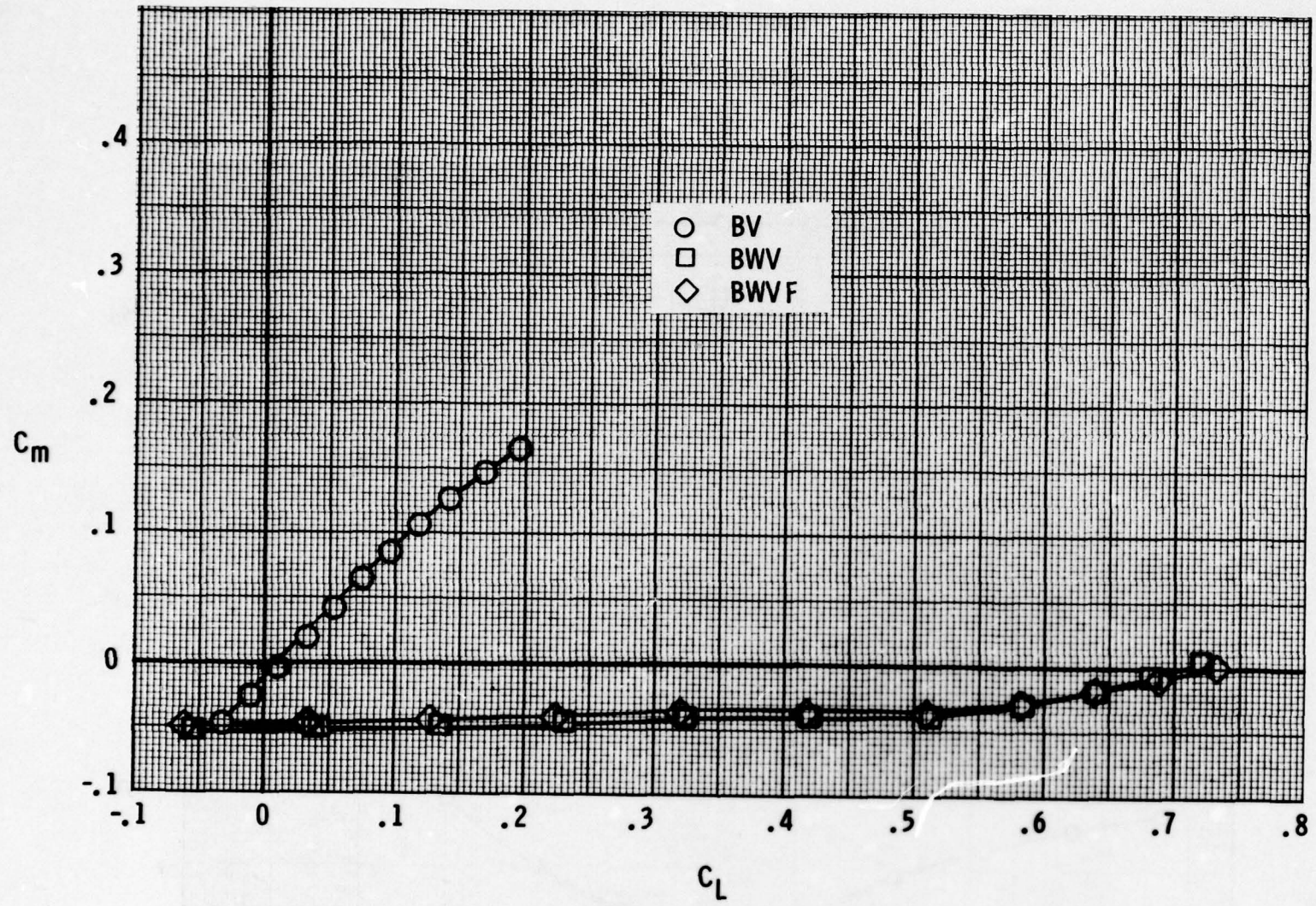

(e) C_m versus C_L.

Figure 28.- Concluded.

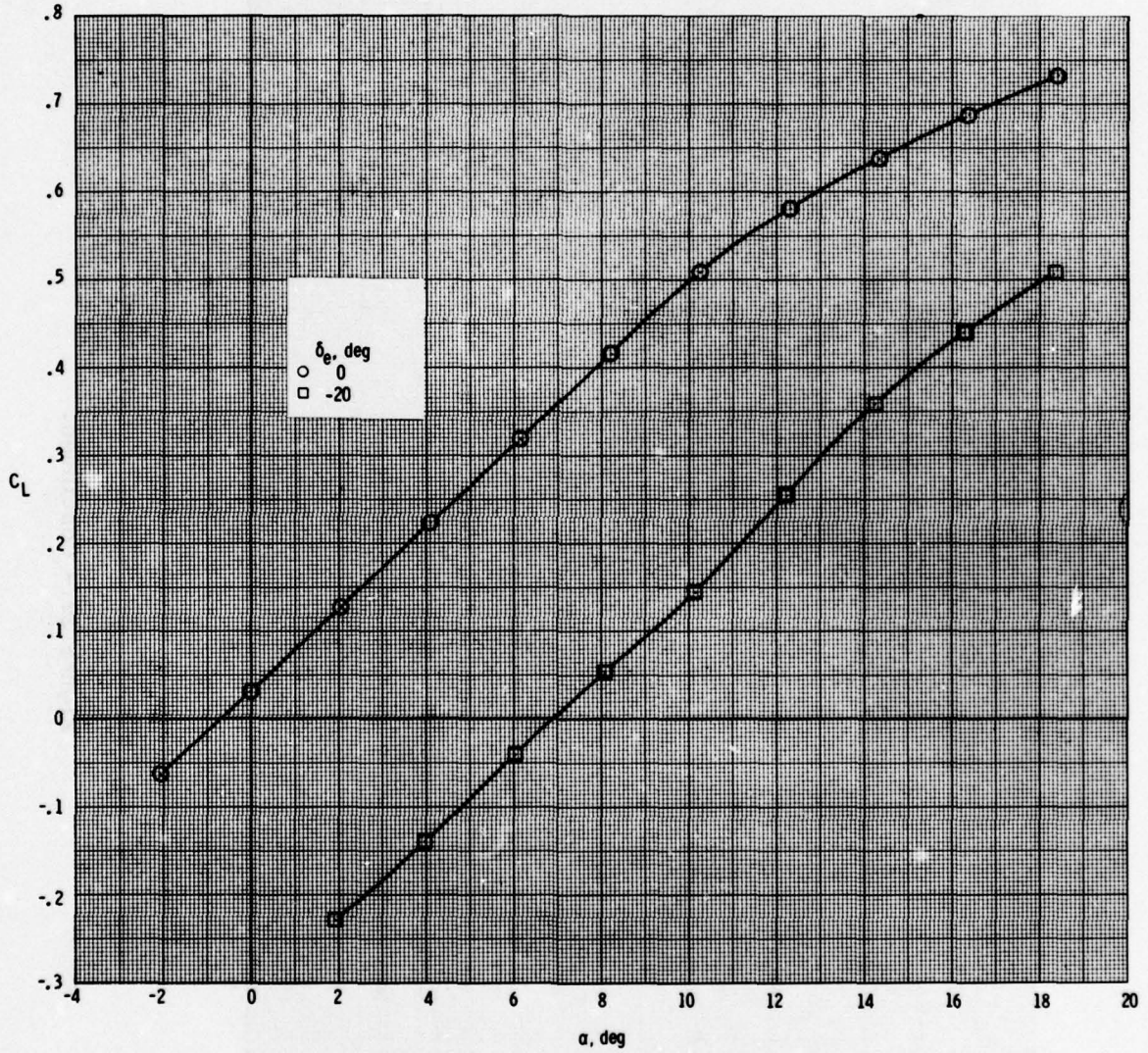

(a) C_L versus α; M = 0.3.

Figure 29.- Longitudinal stability and elevon effectiveness of CCV model. $\delta_F = 0^o$.

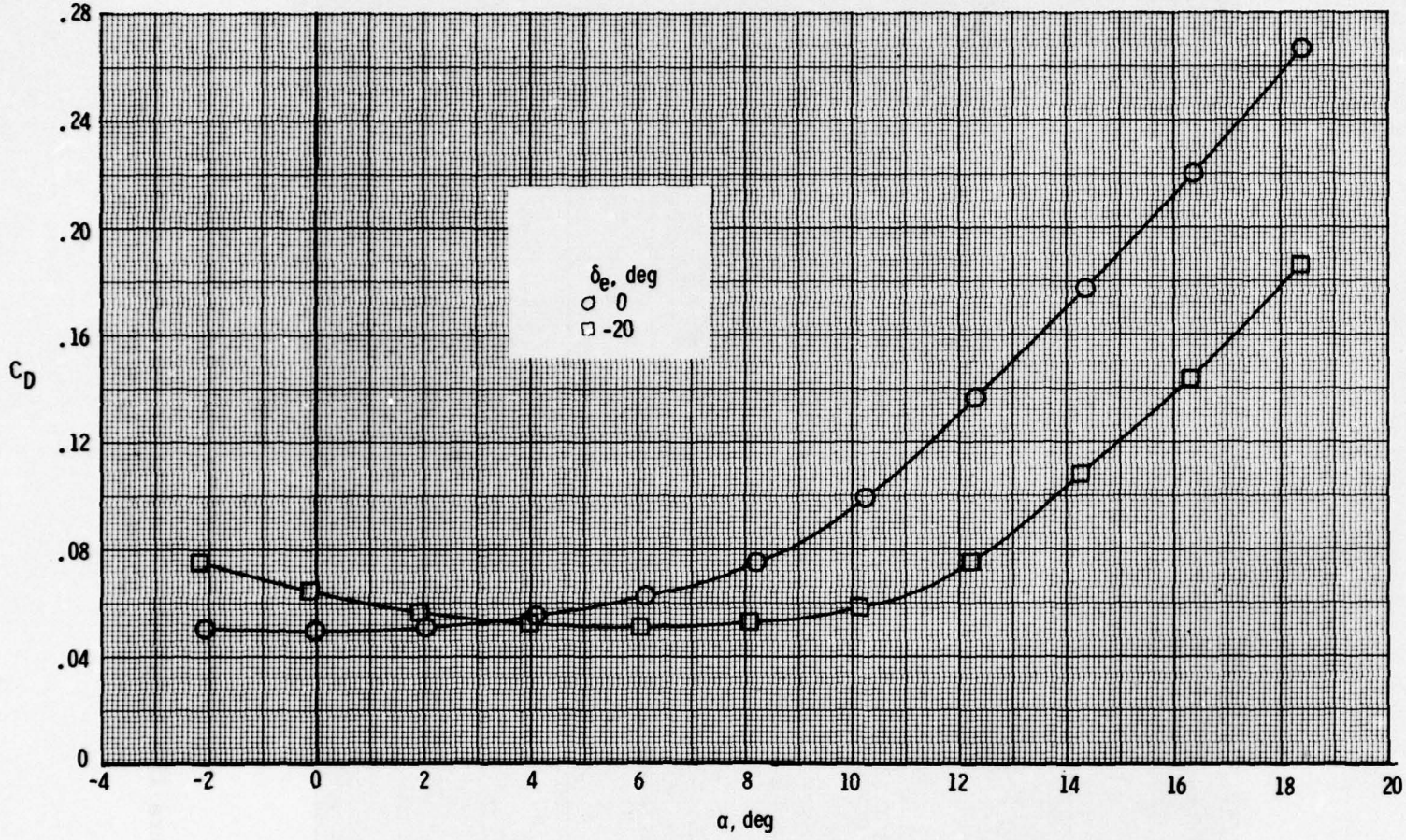

(a) C_D versus α; M = 0.3. Continued.

Figure 29.- Continued.

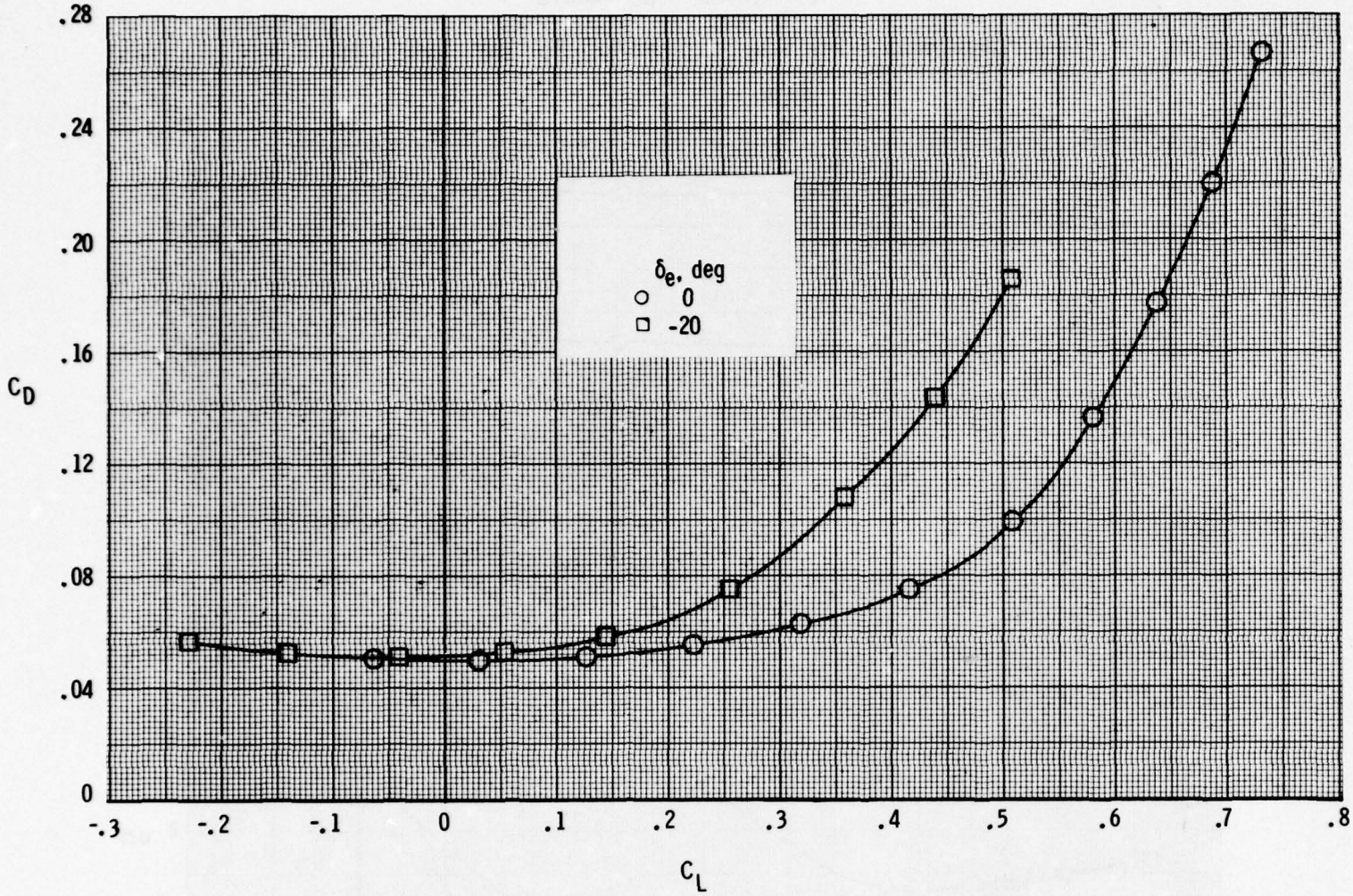

(a) C_D versus C_L; M = 0.3. Continued.

Figure 29.- Continued.

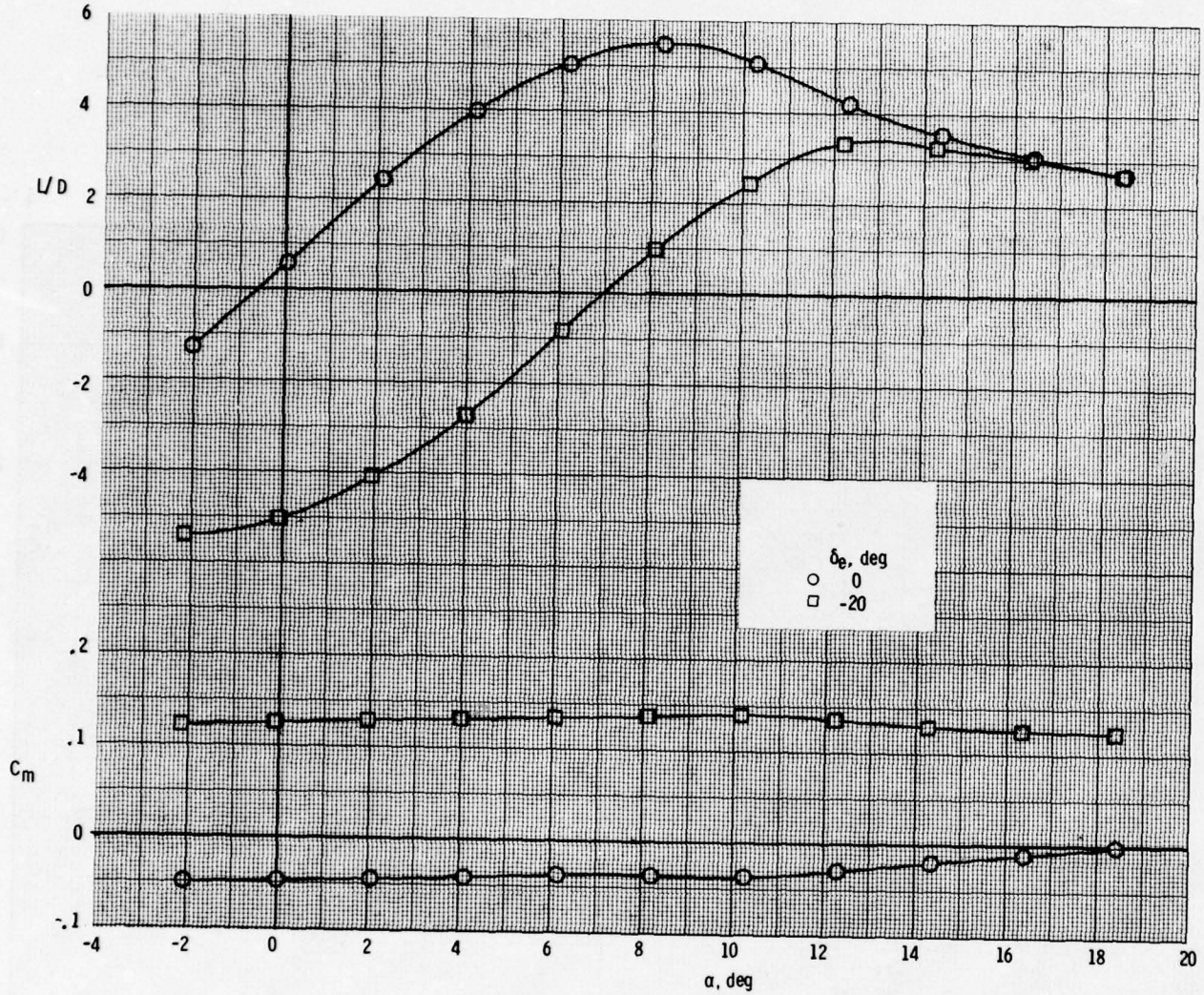

(a) L/D and C_m versus α; M = 0.3. Continued.

Figure 29.- Continued.

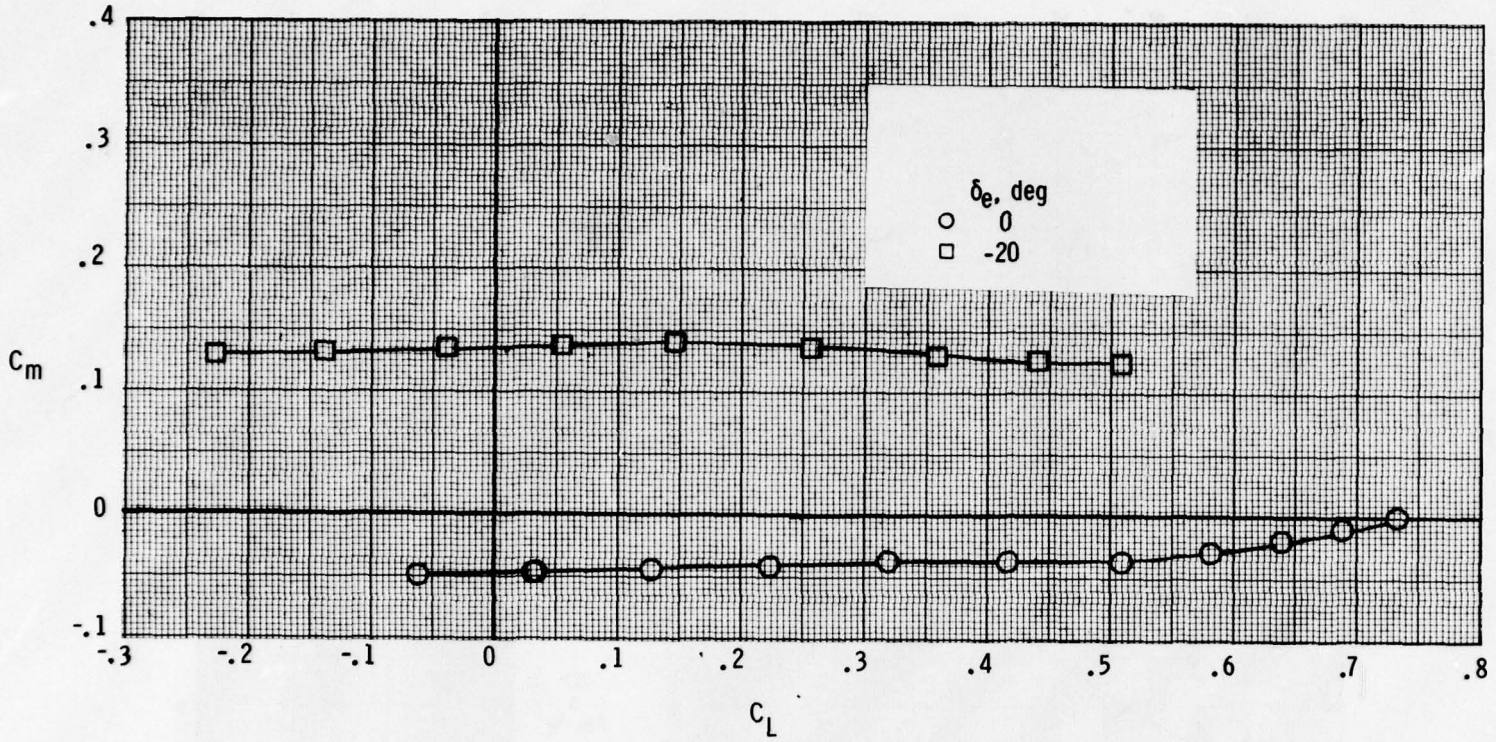

(a) C_m versus C_L; M = 0.3. Concluded.

Figure 29.- Continued.

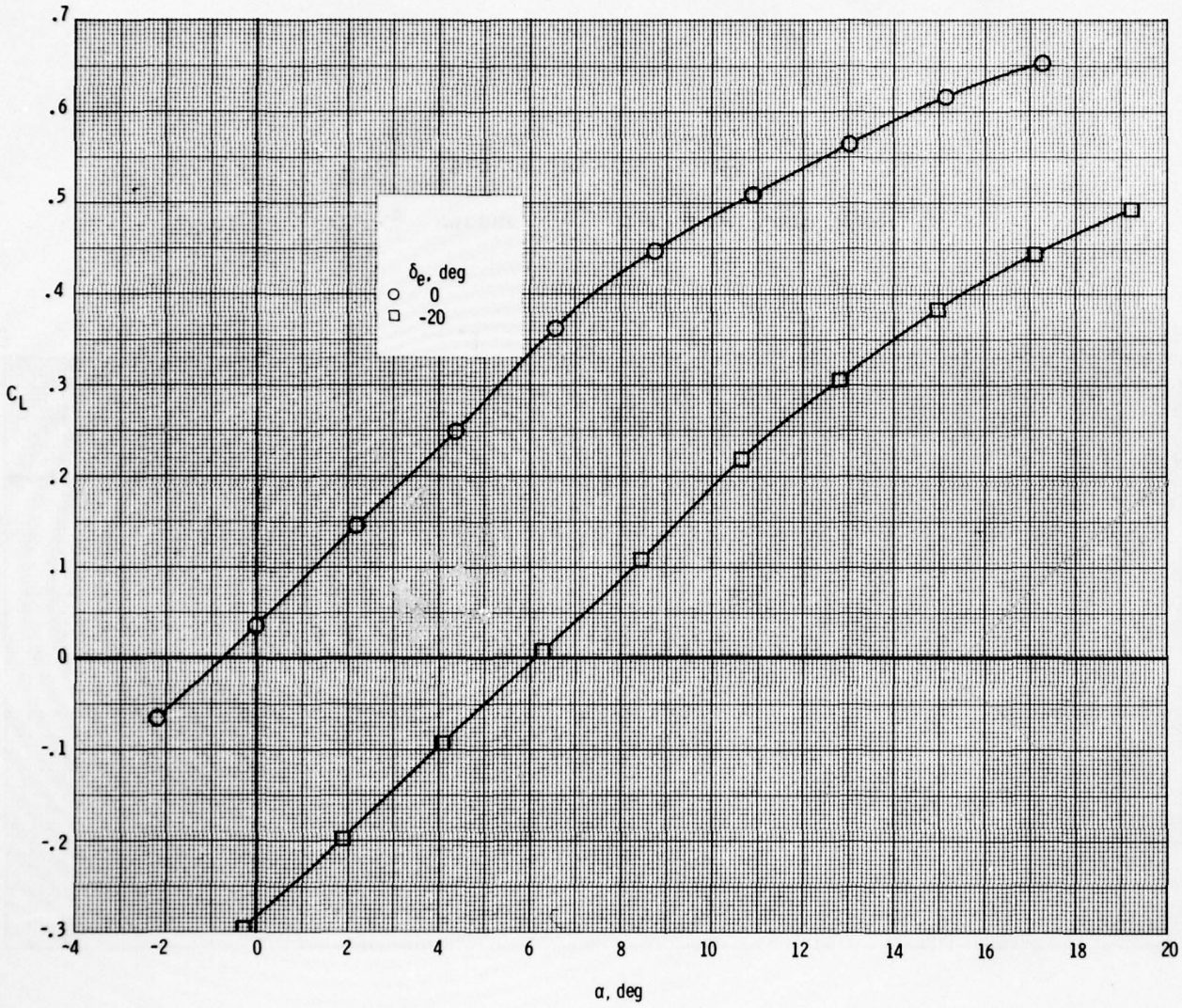

(b) C_L versus α; M = 0.6.

Figure 29.- Continued.

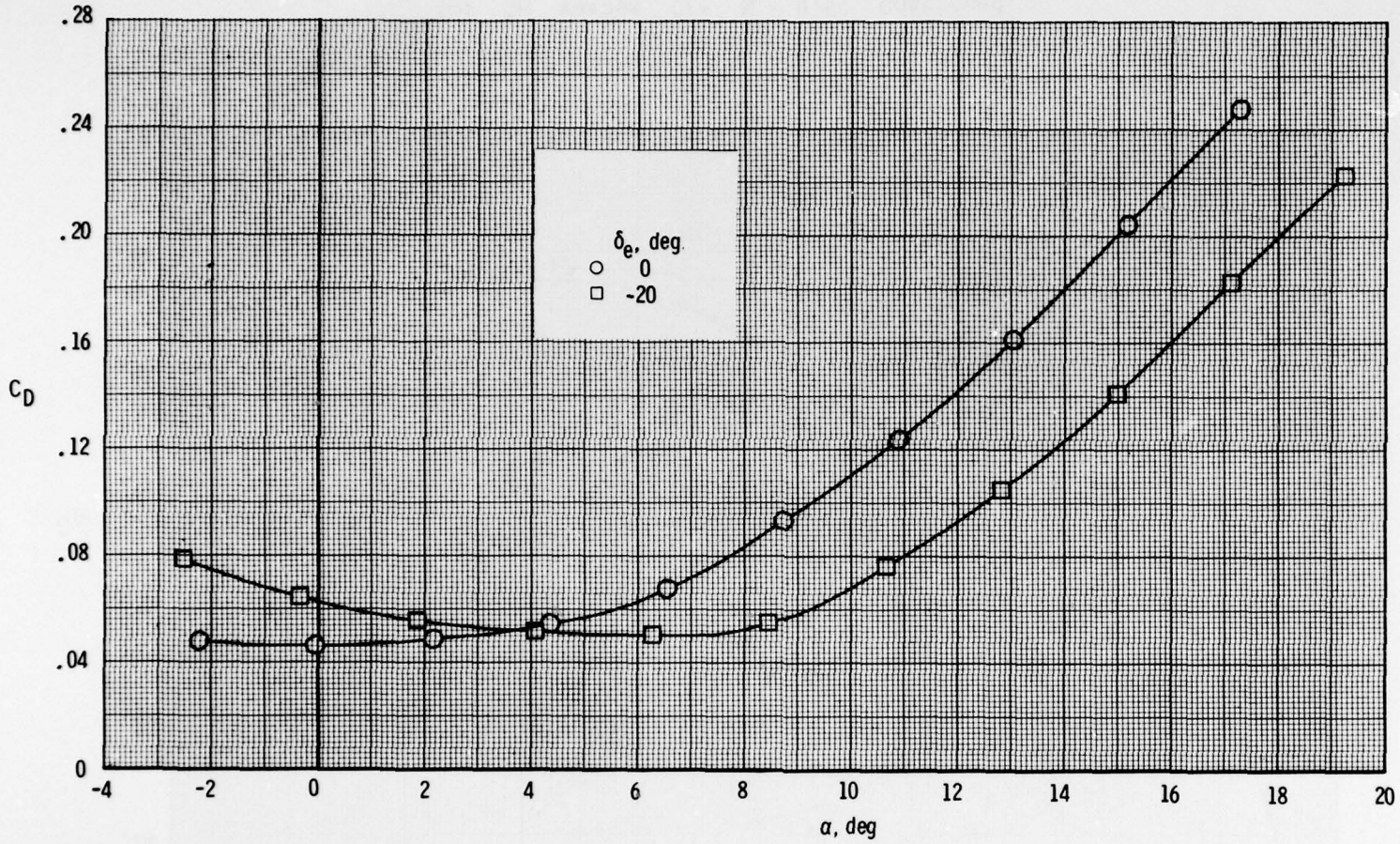

(b) C_D versus α; M = 0.6. Continued.

Figure 29.- Continued.

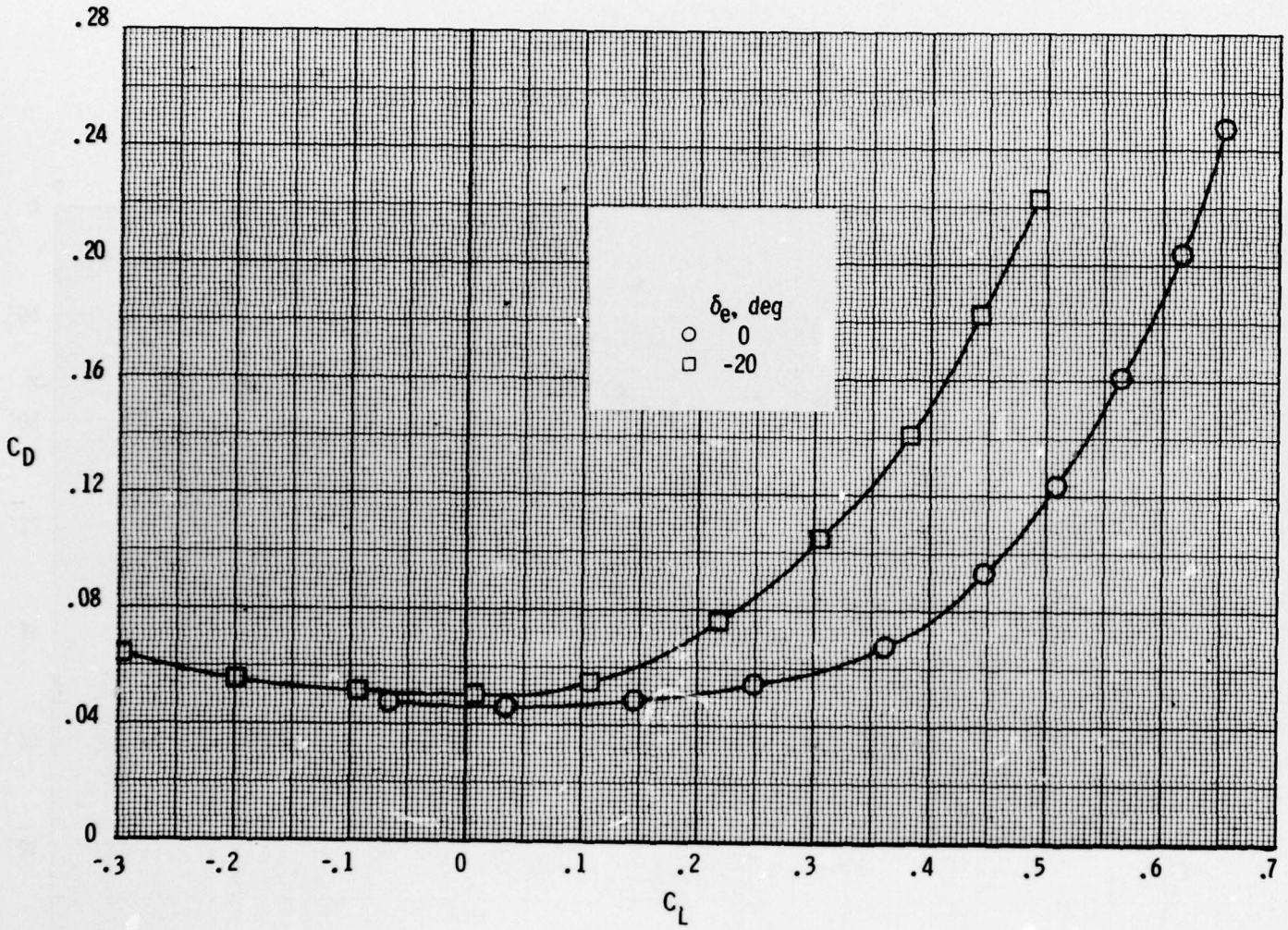

(b) C_D versus C_L; M = 0.6. Continued.

Figure 29.- Continued.

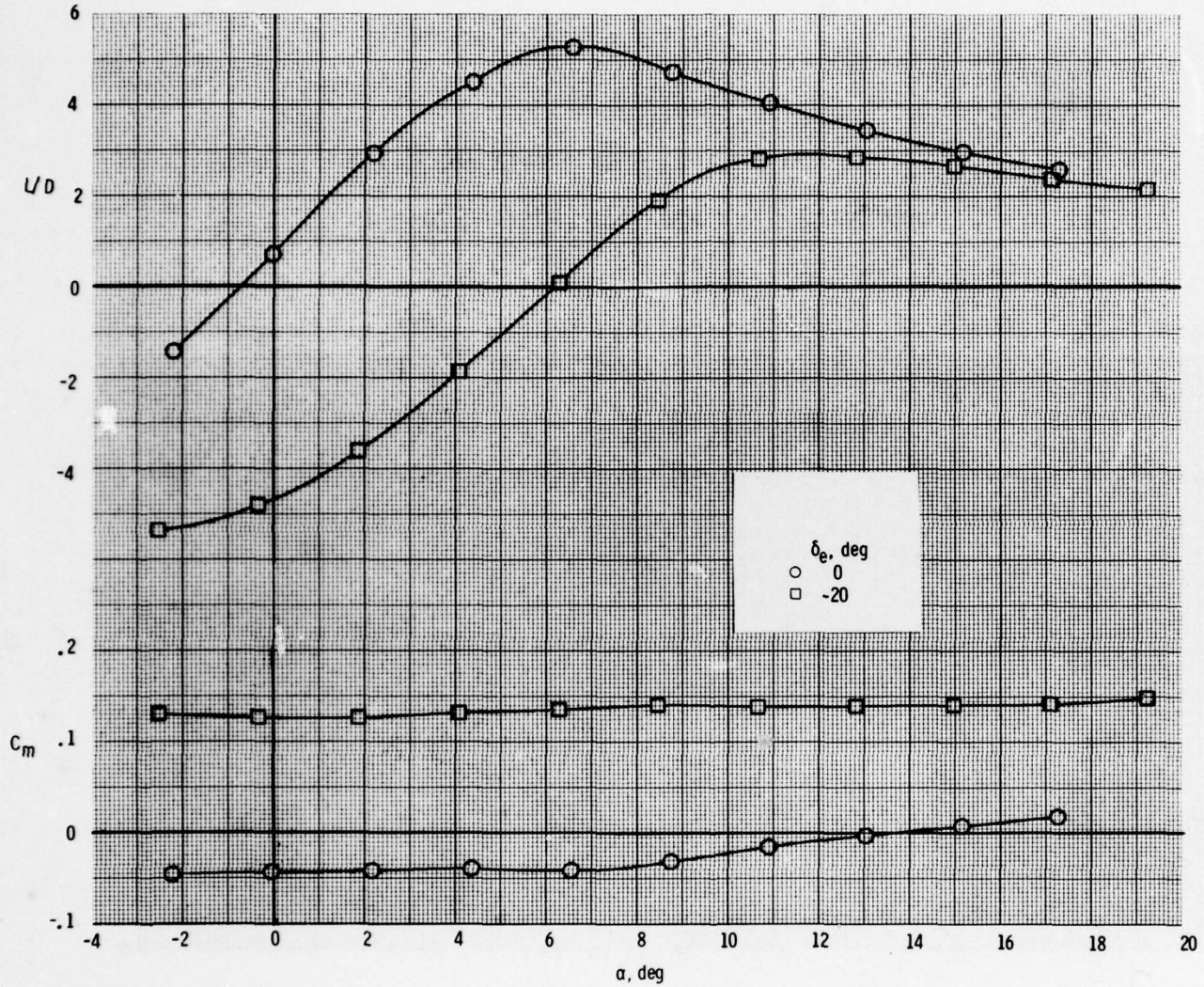

(b) L/D and C_m versus α; M = 0.6. Continued.

Figure 29.- Continued.

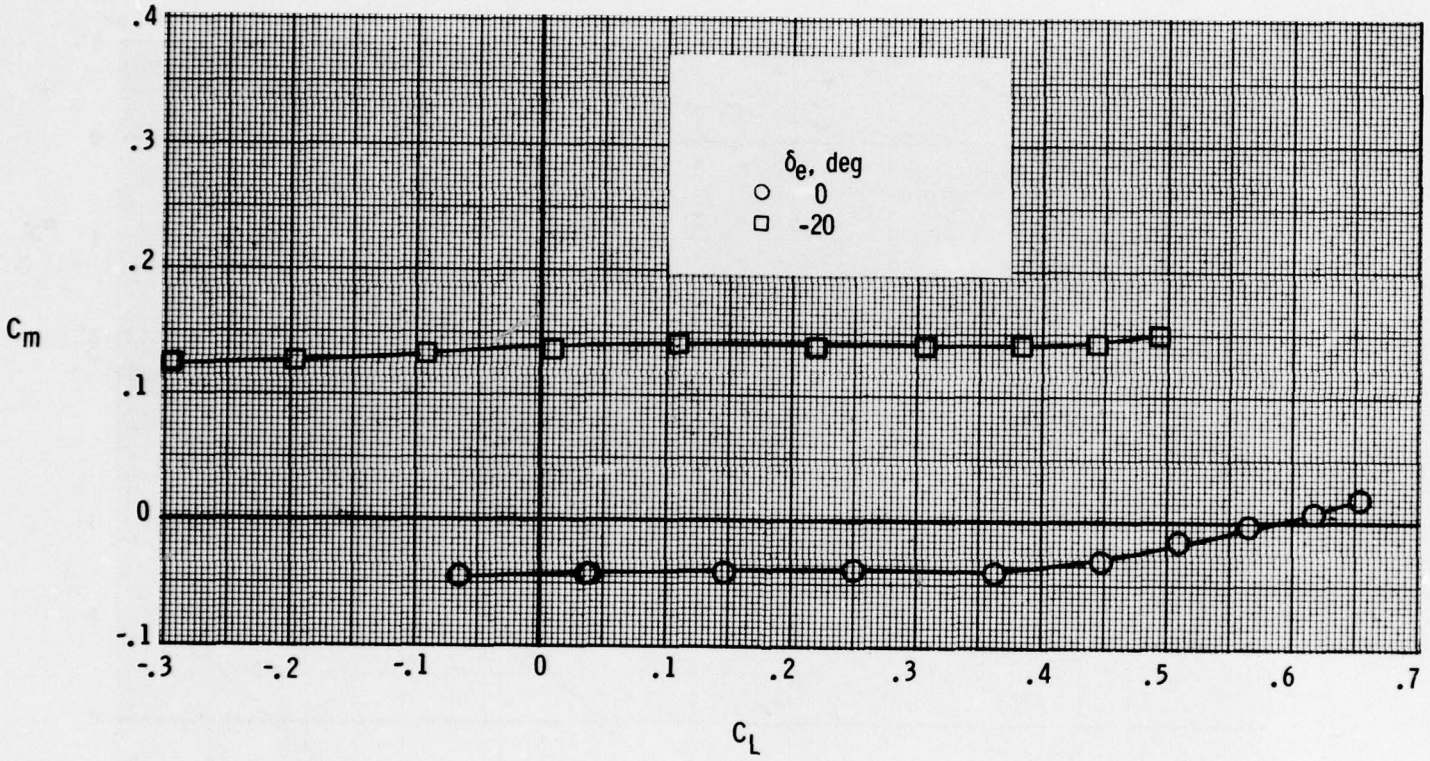

(b) C_m versus C_L; M = 0.6. Concluded.

Figure 29.- Continued.

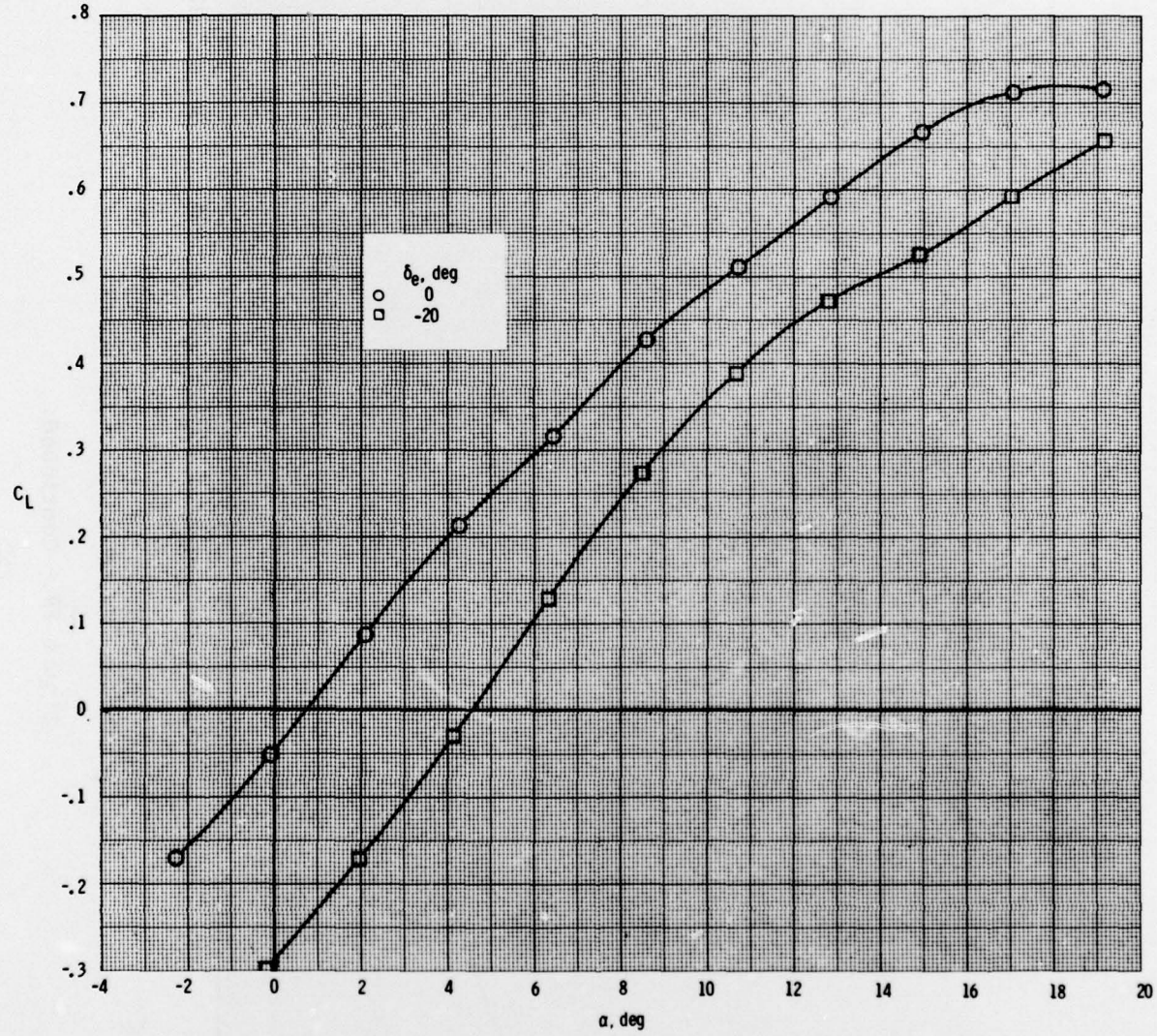

(c) C_L versus α; M = 0.9.

Figure 29.- Continued.

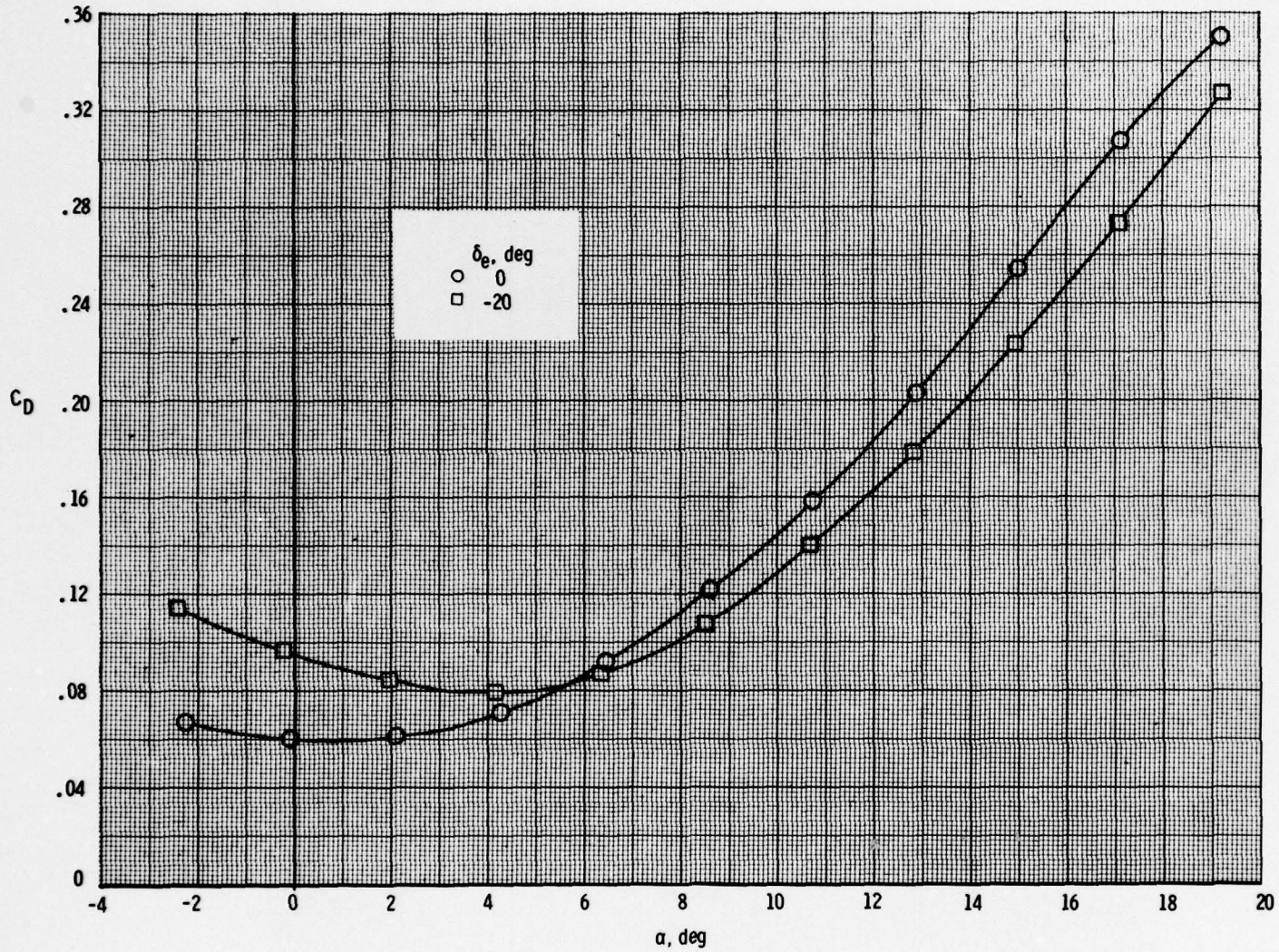

(c) C_D versus α; M = 0.9. Continued.

Figure 29.- Continued.

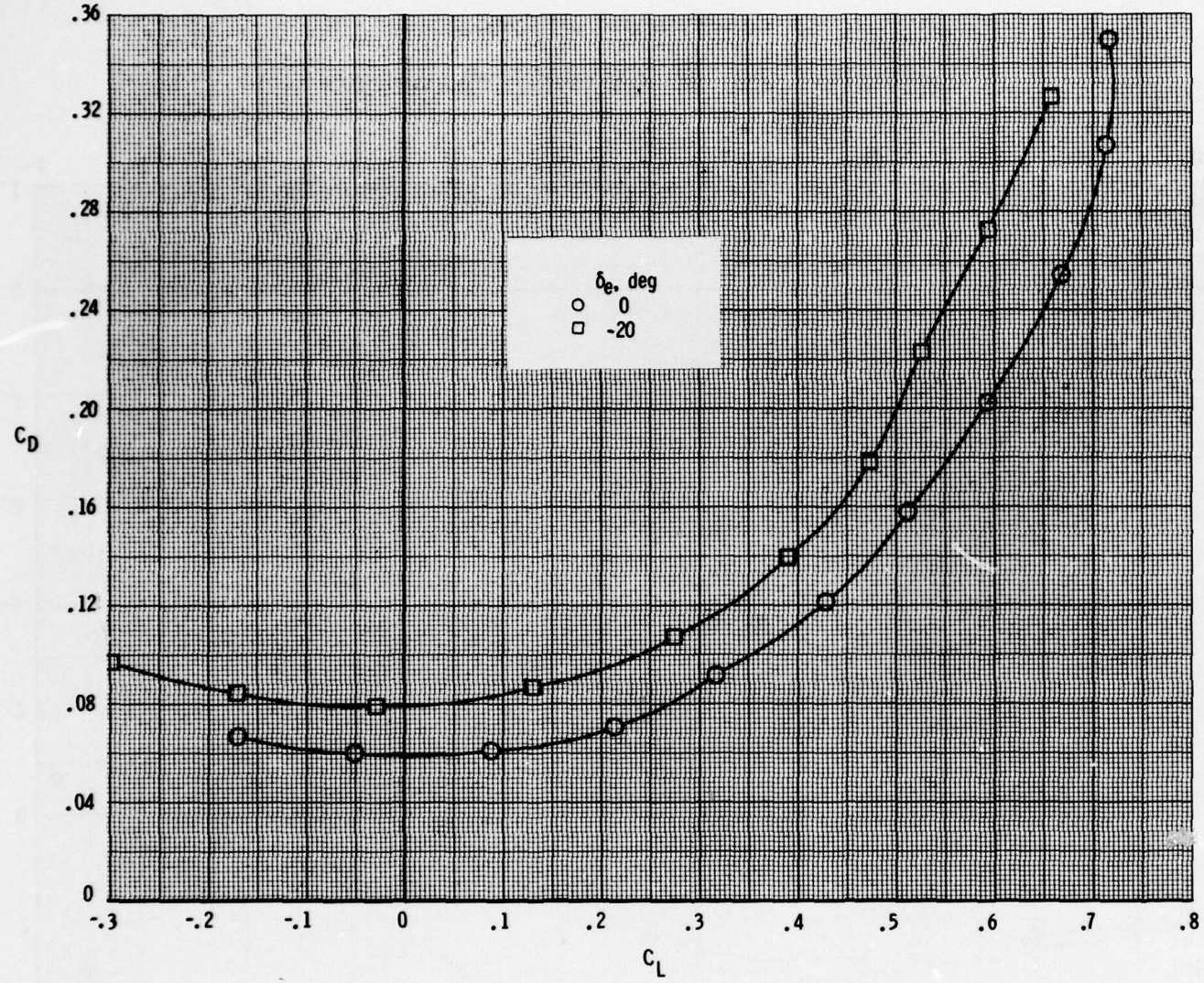

(c) C_D versus C_L; M = 0.9. Continued.

Figure 29.- Continued.

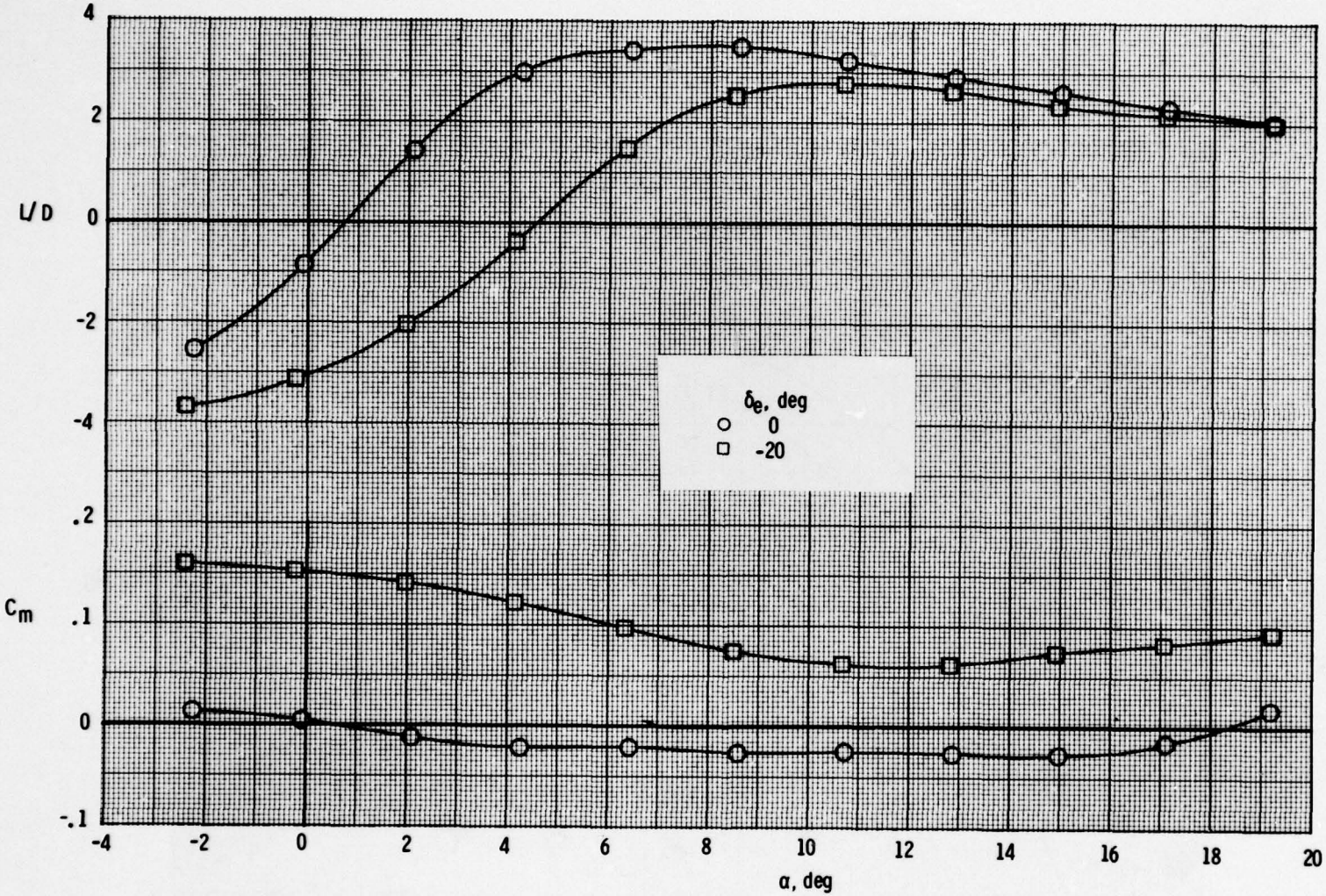

(c) L/D and C_m versus α; M = 0.9. Continued.

Figure 29.- Continued.

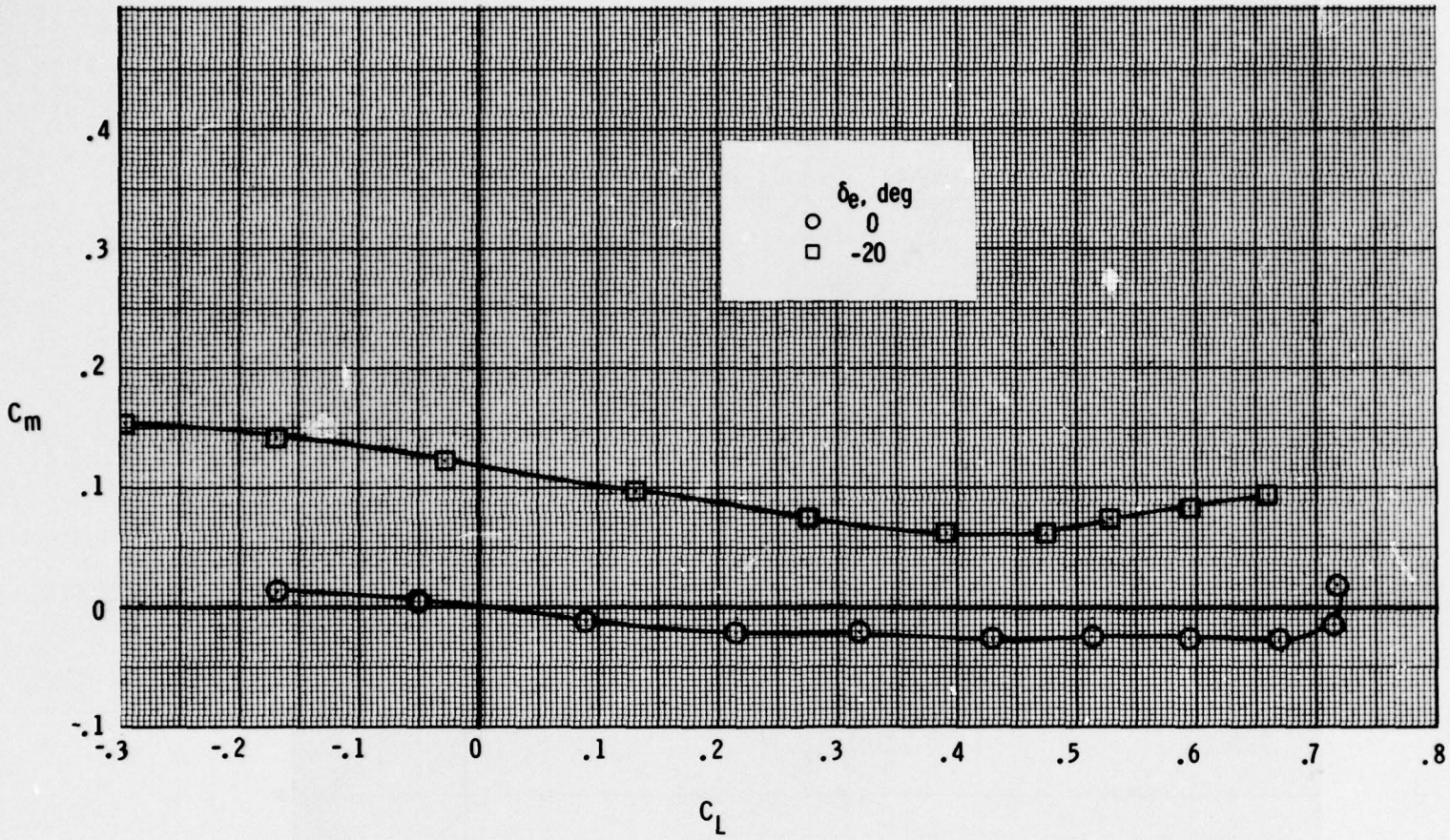

(c) C_m versus C_L; M = 0.9. Concluded.

Figure 29.- Continued.

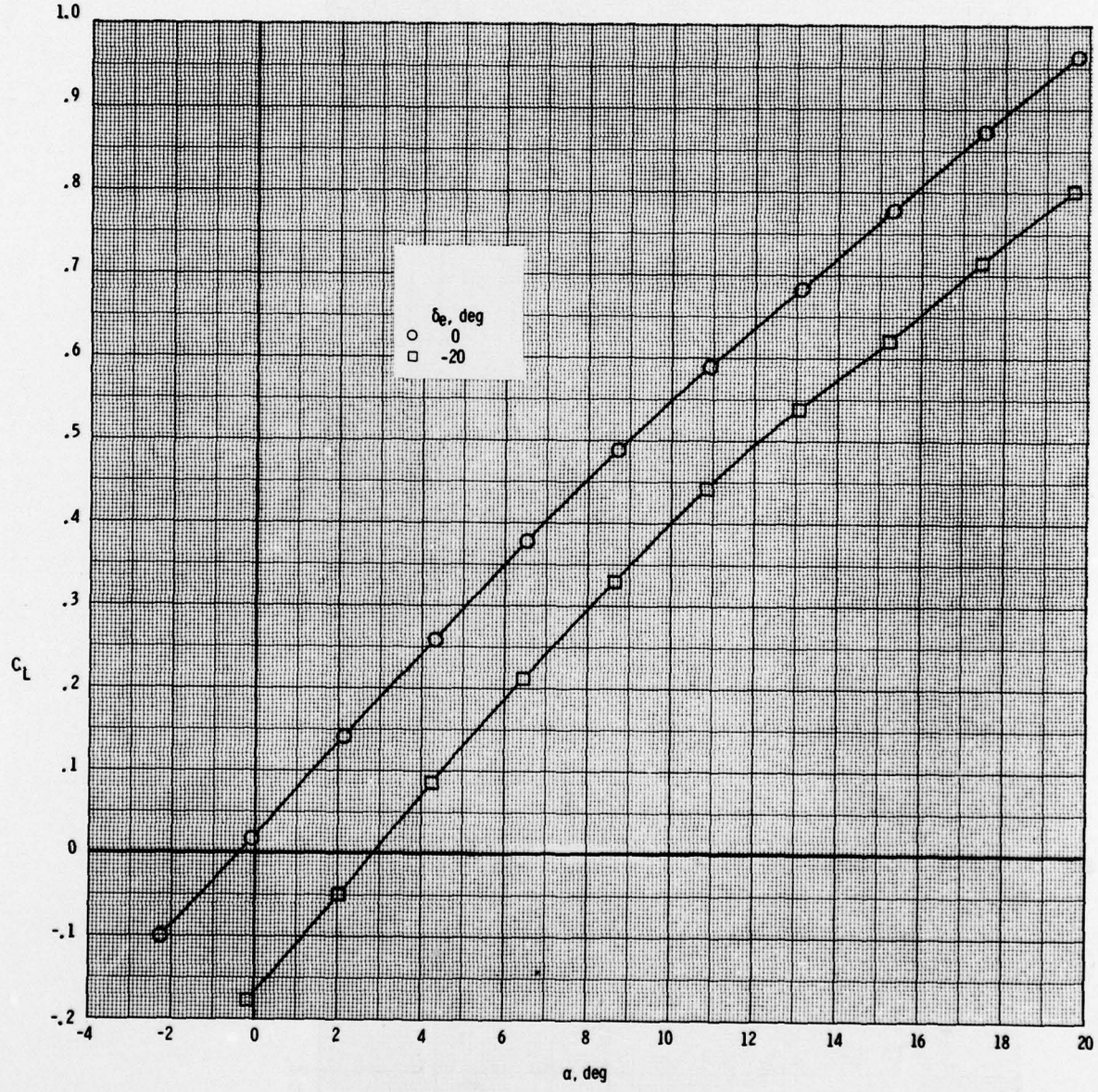

(d) C_L versus α; M = 1.2.

Figure 29.- Continued.

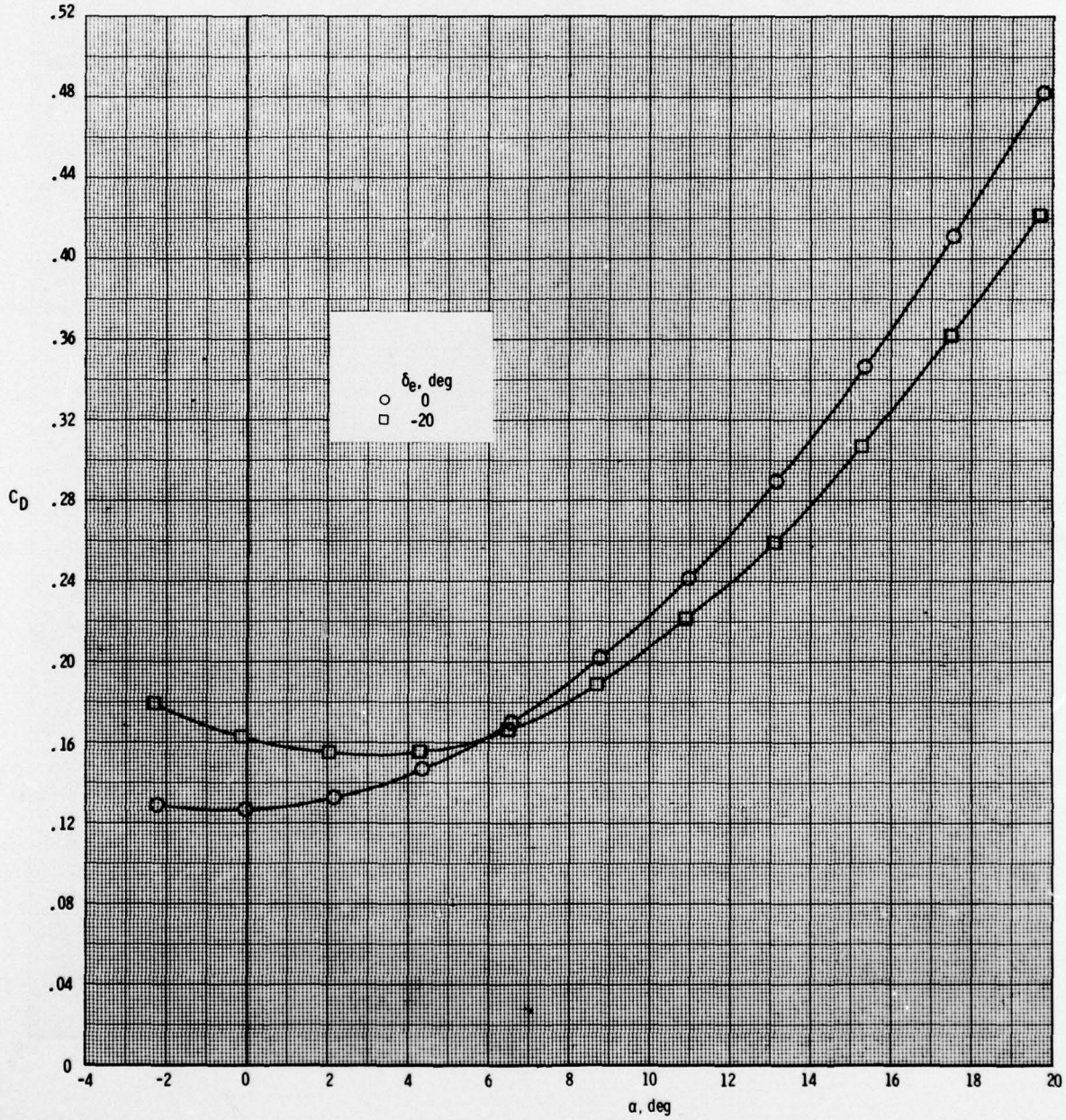

(d) C_D versus α; M = 1.2. Continued.

Figure 29.- Continued.

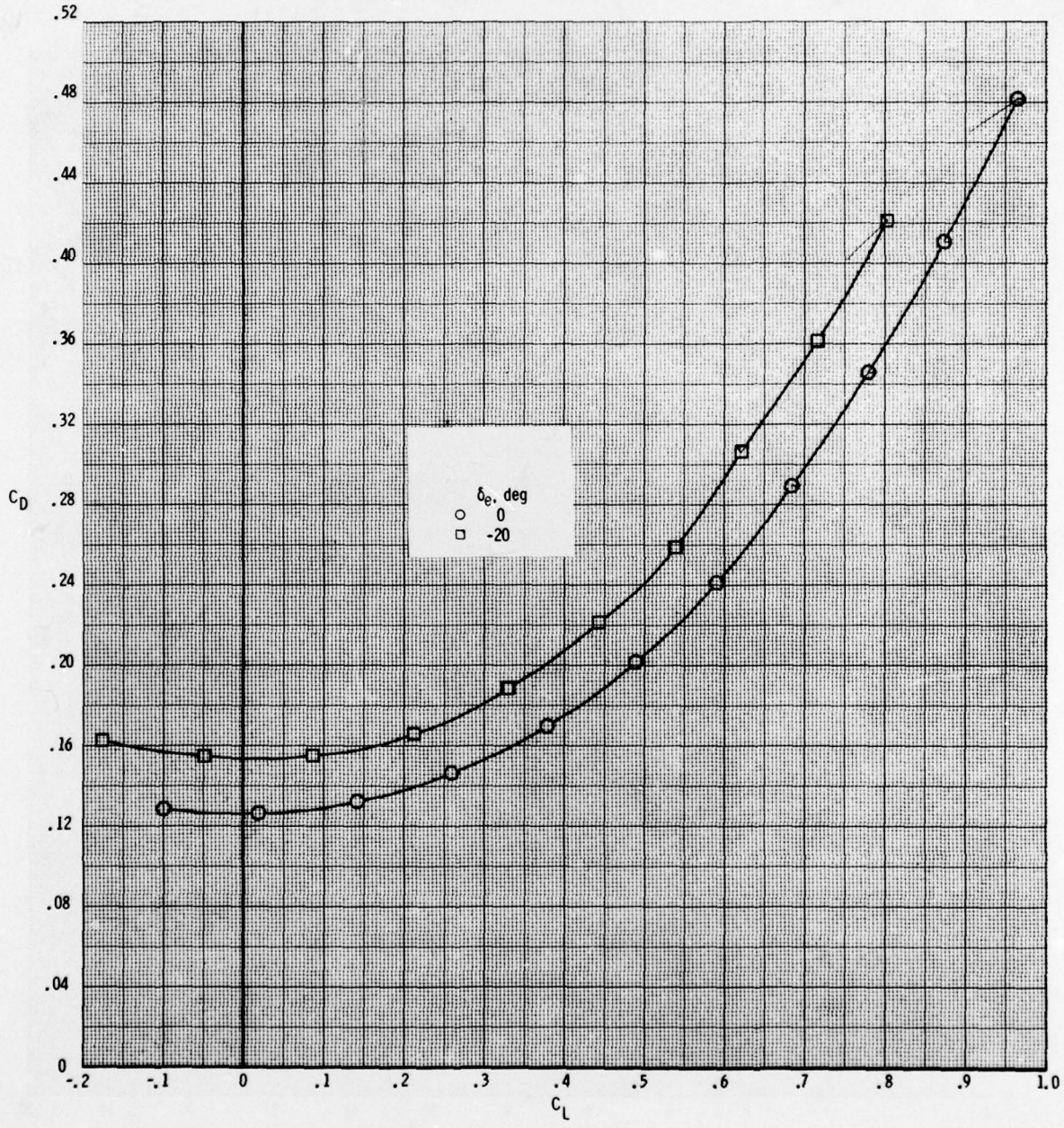

(d) C_D versus C_L; M = 1.2. Continued.

Figure 29.- Continued.

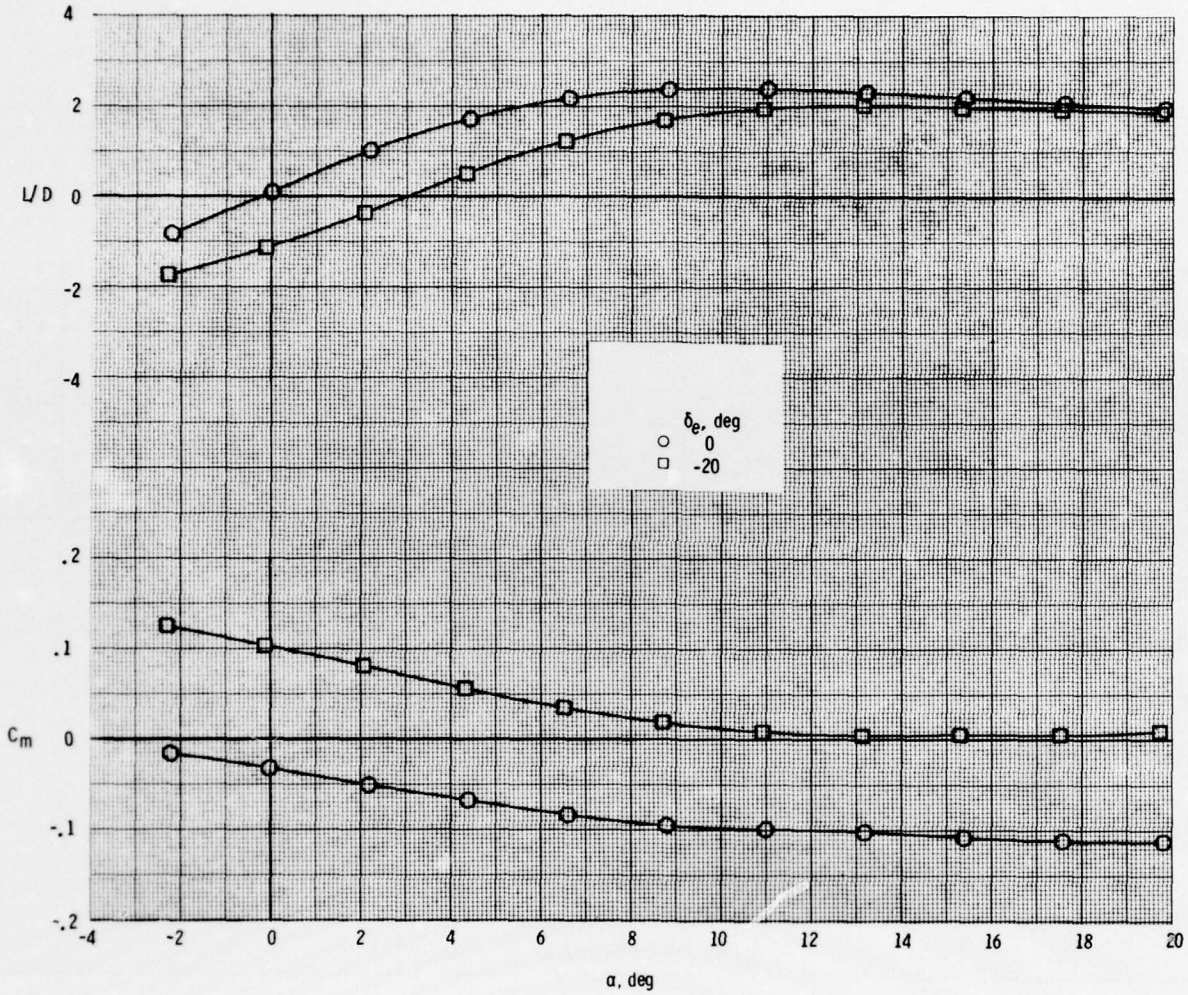

(d) L/D and C_m versus α; M = 1.2. Continued.

Figure 29.- Continued.

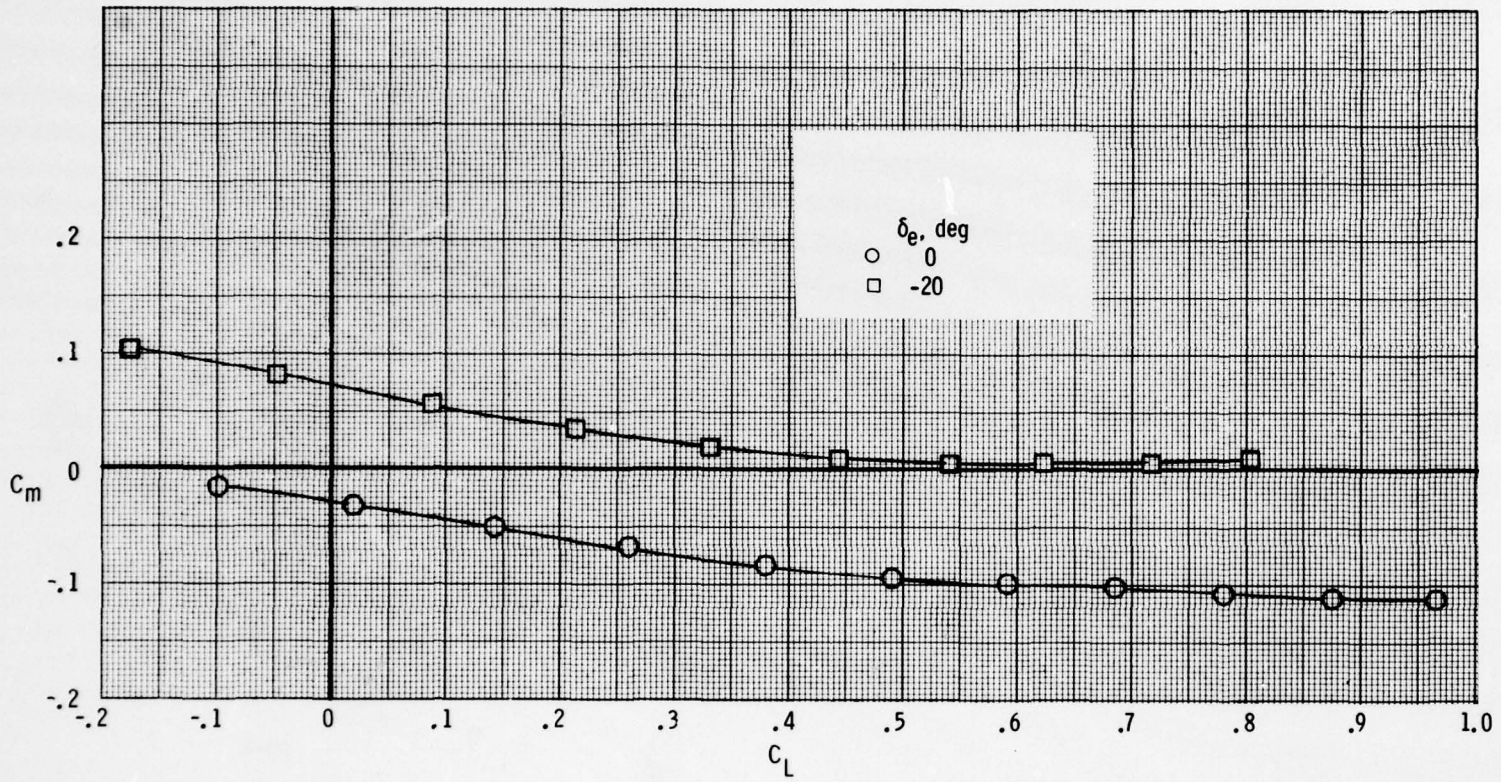

(d) C_m versus C_L; M = 1.2. Concluded.

Figure 29.- Concluded.

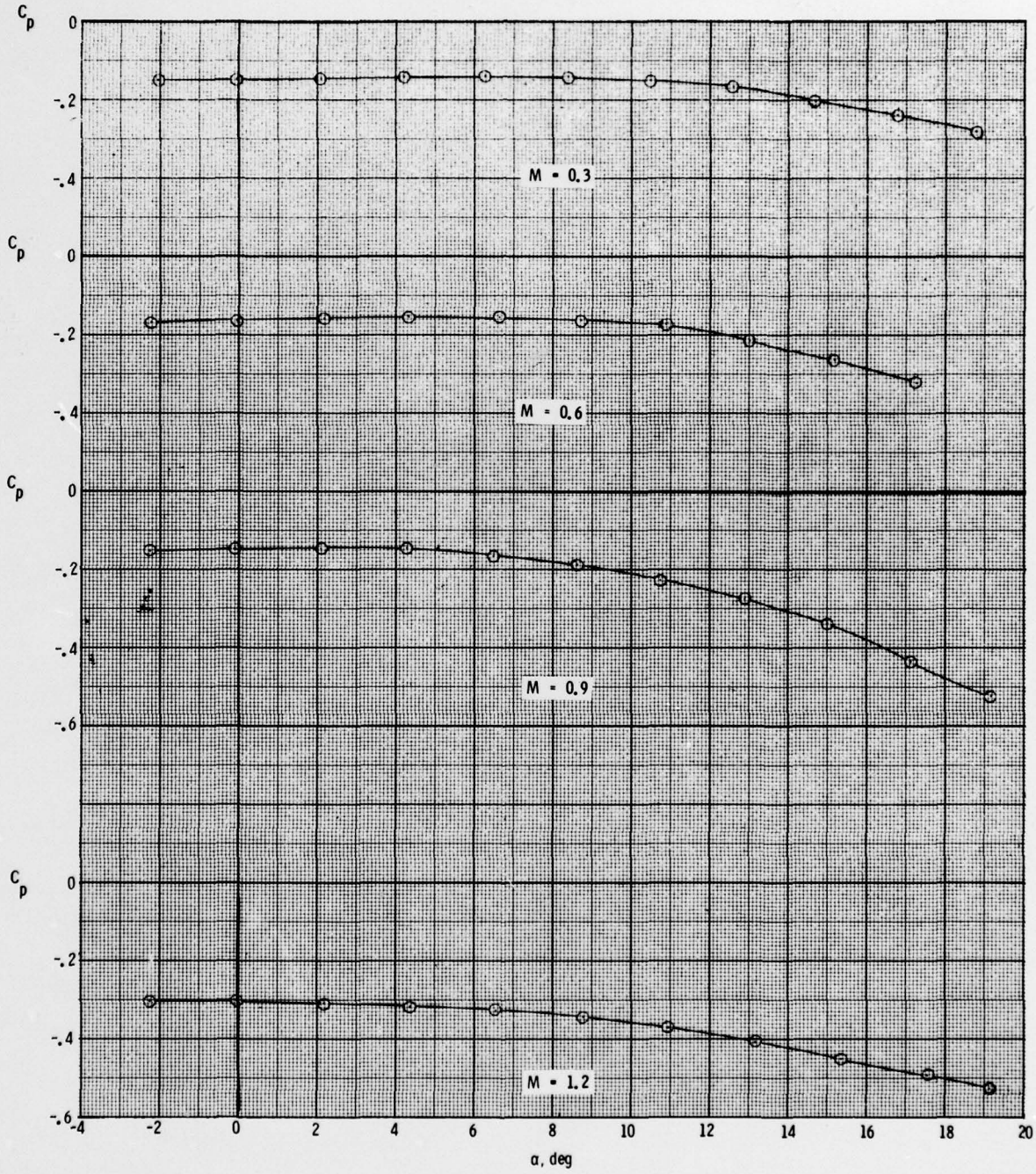

Figure 30.- Base pressure data measured during tests of baseline configuration. $\delta_e = 0^o$; $\delta_F = 0^o$.